



DGK Ausschuss Geodäsie (DGK)
der Bayerischen Akademie der Wissenschaften

Reihe C

Dissertationen

Heft Nr. 977

Bahareh Mohammadivojdan

**A Pipeline for Modeling Point-Sampled Surfaces:
From Preprocessing to Quality Assessment**

München 2026

Verlag der Bayerischen Akademie der Wissenschaften, München

ISSN 0065-5325

ISBN 978 3 7696 5389 2

A Pipeline for Modeling Point-Sampled Surfaces:
From Preprocessing to Quality Assessment

Von der Fakultät für Bauingenieurwesen und Geodäsie
der Gottfried Wilhelm Leibniz Universität Hannover
zur Erlangung des akademischen Grades
Doktor-Ingenieurin (Dr.-Ing.)
genehmigte Dissertation

von

Bahareh Mohammadivojdan, M. Sc.

München 2026

Verlag der Bayerischen Akademie der Wissenschaften, München

Adresse des Ausschusses Geodäsie (DGK)
der Bayerischen Akademie der Wissenschaften:



Ausschuss Geodäsie (DGK) der Bayerischen Akademie der Wissenschaften

Alfons-Goppel-Straße 11 • D – 80 539 München
Telefon +49 – 89 – 23 031 1113 • Telefax +49 – 89 – 23 031 - 1283 / - 1100
e-mail post@dgk.badw.de • <http://www.dgk.badw.de>

Prüfungskommission:

Vorsitzender: Dr.-Ing. habil. Christian Heipke
Referent: Prof. Dr.-Ing. Ingo Neumann
Korreferenten: Prof. Dr.-Ing. habil. Jürgen Müller
Prof. Dr. techn. Corinna Harmening

Tag der mündlichen Prüfung: 31.03.2026

Diese Dissertation ist auf dem Server des Ausschusses Geodäsie (DGK)
der Bayerischen Akademie der Wissenschaften, München unter <http://dgk.badw.de/>
sowie unter Wissenschaftliche Arbeiten der Fachrichtung Geodäsie und Geoinformatik
der Leibniz Universität Hannover (ISSN 0174-1454), Nr. 420,
<https://repo.uni-hannover.de/handle/123456789/21217>, Hannover 2026, elektronisch publiziert

© 2026 Ausschuss Geodäsie (DGK) der Bayerischen Akademie der Wissenschaften, München

Alle Rechte vorbehalten. Ohne Genehmigung der Herausgeber ist es auch nicht gestattet,
die Veröffentlichung oder Teile daraus zu vervielfältigen.

Abstract

The monitoring of the Earth's surface is increasingly driven by dense, point-sampled observations from techniques such as LiDAR, photogrammetry, multibeam echosounders (MBES), and satellite radar products like persistent scatterer interferometry (PSI). Despite their different sensing physics, these techniques typically generate large point clouds whose quality varies spatially and temporally. These point clouds are difficult to interpret because discrete points do not provide information about connectivity. These measurements are often non-uniformly distributed and contain data gaps. They are also contaminated by noise and outliers. Therefore, reliable use requires cleaning, surface modeling, and quality assessment. However, these steps are often handled separately with manual intervention and limited uncertainty reporting, which reduces reproducibility and weakens trust in the resulting products.

This cumulative dissertation presents an end-to-end pipeline for modeling point-sampled surfaces, from preprocessing to quality assessment. It synthesizes four publications that collectively develop and validate the proposed pipeline, including three peer-reviewed journal articles and one published conference paper. The pipeline has been designed to be scalable, reproducible, and uncertainty-aware. The work focuses on 2.5D surfaces, $z = f(x, y)$, balancing geometric suitability for large-scale geospatial products with computational tractability. The pipeline is built around a single multiresolution surface representation based on the Multilevel B-Spline Approximation (MBA) approach. This approach provides a consistent backbone for outlier detection, surface approximation, and uncertainty-aware evaluation. The methodologies are tested using PSI for deformation monitoring applications and MBES data for mapping, navigation, dredging, and infrastructure monitoring.

The preprocessing stage provides two complementary, surface-based outlier detection methods. One method uses a Data Adaptive, coarse-to-fine strategy to target sparse, isolated anomalies in large, heterogeneous deformation point sets, such as those in PSI. For MBES bathymetry, the Iterative Estimation of Surface Parameters (IESP) framework identifies clustered contamination by combining robust estimation and iterative, distribution-guided trimming until the residual behavior stabilizes. In the Hannover PSI case study, the Data Adaptive Outlier Detection method shows high agreement with a published reference filter, achieving a balanced accuracy of 0.95. For Kiel Canal MBES data, IESP achieves a balanced accuracy of 0.99 and reduces manual cleaning time from approximately two days to about 30 minutes. The output is a cleaned observation set for subsequent modeling and assessment. The modeling stage uses MBA as the common surface model and the geometric backbone of the pipeline. Its hierarchical refinement adds detail stepwise and remains robust under irregular sampling and data gaps. The quality assessment stage provides spatially varying uncertainty under two regimes. When observation variances are unknown, non-parametric bootstrapping yields prediction uncertainty and confidence intervals for MBA-based surfaces. When system-level error models are available, a forward uncertainty framework is used to estimate pointwise measurement uncertainty in MBES and propagate it into surface estimation. Simulations with known ground truth demonstrate that uncertainty-aware weighting reduces model error. For example, it decreases model error (1σ) from 0.044 m to 0.023 m. The output consists of uncertainty maps and confidence measures that make the local uncertainty transparent and facilitate interpretation of the results.

In sum, the dissertation presents a coherent pipeline that connects automated cleaning, MBA-based surface modeling, and uncertainty-aware quality assessment for point-sampled surfaces. The dissertation reduces subjectivity in preprocessing, improves the transparency of modeling decisions, and generates surface products with defensible uncertainty information to inform decisions in deformation monitoring and hydrographic applications.

Keywords: Surface model · Outlier detection · MBES · PSI · Deformation monitoring · Bootstrap · Uncertainty propagation · Quality assessment

Kurzfassung

Die Überwachung der Erdoberfläche wird zunehmend durch dichte, punktweise abgetastete Beobachtungen aus Verfahren wie LiDAR, Photogrammetrie, Mehrstrahl-Echoloten (Multibeam Echosounders, MBES) sowie satellitengestützten Radarsystemen wie der Persistent-Scatterer-Interferometrie (PSI) bestimmt. Trotz der Verwendung verschiedener physikalischer Messprinzipien generieren diese Techniken in der Regel große Punktwolken, deren Qualität in Abhängigkeit von der Zeit und dem Ort variiert. Die Interpretation dieser Punktwolken gestaltet sich als Herausforderung, da die einzelnen Punkte keine Informationen über Zusammenhänge liefern. Die vorliegenden Messungen weisen häufig eine ungleichmäßige Verteilung auf und enthalten Datenlücken. Darüber hinaus sind die Daten durch Rauschen und Ausreißer verfälscht. Für eine zuverlässige Nutzung sind daher eine Bereinigung, Oberflächenmodellierung und Qualitätsbewertung erforderlich. Diese Schritte werden jedoch oft separat mit manuellem Eingriff und unter eingeschränkter Berücksichtigung der Unsicherheiten durchgeführt. Dies verringert die Reproduzierbarkeit und schwächt das Vertrauen in die daraus resultierenden Produkte.

In der vorliegenden kumulativen Dissertation wird eine End-to-End-Pipeline zur Modellierung von punktweise abgetasteten Oberflächen vorgestellt. Diese erstreckt sich von der Vorverarbeitung bis zur Qualitätsbewertung. Die vorliegende Arbeit fasst vier Publikationen zusammen, die gemeinsam die vorgeschlagene Pipeline entwickeln und validieren. Darunter befinden sich drei begutachtete Zeitschriftenartikel und ein veröffentlichter Konferenzbeitrag. Die Pipeline ist auf Skalierbarkeit, Reproduzierbarkeit und den expliziten Umgang mit Unsicherheiten ausgelegt. Der Fokus der Arbeit liegt auf 2,5D-Oberflächen, $z = f(x, y)$, und es wird ein Ausgleich zwischen geometrischer Eignung für großräumige Geodatenprodukte und rechnerischer Effizienz geschaffen. Die Pipeline basiert auf einer multiresolutionellen Oberflächendarstellung, die auf dem Multilevel-B-Spline-Approximations-Ansatz (MBA) basiert. Dieser Ansatz bietet eine konsistente Grundlage für die Erkennung von Ausreißern, die Oberflächenapproximation und die Bewertung von Unsicherheiten. Die Methoden werden unter Verwendung von PSI für Deformationsüberwachungen und von MBES-Daten für Kartierung, Navigation, Baggerarbeiten und Infrastrukturüberwachung getestet.

Die Vorverarbeitungsphase umfasst zwei sich ergänzende, oberflächenbasierte Methoden zur Erkennung von Ausreißern. Eine Methode bedient sich hierbei einer datenadaptiven Grob-zu-Fein-Strategie, um isolierte Anomalien in großen, heterogenen Deformationsdatensätzen, wie sie beispielsweise in PSI auftreten, zu identifizieren. Für die MBES-Bathymetrie identifiziert das Iterative Estimation of Surface Parameters (IESP)-Verfahren gruppierte Ausreißerkontaminationen, indem es robuste Schätzungen und iteratives, verteilungsgesteuertes Trimmen kombiniert, bis sich das Restverhalten stabilisiert. In der PSI-Fallstudie Hannover zeigt die datenadaptive Ausreißererkenntnis eine hohe Übereinstimmung mit einem veröffentlichten Referenzfilter und erreicht eine Balanced Accuracy von 0,95. Für MBES-Daten aus dem Nord-Ostsee-Kanal erzielt IESP eine Balanced Accuracy von 0,99 und reduziert die manuelle Bereinigungszeit von etwa zwei Tagen auf rund 30 Minuten. Das Ergebnis sind bereinigte Beobachtungsdaten für die nachfolgende Modellierung und Bewertung. In der Modellierungsphase wird MBA als gemeinsames Oberflächenmodell und geometrisches Fundament der Pipeline verwendet. Die hierarchische Verfeinerung fügt schrittweise Details hinzu und bleibt auch bei unregelmäßiger Abtastung und Datenlücken robust. Die Qualitätsbewertungsphase generiert räumlich variierende Unsicherheiten unter zwei Bedingungen. Unter der Annahme, dass die Beobachtungsvarianzen unbekannt sind, generiert das nichtparametrische Bootstrapping Vorhersageunsicherheiten und Konfidenzintervalle für MBA-basierte Oberflächen. Liegen hingegen systemseitige Unsicherheitsmodelle vor, wird ein Vorwärtsansatz verwendet, um punktweise Messunsicherheiten in MBES zu schätzen und in die Oberflächenschätzung zu integrieren. Simulationen mit bekanntem Ground Truth zeigen, dass eine unsicherheitsbewusste Gewichtung den Modellfehler reduziert. So wurde beispielsweise der Modellfehler (1σ) von 0,044 m auf 0,023 m reduziert. Das Resultat manifestiert sich in Form von Unsicherheitskarten und Konfidenz-

maßen, welche die lokale Unsicherheit transparent machen und die Interpretation der Ergebnisse erleichtern.

Die vorliegende Dissertation präsentiert eine kohärente Pipeline, die automatisierte Bereinigung, MBA-basierte Oberflächenmodellierung und unsicherheitsbewusste Qualitätsbewertung für punktwise abgetastete Oberflächen miteinander verbindet. Die vorliegende Arbeit reduziert die Subjektivität in der Vorverarbeitung, verbessert die Transparenz von Modellierungsentscheidungen und generiert Oberflächenprodukte mit belastbaren Unsicherheitsinformationen. Dadurch können Entscheidungen in der Deformationsüberwachung und in hydrografischen Anwendungen signifikant unterstützt werden.

Schlagwörter: Oberflächenmodell · Ausreißerererkennung · MBES · PSI · Deformationsmonitoring · Bootstrap · Unsicherheitsfortpflanzung · Qualitätsbewertung

Acronyms

AFIS	amtlichen Festpunktinformationssystem	10
BA	Balanced Accuracy	33
BB	Back Board side	15
BfG	Federal Institute of Hydrology	38
BGR	Federal Institute for Geosciences and Natural Resources	12
CAGD	Computer-Aided Geometric Design	26
CI	confidence interval	3
DBM	Digital Bathymetric Model	1
DBSCAN	Density-Based Spatial Clustering of Applications with Noise	39
DEM	Digital Elevation Model	1
FN	False Negative	33
FP	False Positive	33
GIS	Geographic Information System	25
GMM	Gauss-Markov Model	24
GNSS	Global Navigation Satellite System	2
GUM	Guide to the Expression of Uncertainty in Measurements	52
GPU	Graphics Processing Unit	60
IESP	Iterative Estimation of Surface Parameters	32
IHO	International Hydrographic Organization	2
IMU	Inertial Measurement Unit	51
INS	Inertial Navigation System	15
InSAR	Interferometric Synthetic Aperture Radar	2
IRLS	Iterated Re-weighted Least Squares	22
KS	Kolmogorov-Smirnov	37
LS	Least Squares	5
LiDAR	Light Detection and Ranging	1
LOCI	Local Correlation Integral	21
LOF	Local Outlier Factor	21
LOS	Line-of-Sight	10
LR B-splines	Locally Refined B-splines	27
LR-MBA	Locally Refined MBA	27
M-Estimator	Maximum Likelihood Estimator	37
MBA	Multilevel B-spline Approximation	5
MBES	Multi-Beam Echo Sounder	3
MC	Monte-Carlo	17
MCC	Matthews Correlation Coefficient	34
MCM	Monte Carlo Method	52
MLS	Moving Least Squares	25
MRU	Motion Reference Unit	15
PC	point cloud	1
PDF	Probability Density Function	37
PDGPS	Precise Differential Global Positioning System	14
PHT-splines	Polynomial splines over T-meshes	27

PS	Persistent Scatterer	10
PSI	Persistent Scatterer Interferometry	2
RAR	Real Aperture Radar	9
RBF	Radial Basis Function	25
RMSE	Root Mean Square Error	43
RTK	Real Time Kinematic	14
SAR	Synthetic Aperture Radar	1
SBES	Single Beam Echo Sounder	13
SIR	Shuttle Imaging Radar	9
SLAR	Side-Looking Airborne Radar	9
SPDE	Stochastic Partial Differential Equation	61
STB	Star Board side	15
SVP	Sound Velocity Profile	14
T-splines	Truncated splines	27
THB-splines	Truncated Hierarchical B-splines	27
THU	Total Horizontal Uncertainty	15
TIN	Triangulated Irregular Network	25
TN	True Negative	33
TNR	True Negative Rate	34
TP	True Positive	33
TPR	True Positive Rate	33
TPU	Total Propagated Uncertainty	6
TVU	Total Vertical Uncertainty	15
UJL	Uwe Jens Lornsen	15
VCM	Variance Covariance Matrix	170
WAP	Wide Area Product	12
WSA	Elbe-North Sea (Tönning) Waterways and Shipping Office	15
WSV	The German Federal Waterways and Shipping Administration	15

Contents

1	Introduction	1
1.1	Motivation	1
1.2	Objectives and Research Questions	4
1.3	Overview of Original Publications	7
1.4	Datasets and Use Cases	8
1.4.1	PSI Data	9
1.4.2	MBES Data	13
1.5	Structure of the Thesis	18
2	State of the Art	19
2.1	Outlier Detection	19
2.1.1	General Principles	19
2.1.2	Instance-Based vs. Model-Based Approaches	20
2.1.3	Outlier Detection in PCs	21
2.2	Surface-Based Approximation Techniques	23
2.3	Quality Assessment of a Surface Model	28
3	Summary and Integration of Published Research: A Methodological Synthesis	31
3.1	Outlier Detection and Data Cleaning	32
3.1.1	Data Adaptive Outlier Detection	33
3.1.2	The IESP Approach	37
3.1.3	Comparison of Data Adaptive Outlier Detection and IESP	40
3.2	Surface Modeling	41
3.2.1	MBA	41
3.2.2	Evaluation of MBA	42
3.3	Uncertainty Quantification	47
3.3.1	Bootstrapping-Based Uncertainty Estimation	48
3.3.2	Forward Uncertainty Modeling	51
4	Conclusion	55
4.1	Summary	55
4.1.1	Overall Synthesis of the Pipeline	55
4.1.2	Answers to the Research Questions	56
4.1.3	Critical Reflection and Limitations	58
4.1.4	Implications and Generalization of the Pipeline	59
4.2	Outlook	60
5	List of additional publications	63
6	Publications	65
6.1	Publication A	67
6.2	Publication B	91
6.3	Publication C	123
6.4	Publication D	147

A Supplementary Material	163
A.1 MBA	163
A.1.1 B-Spline Approximation	163
A.1.2 Hierarchical B-Spline Approximation	166
A.1.3 Optimization with B-Spline Refinement	167
A.1.4 Stochastic Model of MBA	169
Bibliography	173
List of Figures	187
List of Tables	189
Acknowledgments	193
Curriculum Vitae	195

1 Introduction

1.1 Motivation

Earth surface observation today is possible through a wide range of acquisition technologies, from basic sensors to advanced systems such as airborne Light Detection and Ranging (LiDAR), Synthetic Aperture Radar (SAR) satellites, photogrammetry, mobile mapping platforms, and hydroacoustic sensors. These systems employ both active and passive measurement methods, spanning electromagnetic and acoustic domains, and operate from land, air, and space. They enable the efficient collection of large and complex geospatial datasets (Patane, 2016). Such data are essential for producing Digital Elevation Models (DEMs) and Digital Bathymetric Models (DBMs), updating reference frames, monitoring surface deformation and subsidence, and supporting safety-critical applications such as navigation and charting.

All of these measurement techniques produce different data products that can be represented as discrete, spatially referenced point samples. The discrete point cloud (PC) does not provide information about the connectivity between points. Understanding the underlying patterns in the data is therefore crucial. This not only improves the visibility and interpretation of datasets from different perspectives but also provides the means to track changes in the Earth's surface more effectively. However, the measurements are often non-uniformly distributed, contain large data gaps, and are contaminated by noise and outliers. Beyond the necessary step of data cleaning, it is essential to mathematically model the data to obtain a continuous surface. Such a representation allows estimation at any position and prediction in areas with few observations, helping to overcome these challenges and enabling unique and consistent modeling of the area of interest.

In all cases, the reliability of the resulting models is critical. If errors are ignored or quality is inadequately handled, the consequences can extend to infrastructure risks, poor environmental monitoring, or unsafe navigational information. At the same time, data volumes are growing rapidly while processing capacity has not kept pace. For example, LiDAR acquisition speeds have increased by two orders of magnitude, reaching over one million points per second within only four years (Patane, 2016). At this scale, modeling and processing become bottlenecks, leaving many large datasets underused. Furthermore, PCs from different sources vary in density, coverage, measurement precision, and noise characteristics. These variations make it essential to apply standardized, quality-assured, and consistent processing strategies to ensure reliable and usable models.

To illustrate the implications of these challenges, two contexts of high public relevance are considered. The first concerns inland waterways, where safe and efficient navigation requires reliable bathymetric surfaces, for example DBMs. The second addresses land areas, where ground movement threatens infrastructure and undermines the stability of geodetic reference frames.

Europe operates approximately 41,000 kilometers of inland waterways across 25 member countries and transports around 150 billion tonne-kilometers of cargo annually (European Commission, 2021). The European Union aims to increase this share by 25 % by 2030 and 50 % by 2050 (Niu et al., 2024; European Commission, 2021). Achieving these targets requires efficient, reliable, and safe

navigation, which in turn depends on accurate and up-to-date DBMs of the fairway and surrounding areas (European Commission, 2025). Yet, climate variability and data inconsistency continue to threaten the reliability of these models (Ebner von Eschenbach et al., 2022). As a result, public authorities now emphasize quality assurance and the modernization of digital services as essential components of inland waterway management (Niu et al., 2024; European Commission, 2025; Artz et al., 2021). At the national level, Germany illustrates the stakes. Its federal waterways offer about 10,000 km for commercial and recreational use (BMDV, 2024). Freight transport performance is projected to grow by about 38 % from 2010 to 2030 (BMDV, 2016). The Federal Transport Infrastructure Plan 2030 allocates about 269.6 billion euros, of which about 69 % is designated for maintenance and 9.1 % for federal waterways (BMDV, 2016). Authorities warn that using outdated or deficient charts, paper or electronic, may be considered gross negligence by investigative bodies, with consequences for licensing and insurance (BMDV, 2024). Operating at this scale, and meeting these expectations, requires timely, reliable, and automated production of DBMs with defensible uncertainty, so navigational information remains current and risk is controlled (European Commission, 2025).

This demand for accurate geospatial information also applies on land, where ground movement poses persistent risks. Such movement can result from subsidence, uplift, landslides, groundwater extraction, construction, or mining activity. Even subtle shifts, on the order of millimeters per year, can damage infrastructure, disrupt utilities, or alter surface drainage, as shown in studies from urban areas and river deltas worldwide (Poland, 1984; Barends et al., 1995; Strozzi et al., 2001). In Germany, regions such as Saarland have experienced significant subsidence linked to historical hard coal mining (Spreckels, 2023). Systematic analyses have also shown that about 30 % of Lower Saxony exhibits ground movement (Jahn et al., 2011). These changes also compromise the national geodetic reference frame. Fixed points drift, coordinate systems age, and undetected displacement introduces error into public services and geospatial applications. Maintaining a stable and current reference system requires regular monitoring and demand-driven updates (Brockmeyer, 2024a). While traditional surveying methods such as leveling, Global Navigation Satellite System (GNSS), and total stations offer high precision, they are limited in spatial coverage and costly to repeat at scale (Li et al., 2015; Shamshiri et al., 2014; Harmening & Neuner, 2020). To address this, satellite-based methods such as Interferometric Synthetic Aperture Radar (InSAR), particularly Persistent Scatterer Interferometry (PSI), now offer dense, area-wide coverage with millimeter-level sensitivity. This enables more frequent updates of DEMs (Strozzi et al., 2001). In Germany, the Federal Institute for Geosciences and Natural Resources (BGR) provides PSI-based motion products nationwide through the Bodenbewegungsdienst service (Kalia et al., 2017, 2021; BGR, 2025). Despite their potential, these datasets still contain noise and outliers, and transforming them into reliable DEMs requires robust, automated quality control procedures.

Achieving a continuous representation from a PC is a complex task, both computationally and mathematically. A practical processing strategy can be structured in three stages. The first stage is preprocessing and data cleaning, which removes outliers and reduces noise. The second stage is surface modeling, which transforms the point samples into a continuous representation suitable for downstream use. The third stage is quality assessment, which quantifies uncertainty, validates results against independent data, and documents the model's fitness for use.

Preprocessing is the first step, and it is critical to ensure clean and reliable input data. PCs often include noise, outliers, and artifacts caused by environmental conditions, sensor performance, or the measurement process. This stage is often the most labor-intensive, especially in domains like hydrography, where analysts must distinguish outliers from real seafloor features that may represent navigational hazards. Although such errors account for less than 1 % of the data (Debes, 2007), some resemble real features and must be carefully reviewed to avoid misclassification, as they can distort models and degrade quality. The International Hydrographic Organization (IHO)

recommends documented automated tools, yet it still requires extensive manual inspection by trained experts. As a result, hydrographic data cleaning remains costly, subjective, and slow.

After preprocessing, point samples must be transformed into a continuous surface. Generally, a DEM represents the bare-earth in digital form by defining a function f that describes the terrain. In practice, DEMs are usually restricted to a 2.5D formulation, $z = f(x, y)$, which assigns a single height value to each two-dimensional location. Fully 3D surfaces, capable of modeling features such as overhangs and bridges, are rare and typically used only for small areas (Vosselman & Maas, 2010). During modeling, the characteristics of the data must be considered. Sampled points are typically distributed irregularly, with non-uniform density across the domain. Obstacles, sensor geometry, and acquisition failures often result in coverage gaps. Many workflows rely on fixed representations, such as raster grids or triangulated meshes. However, these formats constrain the handling of irregular sampling and heterogeneous sources. Raster-based methods require a fixed grid, and selecting an appropriate cell size involves trade-offs between resolution, storage, and sensitivity to noise. Grids can also blur sharp features and introduce edge effects. A continuous surface model offers a more coherent and flexible representation of the underlying field (Patane, 2016). B-spline surface models address many of these issues while also reducing data size. They compactly represent smooth surfaces using a limited number of control points or basis function coefficients instead of storing all raw samples. This reduces storage demands and typically improves processing and visualization speed. For example, this is particularly useful for high-density Multi-Beam Echo Sounder (MBES) data (Skytt et al., 2017). In addition, hierarchical and locally refined spline frameworks support efficient surface storage by reducing the effective data dimension while preserving accuracy. When used as the final representation, B-spline surfaces are more compact than raw PCs or dense rasters, which accelerates downstream computation and rendering (Patane, 2016).

A continuous surface model provides a single, reproducible representation of the underlying field. In practice, however, it does not capture variability introduced by acquisition or sampling design. Many workflows address this limitation using multiple realizations of the same phenomenon, each expressing different levels of uncertainty. This concept is common in spatial modeling when inputs are heterogeneous or when occlusions and data gaps are present (Viard et al., 2011). This leads to the third stage: quality assessment and uncertainty determination. Uncertainty in spatial data has several sources. It may arise from limited accuracy or precision, inconsistent or incomplete coverage, or the limitations of the sensor and method. Sampling density and the spatial resolution of observations also play a key role. Sparse sampling relative to surface complexity increases uncertainty. These aspects can be quantified statistically, through confidence intervals (CIs), absolute error measures, or bounded value ranges (Patane, 2016). Quantifying uncertainty is necessary to reveal how much confidence can be placed in different parts of the model. The result is a set of uncertainty bounds and reliability maps. Thresholds for change detection can be adjusted accordingly, high-uncertainty areas can be prioritized for re-survey, and CIs can be reported alongside derived products. Uncertainty statements should accompany every surface model so that end users can judge fitness for use (Patane, 2016; Wackernagel, 2003).

This dissertation addresses the current lack of reproducible, uncertainty-aware processing strategies for heterogeneous PCs. Existing workflows often treat preprocessing, modeling, and quality control as separate, manual, or application-specific steps. This fragmentation limits comparability, increases subjectivity, and weakens trust in downstream decisions. The proposed pipeline integrates automated preprocessing, surface-based modeling, and quality assessment into a coherent and scalable framework. The pipeline is modular, and each stage can in principle be replaced by alternative methods, provided that the stage assumptions and required outputs remain consistent. The methodology is applied and tested for high-impact domains such as MBES and PSI, where data heterogeneity, irregular sampling, and uncertainty propagation pose practical challenges. These

methods are designed to be generalizable to other geospatial datasets and support the growing need for defensible geospatial products in safety-critical and operational contexts. Although the methods are demonstrated for PSI and MBES, they are designed around generic properties of point-sampled surfaces, irregular sampling, data gaps, and spatially varying measurement quality. Under the same 2.5D surface assumption, this design is intended to be transferable to other elevation-type PCs such as airborne LiDAR or photogrammetric surface models, but this transfer is not validated within the scope of this dissertation. Efficiency was treated as a design constraint throughout, both in algorithmic structure and in reducing manual intervention. Apart from the runtimes reported for specific case studies, this dissertation does not provide a dedicated runtime benchmark across all stages and datasets. This work is timely. Geospatial data collection has outpaced our ability to process and use it efficiently. Valuable information remains locked in raw PCs because current tools are not scalable, reproducible, or quality-aware. This pipeline helps unlock that value. It enables more reliable use of existing data, reduces processing effort, and supports applications that depend on trustworthy, uncertainty-informed models. Against this background, there is a need for a coherent, scalable processing pipeline for point-sampled surfaces.

1.2 Objectives and Research Questions

The thesis pursues the following overarching objective and related research questions. Although many individual methods exist for tasks such as outlier detection, surface modeling, and uncertainty analysis, these are typically treated as isolated steps and are often tailored to specific data types or use cases. As a result, there remains no unified approach that systematically integrates all stages of the modeling process. **The overarching objective of this thesis is to develop an end-to-end processing pipeline for surface-based geospatial data that harmonizes and automates preprocessing, surface approximation, and quality assessment in a flexible and scalable framework.**

To reach this objective, three interdependent sub-goals are pursued. The first addresses the critical challenge of outlier detection, which is particularly relevant for large-scale, noisy PC data acquired under operational conditions. Despite broad and ongoing research and investigation on this topic (see Section 2.1), many existing approaches rely on strong assumptions, require expert-defined thresholds, or are unsuitable for datasets where the underlying geometry is unknown. Moreover, in applications such as MBES surveys, outliers may appear in different forms, including both isolated and clustered patterns. Fig. 1.1 illustrates these types. Both isolated and clustered outliers can bias model fitting if left untreated; however, isolated outliers are typically easier to detect and remove, whereas clustered outliers are more challenging and complicate automatic detection. Manual inspection is impractical due to the data volume and the ambiguity at local scales, necessitating the need for automated, data-driven approaches. This challenge motivates the first sub-goal of the thesis:

RQ 1) Design and validate an automatic preprocessing strategy to detect isolated and clustered outliers in heterogeneous PCs without ground truth labels.

After preprocessing, the next step is to approximate the cleaned PC with a continuous surface representation. A suitable surface model is required to transform irregular and discrete samples into a mathematically defined form that preserves the essential characteristics of the observed geometry. B-spline surfaces are well suited to this task: they allow complex geometries to be approximated flexibly, store information compactly in the form of control points, and support efficient storage, exchange, and visualization.

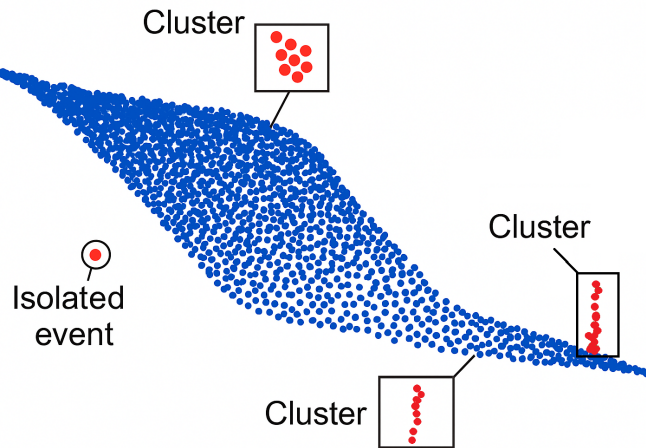


Figure 1.1: *Examples of outlier types: isolated points and spatially coherent clusters.*

Applying B-spline surfaces to geospatial PCs such as those obtained from MBES or PSI is, however, far from straightforward. While many B-spline formulations are effective for structured or dense datasets, they cannot be directly applied to the heterogeneous and irregular data typical in geospatial applications. When dealing with large volumes, uneven sampling, and data gaps, the approximation process becomes computationally demanding. Estimating B-spline parameters requires forming and inverting design matrices composed of basis function evaluations. For very large datasets, this inversion is costly, and in the presence of data gaps, the design matrix may lose rank, making a pure Least Squares (LS) solution infeasible. Regularization strategies are often needed to stabilize the system (Nowacki et al., 1998). Moreover, non-uniform point densities can reduce approximation quality or introduce numerical instabilities, further limiting the robustness of many conventional B-spline approaches (Bracco et al., 2018).

To address these challenges, this thesis employs the Multilevel B-spline Approximation (MBA) approach introduced by Lee et al. (1997). Alternative surface modeling strategies exist, and the rationale for selecting MBA is discussed in Section 2.2. By incrementally refining the approximation across multiple levels, MBA achieves computational efficiency while remaining robust to irregular sampling and data gaps. The method produces a 2.5D B-spline surface, which is also the focus of this dissertation. Here, MBA is applied not only for surface approximation but also as the underlying representation for outlier detection and uncertainty modeling, thereby establishing a unifying element across the pipeline. These considerations define the second sub-goal of the thesis, namely assessing the suitability of MBA for irregular spatial PCs:

RQ 2) Evaluate MBA for representing large, irregular, and noisy spatial PCs, and assessment of its suitability as a common surface model within the processing pipeline.

The third challenge of the pipeline concerns the determination of model quality. Any surface approximation remains incomplete without an assessment of its uncertainty, which reflects both the reliability of the observations and the adequacy of the model (Viard et al., 2011). In general, there are several approaches to quantify uncertainty. When information on observation quality, such as standard deviations, is available, uncertainty can be propagated through the approximation process to obtain prediction uncertainties. If ground truth data are available, model outputs can be compared directly against reference values. Alternatively, cross-validation techniques may be applied, in which part of the dataset is withheld during modeling and later used to evaluate predictive uncertainty. Leave-one-out cross-validation enables direct comparison of residuals with predicted standard deviations to assess model adequacy and bias (Wackernagel, 2003).

In the context of MBA, however, the situation is more complex. Even if observation variances are available, error propagation is not reliable because the hierarchical refinement levels are strongly correlated. These correlations are difficult to incorporate in a closed-form adjustment, and the resulting estimates tend to be overly optimistic (Mohammadijordan et al., 2021). Furthermore, in many practical geospatial applications, ground truth is not accessible. To overcome these limitations, this thesis employs a nonparametric bootstrap approach (Efron, 1981; Efron & Tibshirani, 1994). Bootstrapping provides a realistic method for quantifying the effects of sampling and model complexity on the resulting surface. It yields an empirical estimate of prediction uncertainty without relying on variance assumptions or ground truth data.

For MBES datasets, the difficulty lies in the lack of reliable per-point uncertainty information. To address this, a forward uncertainty model of a specific MBES system is developed based on prediction models proposed by Hare (1995). This model propagates uncertainties from the individual measurement elements through the full processing chain to derive the Total Propagated Uncertainty (TPU). The forward modeling can be applied both to real surveys and to simulated environments with known ground truth. The simulation framework enables testing of how measurement uncertainty affects surface modeling and assessment of whether incorporating this information can improve both the modeling process and the final uncertainty estimates.

RQ 3) Quantifying uncertainty of the MBA surface model under two regimes: (a) when observation variances are unknown (b) when system uncertainty models are available.

These research questions are addressed through studies using real PSI and MBES datasets as well as simulated data. This dissertation is written in a cumulative format and consists of three peer-reviewed journal articles (Publications A, B, and C) and one conference paper without peer-review (Publication D). These publications are integrated and contextualized within this overarching text, which establishes their relevance to the overall research pipeline. Fig. 1.2 provides an overview of the relationship between the research questions and the respective publications. The contributions related to RQ 1, which focuses on outlier detection and preprocessing, are discussed in Section 3.1.1. This section draws primarily on the findings from Publications A and B. The contributions addressing RQ 2, which concerns the development of robust surface modeling approaches, are presented in Section 3.2. This part integrates insights from Publications A, B, C, and D. Finally, Section 3.3 details the results and methods developed in relation to RQ 3, which focuses on uncertainty modeling and quality assessment. Publications A and C contribute partially to this part.

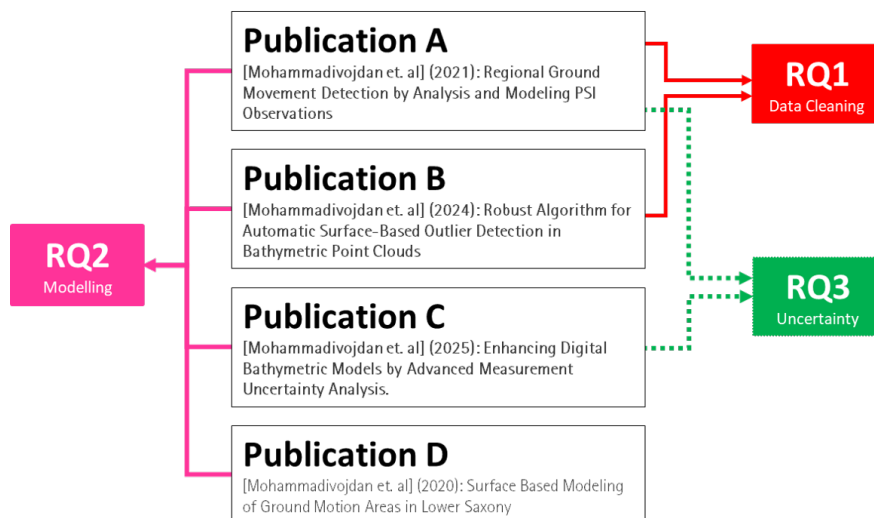


Figure 1.2: Overview of original publications on the cumulative dissertation.

1.3 Overview of Original Publications

These objectives are addressed through methodological contributions and investigations on a pipeline for modeling point-sampled surfaces from preprocessing to quality assessment. The relevant publications of the author are listed in Chapter 6. They were published in peer-reviewed outlets and presented at scientific conferences and workshops, with one additional non-peer-reviewed contribution. Fig. 1.2 illustrates how these publications relate to the research questions. This dissertation draws on three peer-reviewed journal publications (Publications A (Mohammadivojdan et al., 2021), B (Mohammadivojdan et al., 2024), and C (Mohammadivojdan et al., 2025)) and one non-peer-reviewed publication (Publication D (Mohammadivojdan et al., 2020)).

- **Publication A:**
Mohammadivojdan, B.; Brockmeyer, M.; Jahn, C.-H.; Neumann, I.; Alkhatib, H. (2021): Regional Ground Movement Detection by Analysis and Modeling PSI Observations. In: Remote Sensing, 13(12), 2246. <https://doi.org/10.3390/rs13122246>, licensed under CC BY 4.0, <https://creativecommons.org/licenses/by/4.0>
- **Publication B:**
Mohammadivojdan, B.; Lorenz, F.; Artz, T.; Weiß, R.; Hake, F.; Alkhatib, Y.; Neumann, I.; Alkhatib, H. (2024): Robust algorithm for automatic surface-based outlier detection in MBES point clouds. In: Marine Geodesy, 48(2), 141–172. <https://doi.org/10.1080/01490419.2024.2408684>, licensed under CC BY 4.0, <https://creativecommons.org/licenses/by/4.0>
- **Publication C:**
Mohammadivojdan, B.; Hake, F.; Lorenz, F.; Bollert, J.-O.; Weiss, R.; Artz, T.; Neumann, I.; Alkhatib, H. (2025): Enhancing digital bathymetric models by advanced measurement uncertainty analysis. In: The International Hydrographic Review, 31(1), 28–50. <https://doi.org/10.58440/ihr-31-1-a09>
- **Publication D:**
Mohammadivojdan, B.; Alkhatib, H.; Brockmeyer, M.; Jahn, C.-H.; Neumann, I. (2020): Surface Based Modelling of Ground Motion Areas in Lower Saxony. Hannover: Institutionelles Repositorium der Leibniz Universität Hannover, 2020, pp. 107–122. <https://doi.org/10.15488/9344>, licensed under CC BY 3.0, <https://creativecommons.org/licenses/by/3.0>

In the following, the contributions of the individual authors to Publications A–D are presented in detail:

Publication A

- **Main author (B. Mohammadivojdan):** Conceptualization and design of the study, execution of the experiments, data analysis, writing of the manuscript, and correspondence during the review process.
- **M. Brockmeyer:** Support in developing and implementing the comparison methodology and in data visualization.
- **C.-H. Jahn:** Review and revision of the manuscript.
- **I. Neumann:** Methodological advice and technical expertise, review and revision of the manuscript.
- **H. Alkhatib:** Methodological advice and technical expertise, review and revision of the manuscript.

Publication B

- **Main author (B. Mohammadivojdan):** Conceptualization and design of the study, execution of the experiments, data analysis, writing of the manuscript, and correspondence during the review process.
- **F. Lorenz:** Support in preparing the labeled data, reviewing and revising the manuscript.
- **T. Artz:** Review and revision of the manuscript.
- **R. Weiß:** Review and revision of the manuscript.
- **F. Hake:** Review and revision of the manuscript.
- **Y. Alkhatib:** Support in conducting the comparative study of methods.
- **I. Neumann:** Review and revision of the manuscript.
- **H. Alkhatib:** Methodological advice and technical expertise, review and revision of the manuscript.

Publication C

- **Main author (B. Mohammadivojdan):** Conceptualization and design of the study, execution of the experiments, data analysis, writing of the manuscript, and correspondence during the review process.
- **F. Hake:** Support in conducting the simulation experiments.
- **F. Lorenz:** Review and revision of the manuscript.
- **J.-O. Bollert:** Support in conducting the simulation experiments.
- **R. Weiss:** Review and revision of the manuscript.
- **T. Artz:** Review and revision of the manuscript.
- **I. Neumann:** Review and revision of the manuscript.
- **H. Alkhatib:** Methodological advice and technical expertise, review and revision of the manuscript.

Publication D

- **Main author (B. Mohammadivojdan):** Conceptualization and design of the study, execution of the experiments, data analysis, writing of the manuscript, and correspondence during the review process.
- **H. Alkhatib:** Methodological advice and technical expertise, review and revision of the manuscript.
- **M. Brockmeyer:** Support in developing and implementing the comparison methodology.
- **C.-H. Jahn:** Review and revision of the manuscript.
- **I. Neumann:** Methodological advice and technical expertise, review and revision of the manuscript.

Together, Publications A to D cover the main stages of the proposed pipeline, from preprocessing and surface modeling to uncertainty analysis and quality assessment. In Chapter 3, the four publications are summarized, their main contributions are highlighted, and their roles within the overall pipeline are discussed. For all four publications, the methods are implemented and evaluated on PSI and MBES datasets, which are introduced in the following section.

1.4 Datasets and Use Cases

This section introduces the primary PSI and MBES datasets used in the cumulative research, which provide the empirical foundation for developing, testing, and validating the proposed techniques. The work focuses on two main data types: PSI and MBES bathymetric data. Each of these

environments represents a distinct measurement context: land surface deformation and underwater topography. However, both are processed and modeled within a unified pipeline designed for point-sampled surfaces.

A PC is a collection of spatially distributed points, typically in 3D space, that represent samples of a physical surface or object. A key distinction in this context lies between **2.5D** and **3D** PCs. A dataset is referred to as 2.5D if it can be described as a height field, meaning that for each horizontal location (x, y) , there exists at most one corresponding elevation value $z = f(x, y)$, where f is a function mapping a 2D location to height (Vosselman & Maas, 2010). This representation is typical for data acquired from nadir-looking sensors and applies to most DEMs and DBMs. In contrast, 3D PCs may contain multiple points for a given (x, y) location, capturing features such as overhangs, vertical structures, and complex surface geometries.

In the context of this work, the PSI datasets are best classified as 2.5D, as they represent surface displacements over time using sparse, single-valued vertical measurements. The MBES datasets, while predominantly treated as 2.5D for modeling purposes, originate from full 3D sonar measurements and may locally deviate from the height field assumption due to steep slopes, vertical structures, or overlapping swaths in complex bathymetric areas.

1.4.1 PSI Data

1.4.1.1 PSI Measurement Principles

To understand the nature of PSI data, it is necessary to trace the development of the underlying techniques, beginning with radar. Radar, short for radio detection and ranging, refers both to the technique and the instrument. It emits electromagnetic pulses in the radio or microwave domain and records the echoes from objects in its line of sight. From the two-way travel time, the range to the target can be determined, while the intensity of the returned signal provides information on properties such as size or surface roughness. Radar can operate in a monostatic configuration, where a single antenna is used for both transmitting and receiving, or in a bistatic configuration with separate antennas for transmission and reception (Skolnik, 1962; Hanssen, 2001; Moreira et al., 2013). A major advance came with imaging radar, particularly Side-Looking Airborne Radar (SLAR) and later SAR. The side-looking geometry allowed continuous mapping of the Earth's surface without the ambiguities that would arise from nadir-looking systems. Early instruments were incoherent and relied on long physical antennas, known as Real Aperture Radar (RAR), which limited azimuth resolution. The decisive step was the introduction of coherent radar, in which not only the amplitude but also the phase of the signal is preserved. This enabled the principle of synthetic aperture processing, where the motion of the platform is exploited to synthetically create a much larger antenna, combining multiple echoes coherently. First proposed by Wiley (1965) and further developed in subsequent decades (Curlander & McDonough, 1991), this innovation improved azimuth resolution by several orders of magnitude and enabled high-resolution radar imaging from aircraft and satellites. Spaceborne radar missions began with Seasat in 1978, which, despite operating for only 100 days, demonstrated the remarkable capabilities of SAR for Earth observation (Elachi et al., 1982; Henderson & Lewis, 1998). The success of Seasat was followed by the Shuttle Imaging Radar (SIR) missions in the 1980s, which further advanced digital recording and system design. In a SAR acquisition, the basic imaging geometry is such that SAR sensor mounted on a satellite illuminates the Earth's surface with side-looking radar pulses. This covers a swath extending from near to far range in the range direction and from early to late acquisition times in the azimuth direction. Each pulse footprint contributes to the synthetic aperture, enabling high-resolution imaging in the azimuth direction. When two or more co-registered SAR acquisitions

of the same area are combined, the phase difference can be evaluated interferometrically. This is the basis of InSAR and explains how repeated acquisitions can be used to estimate surface deformation (Hanssen, 2001).

PSI extends the principles of InSAR by targeting coherent radar reflections that remain stable across long observation periods. These Persistent Scatterers (PSs), often buildings, infrastructure, or exposed rocks, enable the derivation of deformation histories at millimeter precision. By assembling time series of phase observations from large image stacks, PSI provides both deformation velocities and temporal evolution of motion at individual PS locations (Crosetto et al., 2016). The method is inherently opportunistic: deformation can only be estimated where suitable scatterers exist. PSs are typically sparse in vegetated, snow-covered, or steep areas, while urban environments and exposed rock surfaces yield dense coverage. Surface changes such as construction, repaving, or temporary snow can lead to the partial or complete loss of PS (Crosetto et al., 2016). The primary PSI product is the deformation time series, which offers insight into the kinematics of surface processes, including phases of quiescence, activation, or acceleration (Crosetto et al., 2016). These time series are fundamental for linking observed motion to potential driving factors. However, since they contain one deformation estimate per SAR acquisition, they are highly susceptible to phase noise and should be interpreted with care. A further limitation is that PSI measures only the displacement component in the radar Line-of-Sight (LOS). A generic 3D deformation cannot be fully reconstructed from a single dataset. When both ascending and descending satellite tracks are available, vertical and east–west horizontal components can be derived, while the north–south component remains largely inaccessible (Ferretti et al., 2007).

1.4.1.2 PSI Data of Hengstlage

The Hengstlage region in Lower Saxony has been affected by long-term ground motion due to underground resource extraction and the operation of cavern storage facilities for hydrocarbons and CO₂ (Jahn et al., 2011). These conditions have led to measurable deformation patterns that require regular geodetic monitoring and motivate updates to the spatial reference system. To assess surface motion in this area, a combination of geodetic datasets was analyzed. These include vertical and horizontal velocities from official geodetic benchmarks—amtlichen Festpunktinformationssystem (AFIS), GNSS time series from the SAPOS[®] reference stations, leveling data (1988–2008, 106 benchmarks), and PSI observations (2003–2010, 5962 scatterers after preprocessing). Horizontal velocities were derived from 115 points spanning 1968–2010 (Brockmeyer, 2019). PSI velocities were retrieved from differential InSAR techniques and supplement sparse leveling and GNSS data by providing dense spatial coverage, especially in urban and peripheral regions. All velocity data were assumed uncorrelated. The variance of leveling-derived vertical and horizontal components is given by:

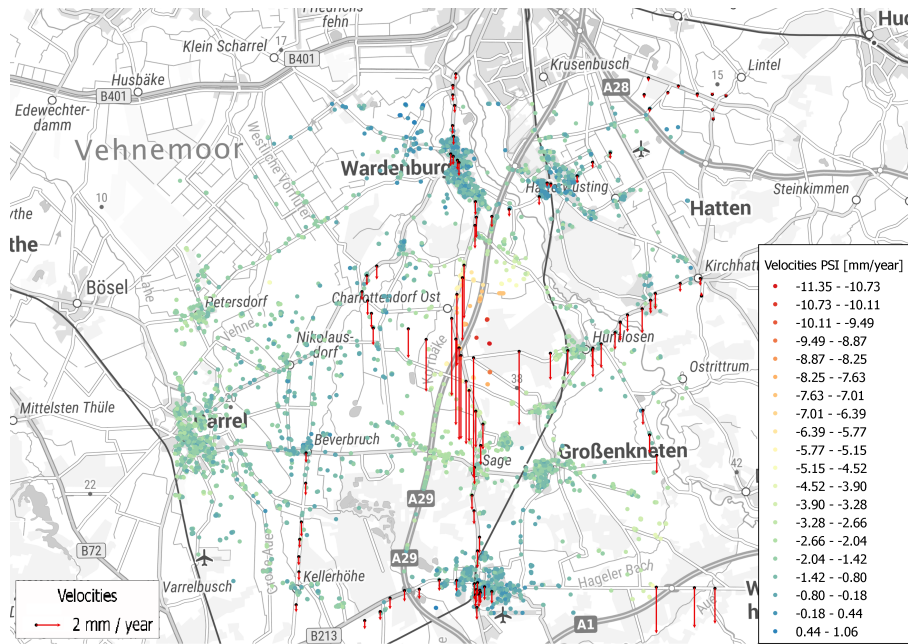
$$\sigma^2 = 2 \frac{1}{\alpha_t^2} \sigma_0^2 \quad (1.1)$$

where $\sigma_0 = 3$ mm and α_t is the temporal baseline between measurements (Brockmeyer, 2019). The variance of PSI velocities includes an additional term to reflect point instability:

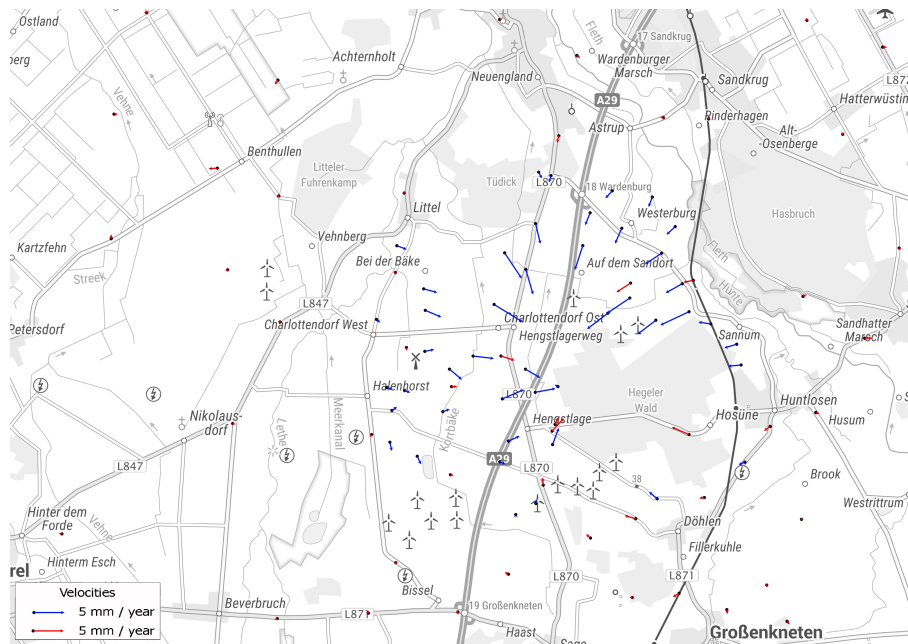
$$\sigma^2 = 2 \frac{1}{\alpha_t^2} \sigma_0^2 + \Delta_{PSI}^2 \quad (1.2)$$

with $\Delta_{PSI} = 2$ mm representing the assumed uncertainty due to temporal decorrelation and processing noise. The maximum vertical deformation observed from leveling reached -9.9 mm/year in the center of the subsiding zone. PSI and leveling data show consistent trends (Fig. 1.3a), while horizontal motions derived from SAPOS[®] and GNSS post-processing reveal systematic displace-

ments (Fig. 1.3b). These datasets are further used for surface-based modeling and validation of deformation representation methods in Publication D.



(a) Height component



(b) Horizontal component

Figure 1.3: (a) PSI and leveling data (red bars), (b) Data from AFIS (red) and SAPOS[®] (blue) in Hengstlage (Brockmeyer (2019); Publication D).

1.4.1.3 PSI Data of Hannover

The second PSI datasets used in this dissertation are based on SAR acquisitions from the Sentinel-1 mission, part of the European Space Agency's Copernicus Earth observation program (European Space Agency, 2020). The twin satellites Sentinel-1A (launched in April 2014) and Sentinel-1B

(launched in April 2016) operate in C-band and acquire data in Interferometric Swath mode with a spatial resolution of approximately $5\text{ m} \times 20\text{ m}$ and a swath width of 250 km. With both satellites operating on the same orbit plane, the combined repeat cycle is six days, providing the temporal density required for interferometric time series analysis. For the case study in Lower Saxony, covering the area of Hanover and Wunstorf, a PSI product was provided by the Federal Institute for Geosciences and Natural Resources (BGR). The dataset was generated using the PSI-Wide Area Product (WAP) processing chain (Kalia et al., 2017) and comprises 138 SAR images acquired between October 2014 and April 2018. A scene from September 2016 was chosen as the interferometric master. After processing, the dataset contains approximately 319,000 PS points with LOS velocity estimates. To mitigate large-scale systematic errors such as residual orbital ramps or atmospheric effects, the PSI velocities were calibrated against independent GNSS reference station measurements. The results are expressed in the LOS direction and, under the assumption of negligible horizontal motion, projected into the vertical component. While this introduces a limitation for areas with significant horizontal displacements, the available dataset provides a dense and consistent vertical deformation signal for the region of interest.

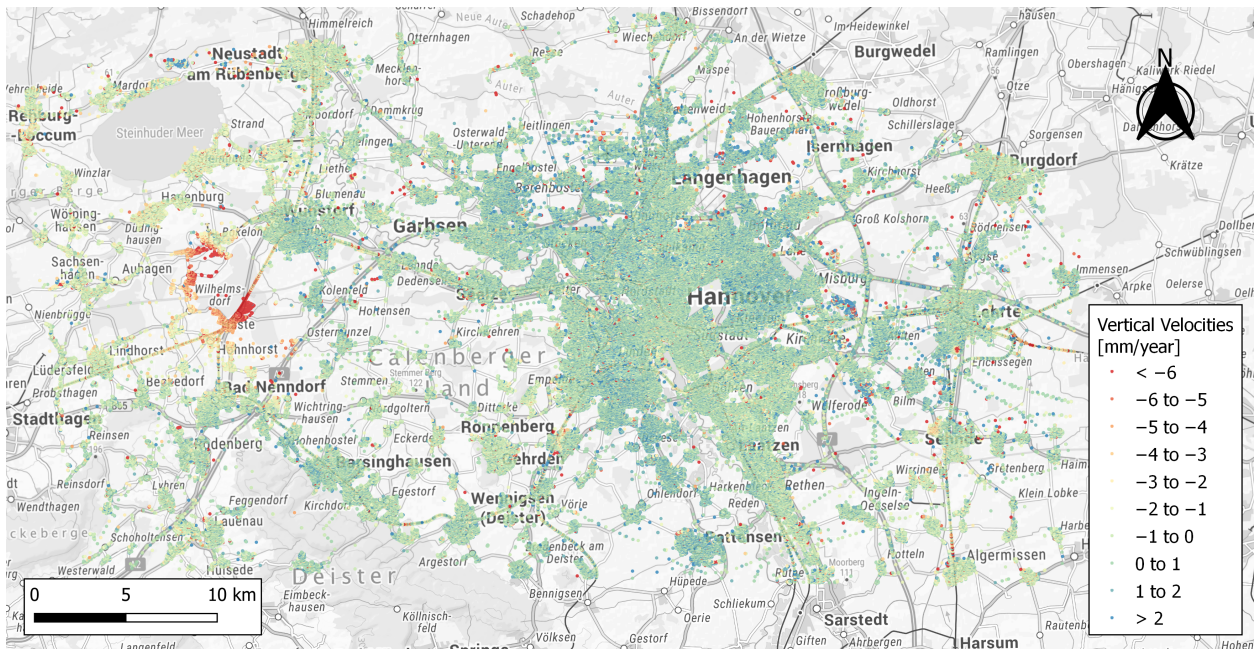


Figure 1.4: *PSI point distribution over the Hanover region. This dataset is used for deformation modeling and outlier detection in Publication A.*

A critical step in preprocessing of the PSI dataset was the removal of unreliable points through temporal outlier detection. The quality of individual PS time series can vary due to factors such as local disturbances, construction activity, or insufficient modeling of atmospheric contributions. To identify unstable scatterers, the PS time series were first de-trended, and then the residuals were evaluated for variability. Following the approach of Brockmeyer et al. (2020), scatterers exceeding a standard deviation threshold of 6 mm in their residual time series were flagged as temporal outliers and excluded from further analysis. As a result, the dataset used in this dissertation represents a temporally cleaned PSI product, in which short-term anomalies have been filtered out while preserving coherent long-term deformation trends. This ensures that the subsequent spatial outlier detection and surface modeling processes are applied to reliable deformation observations only. The spatial distribution of the resulting PS points is illustrated in Fig. 1.4. The figure highlights the clustering of coherent scatterers in urban areas such as Hanover, the occurrence of data gaps in rural regions, and the pronounced ground motion signal west of Hanover caused by salt mining activities. This distribution provides the foundation for the deformation modeling and outlier detection steps conducted in this dissertation.

1.4.2 MBES Data

1.4.2.1 Acoustic Measurement Principles and Error Sources

Accurate bathymetric mapping in shallow waters requires depth measurements with better than 1 % accuracy relative to the water depth, along with high spatial resolution for detecting small features¹. In contrast, deep-water mapping typically tolerates lower accuracy due to different scientific or industrial objectives (Lurton, 2010). Today, MBES are the primary technology for acquiring high-resolution underwater topography (Dineng Zhao et al., 2015). Introduced in the late 1970s, MBES systems quickly gained widespread adoption in disciplines such as hydrography, geology, and the offshore industry. They have since evolved into sophisticated instruments for detailed seafloor mapping (Lurton, 2010).

MBESs expand upon Single Beam Echo Sounder (SBES) systems. While SBES acquires depth at a single nadir point, MBES emits a fan of acoustic beams that span a wide swath perpendicular to the vessel's trajectory, allowing for efficient area-wide coverage (Lurton, 2010). These systems typically operate with narrow individual beam widths (1°) and a broad across-track angle of up to 150° , though their effective swath width is usually limited to 3–5 times the water depth (Wu et al., 2021). In very shallow waters ($<10\text{--}15\text{ m}$), full seafloor coverage can become challenging (Gostnell et al., 2006). A significant advancement in recent years is the use of interferometric MBES systems, which employ phase measurements of the return signal to estimate the angle of arrival. These systems can achieve swath widths of up to 10–15 times the sensor altitude, substantially improving coverage in shallow-water applications.

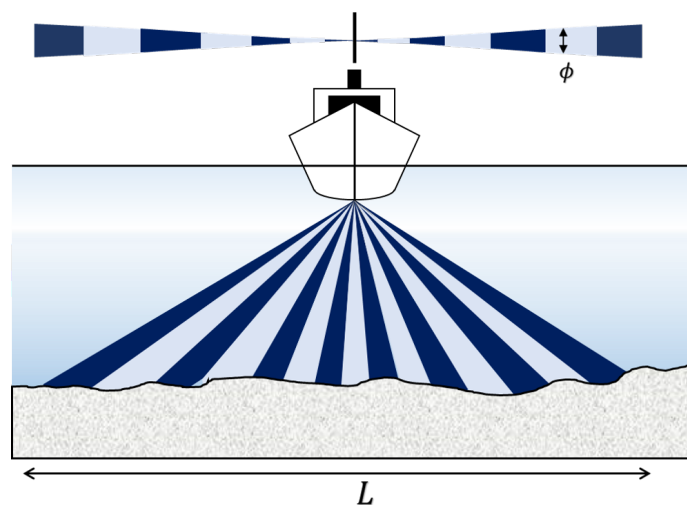


Figure 1.5: Geometry of a MBES system. ϕ illustrates the longitudinal opening angle and the swath width is shown by L . The highlighted beam shapes below the vessel illustrate the across-track beams and their corresponding footprints that cover the seafloor ($\phi =$ longitudinal opening angle, $L =$ swath width) (Lu et al., 2010a).

During each transmission and reception cycle (ping), modern MBES systems collect hundreds of soundings (typically 200 or more) (Wu et al., 2021). The fundamental principle relies on determining two parameters for each beam: the *time-of-flight* (t) and the *angle of incidence* (θ). Assuming a known sound speed c , the slant range R is computed as $R = \frac{ct}{2}$. The corresponding seafloor

¹The IHO specifies performance levels based on application types. These range from the most stringent (Special Order) to Orders 1–3, with periodic updates by a dedicated technical committee.

coordinates are derived via trigonometry:

$$y = \frac{ct}{2} \sin \theta, \quad z = \frac{ct}{2} \cos \theta \quad (1.3)$$

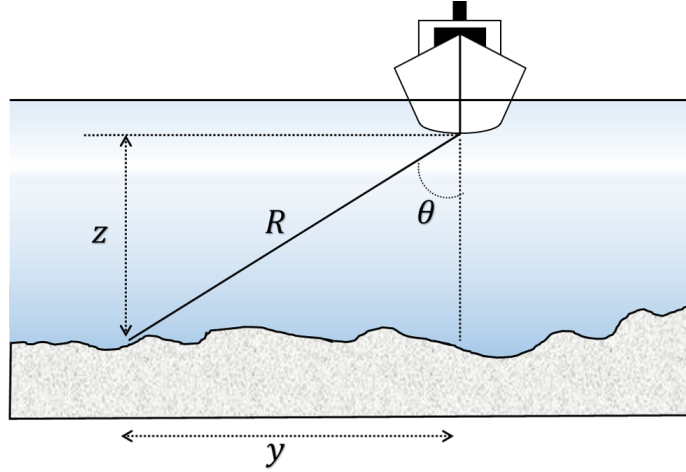


Figure 1.6: *Fundamental time-angle measurement of bathymetry by an MBES system (Lurton, 2010).*

The effective resolution of MBES data depends on beam geometry and pulse characteristics. Footprint size increases with depth and off-nadir angle, reducing resolution and echo strength at swath edges. Near-nadir beams produce smaller footprints and stronger returns, resulting in more accurate depths. Range resolution is further influenced by pulse length and bandwidth; shorter pulses and wider bandwidths yield better echo discrimination.

Detection strategies vary with incidence angle. At low angles, the maximum of the echo envelope is used to derive depth. At higher angles, phase detection is preferred due to its stability under weak or grazing returns. The chosen detection method significantly impacts sounding accuracy.

To ensure correct georeferencing and precise depth computation, MBES measurements must be corrected using data from several ancillary systems (Lurton, 2003):

- **Positioning system:** Typically a GNSS-based solution (preferably in Precise Differential Global Positioning System (PDGPS) or Real Time Kinematic (RTK)) to determine the vessel's absolute position.
- **Motion sensor unit:** Provides real-time measurements of ship motion (roll, pitch, heave, and heading) to correct beam orientations and vertical displacements.
- **Sound Velocity Profile (SVP):** Used to correct refraction along the acoustic paths from transducer to seafloor. SVPs are typically obtained from water column probes or towed sensors.
- **Near-array sound speed:** Measured using on board velocimeters or thermometers near the transducer to improve beamforming accuracy.

Depth measurements are affected by both systematic and random errors, primarily stemming from uncertainties in time and angle estimation. Systematic errors, or biases, arise from stable and predictable sources, such as sensor misalignment or consistent refraction due to a permanent sound speed profile. Random fluctuations, on the other hand, result from environmental noise, vessel mo-

tion, or the varying acoustic properties of the seafloor. Accurate bathymetry depends on minimizing and accounting for various error sources (Hare, 1995; Lurton, 2010; Wu et al., 2021):

- **Acoustic measurement noise:** Affected by signal-to-noise ratio, pulse type, and seafloor characteristics.
- **Platform motion:** Roll, pitch, yaw, and heave can distort swath geometry. Real-time motion compensation is critical to avoid positional offsets.
- **Sound velocity errors:** Incorrect SVP data introduce refraction-related biases, especially at outer beams.
- **Installation errors:** Misalignment of transducer or receiver arrays causes systematic angular offsets.
- **Synchronization errors:** Latency between sensors (GNSS, Motion Reference Unit (MRU), sonar) can lead to misregistration of pings in space and time.

Measurement uncertainties in any MBES system are expected to range between 5–10 cm and may exceed 30 cm, depending on survey depth and conditions (Lucieer et al., 2016; Fonseca & Mayer, 2007). Because many hydrographers rely heavily on outer-beam soundings, the effective uncertainty in practice can surpass these values. In shallow water environments (<50 m), residual depth errors often correspond to about 1–2 % of the measured depth (Vásquez et al., 2007).

To estimate the uncertainty of measured soundings, a TPU model is necessary. This forward modeling strategy propagates known instrumental and environmental uncertainties to obtain predicted horizontal and vertical uncertainty estimates per sounding point (Hare, 1995). The Total Vertical Uncertainty (TVU) and Total Horizontal Uncertainty (THU) components are typically calculated separately, allowing quality assessment of each measured depth.

1.4.2.2 Kiel Canal Survey Data

The Kiel Canal is a man-made waterway in northern Germany. The test area comprises flat sections and zones with small sediment dunes. The bed consists of rock, silt, and gravel. Boundaries include stone-armored banks under bridges and sand banks, with outer margins locally enclosed by vertical sheet piling. Water depth in the test area reaches up to about 13 m.

The German Federal Waterways and Shipping Administration (WSV) conducted the measurements in 2019 through the responsible Elbe-North Sea (Tönning) Waterways and Shipping Office (WSA). A 300 m swath was selected as test data (Fig. 1.7). A 100 m segment is visualized in Fig. 1.9.

The survey vessel Uwe Jens Lornsen (UJL) (Fig. 1.8) is operated by the WSA. Built in 1993, it is used for monitoring and depth surveying of navigation channels, structures, harbors, and dredging areas. The survey vessel UJL employed a dual-head Kongsberg EM2040C MBES (Kongsberg Maritime AS, Rev. C, 2013) (Kongsberg Maritime, 2013). The system comprises:

- Dual-head *Kongsberg EM2040C* MBES with two permanently installed transducers. Heads are oriented port (Back Board side (BB)) and starboard (Star Board side (STB)), each tilted 37° relative to the vessel baseline.
- Integrated positioning and orientation: PDGPS with a Seapath 330+ Inertial Navigation System (INS) and an MRU 5+.

- Auxiliary SBES at nadir for central depth at multiple frequencies. This sensor is not used for computing bathymetry.

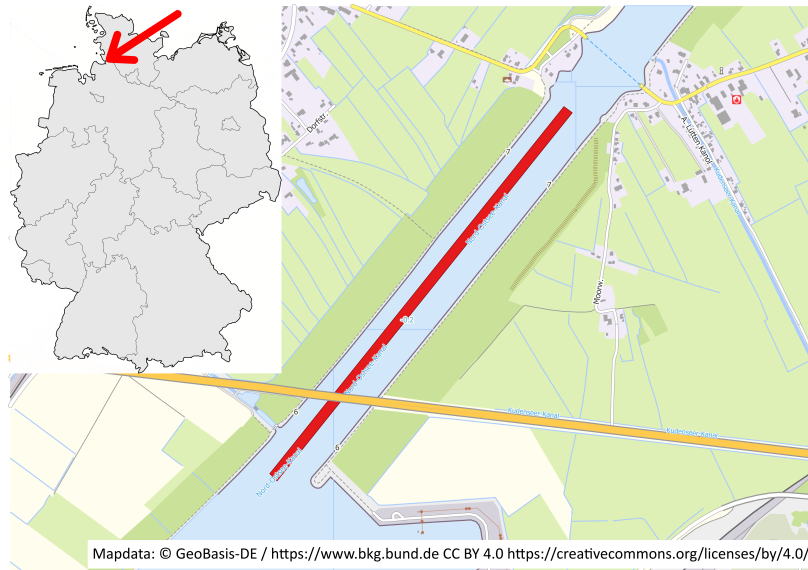


Figure 1.7: Survey area of the Kiel Canal. The 300 m measurement swath is used as test data (Publication C).



Figure 1.8: Survey vessel UJL (WSA, 2023).

Data were collected in *equal-angular* mode, producing 256 beams per ping. Near the vessel's nadir, the across-track spacing was about 0.06 m, increasing to about 0.4 m at the swath edges. Along-track spacing between pings averaged 0.35 m, given vessel speed and sampling rate. The resulting point density was approximately 45 pts/m² close to nadir and decreased to about 15 pts/m² toward the outer swath. These acquisition characteristics provided a heterogeneous distribution of measurement geometry and density, which was particularly suited for evaluating modeling strategies and uncertainty effects.

The 2019 Kiel Canal campaign underpins two studies in this dissertation. A 100 m segment of the raw PC, shown in Fig. 1.9, was used for automatic outlier detection and surface-based modeling in Publication B. The same campaign also supported the uncertainty-driven modeling study in Publication C, where measurement uncertainty was explicitly modeled and integrated in the surface estimation.

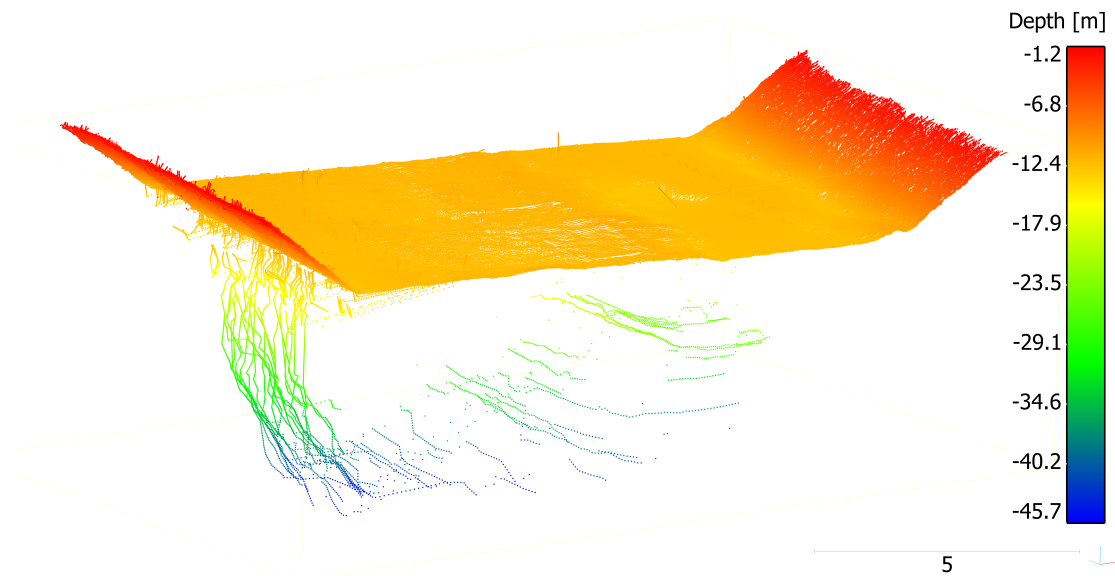


Figure 1.9: A 100 m segment of MBES PC from the Kiel Canal, acquired by WSV. This segment is used for outlier detection and surface modeling (Publication B).

1.4.2.3 MBES Simulated data

The uncertainty-driven modeling in Publication C uses a simulated MBES dataset to enable validation against known ground truth. A synthetic seabed surface is defined analytically using predefined hierarchical B-spline functions (i.e., MBA) and exported as a dense PC with 0.01 m spacing (Fig. 1.10). The surface covers 80 m by 20 m with a total relief of 8 m vertically. MBES measurements are simulated by ray tracing a fan of beams (120° field of view) from four parallel vessel trajectories that are spaced 20 m apart and located about 12 m above the surface. This creates overlap between swaths. To avoid discretization artifacts from meshing, intersection points are projected back onto the analytic surface by recomputing the height from the underlying B-spline functions at the intersected planimetric coordinates. Measurement uncertainty is then added by Monte-Carlo (MC) forward modeling (1,000 realizations per point), yielding per-point uncertainty estimates that are later used for uncertainty-based weighting in surface adjustment.

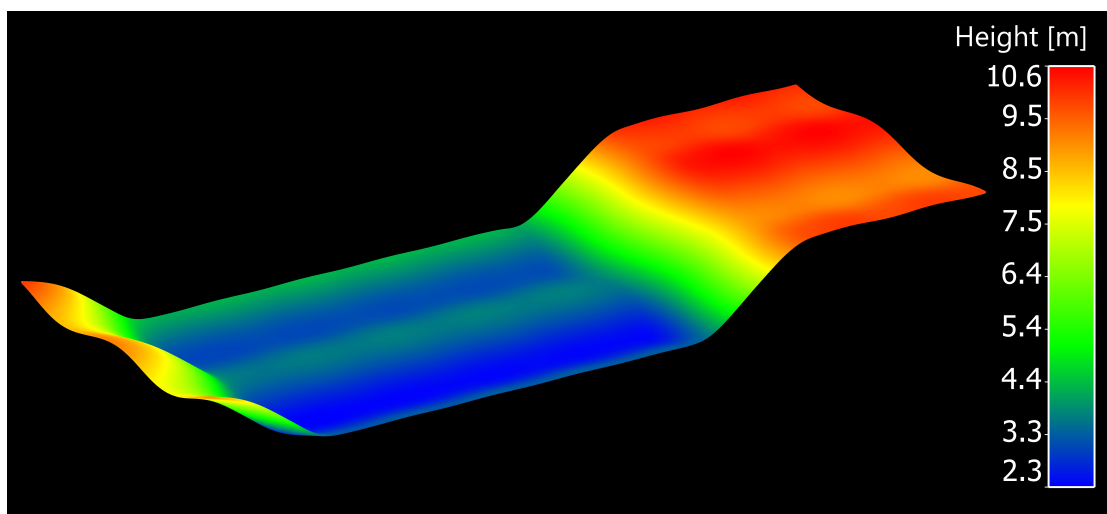


Figure 1.10: Simulated geometry as a PC. The points are color-coded by the height in meters (Publication C).

1.5 Structure of the Thesis

Having outlined the motivation, research questions, publications, and data sources, the thesis is organized in five chapters that follow the stages of the processing pipeline for point-sampled surfaces, from motivation and data description to methodological integration and publication of the original studies.

- Chapter 1 introduces the application context, outlines the motivation (Section 1.1) and research (Section 1.2) questions, and summarizes the original publications (Section 1.3) and datasets used in this work (Section 1.4). It defines the overall processing pipeline and its use cases for PSI and MBES data.
- Chapter 2 reviews the state of the art in methods for processing point-sampled surfaces. It is structured along the main components of the pipeline: outlier detection in spatial PCs (Section 2.1), surface-based approximation techniques with an emphasis on B-spline and multilevel B-spline approaches (Section 2.2), and model quality assessment (Section 2.3).
- Chapter 3 summarizes and integrates the methodological contributions from the individual publications into a coherent processing pipeline. The chapter is organized by pipeline stage, covering data cleaning and outlier detection (Section 3.1), surface modeling with MBA (Section 3.2), and uncertainty quantification (Section 3.3), and shows how the individual studies address the research questions and complement each other.
- Chapter 4 concludes the thesis by summarizing the main findings, revisiting the research questions, and discussing perspectives for future research on robust surface modeling and uncertainty analysis for geospatial PCs.
- Chapter 5 provides an overview of additional publications by the author that are related to the topic of this dissertation but are not included as core papers in the cumulative thesis.
- Chapter 6 reproduces the original publications that underpin this cumulative dissertation in their published or accepted form. They provide the detailed algorithms, experiments, and case studies that support the synthesis presented in the preceding chapters.

Fig. 1.2 and Table 3.1 summarize how the research questions in Section 1.2 and the original publications in Section 1.3 relate to the processing stages reviewed in Chapter 2 and integrated in Chapter 3.

2 State of the Art

In this section, the state of the art in methods for processing point-sampled surfaces is reviewed with a focus on geodetic and hydrographic applications. The discussion follows the main stages of the processing pipeline developed in this thesis: outlier detection, main surface modeling, and quality assessment. Outlier detection aims to identify observations that are inconsistent with an assumed surface model or with the bulk of the data. Main surface modeling constructs a continuous representation of the underlying surface from the cleaned measurements. Quality assessment then characterizes the reliability and uncertainty of the resulting models. The following subsections summarize the most relevant approaches for each of these components.

2.1 Outlier Detection

2.1.1 General Principles

Accurate surface modeling requires reliable input data. Nonetheless, geodetic and geospatial measurements are often contaminated by a variety of uncertainties, which are generally categorized as *random*, *systematic*, or *outliers*. *Random Deviations*, or noise, are an inherent aspect of any measurement process. Measurement noise typically originates from limitations present in sensors utilized during measurement. These phenomena can often be modeled statistically, based on the known characteristics of the sensors. *Systematic Deviations* originate from consistent biases introduced during data acquisition. Such biases may include calibration issues, instrument drift, or flaws in survey geometry. These uncertainties are generally mitigated through the implementation of enhanced calibration procedures or survey design. *Outliers*, also known as *anomalies* or *abnormalities*, are data points that deviate significantly from an expected model. As stated by Hawkins (1980), an outlier is defined as “an observation that deviates so much from other observations as to arouse suspicions that it was generated by a different mechanism.” Such deviations are frequently attributed to irregularities in the data-generating process and may contain significant information regarding measurement failures or environmental anomalies. Consequently, their identification is imperative for ensuring the accuracy of the model and facilitating domain-specific interpretation. The conventional methodologies employed for outlier detection generally yield either *continuous scores* or *binary classifications*. Score-based methods assign a degree of “outlierness” to each observation, while binary methods directly label points as inliers or outliers. Depending on the analysis objective, thresholds can be applied to scores to obtain classifications (Aggarwal, 2017). Assuming that systematic deviations have been mitigated, it is possible to place each observation along a spectrum ranging from normal to noisy to anomalous (see Fig. 2.1). The distinction between noise and anomalies is application-dependent: anomalies generally produce higher scores, but not all high-scoring points represent meaningful deviations. The interpretability and contextual feedback, when available, play a central role in refining this distinction. For instance, as is also common in the field of geodesy, if the distribution of data is known or assumed to be normally distributed, then it can be assumed that observations deviating more than 3σ from the mean are considered to be outliers. Building on these conceptual distinctions, the majority of algorithms are designed to model the standard structure of a dataset and assign outlier scores based on the extent to

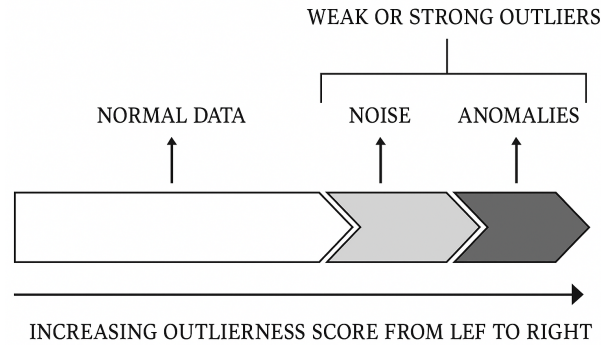


Figure 2.1: *Conceptual view of observation deviation scores (Aggarwal, 2017).*

which individual observations deviate from it. The efficacy of these methods depends on the appropriateness of the underlying model. An overly simplified model may fail to account for relevant anomalies, while an excessively complex model may incorporate outliers into the structure it seeks to describe. The classification of outlier detection approaches is typically based on the extent of supervision provided. *Supervised* methods rely on the existence of labeled examples of both normal and anomalous data. *Semi-supervised* methods assume access to only normal data and attempt to learn a model of regularity. *Unsupervised* methods, which are predominant in geospatial and geodetic contexts, function without the utilization of labeled data. These methods rely on internal assumptions regarding structure or proximity.

The selection of a model in unsupervised settings is contingent upon domain knowledge. Interpretable and efficient models demonstrate superior generalization capabilities and exhibit greater robustness to noise or unidentified anomalies. While outlier detection shares conceptual ties with classification, its distinguishing features are its unsupervised nature and task-specific ambiguity. In the following, we build on these general principles and distinguish between instance-based and model-based approaches to outlier detection.

2.1.2 Instance-Based vs. Model-Based Approaches

A fundamental distinction is made between **instance-based** and **model-based** approaches (Aggarwal, 2017). Instance-based methods, also referred to as diagnostic methods, are decision-making processes that are informed by the local relationships that exist among individual observations. Conversely, Model-based methods construct an explicit representation of the underlying data structure and evaluate deviations with respect to this model.

Instance-Based Methods: Commonly used instance-based methods include statistical, distance-based, density-based, and clustering-based techniques. Their flexibility and nonparametric nature characterizes these models; however, they are frequently susceptible to issues related to data sparsity and high-dimensional effects.

- **Clustering-based methods:** Outliers are defined as data points that do not belong to any existing cluster (Jain et al., 1999; Sotoodeh, 2007).
- **Distance-based methods:** These assumptions are based on the premise that outliers exhibit substantially greater distances from their k nearest neighbors in comparison to the typical points (Knorr et al., 2000; Shen et al., 2011).

- **Density-based methods:** Algorithms such as Local Outlier Factor (LOF) (Breunig et al., 2000) and Local Correlation Integral (LOCI) (Papadimitriou et al., 2003) identify outliers as low-density observations relative to their neighbors.

Despite their apparent intuitiveness, instance-based methods necessitate meticulous parameter tuning and can become computationally demanding, particularly when dealing with substantial or high-dimensional datasets. In regions characterized by sparsity, these systems may encounter difficulties in differentiating meaningful structural variation from true anomalies.

Model-Based Methods: The implementation of model-based methods necessitates the construction of a model that captures anticipated behaviors, against which deviations are subsequently measured. These processes frequently adhere to a two-step sequence: The first step involves the modeling of the expected structure (e.g., via regression or surface fitting). The second step entails assigning scores based on residuals or fit deviation. A key limitation is that the same data are often used for both model training and scoring, making it difficult to isolate the test instance from the model construction. Model-based approaches naturally connect to surface-based outlier detection in geospatial datasets, where the model represents an underlying terrain or bathymetric surface.

A more exhaustive overview of fundamentals concerning outlier detection can be found in classical statistical literature, including the works of Barnett & Lewis (1984), Hawkins (1980), and Rousseeuw (1987). As the field has expanded to incorporate perspectives from machine learning, database systems, and high-dimensional analysis, comprehensive surveys such as Chandola et al. (2009) and Aggarwal (2017) offer broad overviews of the taxonomy, challenges, and application domains. These general frameworks form the basis for the spatial and surface-based approaches discussed in the next subsection.

2.1.3 Outlier Detection in PCs

Building on these general frameworks, the applications of interest in this dissertation focus on PCs, more specifically those sampled from underlying physical surfaces, as commonly encountered in topographic and bathymetric studies. In such contexts, data points represent physical measurements taken over space, and are assumed to be realizations of an underlying spatial geometry. A critical factor in the selection of an appropriate outlier detection method for geospatial data is the consideration of **spatial correlation**, a fundamental property of spatial phenomena. As Tobler (1970) articulated, “Everything is related to everything else, but near things are more related than distant things.” This principle suggests that observations made in close spatial proximity are expected to demonstrate similar behaviors, and any deviations from this pattern may serve as potential indicators of spatial outliers. The objective of spatial outlier detection is to identify *abrupt local deviations* in a behavioral attribute that violate the expected pattern of spatial autocorrelation. The assessment of these deviations is typically accomplished through the analysis of attribute variations within a local neighborhood. The concept of spatial proximity can be defined through the application of multidimensional distance metrics or graph-based connectivity structures, contingent upon the inherent characteristics of the data being analyzed.

Classical approaches have addressed this problem through global statistical assessments, visual methods, and localized testing. For instance, deviations from global distributional assumptions may be evaluated using moments or thresholds (Colin Ware et al., 1991; Herlihy et al., 1992), while graphical tools such as scatterplots or variograms provide exploratory insight into spatial irregularities (Haslett et al., 1991; Pannatier, 2012). Quantitative statistical tests, such as those proposed by Haining (1993) and Anselin (1995), use spatial autocorrelation measures like Moran’s index (Moran, 1950) to identify local anomalies. Subsequent advancements in the field increasingly

incorporated spatial structure to facilitate detection. Du et al. (1996) introduced an adaptive neighborhood selection method based on clustering that is designed to emulate the way a human analyst makes decisions. Similarly, swath-level filtering strategies (Lirakis & Bongiovanni, 2000) employ spatial consistency checks sequentially across transects in bathymetric data.

A significant development in this field was the incorporation of surface modeling into the detection process. Regression modeling, a parametric form of correlation analysis (Rousseeuw, 1987), enables the estimation of an underlying surface against which deviations can be measured. These surface-based approaches, as previously outlined by Le Deunf et al. (2020), capitalize on the geometric structure of geospatial data, conceptualizing outliers as points that deviate substantially from a modeled surface. A variety of implementations exist, including local planes, polynomial approximations, splines, or trend surfaces (Debese & Bisquay, 1999a; Bottelier et al., 2005). The effectiveness of these methods depends heavily on the choice and quality of the surface model. A fundamental distinction exists between local and global models. Local models, such as moving polynomials or splines (Lu et al., 2010a; Debese et al., 2012), are highly responsive to spatial variability; however, they may also be overly sensitive to small clusters of outliers. Global models, including coarse-to-fine B-spline surfaces (Publication A) or Kriging-based interpolants (Bottelier et al., 2005), offer enhanced stability and global coherence. However, these models may encounter challenges with local complexity or sparse sampling.

The majority of surface-fitting techniques depend on LS optimization, a process that is inherently susceptible to outliers. In order to address this limitation, robust estimators have been adopted to reduce the influence of extreme deviations during surface fitting (Debese et al., 1998; Debese & Bisquay, 1999b; Bottelier et al., 2005; Debese et al., 2012; Arnold & Shaw, 1993; Huang et al., 2020; Lorenz et al., 2021; Mohammadivojdan et al., 2021). However, existing implementations often require careful parameter tuning and substantial manual quality control to ensure consistent and reproducible results.

A notable implementation is presented by Debese et al. (2012), who developed a robust and adaptive framework for outlier detection in MBES data. Their methodology integrates Tukey's Iterated Re-weighted Least Squares (IRLS) estimator within a quadtree-based spatial decomposition, which allows the local polynomial fitting kernel to adapt to the scale and complexity of seabed morphology. This hierarchical structure, in conjunction with robust statistical weighting and the use of multi-swath information, facilitates the separation of valid soundings from outliers while preserving key bathymetric features. The approach offers several strengths, including spatial adaptivity, robustness against moderate noise levels, and applicability in both shallow and deep-water settings. At the same time, it relies on piecewise polynomial models defined per quadtree cell, empirical thresholds for scale, noise, and cluster size, and a classification map that still requires operator inspection. As a result, its performance and reproducibility depend on survey-specific parameter tuning and manual intervention, and the handling of heavily contaminated data or complex clustered outliers remains challenging.

The method introduced in Publication B builds on the same basic idea of combining multiscale modeling with robust estimation, but it is designed to address these limitations. Instead of fitting independent local polynomials within a quadtree, the approach employs a hierarchical B-spline surface model that provides a continuous, analytically defined geometry over the full area. This global multilevel representation enables a consistent description of seabed morphology across scales and reduces border effects between neighboring regions. In contrast to the fixed robust kernel applied in Debese et al. (2012), the approach in Publication B formulates the estimation in a contamination framework and uses an iterative M-estimation scheme that re-estimates both surface parameters and robust weights at each refinement level. This improves resistance to high outlier ratios and clustered deviations, and stabilizes convergence toward a representative surface in the

presence of irregular point densities and complex geometry. Furthermore, the multiresolution B-spline formulation and statistically motivated robustness parameters support a highly automated workflow that requires only limited and well-defined manual tuning, which is essential for scalable and repeatable processing of large or virtually endless MBES datasets.

Recent work has begun exploring learning-based methods for automatically cleaning surface-based geodetic datasets. For MBES bathymetry, Stephens et al. (2020) train a 3D convolutional neural network to denoise voxelized MBES PCs by classifying voxels as seabed or noise. In other words, they reject all soundings that do not represent the seafloor without distinguishing between specific error mechanisms. Building on this idea, Long et al. (2023) formulate outlier removal as a point-wise classification problem. They construct a deep network trained on synthetic and real data, including characteristic outlier geometries such as isolated outliers, structured groups, erroneous pings, and sidelobe artifacts. This demonstrates robust performance for both isolated and clustered outliers across different marine environments. In the PSI domain, Aguiar et al. (2021) use convolutional neural networks to classify persistent scatterers as inliers, outliers, or low-coherence candidates based on multi-temporal InSAR parameters and features from neighboring scatterers. They demonstrate that local spatiotemporal patterns can effectively be exploited for multivariate outlier detection, though their models are tied to the deformation patterns observed during training. Overall, these learning-based approaches demonstrate that deep models can minimize manual cleaning efforts and capture complex, data-driven noise structures. However, they rely on representative, labeled training data and lack explicit uncertainty measures and transparent decision criteria. In contrast, robust surface-based approaches, such as least-trimmed-squares bathymetric surface fitting (Lu et al., 2010b) and hierarchical B-spline models with iterative robust estimation (Publication C), operate without labeled data. These approaches detect both isolated and spatially coherent outliers via residuals to an explicit surface model and can be naturally linked to stochastic models. This facilitates their integration into quality-control workflows.

The methodologies previously discussed provide a comprehensive foundation for detecting anomalies in both general and geospatial datasets. Nonetheless, the particular characteristics of spatial PCs, such as those derived from MBES or PSI, pose unique challenges that these general approaches do not fully address. In this dissertation, the aforementioned challenges are addressed by developing and applying robust, surface-based detection frameworks that integrate geometric continuity and spatial correlation, as demonstrated in Publication B and Publication C.

In the next subsection, we review the main surface modeling approaches that provide the geometric backbone for these detection frameworks and for the subsequent quality assessment.

2.2 Surface-Based Approximation Techniques

After discussing outlier detection, we will now turn to surface-based approximation techniques that model the underlying geometry of point-sampled surfaces. A PC is defined as a set of spatially distributed data points, which are typically acquired through 3D sensing technologies such as LiDAR, MBES, InSAR, or photogrammetry. As indicated in the work of Vosselman & Maas (2010), each point is usually associated with a set of spatial coordinates (X, Y, Z), and it may also encompass auxiliary attributes such as intensity, timestamp, or measurement uncertainty. PCs are inherently discrete and lack explicit information about topological connectivity. Consequently, identifying the underlying spatial structure is imperative. Surface-based modeling not only facilitates the geometric interpretation and visualization of the data from multiple perspectives. It also enables quantitative analysis, such as monitoring temporal changes or conducting statistical hypothesis testing on surface evolution.

The objective of modeling PCs centers on estimating a mathematical surface or function that can adequately represent a set of non-uniform and frequently non-homogeneous observations. This challenge is encountered across a wide range of scientific and engineering domains where data are collected pointwise. Such data may originate from physical measurements, experimental observations, or computational simulations (Franke & Nielson, 1991). Applications include geodesy, geology, meteorology, oceanography, cartography, mining, reverse engineering, computer graphics, and computer vision, among others (Lee et al., 1995).

The dimensionality of a PC and the corresponding modeling task vary across applications and measurement systems. In applications such as LiDAR, MBES, or photogrammetry-based surveys, PCs often represent fully 3D structures with spatial variation in all three coordinates (X , Y , Z) (e.g., Publication B, Publication C). In numerous geodetic and geospatial contexts, however, the problem is more appropriately characterized as 2.5D. In this setting, each point is defined by two spatial coordinates (X , Y), while the third dimension (Z) represents a functional or stochastic variable. In essence, the surface is modeled as a function over a 2D domain, with Z denoting elevation, depth, or displacement. This structure is common in DEMs, DBMs, and displacement fields derived from GNSS or InSAR observations (e.g., Publication A). This particular type of dataset is often referred to as scattered data. The manner in which the problem is modeled, namely, whether it is represented as 2.5D or full 3D, exerts a significant influence on the selection of approximation techniques, the computational load, and the formulation of uncertainty models. Despite the development of various methods to address this issue across different fields, spatial data approximation remains challenging and computationally intensive. The primary challenge lies in the fact that many of the available approaches are characterized by limitations in terms of smoothness, time complexity, or allowable data distributions (Franke & Nielson, 1991; Lee et al., 1997).

Surface approximation methods are often used in either a deterministic or a stochastic form. Deterministic models mainly target the trend by fitting an explicit surface function, while stochastic methods rely on spatial correlation to predict values and their uncertainty (Publication D; Publication A). It should be noted that this classification refers to the surface representation, not to the stochastic model used in the parameter estimation. Many deterministic surface models are still estimated within a Gauss-Markov Model (GMM) adjustment and can incorporate stochastic information through a weight matrix derived from the observation variances, and, if available, from a full variance-covariance matrix (Publication C).

From a purely technical perspective, the issue is ill-posed. Given the presence of an observed set of discrete points, the existence of an infinite number of solutions to the underlying continuous surface is possible. The challenges become even more severe when considering the characteristics of real data, such as noise and non-uniform distribution. This data may contain outliers and/or be incomplete in certain areas. Collectively, these issues pose the classical problem of surface reconstruction from PCs as a long-standing challenge that has continuously drawn the attention and efforts of the research community. A multitude of methodologies have been developed for surface reconstruction from PCs. These methodologies have been reviewed in the following sources: Bolle & Vemuri (1991); Lim & Haron (2014); Berger et al. (2017); You et al. (2020); Huang et al. (2022).

A common approach to surface reconstruction from scattered data is based on the weighted contribution of observations around the desired location. This strategy involves computing the value of a function at a specified position as a weighted sum of known observations. This class of methods includes inverse distance weighting, Shepard's method, and its variants. Thorough reviews of initial studies in this field can be found in the works of Barnhill (1977), Franke & Nielson (1991), and Schumaker (1976).

One of the earliest and most widely employed techniques is Shepard's method (Shepard, 1968),

which generates a C^0 -continuous interpolation surface by using weights that decrease inversely with the distance from the interpolation point. Although Shepard's method is characterized by its simplicity and intuitiveness, it has limitations. A key drawback is that all data points influence every query point, which can result in a surface that exhibits flattened behavior near observations. Additionally, adding or subtracting even a single point substantially impacts the entire interpolation field, making it computationally inefficient for large datasets (Patane, 2016). Modified versions, including the quadratic Shepard method, have addressed some of these issues and produce C^1 -continuous surfaces (Franke & Nielson, 1980).

Another well-established approach is based on geometric constructions, such as triangulations. The Triangulated Irregular Network (TIN) is a common example, where a Delaunay triangulation is constructed from the input point set, and interpolation is performed piecewise linearly over each triangle. This method is employed to generate a C^0 -continuous surface in a variety of disciplines, including terrain modeling, computer graphics, and Geographic Information System (GIS) applications. Its popularity stems from its simplicity and computational efficiency. However, methods based on the TIN do not offer smooth derivatives, and the resulting surface can appear faceted or jagged, especially in areas with sparse data. Despite these limitations, Delaunay triangulation remains a standard approach in many surface modeling pipelines, particularly where derivative continuity is not required (Patane, 2016). For a more thorough examination of this topic, please refer to the work of Cazals & Giesen (2006).

An alternative approach involves constructing the surface as a linear combination of radially symmetric basis functions centered at the data points. Radial Basis Function (RBF) methods, exemplified by Hardy's multiquadric interpolation (Hardy, 1971), and referenced in Hoschek et al. (1993), have been extensively adopted in geodetic and geographics applications. While these methods can generate smooth and accurate surfaces, they necessitate the resolution of a complex system of equations, rendering them computationally intensive for substantial datasets. These methods typically solve a dense system of equations to determine the unknown coefficients, making them computationally intensive for large datasets. Additionally, RBFs can be utilized in implicit surface modeling, wherein the surface is defined as a level set of a scalar field that is approximated from the data. This approach enables a flexible and continuous surface representation; however, it comes at the expense of increased computational complexity (Hoschek et al., 1993).

The Moving Least Squares (MLS) method (Lancaster & Salkauskas, 1981) addresses some of the global influence issues in Shepard and RBF interpolation. The methodology entails the implementation of a local polynomial fit to each query point neighborhood, with distance-based weights, thereby yielding surfaces that are smooth and locally controlled. Nonetheless, the efficacy of the method is contingent upon the selection of neighborhood size and weighting function. Furthermore, an increase in computational cost is observed in proportion to the complexity of the neighborhood (Patane, 2016). Robust MLS variants employ forward search to categorize neighborhoods into outlier-free smooth regions, thereby facilitating piecewise smooth surface reconstruction and preserving sharp features (Fleishman et al., 2005). This enhancement, however, comes at the cost of increased computational expense and the potential misclassification of smooth regions as features when the sampling density or signal-to-noise ratio is inadequate. The methods above are typically formulated without an explicit covariance model. When spatial correlation and prediction uncertainty must be modeled directly, covariance-based predictors such as Kriging and LS collocation are commonly used.

In a multitude of interpolation tasks, it is imperative to consider the spatial correlation between measurements. Explicitly modeling this correlation through methods such as Kriging (Wackernagel, 2003; Goovaerts, 1997) overcomes the limitations of methods that treat observations as independent.

¹ C^n -continuous with $n = 0, 1, \dots, n$ means that the function is n times differentiable.

The term "kriging" originated in the field of geostatistics and has since gained wide application in the environmental and geospatial sciences. It estimates values at unsampled locations as weighted combinations of observations, with the weights derived from a covariance model. This approach incorporates both the measurement uncertainties and their spatial structure, producing an optimal estimate under specified statistical assumptions, along with a corresponding variance as a measure of reliability. The primary disadvantage is the computational expense, since solving the required system of equations scales poorly with large datasets. The efficacy of the performance can be enhanced by confining computations to the proximate neighbors through the utilization of spatial search structures, such as kd-trees.

In the field of geodesy, the LS collocation with an empirically determined correlation function is a widely utilized method for computing velocity fields (Straub, 1996; Peter, 2000; Drewes & Heidbach, 2005). As with kriging, collocation provides pointwise estimates and is based on the assumption of data homogeneity. To ensure the reliability of the results, it is imperative to remove any systematic trend present in the data before the application of the method. It is assumed that there is spatial correlation among the data points, meaning neighboring points behave similarly. However, this may not always be the case, especially in areas with complex or discontinuous spatial patterns. In addition to these pointwise interpolation and collocation methods, free-form spline surfaces play a central role in approximating complex geometries from PCs.

The utilization of techniques based on free-form surfaces facilitates the transition from discrete point samples to continuous surface representations. These surfaces offer a compact and flexible approach to modeling complex geometries. In the field of Computer-Aided Geometric Design (CAGD), the B-spline, Bézier, and NURBS (Piegl & Tiller, 1997) methods are recognized as foundational tools. However, it should be noted that these methods were initially developed for constructive modeling purposes, rather than for the purpose of approximating measured data (Nuckelt, 2007). In recent decades, however, free-form surface techniques have become increasingly important in reverse engineering applications (Raja & Fernandes, 2008). Reverse engineering serves as a methodological bridge between geodesy and CAGD (Herrmann & Möser, 2008). The utilization of free-form curves and surfaces establishes a cohesive mathematical framework capable of describing a wide range of shapes. The associated algorithms are generally characterized by their rapid processing speed and numerical stability, thereby facilitating the execution of data processing operations in near real-time (Harmening, 2020). The broad range of applications of these methods is indicative of their versatility. These methods have been employed in a variety of settings, including the construction of engineered structures such as bridges (Paffenholz & Wujanz, 2019) and architectural landmarks like basilicas (Oreni et al., 2014), as well as natural forms including leaves (Harmening & Neuner, 2015), trees (Pfeifer & Winterhalder, 2004), and railway tracks (Bureick et al., 2019).

One of the earliest computational approaches in this field was proposed by Cox (1971), who applied an LS method to fit spline surfaces to observed data. This approach, which remains in wide use at present, seeks to minimize the L2 norm between the observations and the parametric surface. The objective is to estimate a set of parameters, or control points, that define the underlying function using spline basis functions. The approximation process involves computing the pseudoinverse of a matrix composed of B-spline basis function evaluations. This operation is computationally expensive, especially when dealing with large datasets and models that have numerous control points. The cost of matrix inversion increases exponentially with the number of observations and parameters, which limits the method's practical applicability to large-scale problems.

The B-spline surface approximation can be challenging when the model, parameterization strategy, or data characteristics, such as noise, irregular sampling, or data gaps, affect the system's numerical stability. A common issue arises when certain basis functions have no data points within their support. In such cases, the resulting design matrix is found to lack full row rank, and consequently,

a pure LS solution cannot be computed. To address this issue, the minimization functional is frequently extended with a smoothness term to regularize the solution (Nowacki et al., 1998). Despite the assumption of linear independence of basis functions and the avoidance of data gaps, the non-uniform density characteristic of real-world PCs can impede the efficacy of global approximation strategies. It has been demonstrated that irregular sampling has the potential to compromise the quality of approximations and introduce numerical instability (Bracco et al., 2018). These effects frequently necessitate local refinement or adaptive modeling techniques to ensure robust and accurate surface reconstruction.

The hierarchical B-spline refinement framework was first proposed by Forsey & Bartels (1992), who introduced an approximation technique based on a control lattice hierarchy (Forsey & Bartels, 1995). The interpolation process is executed sequentially, from the coarsest to the finest level, thereby progressively enhancing the approximation. However, this approach is predicated on the assumption of a regular data distribution, which renders it ill-suited for data that is scattered or sampled irregularly. To address this limitation, Lee et al. (1997) developed the MBA method, which extends the hierarchical concept to irregular data in a computationally efficient manner. MBA leverages the compact support of B-spline basis functions. Each basis function influences only a subset of the data, and each data point is affected by a limited number of coefficients. The surface is constructed level by level, and the coefficients at each level are computed explicitly. MBA is typically implemented in an adaptive setting, thereby yielding a multi-resolution surface representation.

However, in regions with sparse data, deeper refinement levels may lead to overfitting when modeling noise instead of the underlying surface. A range of local refinement strategies has been developed to circumvent the inefficiencies associated with global refinement, particularly in regions where high resolution is not necessary. These approaches enable a spatially adaptive representation, thereby allowing models to capture fine detail only where necessary without increasing complexity across the entire surface (Skytt et al., 2017). A number of noteworthy techniques have been identified, including Truncated Hierarchical B-splines (THB-splines) (Giannelli et al., 2012), Locally Refined B-splines (LR B-splines) (Skytt et al., 2017; Patrizi et al., 2020), Polynomial splines over T-meshes (PHT-splines) (Li et al., 2010; Schumaker & Wang, 2012), and Analysis-suitable T-splines (Sederberg et al., 2003; Li et al., 2012; Scott et al., 2012).

Building on these advances, recent work has explored the integration of local refinement with multilevel approximation. For instance, Patane (2016) integrated the MBA framework with locally refined B-spline, yielding the Locally Refined MBA (LR-MBA). This approach inherits the efficiency of the multilevel scheme while adapting flexibly to heterogeneous data density. Similarly, Kermarrec & Morgenstern (2022) proposed a Multilevel Truncated splines (T-splines) approximation by integrating the hierarchical structure of MBA with the local refinement capabilities of T-splines. These hybrid methods offer promising pathways for scalable and adaptive surface modeling in complex and irregular data settings. Although locally refined spline methods, such as LR B-splines, THB-splines, and T-splines, offer advanced flexibility through adaptive resolution, they also introduce several known limitations. These include increased implementation complexity, higher memory usage, and more elaborate refinement tracking structures (Skytt et al., 2017). In scenarios where large datasets or high-resolution modeling are required, these factors can impede computational efficiency and scalability. Additionally, irregular data distributions and sparse regions can complicate the decision-making process during refinement, potentially resulting in suboptimal surface representation, as evidenced by studies conducted by Skytt et al. (2017) and Kermarrec & Morgenstern (2022). Conversely, the fundamental form of the MBA employs a simple hierarchical structure, utilizes explicit coefficient computation, and circumvents the overhead associated with managing complex mesh structures. In light of these characteristics, the MBA remains a practical and effective alternative for the approximation of scattered data, especially when robustness and

computational efficiency are paramount.

In recent years, deep learning-based approaches have become a prominent research direction for surface reconstruction from PCs (Huang et al., 2022). In this literature, “reconstruction” usually refers to estimating either an explicit surface representation (for example, a polygon mesh) or an implicit field whose zero-level set defines the surface (Huang et al., 2022). Most learning-based pipelines rely on auxiliary training data paired with ground-truth geometry, which makes them supervised with respect to the target surface representation (Huang et al., 2022). Training-free variants also exist and optimize an untrained network per object or scene, using the network structure itself as a geometric prior (Huang et al., 2022). Despite rapid progress, a recent large-scale benchmark reports that deep learning methods can struggle to generalize to complex shapes and that several classical methods remain competitive, particularly under scanning imperfections such as misalignment, missing points, and outliers (Huang et al., 2022). In parallel, recent overviews emphasize that geometric deep learning on PCs increasingly needs explainable and human-interpretable model behavior, which is still an active research topic (Saranti et al., 2024). Conversely, MBA-based spline models provide an explicit parametric surface with a controllable level of detail and an adjustment-compatible formulation, which supports scalable processing and traceable uncertainty and quality assessment without reliance on task-specific training data.

In this dissertation, MBA-based surface models provide the main approximation framework for large-scale PCs and form the geometric basis for the subsequent quality assessment.

2.3 Quality Assessment of a Surface Model

Building on the surface-based approximation techniques reviewed in the previous section, we now address the quality assessment of the resulting surface models. Quality assessment is the final step in the surface modeling pipeline because it determines how reliably the model can be used in downstream tasks such as measurement planning, deformation monitoring, and risk management in engineering contexts (Eakins & Taylor, 2010; Hare et al., 2011). In these applications, it is necessary to quantify the remaining model uncertainty, describe its spatial variability, and assess the reliability of predictions derived from the surface.

Uncertainty in a surface model originates from two main sources. The first source is the uncertainty of the input PC, which is driven by the sensor system, environmental conditions, and processing steps. The second source is the uncertainty introduced by the modeling procedure itself, including model choice, parameterization, regularization, and the interaction between the model resolution and the local data support. Quality assessment methods can be organized from two complementary viewpoints. A backward approach starts from the available PC and evaluates uncertainty from data evidence, for example, through residuals, validation against reference data, or resampling. A forward viewpoint starts from a measurement model and propagates the measurement uncertainty through the modeling step to obtain an uncertainty description for the surface model.

From the backward viewpoint, one way to quantify the uncertainty of a deterministic surface model is to evaluate residuals against held-out data or external reference information. This approach is data-driven and yields spatially localized uncertainty metrics across the modeled domain. When a probabilistic description of the residual field is available, CIs can be derived from the assumed distribution. In cases with heterogeneous input density or missing observations, the surface model may be augmented by a variance map derived from a fitted statistical model. Alternatively, the model may be supplemented with multiple stochastic realizations based on a random-function representation of the residuals (Patane, 2016; Wackernagel, 2003). A related backward strategy

targets the PC itself. When a reference object, a reference surface, or repeated measurements are available, deviations between the measured PC and the reference can be used to infer the uncertainty level of the acquisition platform and to support measurement planning in situations where the full sensor chain is not documented.

From the forward viewpoint, quality assessment incorporates knowledge of the measurement process and propagates it through the modeling step. Reproducing and quantifying measurement uncertainty based on known influencing factors can be achieved by forward uncertainty modeling in the sense of the ISO/GUM:1995 (E) framework. This approach integrates sensor characteristics, environmental conditions, installation parameters, and other contributing factors into an uncertainty budget for each observation. These quantified uncertainties, including their correlations when available, can then be propagated through the approximation process to estimate the uncertainty of the resulting surface model. For complex and nonlinear measurement models, MC based propagation is often preferred over linearized variance propagation because it yields an empirical uncertainty distribution rather than only a single variance value.

However, in many real-world applications, detailed uncertainty information is not available or only partly documented. Even when uncertainty budgets exist, analytical propagation may not be tractable for large-scale data or for hierarchical surface representations. In the case of the MBA, the surface is constructed through multiple nested refinement levels, and each level depends on the residual structure of the previous one. This recursive structure induces strong dependencies across levels, which makes analytical propagation complex and computationally demanding (Publication A). In such cases, nonparametric uncertainty estimation methods provide a practical alternative.

Bootstrapping estimates model uncertainty by repeatedly resampling from the original dataset and recomputing the model on each synthetic sample (Efron, 1981; Efron & Tibshirani, 1994). This yields an empirical sampling distribution from which standard errors and CIs can be derived. Within geodetic time series analysis, Alkhatib et al. (2018) combined a robust generalized Expectation Maximization algorithm with a MC bootstrap scheme to obtain covariance matrices and CIs for multivariate nonlinear regression parameters in GNSS time series with autoregressive and heavy-tailed noise, illustrating that bootstrap-based quality assessment is feasible even for complex and robustly estimated models. In prior studies, bootstrapping was employed to assess the reliability of MBA surfaces derived from PSI observations, providing spatially explicit confidence measures in scenarios where input uncertainty is unavailable and analytical propagation is impractical (Publication A; Brockmeyer (2024b)). This approach complements forward modeling because it quantifies model sensitivity directly from the data and reflects the impact of heterogeneous density and data gaps.

In hydrographic applications, these general concepts specialize to quantifying the total propagated uncertainty of MBES derived bathymetric surface models. Despite the high spatial resolution of MBES data, typically around 1/50 of the water depth, measurement accuracy is not guaranteed. Each sounding is affected by both vertical and horizontal uncertainties (Lucieer et al., 2016). Nonetheless, dense coverage and fine resolution can lead users to overestimate the reliability of the measurements. Quantifying these uncertainties and understanding their influence on derived bathymetric products remains a fundamental challenge for the marine geospatial community. The IHO establishes formal standards for hydrographic surveys, including acceptable thresholds for depth measurement uncertainty arising from data acquisition and processing (International Hydrographic Organization, 2022; Hare et al., 2011). These guidelines are widely used, but they function as general targets rather than detailed models of system behavior.

As resolution and data volume increase, so does the importance of uncertainty modeling to assess the detectability and reliability of small-scale seabed features. This has led to growing interest

in the spatial characterization of uncertainty in MBES data (Hare, 1995; Lurton, 2003; Lurton & Augustin, 2010; Dolan & Lucieer, 2013). Researchers have increasingly focused on how sensor limitations, environmental conditions, and processing workflows contribute to TPU in bathymetric products. A foundational contribution was made by Hare (1995), who developed an algorithm to estimate depth uncertainty by accounting for multiple uncertainty sources, including the echo sounder system, vessel motion (roll, pitch, heave), refraction, dynamic draught, and tidal water level. Other components, such as positioning errors, transducer-to-sensor offsets, heading, and antenna location, are also considered part of the total uncertainty budget. The Law of Propagation of Variances provides a theoretical framework to integrate these sources, resulting in TPU estimates that are typically divided into vertical uncertainty, denoted by TVU, and horizontal uncertainty, or THU (Hare, 1995; Hare et al., 2011).

Subsequent studies have extended this framework by incorporating additional factors, such as Doppler frequency shifts and baseline decorrelation effects in frequency-modulated signals (Haji Mohammadloo et al., 2018, 2019). Other works have evaluated the predictive performance of uncertainty models with respect to depth measurements and grid quality (Haji Mohammadloo et al., 2018; Tengku Ali et al., 2022; Abubakar & Poerbandono, 2023). Maleika (2013) investigated how acquisition parameters, such as vessel speed, swath width, track layout, and measurement density, affect the resulting bathymetric grid using a virtual survey simulator. These findings highlight the sensitivity of uncertainty to sensor dynamics and survey design. Despite this progress, a key limitation remains the lack of reliable ground truth for underwater geometry, which restricts direct validation and complicates backward uncertainty evaluation for real surveys.

To address this limitation, the third contribution of this dissertation introduces a simulation-based framework for modeling TPU in MBES derived bathymetric surface models. The approach uses a configurable survey simulator to reproduce realistic acquisition scenarios, incorporating sensor configuration, vessel dynamics, and environmental conditions. Uncertainty is generated through Monte Carlo simulation, enabling spatially explicit estimation of both TVU and THU without requiring ground truth in the field. These uncertainty estimates are then introduced into the surface modeling process as observation weights, allowing uncertainty-aware adjustment and integrated quality assessment of the final bathymetric model. Methodological details and results are presented in (Publication C).

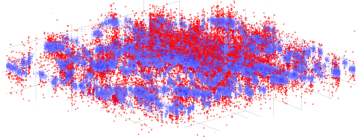
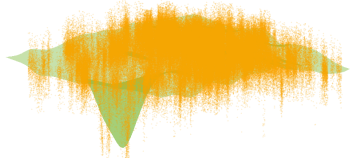
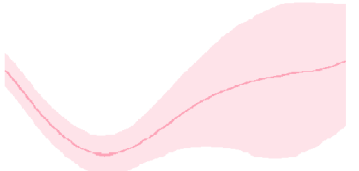
Together with the surface approximation methods discussed above, this uncertainty framework completes the conceptual pipeline for modeling, assessing, and interpreting point-sampled bathymetric surfaces in this dissertation.

3 Summary and Integration of Published Research: A Methodological Synthesis

This chapter presents a synthesis of the methodological advancements and principal findings derived from the key scientific publications that form the basis of this cumulative dissertation (see Section 1.3). Rather than summarizing each publication independently, the discussion is structured according to the three core stages of the proposed modeling pipeline for point-sampled surfaces: (i) data cleaning and outlier detection, (ii) surface modeling, and (iii) uncertainty modeling and quality assurance. The mapping between publications, pipeline stages, and the sections of this chapter is summarized in Table 3.1.

The cumulative body of work comprises three peer-reviewed journal articles, each contributing to one or more stages of the pipeline. In addition, one supplementary study is referenced: a contribution focusing on surface-based modeling using MBA (Publication D). The supplementary research is not part of the cumulative core, yet it provides essential conceptual and methodological support for surface representation and evaluation.

Table 3.1: *Mapping of research questions to publications.*

Research Question	Relevant Publications	Relevant Sections
RQ 1 	Publication A Publication B	Section 3.1 Data Adaptive Outlier Detection (3.1.1) The IESP Approach (3.1.2)
RQ 2 	Publication A Publication B Publication C Publication D	Section 3.2 Surface Modeling with MBA
RQ 3 	Publication A Publication C	Section 3.3 Bootstrapping (3.3.1) Forward Uncertainty Modeling (3.3.2)

The structure of this chapter follows the logic of the pipeline, with each section referencing the relevant publication. Section 3.1 addresses preprocessing and outlier removal. It contains two methods: Section 3.1.1 presents the Data Adaptive Outlier Detection from Publication A, including the algorithmic workflow and evaluation settings. Section 3.1.2 introduces the Iterative Estimation of Surface Parameters (IESP) approach from Publication B for challenging datasets. Section 3.2 is the core of the pipeline and defines the surface representation used throughout Publication A, Publication B, Publication C, and Publication D. Section 3.2.1 details approximation with MBA and the design choices that control complexity. Section 3.2.2 reports a broad evaluation based on Publication D. Section 3.3 quantifies model uncertainty. Section 3.3.1 uses bootstrapping when observation variances are not available, following Publication A. Section 3.3.2 performs forward uncertainty modeling when system uncertainty models are available, following Publication C.

3.1 Outlier Detection and Data Cleaning

High-quality surface modeling requires input data that is minimally contaminated by noise or artifacts. However, these PCs often contain measurement noise, irregular sampling, spatial gaps, and anomalous points that can distort the final model if not properly addressed. Therefore, the first stage of the processing pipeline is dedicated to outlier detection, which aims to identify observations that deviate from the expected spatial structure of the surface. This step is designed to be platform-independent and applicable to any PC representing a physical surface, regardless of the sensing system used.

A critical requirement in selecting an appropriate outlier detection method is to understand the nature of the data and define what constitutes an outlier in this context. Following Hawkins (1980), an outlier is “an observation that deviates so much from other observations as to arouse suspicions that it was generated by a different mechanism.” In a geospatial PC, such deviations may originate from sensor failure, environmental interference, or post-processing artifacts. In this dissertation, outliers are defined as observations that violate the expected local or global surface structure inferred from the majority of the data. Here, it is assumed that the majority of data points represent a dominant spatial structure corresponding to the physical surface. Outlier detection is, therefore, a process of identifying observations that violate this underlying assumption. To formalize this, we consider a standard contamination model for the distribution of observation error. In most practical cases, the majority of observations follow a main distribution $F_G(\cdot)$, while a small fraction ϵ originates from an outlier-generating process $F_o(\cdot)$ (cf. Huber & Ronchetti, 2009, p. 2). The resulting contaminated error distribution (F_e) is modeled as:

$$F_e(e) = (1 - \epsilon) F_G(e) + \epsilon F_o(e) \quad \epsilon \ll 1, \quad (3.1)$$

where ϵ denotes the outlier proportion. This mixture model typically assumes that most errors are Gaussian, reflecting sensor precision and environmental stability, while outliers come from an unknown, potentially heavy-tailed distribution.

To address the challenges, two complementary surface-based outlier detection algorithms were developed and evaluated:

1. **Data Adaptive Outlier Detection:** Introduced in Publication A, this method identifies outliers based on deviations from a locally approximated surface. It adapts to variations in surface geometry and noise levels, making it suitable for heterogeneous datasets (Section 3.1.1).
2. **IESP:** Presented in Publication B, this method builds on the Data Adaptive concept and

complements it through an iterative estimation framework. It jointly refines the surface model and the influence of observations, allowing for more robust detection in complex cases, such as spatially clustered or high-density outliers (Section 3.1.2).

3.1.1 Data Adaptive Outlier Detection

The Data Adaptive Outlier Detection algorithm presented in Publication A leverages the deviation of each observation from a fitted surface model. The aim is to assess the distance of the observations to the approximated model, with the judgment that observations with the highest deviation are more likely to be outliers. However, two core challenges must be addressed:

- **Underfitting:** If the surface model is too smooth (i.e., of low complexity), legitimate local features may be misclassified as outliers.
- **Masking:** Extreme outliers can distort the model fitting, thereby hiding neighboring outliers and misclassifying them as inliers.

To mitigate these issues, the algorithm proceeds iteratively. At every iteration, a surface model is approximated, and consequently, the deviations of the data from the model are calculated. In the first iteration, a coarse global model with minimum required complexity is applied to obtain a rough approximation of the data. This helps reduce the risk of underfitting, where a model that is too smooth may wrongly classify valid local features as outliers. Prior knowledge about the data's expected behavior can guide this initial model selection. In subsequent iterations, model complexity is gradually increased to progressively reduce smoothing effects and better capture finer surface details. Fig. 3.1 illustrates the iterative coarse-to-fine strategy, where residuals are trimmed in successive steps.

At each step, the surface is estimated via GMM with L2-norm estimator. The residuals are calculated based on the distance between the observations and the estimated model and are assumed to be normally distributed. Observations with residuals that exceed a trimming threshold are flagged as outliers. Iterations continue until the residual distribution approximates the expected noise characteristics of the dataset, indicating convergence without overfitting. Selecting the trimming threshold is a critical step in the algorithm. It is defined as $T \cdot \sigma_r$, where σ_r is the residual's standard deviation in each iteration, and T is a chosen factor. Interpreting $T \cdot \sigma_r$ as a distribution-level CI threshold yields a single, computationally stable decision rule per iteration for large PCs. This avoids per-point hypothesis tests with many simultaneous decisions and improves robustness when residuals are dependent, and outliers occur in clusters, where masking can occur (Davies & Gather, 1993). A detailed sensitivity analysis of the threshold parameter T in the range $[1.5, 5]$ revealed optimal performance with $T \in [2.8, 3.5]$ under moderate noise conditions. The analysis indicated that the ideal threshold varies with both the noise level and the outlier percentage (Publication A).

For performance evaluation, the detector is treated as a binary classifier that assigns each point to the positive class (outlier) or the negative class (inlier). Results are summarized in a two-by-two confusion matrix (Table 3.2). A True Positive (TP) is an actual outlier predicted as an outlier. A True Negative (TN) is an actual inlier predicted as an inlier. A False Positive (FP) is an inlier predicted as an outlier. A False Negative (FN) is an outlier predicted as inlier. To assess the performance of the algorithm, we use precision, recall, the F_1 -score, and accuracy. Precision quantifies the proportion of detected outliers that are correct, while recall measures how many true outliers are identified. The F_1 -score summarizes both measures. Accuracy reports the overall proportion of correctly classified points. Because class imbalance may occur in the datasets, Balanced Accuracy (BA) is also reported. It is obtained by averaging the True Positive Rate (TPR) and the

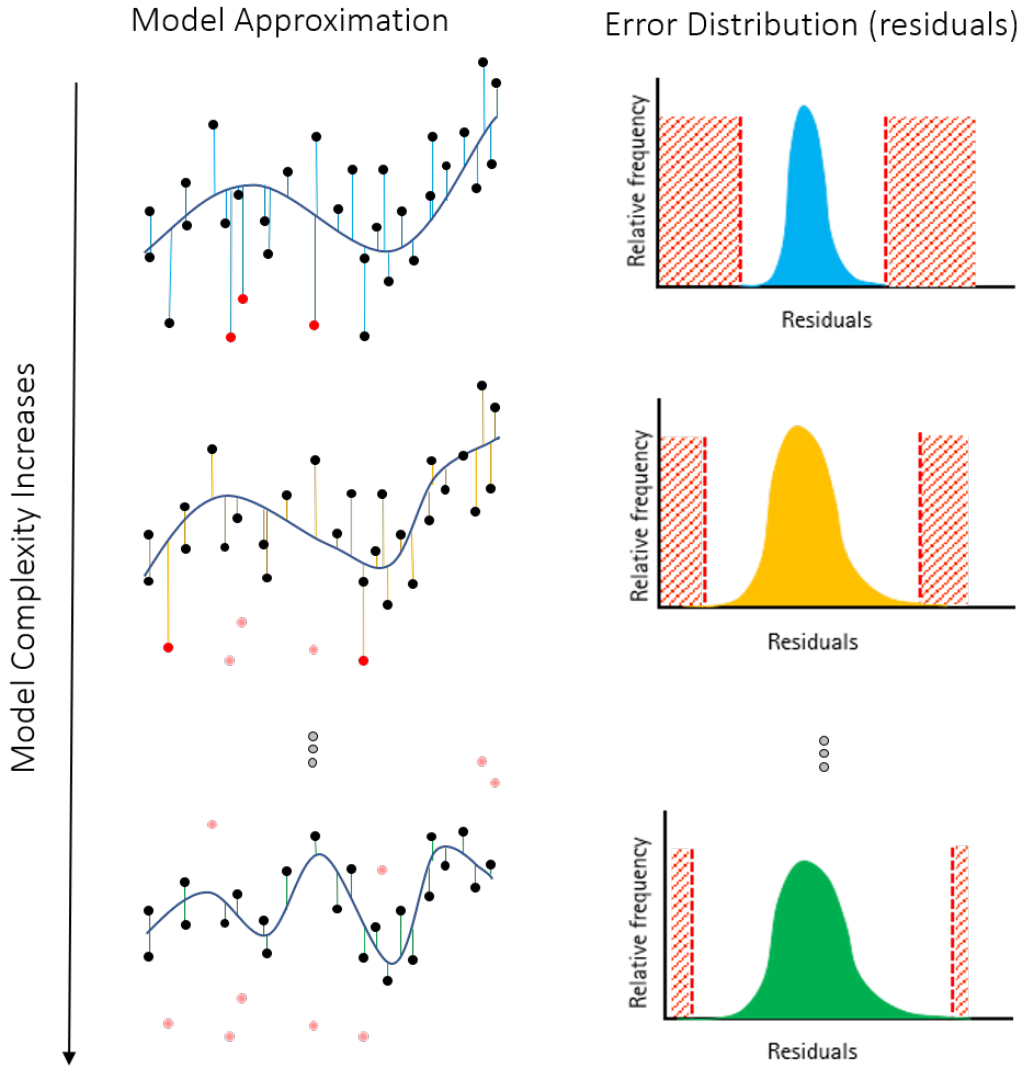


Figure 3.1: Schematic representation of the "Data Adaptive Outlier Detection" approach; iterative hierarchical process: coarse-to-fine surface fitting with residual trimming. The right panels show how the residual distribution narrows through successive iterations.

True Negative Rate (TNR). In addition, the Matthews Correlation Coefficient (MCC) is included, since it provides a single-score summary of classification performance that remains reliable under imbalance. All metrics are calculated according to the formulas in Table 3.3.

To evaluate performance, the algorithm was assessed in an MC simulation with 1000 runs using simulated datasets with varying levels of Gaussian noise and outlier contamination ($\varepsilon \in 5, 10, 15\%$). In each run, only the z component is treated as stochastic and observations are generated as $z = z_{\text{trend}} + e_n + e_o$, where $e_n \sim \mathcal{N}(0, \sigma_n^2)$ with $\sigma_n \in \{0.05, 0.1, 0.5\}$ m. An outlier term e_o is added to an ε -percent subset of points selected uniformly at random (and set to zero for all remaining points). The outlier magnitudes are sampled from a χ^2 distribution and scaled to fall within the outer 15% tails of a $\mathcal{N}(0, 0.5^2)$ distribution; the injected indices define the ground-truth outlier labels, and no explicit spatial clustering is enforced (Publication A).

The algorithm was applied to PSI data from Hannover, which is described in Section 1.4.1.3. For PSI data, each scatterer is derived from a time series. A temporal preprocessing step is applied based on Brockmeyer et al. (2020). The PSI time series are first de-trended using linear regression, and the residual standard deviation is used as a variability indicator. If this exceeds an experimental

Table 3.2: *Confusion matrix.*

		Actual	
		Inliers /Negative	Outliers/Positive
Predicted	Inliers /Negative	True Negative (TN)	False Negative (FN)
	Outliers/Positive	False Positive (FP)	True Positive (TP)

Table 3.3: *Performance metrics for outlier classification based on confusion matrix elements; TP, TN, FP, and FN.*

Performance Metric	Formula
Precision	$\frac{TP}{TP+FP}$
Accuracy	$\frac{TP+TN}{TP+FN+FP+TN}$
Recall/TPR	$\frac{TP}{TP+FN}$
TNR	$\frac{TN}{FP+TN}$
F1-Score	$\frac{2}{\text{precision}^{-1} + \text{recall}^{-1}}$
BA	$\frac{TPR+TNR}{2}$
MCC	$\frac{TP \times TN - FP \times FN}{\sqrt{(TP+FP)(TP+FN)(TN+FP)(TN+FN)}}$

threshold of 6 mm, the scatterer is marked as an outlier and removed from further processing. Even after temporal filtering, the vertical velocities derived from PSI still show strong spatial variability due to differing movement behaviors among neighboring scatterers. As described in Section 1.4.1.3, the PSI dataset covers a large area and consists of irregularly distributed 3D points with only vertical velocities considered. The data are sparse in some regions and exhibit variable point densities due to clustering effects typical of urban PSI observations. This results in areas with low coverage or data gaps. Because only vertical motion is analyzed, the PSI data are treated as 2.5D. A corresponding B-spline surface model is used. Outliers are iteratively detected using hierarchical surface fitting.

In Fig. 3.2, the peak of the fitted normal curve is clearly lower than the central bin of the histogram, although the residuals become more symmetric over the iterations. This is to be expected when the residuals are still a mixture of an approximately Gaussian inlier component and a small fraction of large deviations (remaining outliers or local model mismatch), which produces heavy tails. Those heavy tails inflate the empirical variance used for the normal fit, which widens the curve and reduces its apex relative to the histogram. Therefore, normality is used here as a working model for the inlier component rather than as a strict assumption for the full residual distribution. The final outlier map is visualized in Fig. 3.3. Red points indicate outliers; blue points are retained for modeling. For benchmarking, our results were compared with those from Brockmeyer et al. (2020), who applied a local-neighborhood filtering approach. Their method identified 15.609 outliers, while ours detected 15.201. Table 3.4 summarizes the comparison, demonstrating comparable performance despite differing methodological principles.

The "Data Adaptive Outlier Detection" algorithm demonstrated strong performance in handling outliers within simulation and PSI datasets. In particular, it proved highly effective at identifying and removing isolated deviations from consistent spatial trends, even in large-scale and noisy PSI

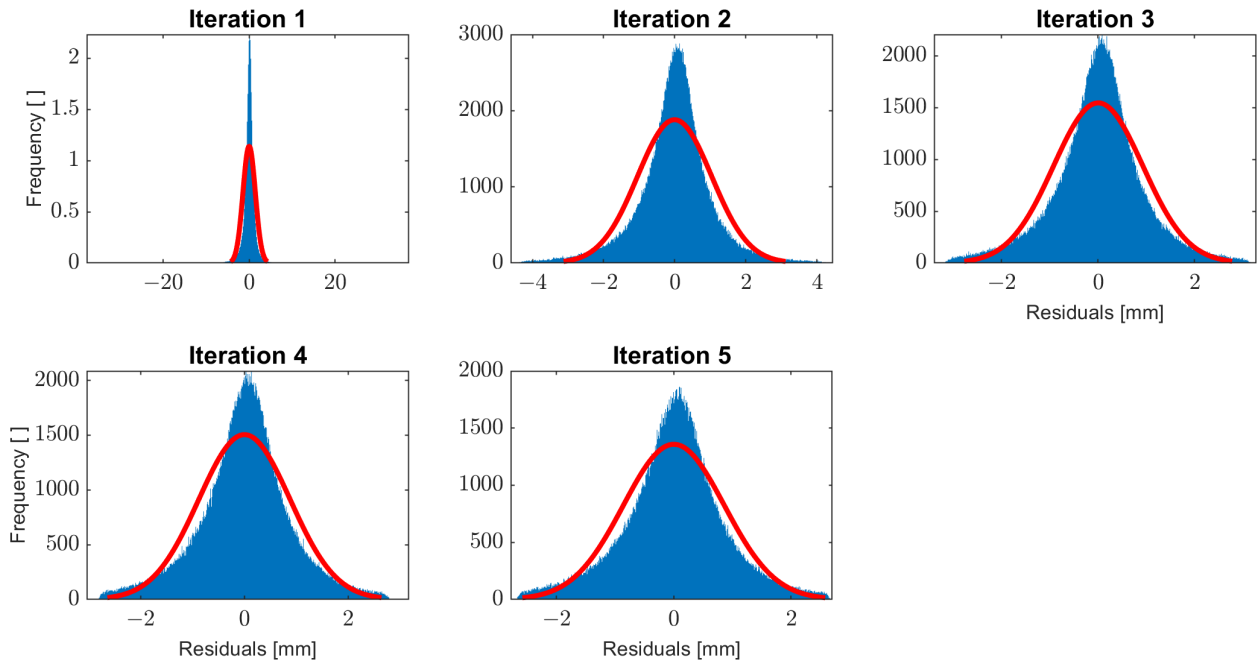


Figure 3.2: Histogram of residuals after each iteration of the IESP algorithm. The red curve shows the best-fit normal distribution to the residuals at each iteration (Publication A). Residuals become more symmetric, and the mean shifts toward zero as contaminated observations are trimmed.

observations. The application to real PSI data confirmed that the method is well-suited for detecting sparse, non-systematic anomalies. In summary, the method's novelty lies in its coarse-to-fine surface fitting with residual trimming, which yields a stable, data-adaptive filter without relying on fixed neighborhood definitions. However, in more complex data scenarios, especially those involving clusters of outliers, the underlying assumptions of this approach become less valid. When outliers do not appear as independent, isolated points but instead form dense groups or spatially structured patterns, the model fit can be distorted. In such cases, the residual-based identification of outliers becomes less reliable, as these artifacts can closely resemble valid surface features. Publication B addresses these issues by developing a new surface-based cleaning algorithm tailored to clustered and spatially structured outliers, described in Section 3.1.2.

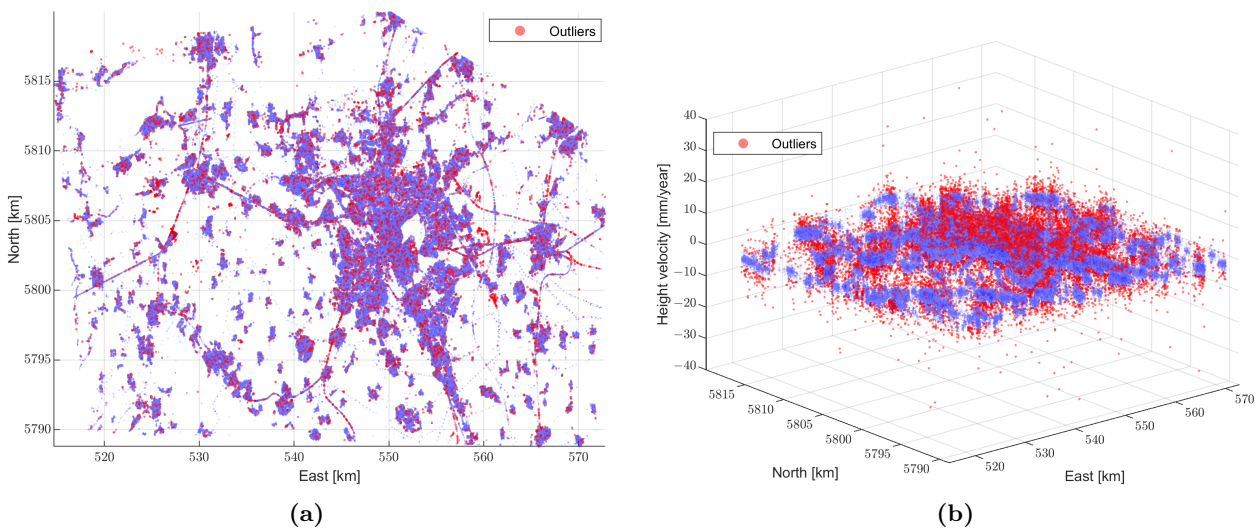


Figure 3.3: Detected outliers (red) vs. inliers (blue). (a) 2D view; (b) 3D view (Publication A).

Table 3.4: Comparison of the "Data Adaptive Outlier Detection" algorithm with the results from Brockmeyer et al. (2020) (Publication A).

Performance Measure	Precision	Recall	Accuracy	F1-score	BA	MCC
Value	0.93	0.89	0.99	0.91	0.95	0.91

3.1.2 The IESP Approach

In the "Data Adaptive Outlier Detection" approach, the estimation of the surface parameters Eq. (A.27) is a core step. If the level of contamination is high and/or the outliers present themselves in clusters, the Data Adaptive algorithm will not perform as expected. Parameter estimation, as it will be described in Appendix A.1, is based on minimizing the sum of squared residuals, which is highly sensitive to outliers due to the quadratic loss function. Publication B suggests adapting a robust Maximum Likelihood Estimator (M-Estimator) to limit the influence of extreme or anomalous observations so that they don't overly skew the result.

The first step in selecting an estimator is to state how outliers are defined and what is assumed about them. In GMM with L2-norm estimator the working assumption is that measurement errors, and thus the observations, are normally distributed. Here, the assumption on the cumulative distribution of errors with outliers aligns with Eq. (3.1). In many robust estimation problems, particularly those involving M-Estimator, the goal is to reduce the influence of outliers by replacing the standard LS loss with a more tolerant function, such as the Huber function. These robust loss functions assign less weight to observations with large residuals, which makes the estimator more resilient to anomalies in the data. However, the resulting optimization problem is no longer linear and cannot be solved in closed form. Instead, it is typically addressed using the IRLS algorithm. In this approach, the estimation is reformulated at each step as a weighted LS problem, where the weights depend on the residuals from the previous iteration. Observations with small residuals receive higher weights, while those with large residuals are down-weighted, often significantly. This process is repeated until convergence, meaning that the parameter estimates and the weights become stable. The need for iteration arises directly from the dependency between residuals and weights: the weights are a function of the residuals, but the residuals themselves depend on the current model parameters. IRLS provides a practical way to resolve this circularity by updating both in tandem.

While robust estimators offer resilience to outliers, their effectiveness is typically limited to small deviations from a predefined model. In real-world scenarios, however, neither the underlying model nor the degree of data contamination is known. This uncertainty introduces the risk of masking, where clustered outliers evade detection due to mutual reinforcement. To address this, the proposed outlier detection procedure adopts an iterative strategy. Specifically, the surface parameters are estimated via IRLS, and in each iteration, the distribution of residuals is examined. A CI is derived based on an assumed contamination level, and observations outside this interval are trimmed. Only the observations falling within this CI are retained for the next round of IRLS. This cycle continues until the fitted residual model stabilizes. Convergence is assessed using the two-sample Kolmogorov-Smirnov (KS) test (Massey Jr, 1951) as a practical stability check between successive iterations. After fitting a χ^2 model to the squared residuals in each iteration, the corresponding Probability Density Function (PDF) is evaluated on a fixed support grid, and the resulting vectors of density values are compared across iterations. This use of the KS test is not a normality test and should be interpreted as an indicator of stability of the fitted residual model rather than a formal test of equality between residual PDFs. In practice, this stability coincides with negligible changes in the estimated χ^2 parameters. When the test indicates no significant change between successive iterations at the chosen significance level, the process terminates. This iterative scheme, referred to

as the IESP approach, effectively increases the likelihood of detecting masked outliers and enhances the robustness of the overall estimation. Fig. 3.4 illustrates the structure of the proposed method, which comprises two main components: the IRLS-based estimation of surface parameters and the iterative trimming of the residual distribution.

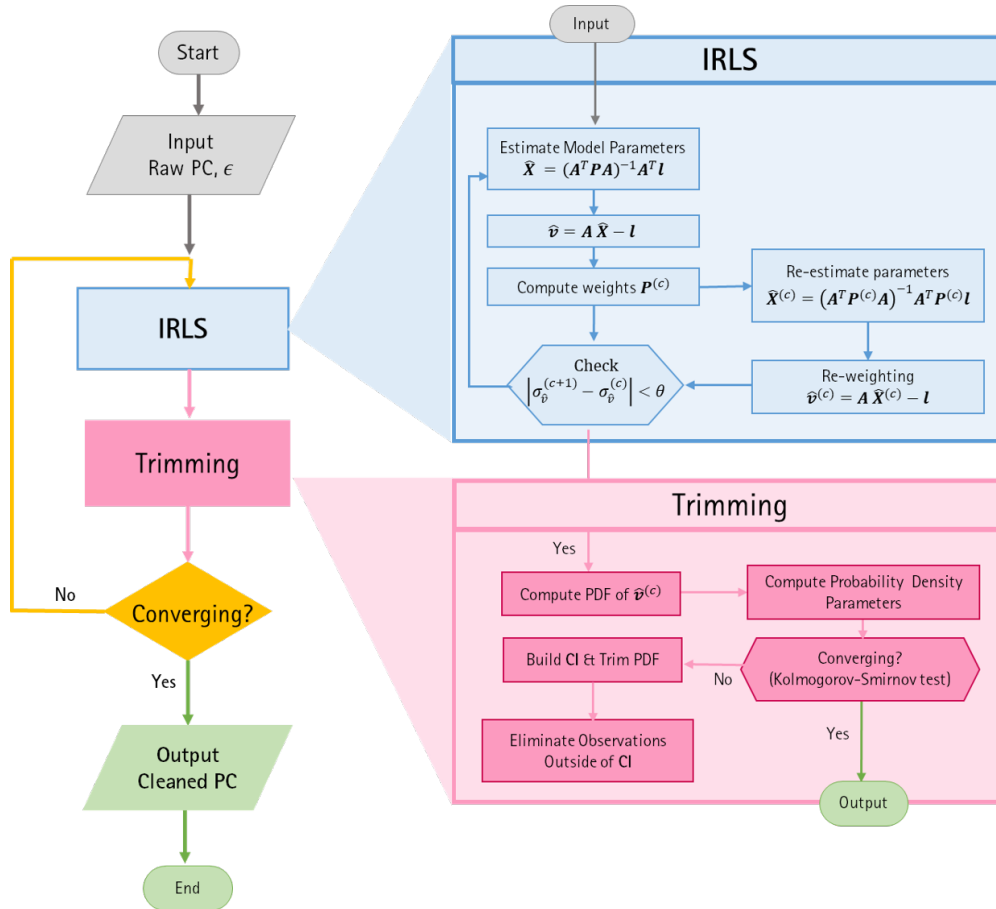


Figure 3.4: Flowchart of the proposed algorithm for outlier detection: Iterative Estimation of Surface Parameters (IESP).

MBES data are inherently prone to challenges such as spatially clustered outliers, inconsistent point densities, and systematic measurement uncertainties stemming from environmental and instrumental factors. These anomalies complicate surface modeling and often demand manual preprocessing.

To address these issues, the IESP method was applied with a preset contamination level of 3%. The algorithm iteratively models the squared residuals using a Chi-squared distribution, identifying and trimming outliers based on the 97% CI. Convergence is achieved when the parameters of the distribution stabilize. Over 10 iterations, the process gradually refines the model and improves outlier separation. Figure 3.5 illustrates this iterative workflow on a subset of Kiel Canal data. It shows how residuals evolve, how the Chi-squared model fits to squared errors, and how outliers are progressively detected and visualized spatially.

Applied to real MBES datasets (Section 1.4.2.2), including complex seafloor areas with rapid depth changes, the method demonstrated strong performance without requiring prior sensor or environmental metadata. Compared against manual cleaning by hydrographers, it achieved 97% detection accuracy and a BA of 0.99. Qualitatively, the method preserved important topographic features while effectively removing spurious measurements that typically bias surface modeling and uncertainty estimation. Quantitative benchmarking further confirmed IESP's superiority over standard methods like Method 1 (One approach developed at the Federal Institute of Hydrology (BfG) is an

applied strategy used in practice, for instance, in use by organizations such as WSV), LOF, and Density-Based Spatial Clustering of Applications with Noise (DBSCAN). Table 3.5 presents the results. IESP maximizes sensitivity and class balance, reaching TPR 1.00 and BA 0.99, consistent with its overall detection accuracy of 0.97 reported in the paper. The gain comes with lower precision 0.68 and more FPs, which are preferable to missed outliers for downstream modeling. Method 1 delivers the highest nominal accuracy, 0.99, and strong precision of 0.90, but with a lower recall of 0.84. DBSCAN yields very high precision 0.97 and the fewest FPs, yet misses many true outliers (TPR 0.65, BA 0.83). LOF underperforms across metrics (TPR 0.24, BA 0.62). Overall, IESP offers the most reliable outlier screening when preserving seafloor structure and avoiding missed errors is the priority, while requiring minimal tuning and no sensor metadata.

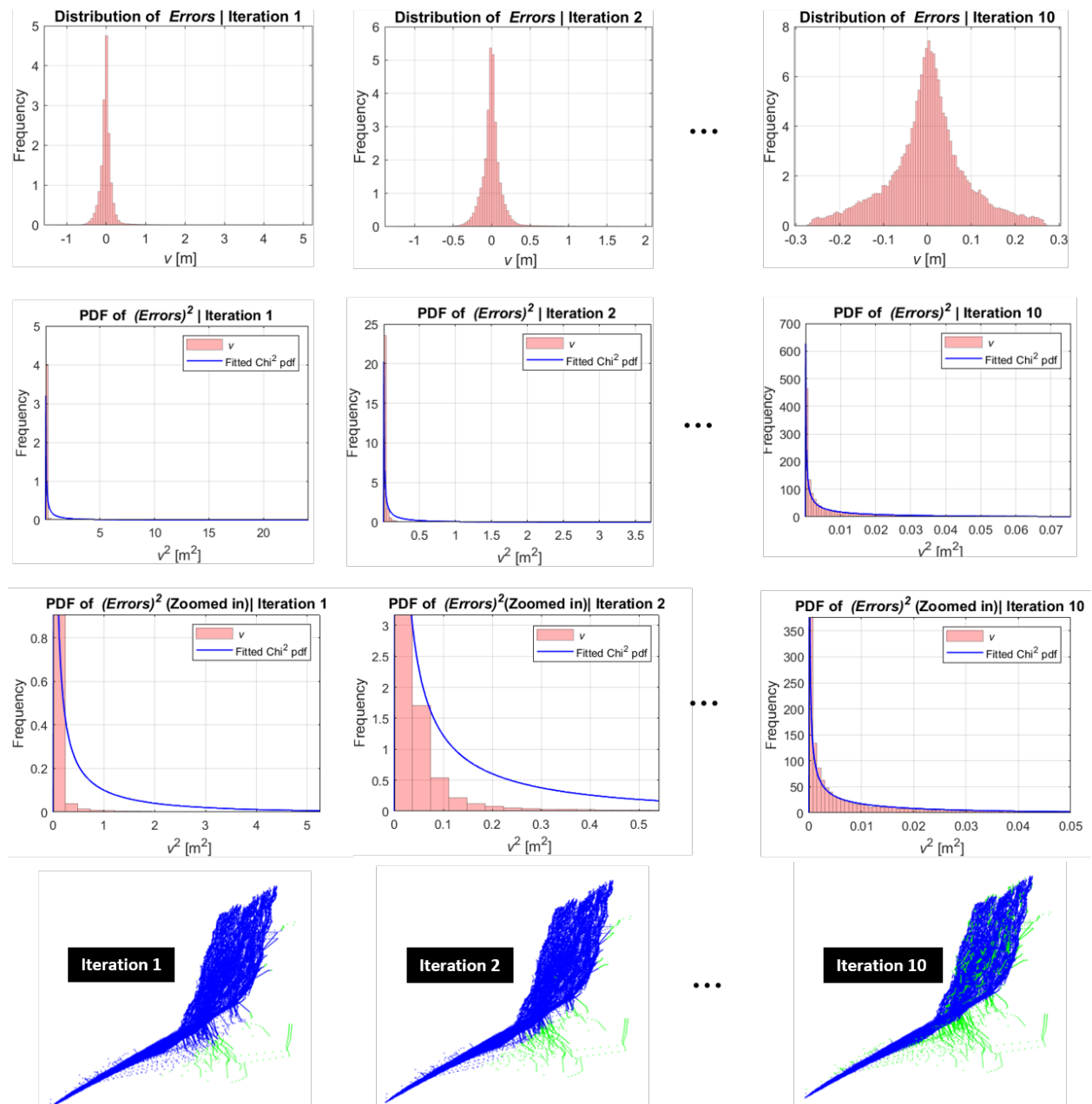


Figure 3.5: Details of IESP iterations on a section of the Kiel Canal data. The first row shows the histogram of residuals in each iteration. The second row shows the histogram of squared residuals along with the fitted PDF. The third row illustrates a zoomed-in view of the fitted PDF. The fourth row shows 3D visualization of the points (green points illustrate the detected outliers in each step) (Publication B).

Although computationally more intensive, IESP’s robustness stems from its minimal hyperparameter dependency, mainly limited to the contamination estimate, and its capacity to operate without prior environmental or sensor-specific information. This significantly reduces manual intervention and accelerates the preprocessing step. In terms of runtime, the implementations (MATLAB and Python) were benchmarked on a single-core machine (3.60 GHz CPU, 64 GB RAM). For the example dataset, DBSCAN required about 10 s, LOF about 3 min, IESP about 30 min, and the semi-manual Method 1 required about 1 to 2 days due to interactive processing.

Table 3.5: *Results of IESP’s algorithm on the Kiel Canal data (Publication B). Best values are in bold (higher is better, except FN and FP). Takeaway: IESP attains perfect recall (1.00) and the highest BA (0.99), which minimizes missed outliers at the cost of more FPs.*

Performance Metric	Method 1	IESP	LOF	DBSCAN
TN	445502	435636	444634	447233
FN	4332	53	19994	9181
FP	2347	12213	3215	616
TP	21930	26209	6268	17081
Precision	0.90	0.68	0.62	0.97
Recall/TPR	0.84	1.00	0.24	0.65
Accuracy	0.99	0.97	0.95	0.98
F1-score	0.87	0.81	0.35	0.78
BA	0.92	0.99	0.62	0.83
MCC	0.86	0.81	0.38	0.78

3.1.3 Comparison of Data Adaptive Outlier Detection and IESP

Both approaches were designed to be general and platform-independent. Each follows an iterative, surface-based strategy that serves the first stage of the pipeline and addresses RQ 1 (Section 1.2) by preparing cleaned observations for modeling. The Data Adaptive method fits a surface with LS and thresholds residuals per iteration. It is easy to configure. In our implementations, it typically completes within minutes for the PSI-scale datasets used in this thesis, although this runtime is not directly comparable to the benchmark results reported in Publication B because dataset size and characteristics differ. It works well when spurious points are sparse and spatially isolated. Its main weakness is sensitivity to clustered errors, where the intermediate surface can be biased and local morphology can be distorted.

The IESP method was developed to address these limits. In the estimation stage, surface parameter estimation is integrated with a robust estimator. An inner iterative reweighting is embedded within each outer iteration, so parameters and weights are updated together. This increases computational cost but improves stability in the presence of clusters, nonuniform sampling, and steep gradients. In the benchmark reported in Publication B, DBSCAN required about 10 s, LOF about 3 min, and IESP about 30 min on a single-core (3.60 GHz CPU, 64 GB RAM), while the practical effort for Method 1 required about 1 to 2 days due to manual interventions. Platform metadata is not required, and hyperparameter demands remain modest. When reliable information on observation uncertainty is available, it can be incorporated in the weighting, which is expected to improve the quality of the procedure. This extends the method’s utility beyond the initial design goals.

From a pipeline perspective, the main contribution is that both methods operationalize outlier detection through the same surface modeling backbone while targeting different contamination

regimes. They differ in complexity and in how they manage clustered structure, yet both reduce manual effort and preserve terrain features needed for subsequent modeling. Neither method is fully automatic, but each operates with minimal manual intervention and delivers dependable preprocessing for surface reconstruction. With the outlier detection stage complete, the pipeline shifts from removing contamination to modeling the surface geometry.

3.2 Surface Modeling

After the preprocessing stage provides a clean and reliable PC, the next step in the pipeline is to construct a continuous surface model suitable for prediction, quality analysis, and uncertainty propagation. Due to the irregular sampling and noise sensitivity inherent in spatial PC, interpolation and approximation techniques that preserve structural integrity are required. A core challenge in many applications, such as quality control, uncertainty estimation, and data fusion, is the construction of a continuous surface model from discrete, scattered observations. To address this, a mathematical parametric surface model offers several advantages: it allows for efficient data handling, supports spatial prediction at unsampled locations, and enables downstream processes such as uncertainty propagation and topographic analysis. Given the large volume and spatial heterogeneity of the target datasets, we employ a 2.5D representation, modeling depth as a single-valued function of horizontal coordinates, i.e., $z = f(\mathbf{x}, \mathbf{y})$. This ensures that each planar location is represented by a single z value. Therefore, multi-layer structures, vertical faces, and overhangs cannot be modeled explicitly. Consequently, the stochastic description and subsequent uncertainty analysis are restricted to the scalar height field. Uncertainty is quantified in the vertical direction, and lateral effects are captured implicitly by the surface model.

This simplification is a deliberate trade-off between geometric completeness and computational tractability. It reduces computational complexity and mitigates the numerical instabilities that often occur in full 3D surface modeling. This approach is also suitable for large PCs and grid-based products. In this setting, we adopt the MBA approach to balance flexibility with efficiency. The MBA approach is particularly well-suited to irregularly spaced data because it combines local support with multiscale refinement at moderate model complexity. To maintain the focus of this chapter on synthesis, only the conceptual components necessary for understanding the papers are summarized here. The full deterministic and stochastic formulations are provided in Appendix A.1.

3.2.1 MBA

MBA provides a hierarchical framework for surface approximation based on tensor-product B-spline surfaces. Originally developed in the 1990s for image processing tasks such as morphing (Lee et al., 1995, 1996), a general formulation for scattered data approximation was later introduced by Lee et al. (1997).

In this dissertation, MBA is used as a common surface model to represent large and irregular point clouds as a continuous 2.5D surface. The model is defined by a regular control lattice over the planar domain, and the unknown parameters are the control point values on that lattice. A key practical property is local support: the surface value at a given planar location depends only on a small neighborhood of nearby control points. This keeps the estimation scalable and makes the model less sensitive to nonuniform sampling and local data gaps.

The multilevel structure addresses the trade-off between smoothness and local detail. The approximation starts with a coarse lattice that captures long-wavelength structures. The remaining

residuals to the observations are then approximated again using a refined lattice. Repeating this refinement adds details step by step without forcing a single very dense lattice from the start. The final surface is obtained as the sum of the level-wise contributions. Figure 3.6 summarizes this construction schematically.

The full mathematical formulation is provided in Appendix A.1 to keep this chapter focused on synthesis rather than derivations. Appendix A.1 includes the deterministic construction (Section A.1.1), multilevel residual refinement (Section A.1.2), refinement-based optimization (Section A.1.3), and the stochastic formulation (Section A.1.4) used later for uncertainty propagation.

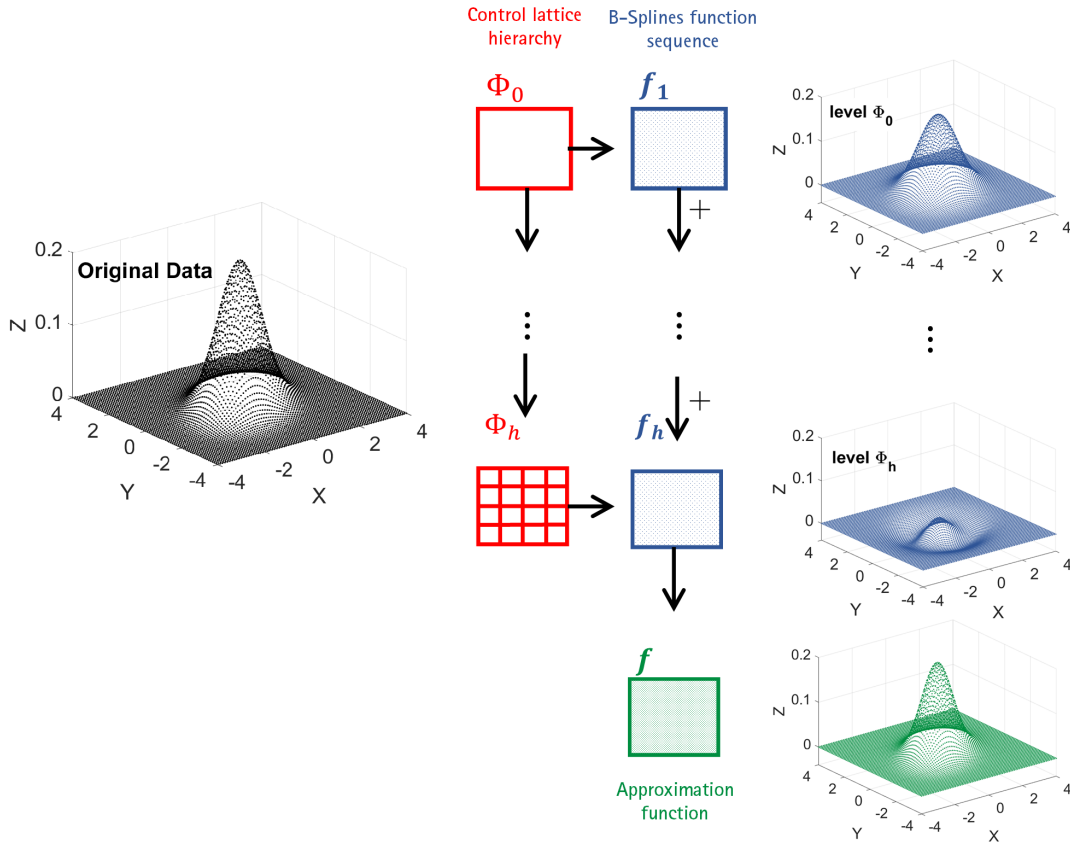


Figure 3.6: Schematic representation of the MBA concept. A coarse lattice captures the large-scale surface, refined lattices approximate residuals to add local detail, and the final surface is formed by summing the contributions across levels (Publication D).

3.2.2 Evaluation of MBA

With the core idea of MBA established in Section 3.2.1, this subsection assesses its practical performance as a surface model under conditions that resemble the intended applications. The mathematical details required to reproduce the model are provided in Appendix A.1, while this subsection focuses on the evaluation design and the main conclusions. The findings are presented in detail in Publication D. The evaluation proceeds along two tracks. First, controlled simulations with known ground truth are used to test performance under noise and missing coverage. Second, an application to the Hengstlage dataset (Section 1.4.1.2) assesses behavior on real observations and links the method to the broader processing pipeline. The simulated track uses segmented cross-validation combined with MC repetition. Test subsets are withheld to create training gaps of controlled size and layout. For each MC run a new noise field is drawn while cross-validation

varies the partitions. Prediction accuracy is summarized by the Root Mean Square Error (RMSE) at withheld locations. Full simulator settings and results are given in Section 3.2.2.1.

The real-data track applies the same modeling setup to the Hengstlage data and fits both MBA and Ordinary Kriging for comparison. No ground truth is available, so performance is measured by internal prediction errors. Each observation is treated as a potential test point through cross-validation, and predictions are compared at the observed positions. The resulting RMSE provides a common error measure for both methods. Ordinary Kriging is used as a benchmark. It relies on a stochastic covariance model specified by a variogram. Here, an exponential variogram is adopted, and the search neighborhood is the full field. These settings are held fixed across both tracks to enable a transparent comparison of error measures and modeled surfaces.

3.2.2.1 Evaluating MBA with Simulated Data

The simulator generates a 2.5D field on a uniform grid with deterministic planimetry and stochastic height. The domain is $-4 \leq x, y \leq 4$ with spacing 0.1, which yields 6561 points. The simulation is performed in an abstract coordinate system without assigned physical units. Accordingly, the reported amplitudes and error measures (including RMSE) are unitless and should be interpreted relative to the domain scale. The field is the sum of a fixed trend and an additive noise term. The trend is produced by a two-component Gaussian mixture that sets smooth large-scale variation. Full mixture parameters are reported in Publication D, and the trend is fixed across all runs. The additive noise is Gaussian with zero mean and standard deviation 0.001:

$$\text{noise} \sim \mathcal{N}(0, 0.001^2). \quad (3.2)$$

A fresh noise realization is drawn in each MC run. Within a run, the same noise field is used for all cross-validation iterations. This design separates randomness due to measurement noise from randomness due to the selection of the test set. The chosen amplitude is small relative to the trend range, so recovered errors near this level indicate that the method tracks the underlying surface rather than the noise. Fig. 3.7 visualizes the fixed trend, a representative noise field, and their sum. Only this figure is retained for documentation of the simulator input to the evaluation.

Performance is measured by segmented cross-validation (repeated random subsampling) embedded in a MC scheme (Arlot & Celisse, 2010; Esbensen et al., 2010). In each cross-validation iteration, a random test subset of size q % is withheld, the model is fit to the remaining training data, and predictions z^* are computed at test locations. The prediction error is quantified by

$$RMSE = \sqrt{\frac{1}{n} \sum_{i=1}^n (z_i - z_i^*)^2}. \quad (3.3)$$

Cross-validation alone is not sufficient because one realization of the noise may bias conclusions. Therefore, the process is repeated within an MC loop. For each run, a fresh noise field is drawn, then k_1 cross-validation iterations are carried out. The process is summarized in Algorithm 1.

Ordinary Kriging uses an exponential variogram and the full field as the search neighborhood. MBA uses the coarsest lattice Φ_0 with $m_0 = n_0 = 5$ control points and $h = 3$ refinement levels. These settings were selected by sensitivity analysis to balance approximation accuracy and computation. Five cross-validation scenarios are evaluated with q from 10 % to 50 %. Fig. 3.8 reports the mean RMSE across all MC runs for each scenario. Both methods recover the trend within the noise level when training coverage is dense. As the withheld fraction grows and training gaps widen,

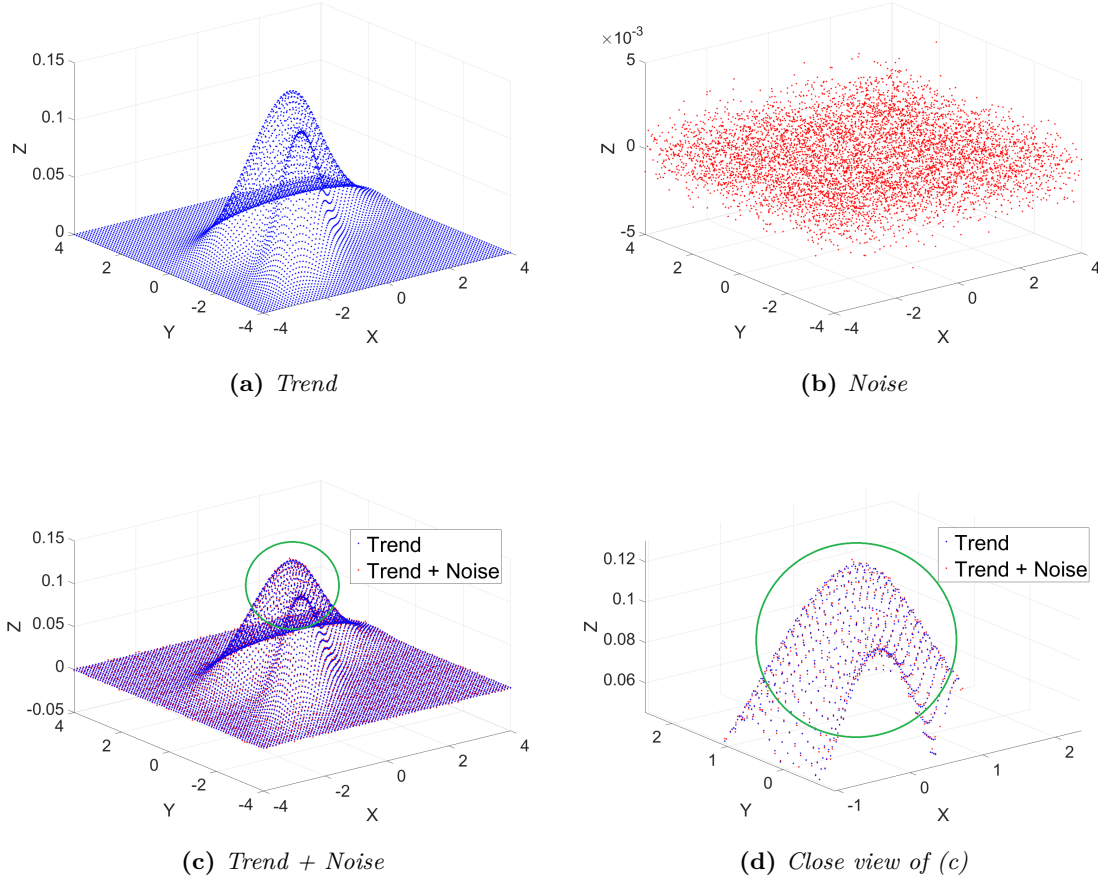


Figure 3.7: Simulator input for the evaluation of MBA: (a) fixed trend, (b) Gaussian noise, (c) both trend and noise, and (d) a close view of (c) (Publication D).

Algorithm 1: MC Simulation (Publication D).

```

1 Input: trend part of dataset  $\mathbf{Q}_{[n \times 3]} = [\mathbf{x} \ \mathbf{y} \ \mathbf{z}]$ 
2 Output: prediction for removed observations, RMSE of cross-validations, mean of RMSEs
3 for  $i = 1 \rightarrow k_2$  do
4   generate noise vector ( $\mathbf{noise}_{[n \times 1]}$ ) from Eq. (3.2)
5   set  $\mathbf{D}_{[n \times 3]} = \mathbf{Q}_{[n \times 3]} + \mathbf{noise}_{[n \times 1]}$ 
6   for all surface approximation methods (Ordinary Kriging and MBA) do
7     for  $j = 1 \rightarrow k_1$  do
8       remove  $m$  points ( $q$  %) from  $\mathbf{D}$ 
9       test dataset ( $\mathbf{D}''$ ) = the removed  $m$  data points
10      training dataset ( $\mathbf{D}'$ ) = dataset  $\mathbf{D}$  after removing test data  $\mathbf{D}''$ 
11      model estimation based on  $\mathbf{D}'$ 
12      for  $k = 1 \rightarrow m$  do
13        prediction in  $D''_k = (x_k, y_k)$ 
14        calculate RMSE (Eq. (3.3))
15 calculate mean of  $k_1 \times k_2$  RMSEs

```

prediction errors increase for both methods. The increase is smaller for MBA across all scenarios in this study. The relative gap between the curves widens with larger q , which indicates that MBA is less sensitive to the loss of training points under the tested settings. The visual comparison on real data in Fig. 3.9 shows that the multiscale spline representation preserves smooth long-wavelength

behavior while capturing spatial variation needed for displacement interpretation.

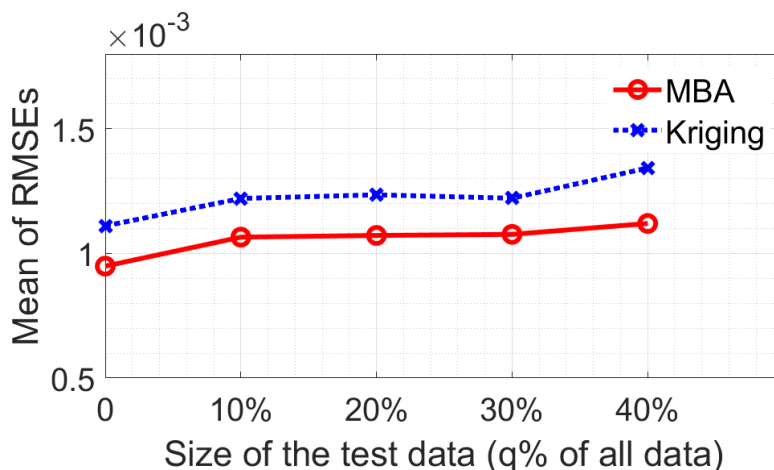


Figure 3.8: MC simulation results; Mean RMSE across MC runs for test set sizes $q \in \{10, 20, 30, 40, 50\}$ (Publication D).

Under controlled noise and increasing data gaps, MBA provides lower prediction errors than Ordinary Kriging and maintains approximation quality as training coverage decreases in the tested range. The hierarchical refinement offers a stable mechanism to add details without amplifying the additive noise. These properties and the observed error behavior support MBA as a suitable common surface model for large and irregular point clouds within the proposed processing pipeline.

3.2.2.2 Evaluating MBA with Real Data

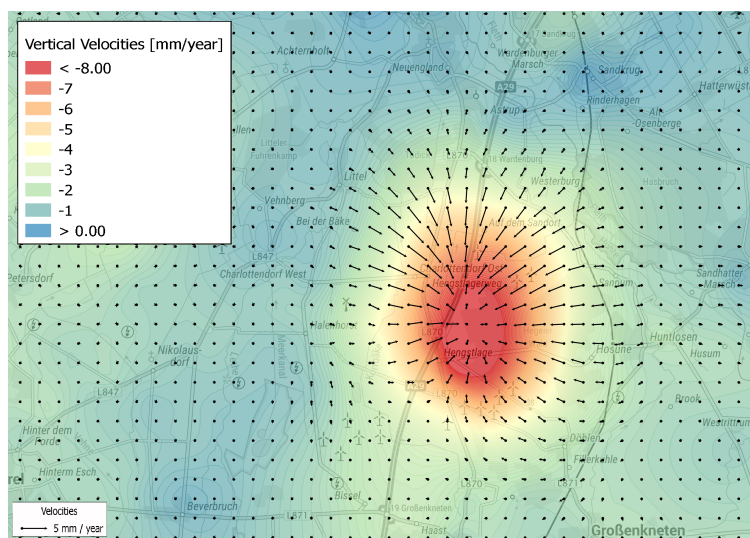
MBA and Ordinary Kriging are fitted to the Hengstlage data and compared by internal prediction errors and by visual agreement of modeled patterns. MBA uses three refinement levels with control lattices Φ_4 , Φ_8 , and Φ_{16} , with Φ_4 defined by $m = n = 4$. Kriging uses an exponential variogram and the full field as the search neighborhood.

Fig. 3.9 shows the modeled ground movement from both methods. Height change is displayed as a heatmap. Horizontal displacement is shown as a vector field from the east and north components. The central subsidence and its margins appear in both models with similar location and magnitude. Horizontal velocities peak around the subsidence edges and approach zero at center. A map of the model differences and a detailed discussion of these discrepancies are provided in Publication D.

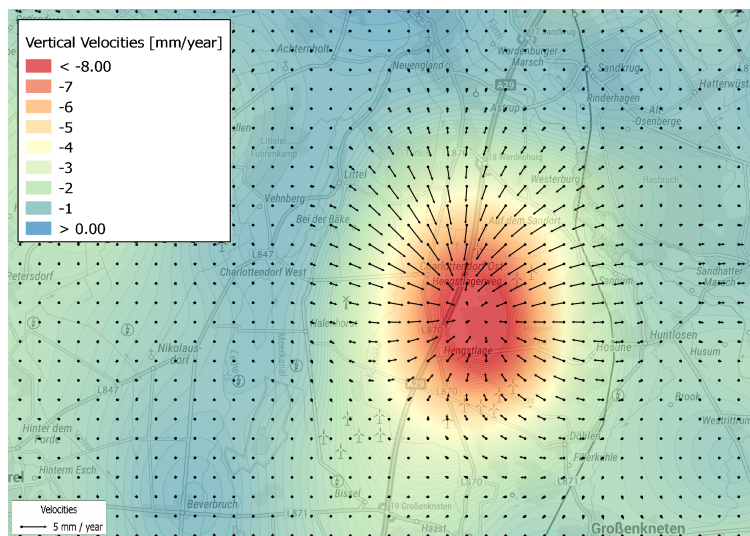
Prediction errors at the observation locations are comparable. The RMSE for Kriging is 0.44 mm/year and for MBA is 0.47 mm/year. Differences between the two modeled surfaces concentrate where observations are sparse, and the histogram of differences shows no coherent structure across the field. This indicates that MBA delivers results in line with Kriging on these data (Mohammadivojdan et al., 2020). The small RMSE advantage of Kriging in the Hengstlage case study is plausible given the different information content of the real and simulated datasets. In the simulations, the stochastic component is modeled as independent Gaussian noise added to a fixed smooth trend, so the data contain little spatial dependence beyond the deterministic structure. In contrast, real deformation observations can exhibit spatially correlated residuals due to unmodeled processes, acquisition effects, or heterogeneous sampling. Because Kriging explicitly exploits spatial dependence through the variogram, it can benefit from such correlation when the variogram provides an adequate fit. This helps explain why Kriging performs slightly better on the real data without contradicting the simulation result that MBA is more robust under controlled data gaps in the tested simulation scenarios.

The comparison also has an efficiency dimension. Ordinary Kriging relies on covariance-based prediction and requires specifying a variogram model. When the full field is used as the search neighborhood, the computational cost increases with the number of observations, and practical implementations often require neighborhood restriction or other approximations to remain tractable. In contrast, MBA represents the surface on a hierarchical basis. After fitting, predictions are obtained by evaluating the fitted surface model, which is typically efficient for repeated queries and dense gridding.

Although the MBA framework allows for flexible, hierarchical surface modeling of irregular geospatial PCs, its predictions do not inherently reflect their reliability. For applications where such models support critical decisions, understanding and quantifying uncertainty is essential. The next section introduces strategies for evaluating this uncertainty, both through empirical resampling and forward modeling approaches.



(a) Kriging



(b) MBA

Figure 3.9: Modeled ground movement in Hengstlage. Height change as a heatmap; vectors show horizontal displacement. (a) Kriging, (b) MBA (Publication D).

3.3 Uncertainty Quantification

A reliable surface model must not only approximate the observed phenomena but also convey how trustworthy its predictions are. In geodetic applications, where modeled surfaces support operational or interpretive decisions, quantifying uncertainty is essential. Users must be able to evaluate each estimated value together with a local measure of quality, especially when working with spatially distributed data affected by noise, outliers, and irregular coverage. The uncertainty analyses in this section assume that the input data have already passed the preprocessing stage and that outliers have been removed. The remaining deviations are treated as measurement noise and modeling error. If substantial outliers remain, both bootstrapping and forward propagation can yield misleading uncertainty estimates.

Two main components determine the uncertainty of a surface model. The first is the quality of the observations, including their measurement precision and spatial distribution. The second is the structure and complexity of the modeling approach. When observations are accompanied by well-characterized uncertainty, classical variance propagation can be applied. For example, in LS-based surface fitting, variances can be propagated through the design matrix to estimate prediction uncertainty.

In more complex frameworks, this becomes difficult. The MBA method used in this work constructs the surface in sequential stages, where each refinement level relies on residuals from the previous one. Although uncertainty can be derived within each level, the full variance covariance structure, including off-diagonal covariances, can in principle be propagated through the hierarchy by carrying complete covariance matrices between levels (Appendix A.1.4). In the present implementation, propagation is performed in variance form only, meaning that only diagonal entries are carried forward, because the full matrices become dense and quickly exceed feasible memory and runtime for large PCs. Neglecting these correlations can affect the calibration and coverage of the reported CIs and often leads to overly optimistic uncertainty estimates.

This motivates the use of more flexible strategies that do not depend on complete knowledge of the observational covariance structure. The first method adopted here is a nonparametric, data-driven approach based on bootstrapping. By repeatedly resampling the observations and recomputing the surface, an empirical distribution of model outcomes is obtained. This distribution provides local estimates of standard errors and CIs without requiring explicit analytical propagation (Section 3.3.1). Bootstrapping also does not require an explicit measurement uncertainty model. However, it does not disentangle systematic effects from random variability. If systematic or spatially structured error components are present in the observations, resampling tends to reproduce them rather than identify them as such.

While the bootstrapping approach addresses uncertainty retrospectively, it neither incorporates known measurement uncertainties, nor explains how observation uncertainty propagates through the modeling step. More generally, uncertainty can be approached from two directions. A backward strategy infers uncertainty from deviations to a reference object, a reference surface, or repeated measurements, but such reference information is often unavailable for geospatial PCs and especially for underwater surveys. A forward strategy instead starts from the measurement process and propagates modeled observation uncertainty through the processing chain. This is why forward uncertainty modeling is included in this dissertation: it provides spatially varying uncertainty estimates when no ground truth is available, and it allows testing how uncertainty assumptions, including spatially varying or systematic components when modeled, affect surface adjustment and weighting decisions. The forward-modeling approach used in this dissertation builds on a measurement uncertainty model for MBES and integrates these uncertainties directly into the surface adjustment. This complementary perspective allows the uncertainty of the final surface to

reflect the quality of the underlying measurements, rather than relying solely on data resampling (Section 3.3.2).

3.3.1 Bootstrapping-Based Uncertainty Estimation

Bootstrapping is a flexible, distribution-free alternative. This method involves repeatedly resampling the original observations with replacement to generate multiple synthetic datasets. For each resampled set, the model is reconstructed, and the prediction at a target location is evaluated. This results in an ensemble of predictions that approximates the empirical sampling distribution of the model output at that location. From this distribution, both a standard deviation and non-parametric CIs can be computed. This yields local uncertainty estimates that adapt to spatial data support.

To illustrate the core idea of the bootstrapping approach, consider the simplified, two-dimensional case of fitting a B-spline curve to scattered observations. Generating multiple resampled datasets from the original observations yields a family of curve realizations. Each realization corresponds to a slightly different approximation of the curve, depending on the sample used. These predictions form an ensemble that can be used to derive local uncertainty measures, such as CIs. Fig. 3.10 shows this process. The original noisy observations are shown alongside the resulting bootstrap realizations of the fitted curve and the final estimated curve with its associated confidence band. Even in this basic case, a confidence envelope clearly emerges around the curve, illustrating the method's key principle.

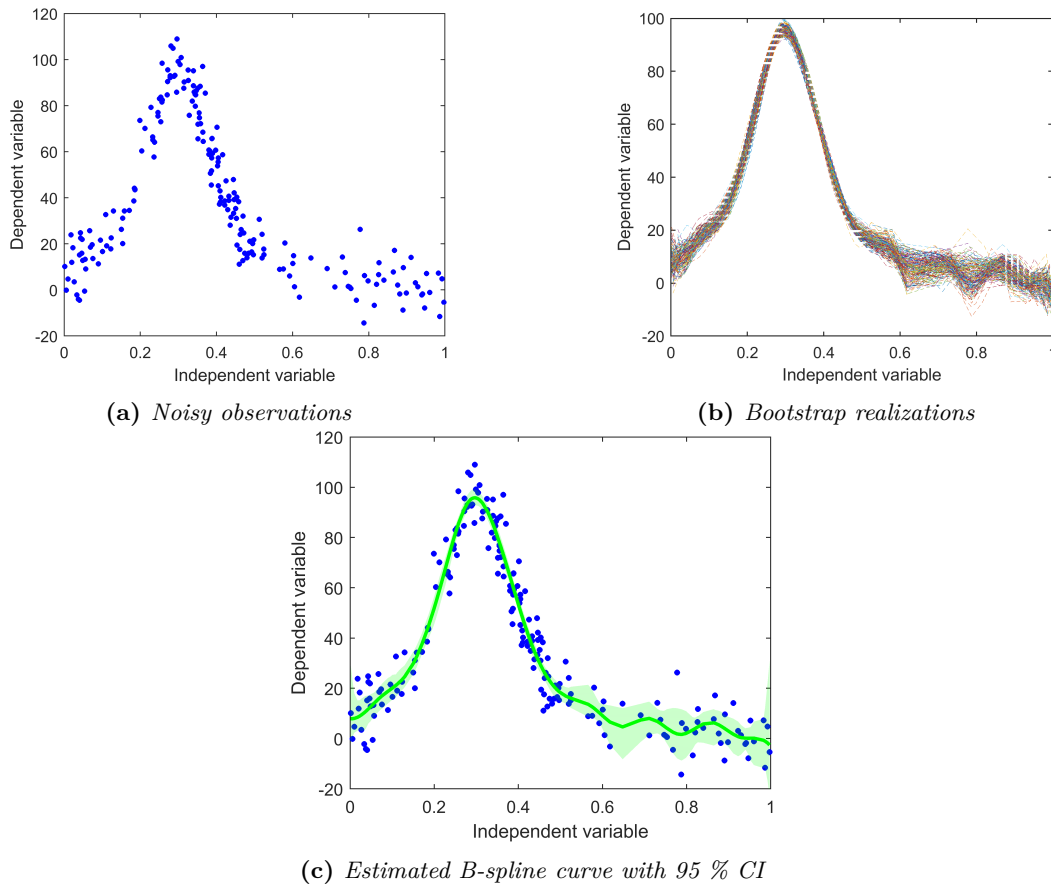


Figure 3.10: Illustrative 2D example of the bootstrapping method. From noisy observations (a), multiple B-spline curve realizations are generated via resampling (b). The final curve and associated CIs (c) are derived from the distribution of predictions.

The bootstrapping-based uncertainty modeling approach was applied to real geodetic data, specifically PSI observations over Hannover (see Section 1.4.1.3). The surface was constructed using the MBA method. The PSI dataset is characterized by a highly irregular and sparse spatial distribution, which presents challenges for stable surface reconstruction. Bootstrapping was used to estimate local CIs for the fitted surface while accounting for spatial gaps and model complexity. Fig. 3.11 presents a three-dimensional view of the estimated surface, together with the upper and lower bounds of the 95 % CI. This layered visualization highlights the surface nature of the model and enables spatially detailed inspection of uncertainty. A complementary heatmap representation, provided in the original publication, allows confidence information to be compared directly with the modeled displacement field. To further investigate the local uncertainty structure, two profile lines

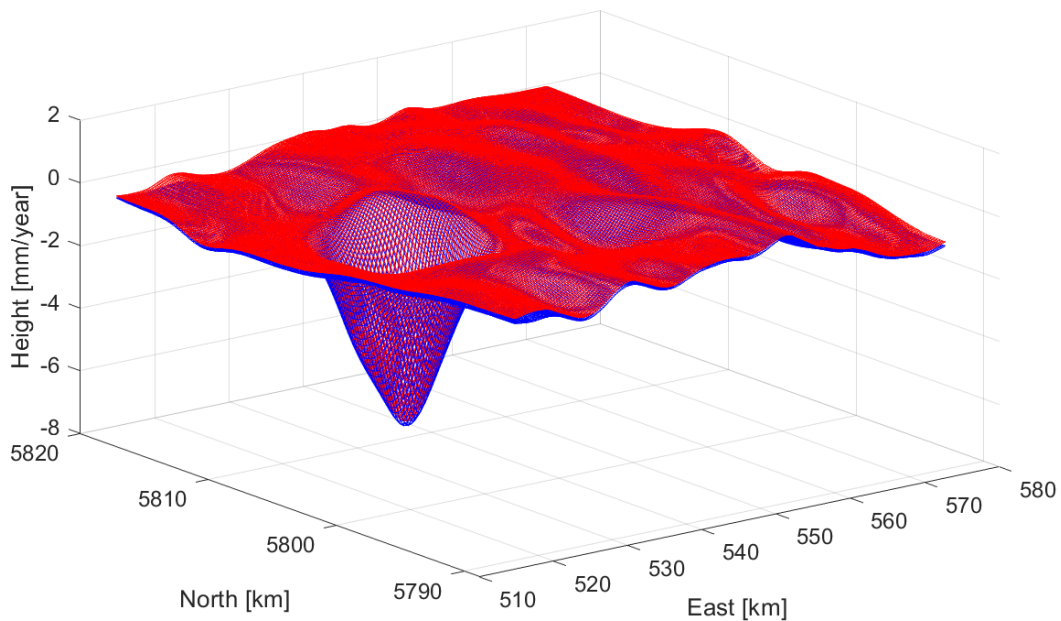


Figure 3.11: 3D visualization of CIs for the MBA model, obtained via bootstrapping. The two bounding surfaces represent the upper and lower limits of the 95 % CI.

were selected across the modeled region. As shown in Fig. 3.12, these profiles cut through areas with varying data availability, some with dense PSI observations, others with large gaps. In both 3D and top-down views, it becomes evident how critical the spatial context is in understanding the reliability of surface predictions.

The CIs along these profiles are shown in Figures 3.13 and 3.14. Each profile is evaluated using two MBA models with different complexity levels: $\Phi_1 = \{\Phi_{10,5}, \Phi_{20,10}, \Phi_{25,15}\}$ and $\Phi_2 = \{\Phi_{10,5}, \Phi_{20,10}, \Phi_{25,15}, \Phi_{30,20}, \Phi_{35,25}, \Phi_{40,30}\}$. The profiles reveal a clear relationship between data density and confidence band width. Where PSI observations are abundant and stable, the CI remains narrow, indicating high model reliability. Conversely, in regions with large observational gaps, the interval broadens substantially. This effect is more pronounced in the higher-complexity model (Φ_2), which, while offering more flexibility, is more sensitive to local data deficiencies. The added degrees of freedom in Φ_2 allow the surface to fit finer features but also introduce instability where data support is weak.

To better understand this trade-off, we examine a sequence of models with increasing complexity, from 3 to 6 layers of control lattices (Fig. 3.15). The smallest mesh size decreases from 2.3 km to 1.45 km across these configurations. While finer meshes theoretically allow better spatial resolution, they also amplify the effect of noise and missing data, resulting in elevated local uncertainty. Yet,

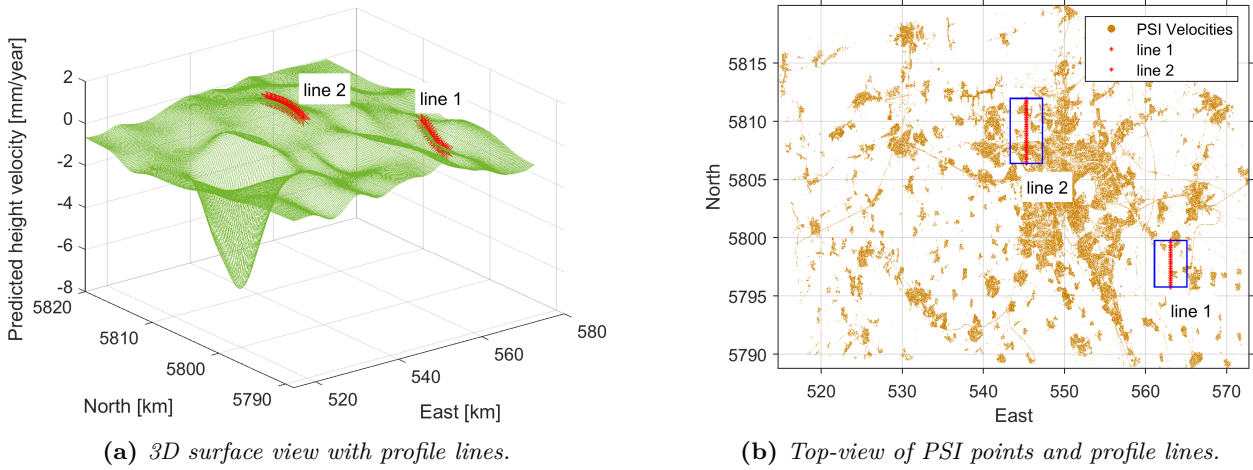


Figure 3.12: Profile line selection and observational context. (a) shows two profile lines on the MBA model in 3D. (b) indicates PSI points and the local neighborhoods used in the analysis.

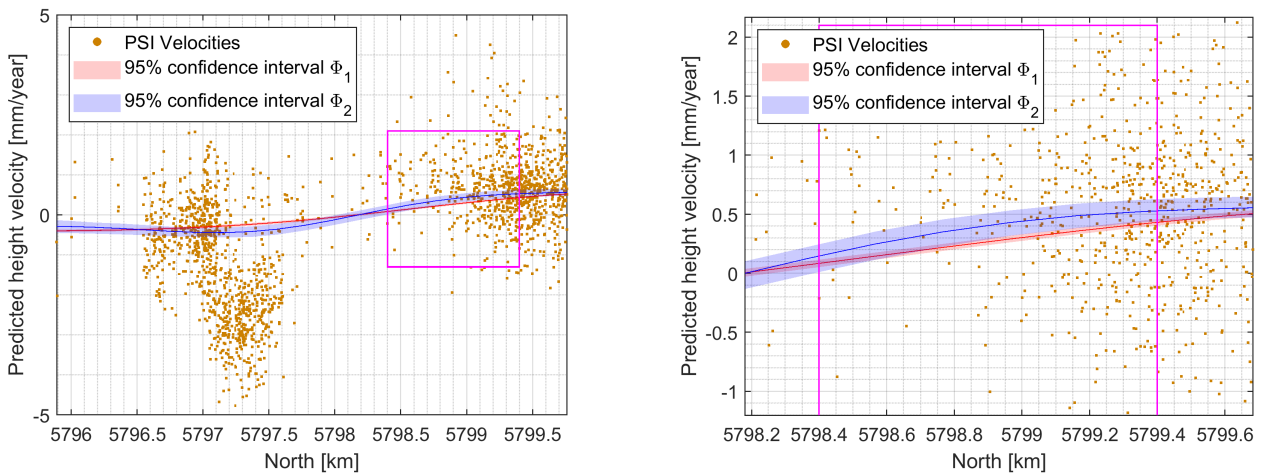


Figure 3.13: CIs along Line 1. Left: full profile for Φ_1 . Right: zoomed-in subsection. Orange points indicate PSI height velocity observations.

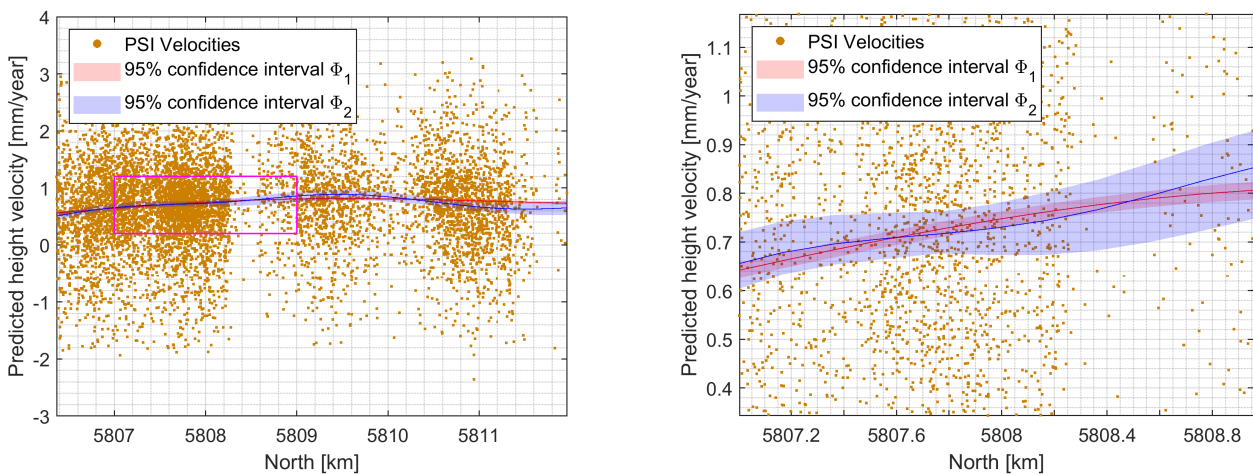


Figure 3.14: CIs along Line 2. Left: full profile for Φ_1 . Right: zoomed segment. Wider bands appear in regions with sparse observations.

this increase is not uniform: in well-observed regions, the CI remains stable even as complexity increases. This contrast highlights the importance of spatially-aware model selection.

These observations demonstrate the importance of matching model complexity to data quality. Overfitting can lead to misleading confidence surfaces, particularly in geospatial applications, where spatial gaps are common. Generating DEM or DBM, for example, benefits from prior knowledge or estimates of expected variability, such as from historic maps or simulation outputs. This information can help select the most appropriate model configuration, avoiding both underfitting and overfitting.

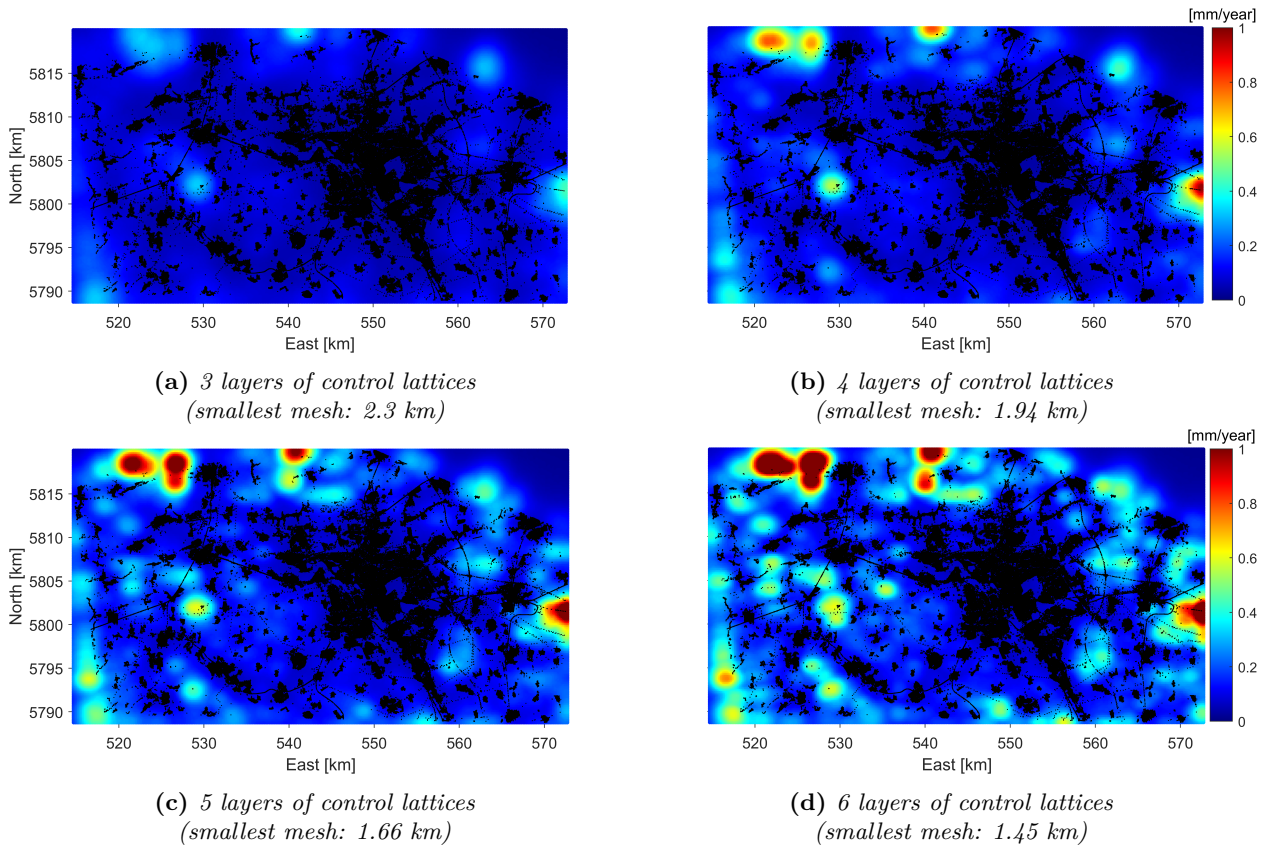


Figure 3.15: Estimated 95 % CI heatmaps for PSI-based regional ground movement modeled using MBA. Panels (a) to (d) correspond to 3, 4, 5, and 6 layers of control lattices, with smallest mesh sizes of 2.3, 1.94, 1.66, and 1.45 km, respectively. Increasing model complexity increases the estimated uncertainty, particularly in under-sampled regions, which is reflected in the CIs.

3.3.2 Forward Uncertainty Modeling

When uncertainty estimates for measurement data are available or can be reliably modeled, they should be used. They can improve surface modeling, for example, through uncertainty-aware weighting and uncertainty-aware interpolation. This is particularly relevant for DBM, where MBES measurements often show spatially variable error characteristics.

The third paper of this dissertation, Publication C, explores this idea through a concrete example and develops and validates a framework to estimate and propagate uncertainty in MBES measurements. Acquiring MBES data involves interconnected subsystems, including GNSS, Inertial Measurement Unit (IMU), sonar hardware, and vessel geometry. Each of these introduces biases and random errors. Environmental influences, such as refraction and seafloor morphology, further

complicate the process. Consequently, the assumption that cleaned MBES data are equally reliable is rarely valid. Publication C addresses this by presenting a forward uncertainty modeling pipeline that explicitly quantifies, simulates, and propagates measurement uncertainty throughout the surface generation workflow. The approach is structured into the following main stages:

- **Measurement Uncertainty Modeling.** A detailed uncertainty model is formulated based on the law of variance propagation, refining previous approaches such as those by Hare (1995); R. Hare et al. (2011). The resulting TPU is decomposed into vertical TPU and horizontal THU components. It incorporates uncertainties from GNSS, IMU, MBES, sensor installation, and environmental conditions within a unified covariance structure. The uncertainty calculations utilize the Guide to the Expression of Uncertainty in Measurements (GUM) Monte Carlo Method (MCM) (ISO/GUM-Suppl1:1998, E), effectively managing the nonlinear nature of MBES measurements. This model is specifically calibrated for the survey vessel UJL, with validation conducted against established commercial hydrographic software outcomes (Publication C).
- **Simulation-Based Propagation.** A simulation framework assesses how modeled uncertainties propagate into the DBM. A custom-developed survey simulator generates synthetic MBES data under controlled, realistic scenarios, enabling thorough analysis of the influence of measurement uncertainties on the spatial distribution and quality of the resulting PC.
- **Integration into Surface Modeling.** A key contribution is integrating point-wise uncertainty estimates directly into the GMM adjustment as observation weights. This replaces uniform weighting by a scheme that reflects spatially variable measurement quality. Its impact is evaluated through an MC simulation experiment (Fig. 3.16).

The simulation generates both geometry and corresponding uncertainties from the established TPU model. Two modeling scenarios are compared: Case 1 (unweighted observations) and Case 2 (weighted observations based on uncertainties). The outcomes include optimized surface models and associated uncertainty maps, which enable direct assessment of the effect of uncertainty integration on model quality.

Details on parameter selection and uncertainty simulation results are extensively discussed in Publication C. Fig. 3.17 illustrates the outcomes of the MC simulation, presenting surface models and their uncertainty distributions for both cases. Here, the metric $\hat{\sigma}_0$ (the square root of the "a posteriori variance factor", see Eq. 17 in Publication C) reflects adjustment consistency, while σ_{Model} (RMSE against the simulated reference surface) quantifies the fidelity of the model to reality.

Overall, the uncertainty maps indicate lower modeling uncertainty (σ_{Model}), in overlapping regions between adjacent swaths and generally lower magnitudes compared to the simulated input uncertainties (see Fig. 19 in Publication C). Although visually similar, quantitative analysis reveals that Case 2 (weighted observations) demonstrates consistently smaller σ_{Model} (average 0.023 m) compared to Case 1 (average 0.044 m), indicating closer agreement with the simulated reference surface. The estimated $\hat{\sigma}_0$ values are comparable (0.087 m in Case 2 versus 0.081 m in Case 1). Validation against known ground-truth surfaces indicates that incorporating measurement uncertainties into DBM generation reduces model biases and enhances reliability. Although the differences between weighted and unweighted approaches are small, incorporating uncertainties consistently improves model fidelity and produces more realistic uncertainty representation that supports reliable navigational decision-making.

Forward uncertainty modeling and bootstrapping serve different purposes, and the choice should be guided by available information and computational feasibility. Forward modeling is appropri-

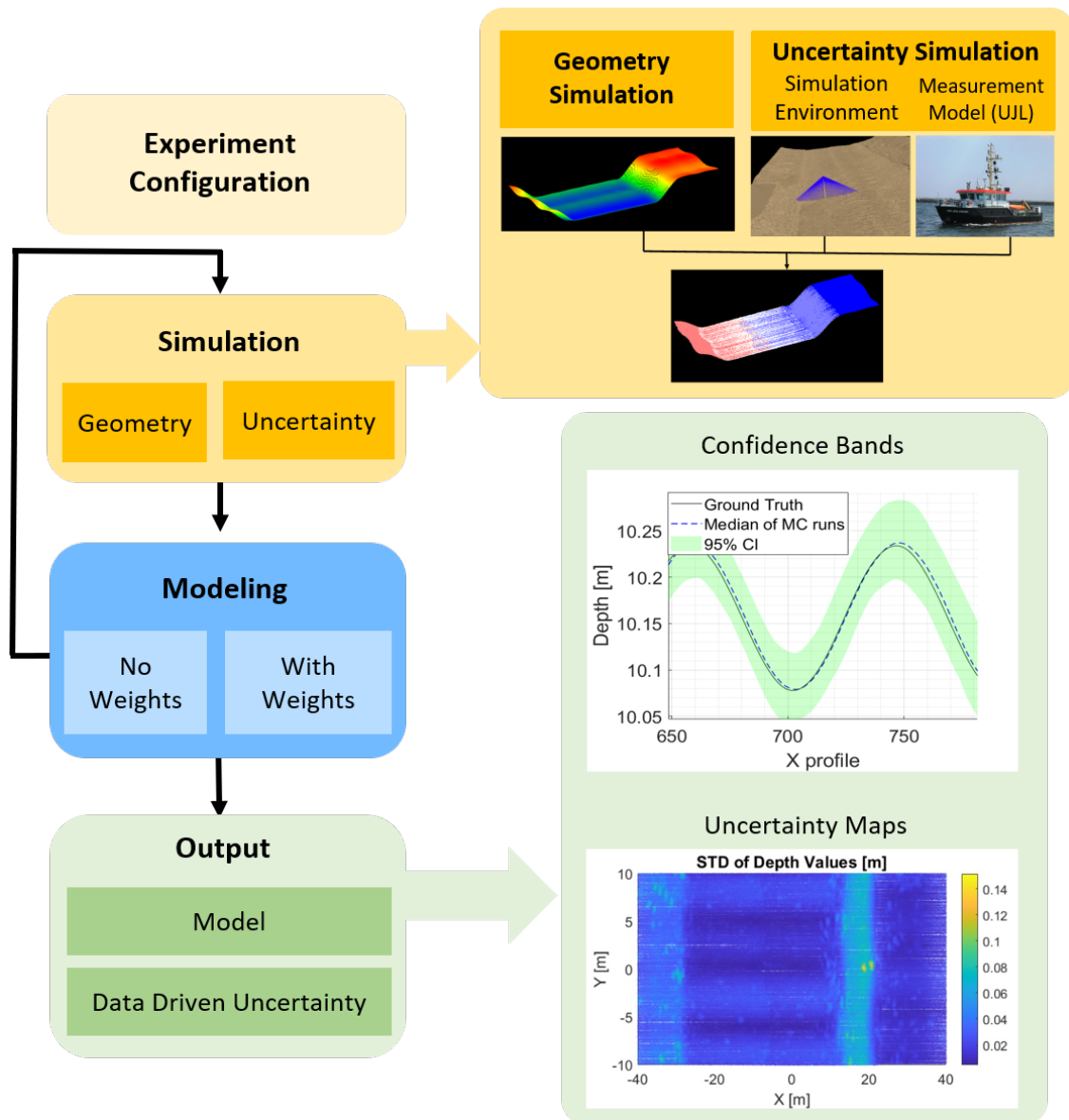


Figure 3.16: Overview of the MC simulation experiment workflow for uncertainty integration.

ate when a defensible measurement uncertainty model can be formulated and when uncertainty is intended to enter the adjustment explicitly, for example, through uncertainty-aware weighting or sensitivity studies. Its main limitations are the effort required to specify and validate the measurement model and the computational cost of simulation-based propagation. In this work, the required MC experiments were therefore executed on a university computing cluster. Bootstrapping is appropriate when observation uncertainties are unknown, incomplete, or not sufficiently trustworthy for forward propagation. It provides empirical confidence information that reflects data support and model sensitivity, but it also requires repeated re-fitting and can become computationally demanding as the number of resamples and the model size increase. In practice, forward modeling is used when uncertain knowledge is available and should influence the adjustment, whereas bootstrapping provides a robust alternative when forward modeling is infeasible or its assumptions are difficult to justify. In both approaches, uncertainty is reported in variance form, that is, only diagonal entries are provided as pointwise variances (or standard deviations) per location. Off-diagonal covariances and spatial correlations are not propagated, stored, or reported because the required correlation structure of the observation errors is not sufficiently known for the considered data sources, and because the computation and storage of a full covariance matrix is prohibitive at the scale of the

investigated PCs. Capturing spatial dependence would require an explicit correlation model or a dedicated resampling scheme (for example, a block bootstrap), which is beyond the scope of this thesis. The following chapter concludes the dissertation by summarizing the main findings and contributions, and by outlining limitations and directions for future research.

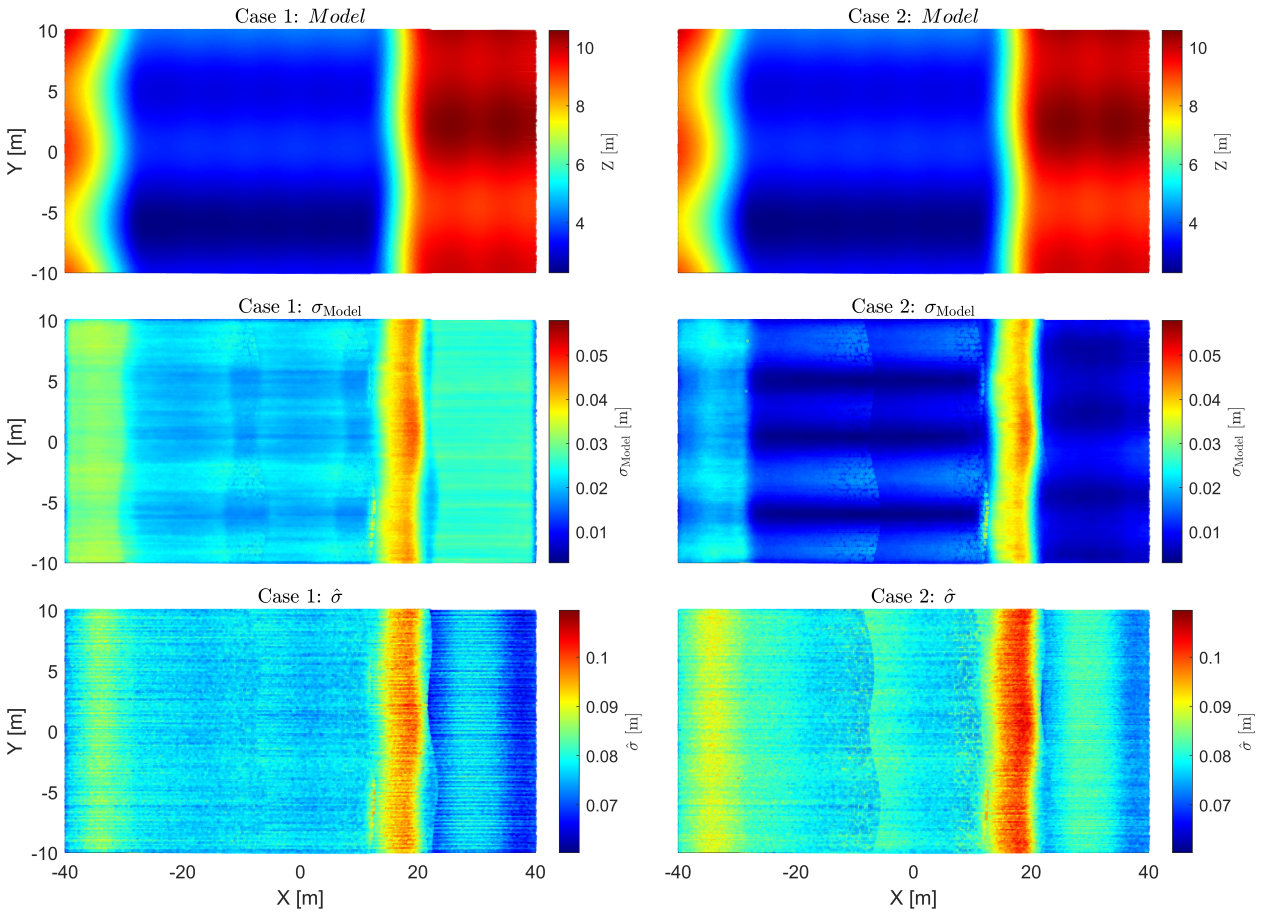


Figure 3.17: Comparison of surface models and their uncertainty distributions. The left column shows Case 1 (unweighted), and the right column shows Case 2 (weighted). The top row shows the estimated surface model. The middle row shows model error (σ_{Model}) as a spatial map. The bottom row shows the estimated a-posteriori variance factor ($\hat{\sigma}_0$) (Publication C).

4 Conclusion

4.1 Summary

This chapter synthesizes the thesis contributions and closes the research questions. Section 4.1.1 summarizes the pipeline, Section 4.1.2 answers RQ1 to RQ3, Section 4.1.3 defines the range of validity, and Section 4.1.4 discusses implications and generalization. Section 4.2 outlines directions for future work.

4.1.1 Overall Synthesis of the Pipeline

The central aim of this dissertation is to design and analyze a pipeline for modeling point-sampled surfaces, from preprocessing to quality assessment. The pipeline integrates three stages: outlier detection and data cleaning; surface modeling; and uncertainty quantification. The work is based on a practical assumption that many geodetic and hydrographic observables vary continuously in space and can be represented as a 2.5D surface ($z = f(x, y)$). Under this assumption, discrete measurements are treated as samples of an underlying continuous field, and the goal is to reconstruct a continuous surface together with spatially resolved quality information. The methodology is designed around generic point cloud characteristics, including irregular sampling, data gaps, and spatially varying measurement quality, and is intended to be transferable to other elevation-type datasets that satisfy the same surface assumption. In this dissertation, the pipeline is implemented and validated on two representative data classes: PSI-derived ground motion velocities on land and MBES bathymetric measurements in underwater environments.

The first stage involves surface-based preprocessing, which identifies outliers by comparing observations to an MBA reference surface. A Data Adaptive Outlier Detection method targets sparse, isolated anomalies (Publication A), and the IESP robust estimation variant is designed for clustered contamination (Publication B). The second stage approximates the cleaned observations with an MBA model as a common multiresolution surface model for PSI deformation fields and MBES bathymetry products (Publications A-D). The third stage quantifies model uncertainty under two regimes: nonparametric bootstrapping when observation variances are unavailable (Publication A) and forward uncertainty modeling with TPU-based weighting when system error models are available (Publication C).

When considered as a whole, these three stages define a coherent, surface-based pipeline that originates from raw, contaminated PCs and ultimately results in modeled surfaces equipped with uncertainty estimates. MBA functions as the standard representation for reference surfaces in outlier detection, for the final approximation of deformation and bathymetry models, and as the carrier of uncertainty information. This approach mitigates fragmentation between preprocessing, modeling, and quality assessment and provides a consistent framework for managing point-sampled surfaces across diverse application domains. The next subsection revisits RQ1-RQ3 and links each answer to the evidence from Chapter 3 and Publications A-D.

4.1.2 Answers to the Research Questions

In this subsection, the research questions formulated in Section 1.2 are revisited in light of the results in Chapter 3 and Publications A through D. Each question is addressed explicitly and linked to the corresponding stage of the pipeline.

RQ1 calls for the design and validation of an automatic preprocessing strategy that can detect isolated and clustered outliers in heterogeneous PCs without ground truth labels. This thesis tackles the aforementioned question through two complementary surface-based methods. The first method is the Data Adaptive Outlier Detection algorithm, and the second method is the IESP framework. The utilization of MBA surfaces as reference models, and the reliance on residuals for the identification of inconsistent observations are two key features that enable the methods to function without requiring labeled outlier classes as input.

The Data Adaptive method is performed iteratively in a coarse-to-fine scheme with residual trimming, and it is efficient for sparse, isolated outliers. In MC simulations (1000 runs), it shows reliable performance up to moderate contamination (up to 10 % outliers), while performance degrades at higher contamination due to masking effects (Table 4.1). For example, the median F1-score remains high at 10 % contamination (about 0.97), whereas at 15 % contamination the median Recall drops to 0.51, consistent with masking effects (Publication A). In the real PSI case study (Hannover), the method shows high agreement with a published local-neighborhood filtering approach (Brockmeyer et al., 2020), treating that method as a reference. The resulting performance is summarized in Table 4.1 and can be represented by an F1-score of 0.91 and an Accuracy of 0.99 (Publication A).

The IESP extends this concept with a robust M-Estimator and iterative reweighting, which stabilizes the estimation under clustered contamination and steep gradients. Its validation on MBES data from the Kiel Canal yields BA of 0.99 with an Accuracy of 0.97, where the reference labels are obtained from manual cleaning for evaluation (Table 4.1) (Publication B).

Table 4.1: Evidence supporting RQ1. Reported metrics follow the referenced publications.

Dataset/Experiment	Method	Precision	Recall	F_1	BA	Source
Simulated MC (1000 runs), $\sigma_n = 0.05$ m, 5 % outliers	Data Adaptive Outlier Detection	0.91	1.00	0.95	–	Publication A
Simulated MC (1000 runs), $\sigma_n = 0.05$ m, 10 % outliers	Data Adaptive Outlier Detection	0.94	1.00	0.97	–	Publication A
Simulated MC (1000 runs), $\sigma_n = 0.05$ m, 15 % outliers	Data Adaptive Outlier Detection	0.91	0.51	0.65	–	Publication A
PSI case study: Hannover (Section 1.4.1.3)	Data Adaptive Outlier Detection	0.93	0.89	0.91	0.95	Publication A
MBES case study: Kiel Canal (Section 1.4.2.2)	IESP	0.68	1.00	0.81	0.99	Publication B

Together, these methods form an automatic, surface-based preprocessing strategy for both isolated and clustered outliers. Accordingly, RQ1 is answered in the affirmative for the evaluated simulation settings and the considered PSI and MBES case studies, under the assumption that the data can be represented as a single-valued 2.5D surface at the modeling scale.

RQ2 explores the suitability of MBA as a common surface model for large, irregular, and noisy spatial PCs within the pipeline. The evaluation combines simulated PSI data, the Hengstlage deformation field, and MBES bathymetry (Publication D; Publication A and Publication B). For PSI, MBA is formulated with an explicit stochastic model and compared to Ordinary Kriging in two tracks: (i) segmented cross-validation embedded in an MC loop for simulated data with known ground truth, and (ii) cross-validated prediction errors at the observation locations for the Hengstlage dataset, where no ground truth is available. Under dense coverage, both methods demonstrate comparable accuracy. For the Hengstlage case study, the RMSE of cross-validated prediction errors is 0.44 mm/year for Kriging and 0.47 mm/year for MBA, confirming comparable performance under dense coverage. However, under reduced training coverage and in the presence of data gaps, MBA shows a smaller degradation in prediction accuracy and maintains more consistent performance (see the corresponding validation results in Section 3.2.2.1). For MBES, MBA is employed to generate DBMs from cleaned soundings and captures relevant seabed structures at multiple resolutions without excessive model complexity. The multiresolution construction provides direct control over model complexity via the chosen level structure, allowing detail to be increased when supported by the data. Across these applications, MBA functions as a unifying geometric backbone: it provides reference surfaces for preprocessing, yields compact mathematical models of the final displacement or depth fields, and, through its stochastic formulation with simplifying assumptions, permits the integration of observation weights and uncertainty information into the approximation. Accordingly, under the explicit 2.5D assumption and the stated stochastic simplifications, RQ2 is answered in the affirmative. This conclusion is restricted to single-valued 2.5D surfaces (for example deformation fields and bathymetry grids) and does not cover fully 3D geometries with overhangs or multi-valued surfaces in (x, y) .

RQ3 focuses on quantifying the uncertainty of the MBA surface model in two information regimes: when observation variances are unknown and when system error models are available. For PSI and similar datasets lacking reliable variance information, the thesis uses a nonparametric bootstrap on the input observations and the MBA adjustment. Repeated resampling produces ensembles of MBA surfaces from which empirical standard errors and CIs are derived. The resulting uncertainty maps reflect data gaps and heterogeneous point densities and provide realistic spatial patterns under the bootstrap resampling assumptions, without relying on analytic error propagation (Publication A). This bootstrap-based uncertainty primarily reflects sampling variability induced by the observations and does not capture systematic effects that are not represented by resampling. For MBES, where a system-specific error model can be formulated, a forward uncertainty model and a survey simulator generate TPU for individual soundings. These TPU values are used as observation weights in the MBA adjustment, linking the sensor error model directly to the surface estimation. The uncertainty information is supported by two consistency checks: an overlap-based analysis using measurements from two transducers as an empirical proxy for interval plausibility, and a residual-based comparison showing that the weighted adjustment residuals follow the simulated error distribution without introducing bias (see Fig. 20 in Publication C). In the synthetic MC experiment with known ground truth, uncertainty weighting improves the vertical model quality, reducing σ_{Model} from 0.044 m (unweighted) to 0.023 m when weighting by σ_Z (Publication C). Together, these two approaches provide practical tools for quantifying MBA surface uncertainty in both regimes and demonstrate their impact on model quality. Thus, RQ3 is answered in the affirmative for the considered information regimes: (i) bootstrap-based uncertainty when observation variances are not available, where the uncertainty reflects sampling variability under resampling assumptions, and (ii) TPU-based forward uncertainty when a sensor error model is available, where results depend on the validity of the adopted error model.

A comprehensive evaluation of the results for RQ1 to RQ3 reveals that the overarching objective of the thesis has been achieved. The pipeline has been developed to deliver automated surface-based

outlier detection, a unified MBA surface model, and uncertainty quantification strategies that cover both missing and explicit variance information from preprocessing to quality assessment. While these results show that the proposed pipeline answers the research questions for the considered PSI and MBES datasets, they rely on specific modeling choices and assumptions that restrict the generality of the conclusions.

4.1.3 Critical Reflection and Limitations

The conclusions in Section 4.1.2 are bounded by the following assumptions and practical constraints. The primary limitations of the proposed pipeline concern geometry and representation, stochastic modeling and uncertainty information, computation and implementation, and the scope of the datasets utilized for evaluation.

Geometry. It is evident that all applications within this thesis conceptualize data as realizations of 2.5D surfaces, that are, height fields of the form ($z = f(x, y)$). This excludes multi-layer geometries, vertical faces, bridges, and overhangs. In urban areas or complex underwater environments, elements of the true geometry are therefore not representable. Consequently, the pipeline is optimally suited for deformation fields and seabed surfaces that can be representable as single-valued functions.

Stochastic model. The stochastic models used in this thesis are intentionally simplified. Observations are treated as largely uncorrelated, and the covariance structure is level-dependent but otherwise basic. These assumptions support scalability, but they do not capture all spatial dependencies in real PCs. For many PSI products, observation variances or full covariance matrices are not available. Therefore, bootstrap techniques are used as an empirical alternative to analytic error propagation (Publication A). For MBES, the forward uncertainty model relies on manufacturer specifications and generic models of sensor behavior (Publication C). Direct validation against a known underwater reference surface is not possible. As a result, the TPU can only be checked indirectly using overlap statistics and simulations.

Computation. The MBA algorithm is numerically efficient and handles irregular point distributions and varying resolutions within practical computation times, as evidenced by empirical evaluations of the datasets in this thesis. The computational effort is approximately linear in both the number of input points and the number of active spline coefficients. This is advantageous for conventional regional datasets. However, for surveys with tens of millions of points and continuous high resolution, processing entire areas in a single adjustment can become challenging in terms of time and memory. In such cases, it is advisable to partition the domain into tiles with overlap or to adapt the target resolution to the information content of the data. The IESP is computationally demanding due to its integration of robust estimation, iterative reweighting, and repeated local surface fitting. In its present implementation, the system is well-suited for offline processing and quality control. However, it is not optimized for real-time shipboard cleaning of large MBES surveys. Bootstrap and MC simulations for uncertainty estimation also require substantial computation time, especially for large national or regional datasets. The parameter choices for MBA, for the outlier detection methods, and for the uncertainty simulations are based on expert knowledge and targeted experiments rather than on fully automatic procedures.

Data scope. The evaluation is grounded in a select number of case studies. The analysis focuses on one deformation test field and one type of PSI product (Publication D; Publication A). For MBES, the results are derived from specific sensor configurations, survey settings, and seabed types in the study area (Publication B; Publication C). Consequently, the conclusions concerning performance and robustness are most reliable when comparing analogous acquisition setups. Transfer to other

platforms or environmental conditions may be possible. However, it has not been systematically demonstrated within the scope of this thesis.

A thorough examination reveals that these limitations do not contradict the primary findings; rather, they define the range of validity of the pipeline. Furthermore, these factors provide a foundation for the subsequent work outlined in the following subsection.

4.1.4 Implications and Generalization of the Pipeline

The limitations outlined in Section 4.1.3 define the scope of application of the proposed pipeline. Within this scope, the results have several implications for geodetic deformation monitoring, hydrographic surveying, and the treatment of point-sampled surfaces in general.

Geodetic deformation monitoring. For PSI-based ground motion analysis, the results show that working with surface representations instead of directly with pointwise displacements provides a practical basis for interpretation and decision-making. Surface-based preprocessing reduces the influence of outliers before deformation patterns are interpreted. The MBA approximation preserves regional deformation signals even in the presence of data gaps. Bootstrap-based uncertainty estimates and CIs are provided on the same surface. Therefore, deformation magnitude and local reliability can be combined in a single product to prioritize follow-up actions, for example, by targeting areas with large estimated deformation and wide CIs for additional monitoring or independent checks.

Hydrographic surveying and DBMs. For MBES, the pipeline integrates robust cleaning, continuous modeling, and uncertainty information into a single workflow. The IESP method provides a structured approach for identifying individual and clustered artifacts in dense bathymetric PCs and reduces the subjectivity of interactive cleaning. Subsequent MBA modeling yields DBMs with controlled smoothness and flexible resolution. Using TPU values from the forward uncertainty model as observation weights ties the depth grid estimation and the resulting grid-level quality measures directly to the same TPU concept used at the sounding level. This supports routine TPU-weighted DBM production and enables quality control actions that combine overlap analysis with modeled uncertainty, for example, by flagging areas where overlap differences are large relative to the modeled uncertainty or where uncertainty remains high for targeted review or resurvey. When TPU information is available, it can also serve as a prior quality indicator during preprocessing; its direct use as a cleaning criteria is a natural extension of the pipeline beyond the residual-based methods evaluated in this thesis.

Cross-domain perspective and generalization. Many other geospatial datasets share the same structure as the case studies in this thesis. Airborne laser scanning-based DEMs, photogrammetric surface models from unmanned aerial systems, and similar products consist of irregular PCs that can often be interpreted as samples of a predominantly single-valued 2.5D surface and frequently lack complete stochastic information. Within these conditions, this thesis demonstrates that a shared surface representation can support preprocessing, interpolation, and uncertainty analysis in a consistent way. When observation variances are unavailable, bootstrap-based uncertainty estimation on MBA-type surfaces is a practical option. When sensor error models exist, using them to derive observation weights in surface adjustments connects instrument specifications with grid-based products. Thus, the pipeline provides a consistent processing pattern for point-sampled elevation and depth measurements across applications. Although MBA is used as the common backbone in this thesis, the general concept can be transferred to other adaptable surface models if they provide comparable multiresolution refinement, local support, and an adjustment-based formulation for integrating stochastic information. The pipeline is not intended for fully 3D geometries

with overhangs or multi-valued surfaces in (x, y) , which require different surface representations.

The following section translates the identified limitations into a concrete research and implementation roadmap.

4.2 Outlook

The results and limitations of this thesis motivate several directions for future research. This outlook is structured into near-term, mid-term, and long-term steps with concrete deliverables. The cited references are included as starting points and examples of related ideas. Integrating these ideas into the proposed pipeline and validating them under the data characteristics and accuracy requirements of this thesis remains future work.

Near-term: operational implementation and targeted validation.

- **Tile-based processing for large PCs.** Couple MBA and IESP with tiling and hierarchical index structures so that processing is organized tile-by-tile with controlled overlap and fast access to local neighborhoods for cleaning and surface fitting (Ogayar-Anguita et al., 2023; Schütz et al., 2020; Cong et al., 2023).
- **Profiling and parallelization.** Profile the current implementation, identify dominant cost factors, and redesign the most expensive components for multicore and Graphics Processing Unit (GPU) execution using per-tile processing and batched evaluation of spline basis functions (Montella et al., 2018).
- **Targeted bootstrap for large-scale PSI.** Apply a two-stage strategy: a fast pass over the full domain using the nominal stochastic model and basic quality indicators, followed by bootstrap-based uncertainty estimation restricted to tiles with strong deformation, sparse coverage, or large residuals. This mirrors operational large-scale InSAR services, where computation is shifted to distributed platforms (Ronczyk et al., 2022; Foumelis et al., 2022; Crosetto et al., 2021).
- **Dedicated uncertainty validation experiments.** Extend indirect checks with targeted validation campaigns for both PSI and MBES. For MBES, conduct repeated surveys of stable seabed regions under varying acquisition geometries and sound speed conditions, and compare predicted TPU fields with observed depth differences. For PSI, use independent measurements such as leveling or GNSS campaigns at selected benchmarks to validate displacement surfaces and bootstrap-based uncertainty estimates.

Mid-term: improved 2.5D surface backbones and stochastic modeling. The following directions build on existing concepts, but robust refinement decisions, tractable stochastic modeling, and empirical validation at scale remain open.

- **Hybrid surface backbones with local refinement.** Investigate hybrid backbones in which a global MBA surface provides a stable coarse model, while local refinement is activated only in selected subregions. Candidate refinement concepts include hierarchical and locally refined B-spline constructions, for example THB-splines and LR B-splines (Giannelli et al., 2012; Skytt et al., 2017; Kermarrec & Morgenstern, 2022). Refinement decisions can be driven by quantities already produced by the pipeline, such as residuals, curvature indicators, or uncertainty-derived measures.

- **Sparse correlation models for MBA surfaces.** Extend the intentionally simple stochastic model by developing sparse approximate covariance or precision structures that capture key spatial correlations while remaining computationally tractable. One direction is to adapt Stochastic Partial Differential Equation (SPDE)-based ideas for constructing sparse precision models of spatial fields (Lindgren et al., 2011). A complementary direction is to combine analytic covariance approximations with bootstrap-based calibration, where resampling corrects model misspecification rather than replacing analytic propagation entirely.

Long-term: extended geometry and multi-sensor integration. These topics require methodological advances and careful validation because they relax core assumptions of the current pipeline and introduce additional sources of uncertainty.

- **Local 3D modeling in geometrically complex regions.** Extend the pipeline beyond the strict 2.5D by using local 3D surface models where needed, for example, around quay walls, breakwaters, or engineered structures, while retaining a 2.5D MBA backbone elsewhere. This requires robust parameterization and constraints to remain stable under irregular sampling and noise (Bracco et al., 2018; Harmening, 2020).
- **Multi-sensor and multi-temporal surface integration.** Use surface-based models as a common domain for combining sensors and epochs. Examples include fusing MBES, airborne LiDAR, and satellite-derived bathymetry for seamless coastal DBMs, and jointly analyzing PSI with terrestrial survey data for deformation monitoring. In these settings, MBA-type surfaces or their successors can act as shared reference representations to which datasets are adjusted with sensor-specific weights, enabling consistent separation of signal and noise over time.

These directions remain consistent with the thesis’s central concept: a single, well-controlled surface representation connects preprocessing, modeling, and quality assessment for point-sampled surfaces.

5 List of additional publications

This chapter lists further publications by the author of this dissertation. These publications differ from those presented in Section 1.3 in that their content has already been covered elsewhere in the dissertation or is not directly related to its core subject.

Omidalzarandi, M.; Shahryarinia, K.; **Mohammadivojdan, B.**; Iqbal, W.; Wübbena, J. B.; Ruffer, J.; Paffenholz, J.-A.; Neumann, I. (2024): Accurate and large-scale monitoring of civil engineering infrastructures through quality ensured Persistent Scatterer Interferometry, corner reflectors, and GNSS equipment. In: 23. Geokinematischer Tag, Freiberg, Germany, 16 May 2024-17 May 2024.

Omidalzarandi, M.; Shahryarinia, K.; **Mohammadivojdan, B.**; Neumann, I. (2024), Quality assessment of Persistent Scatterer Interferometry time series using vector-autoregressive-based spatio-temporal (VAR-ST-PS) modelling. In: EGU General Assembly 2024, Wien, Austria, 14 Apr 2024-19 Apr 2024 pp. EGU24-17912. <https://doi.org/10.5194/egusphere-egu24-17912>

Omidalzarandi, M.; **Mohammadivojdan, B.**; Alkhatib, H.; Paffenholz, J.-A.; Neumann, I. (2023), On the quality checking of persistent scatterer interferometry data by spatial-temporal modelling. In: Journal of Applied Geodesy, vol. 17, no. 2, pp. 119-131. <https://doi.org/10.1515/jag-2022-0043>

Omidalzarandi, M.; **Mohammadivojdan, B.**; Alkhatib, H.; Paffenholz, J.-A.; Neumann, I. (2023), A quality model of open-source Sentinel-1 SAR data by temporal and spatial modelling. In: GeoMonitoring 2023, Hannover, Germany.




Mohammadivojdan, B.; Hake, F.; Alkhatib, H.; Neumann, I.; Weiss, R.; Artz, T. (2022), Preprocessing and Analysis Strategies for Hydrographic Measurements at Very Shallow Water Depths. In: Hydrographie – Messen mit allen Sinnen: Beiträge zum 204. DVW-Seminar und 35. Hydrographentag vom 14. bis 16. Juni 2022 in Bremerhaven. vol. 102, DVW-Schriftenreihe, vol. 102/2022, Wissner Verlag, pp. 65-68.

Mohammadivojdan, B. and Aghayari, R. (2017). Investigating the seismic behavior of RC shear walls with openings strengthened with FRP sheets using different schemes. In: Scientia Iranica, vol. 24(4), pp.1855-1865.

6 Publications

Article

Regional Ground Movement Detection by Analysis and Modeling PSI Observations

Bahareh Mohammadiojdan ^{1,*} , Marco Brockmeyer ², Cord-Hinrich Jahn ², Ingo Neumann ¹  and Hamza Alkhatib ¹ 

¹ Geodetic Institute, Leibniz Universität Hannover, Nienburger Str. 1, 30167 Hannover, Germany; neumann@gih.uni-hannover.de (I.N.); alkhatib@gih.uni-hannover.de (H.A.)

² Landesamt für Geoinformation und Landesvermessung Niedersachsen (LGLN), Podbielskistraße 331, 30659 Hannover, Germany; Marco.Brockmeyer@lgl.niedersachsen.de (M.B.); cord-hinrich.jahn@lgl.niedersachsen.de (C.-H.J.)

* Correspondence: mohammadiojdan@gih.uni-hannover.de; Tel.: +49-511-76214736

Abstract: Any changes to the Earth's surface should be monitored in order to maintain and update the spatial reference system. To establish a global model of ground movements for a large area, it is important to have consistent and reliable measurements. However, in dealing with mass data, outliers may occur and robust analysis of data is indispensable. In particular, this paper will analyse Synthetic Aperture Radar (SAR) data for detecting the regional ground movements (RGM) in the area of Hanover, Germany. The relevant data sets have been provided by the Federal Institute for Geo-sciences and Natural Resources (BGR) for the period of 2014 to 2018. In this paper, we propose a data adoptive outlier detection algorithm to preprocess the observations. The algorithm is tested with different reference data sets and as a binary classifier performs with 0.99 accuracy and obtains a 0.95 F_1 -score in detecting the outliers. The RGMs that are observed as height velocities are mathematically modeled as a surface based on a hierarchical B-splines (HB-splines) method. For the approximated surface, a 95% confidence interval is estimated based on a bootstrapping approach. In the end, the user is enabled to predict RGM at any point and is provided with a measure of quality for the prediction.

Keywords: regional ground movement; PSI; outlier detection; uncertainty modeling; bootstrapping



Citation: Mohammadiojdan, B.; Brockmeyer, M.; Jahn, C.-H.; Neumann, I.; Alkhatib, H. Regional Ground Movement Detection by Analysis and Modeling PSI Observations. *Remote Sens.* **2021**, *13*, 2246. <https://doi.org/10.3390/rs13122246>

Academic Editor: João Catalão Fernandes

Received: 30 April 2021
Accepted: 5 June 2021
Published: 8 June 2021

Publisher's Note: MDPI stays neutral with regard to jurisdictional claims in published maps and institutional affiliations.



Copyright: © 2021 by the authors. Licensee MDPI, Basel, Switzerland. This article is an open access article distributed under the terms and conditions of the Creative Commons Attribution (CC BY) license (<https://creativecommons.org/licenses/by/4.0/>).

1. Introduction

Monitoring the RGMs and detecting any changes to the Earth's surface is important in updating the spatial reference system [1]. This is especially of high interest in areas that are affected by activities such as salt mining, gas, and oil extraction, as well as fossil fuel storage. In this research, we focus on the modeling RGMs. The area under study is located in the region of Lower Saxony in Germany.

Ground movement detection on a large scale depends on the measurement approach, as well as the modeling technique. One necessary step is to mathematically model the measurements as a surface, therefore allowing the user to predict the changes to the Earth's surface at any position where measurements could be unavailable. The modeling and spatial representation of such data come with different challenges. These types of data are usually contaminated with noise and outliers and the main challenges include the irregular distribution of data and the high variability of the precision of the measurements.

From the aspect of the measurement approach, there are different methods that can be applied to track the changes through repeated point-wise measurements. Conventional surveying approaches, such as levelling, the Global Navigation Satellite System (GNSS), or total station will result in a limited number of observations. Although the resulted observations are considered precise, they have low spatial density and are usually restricted to known geodetic stations. Additionally, these approaches are typically expensive, time-consuming, and usually labor-intensive [2–4]. The disadvantage of sparse measurements

can be mitigated by using satellite-based remote-sensing methods that can provide observations on a larger scale. The advanced methods of Interferometric Synthetic Aperture Radar (InSAR), particularly the Persistent Scatterer Interferometry (PSI), are able to detect and quantify the ground deformation in the range of millimeters per year [mm/year] in many application fields [5–8]. In the current study, PSI observations are used to model RGM specifically in the area of Hanover in Lower Saxony, Germany.

The PSI observations are prone to outliers. There are observations that might deviate from the global or local distribution of the whole data set. Hawkins [9] defines an outlier as “an observation that deviates so much from other observations as to arouse suspicions that it was generated by a different mechanism”. The PSI observations show high spatial variability due to different movement behavior of neighboring scatterers. These variations might represent only an anomaly related to individual object movements, that does not necessarily follow the global ground movement in the region. To accurately model the true RGM, detecting and removing these outliers is an important step. There are a variety of methods, which have been developed to detect outliers specifically in the field of statistics [9,10]. According to Papadimitriou et al. [11], they are mainly categorized into distance-based, density-based, clustering-based, depth-based and distribution-based methods. Distance-based methods were first introduced by Knorr et al. [12], and applied by, for example, Shen et al. [13], which defines an outlier as a point from which a certain portion of the neighbouring data has a distance more than a specific threshold. However, such a method can lead to problems when it comes to non-homogeneous distributed data [14]. Breunig et al. [14] proposed a density-based approach, which is based on the Local Outlier Factor (LOF). This factor could be derived by analyzing the data distribution density. In clustering-based approaches, those data which are not assigned to any cluster are labeled as outliers [15]. Clustering for detecting outliers have been used in different applications, which deal with point clouds, such as laser scanning data and sonar data [16,17]. Distribution-based approaches focus on a standard distribution model (e.g., Gaussian) and identify outliers as those points that deviate from this distribution [9,10]. Finally, the depth-based approaches concentrate on computational geometry, and the data are divided into different layers, wherein shallow layers are more probable to contain outliers [18,19].

In detecting anomalies for spatial data, one should consider an important characteristic of these data types, which is spatial correlation. Tobler [20] expresses this as: “Everything is related to everything else, but near things are more related than distant things”. Algorithms designed to deal with spatial data can be categorized into graphic approaches [21,22] and quantitative tests [23,24]. The methods of Scatterplot [23] and Moran Scatterplot [24] can be mentioned, which work with quantitative tests in detecting anomalies. In the direction of quantitative testing, Liu et al. [25] used a local adoptive statistical analysis to detect outliers, which was tested on SAR data. Lu et al. [26] proposed several statistical outlier detection algorithms, and similarly, Chen et al. [27] introduced a robust median algorithm to detect spatial outliers.

In this paper, a data adaptive algorithm is proposed to process the data and identify the outliers. The anomalies are detected based on the deviation of the observations to a fitted model in a hierarchical approach. The algorithm considers local behavior of the data while globally testing the deviations of the observations to the model.

The other aspect in detecting RGMs is the modeling technique, which is mainly the problem of finding the underlying function in the data set as a continuous surface that best describes the behavior of the data. This makes it possible to propagate information from the positions where information is available to new positions where no data exists. Despite a flurry of activity in this area, scattered data interpolation remains a difficult and computationally expensive problem. Mostly, the developed approaches do not allow different data distributions or remain computationally inefficient [28,29]. In modeling such data, one needs to consider the fact that it contains both deterministic and stochastic parts [30]. Deterministic approaches mainly focus on the trend in the data, for example, traditional polynomial surfaces and free-form surfaces, such as Bézier, B-splines, and non-

uniform rational B-splines [31] (see Bureick et al. [32]). The stochastic methods model the stochastic part of the data based on the spatial correlation among the data sets. The Least Squares Collocation [33], Gaussian Processes [18] and Kriging [34] are examples of such stochastic approaches.

In practice, for large data sets with high variability and large spatial gaps, it is challenging to choose a suitable approach. Mohammadiojdan et al. [35] modeled such a dataset by using both ordinary Kriging and Multilevel B-splines Approximation (MBA) methods. Ordinary Kriging is a powerful stochastic method that uses variograms to model the correlation among data points; however, this approach has several drawbacks. Firstly, as a stochastic method, this method best models the stochastic part of the data; therefore, in order to have a reliable estimation, the trend in the data should be modeled separately. Additionally, this method is computationally expensive, especially for large data sets. In this study, an approach based on HB-splines was adopted to model the PSI observations. Forsey and Bartels were the first to introduce a method for HB-splines refinement to interpolate a grid of data [36–38]. Lee et al. [29] proposed a similar approach that is also able to approximate scattered data. The suggested MBA method generates a series of bicubic B-splines functions based on a coarse to fine control lattice hierarchy. The approximation at each level is improved by a correction term from the next level, and the sum of all the levels forms the final approximation. Compared to Ordinary Kriging, the deterministic method of MBA does not require a separate model for estimating the trend, takes less computational time, and shows robust behavior against data gaps. At the same time, the disadvantage of the MBA approach lies in model selection and choosing an optimal control lattice hierarchy [35].

It is of high importance to also model the uncertainty of the approximated RGM. Therefore, based on the modeled movement, a user should be able to predict deformation at any position and have a measure of quality for the prediction. The uncertainty in the model can be due to different reasons, namely noise and data gaps. The approximated model based on MBA in each level is derived based on least squares minimization. Therefore, based on the precision of the observations, an uncertainty measure could be derived mathematically for the approximated model. However, the final model in MBA consists of more than one level. Because each level is derived from the previous one, a highly mathematical correlation exists between different levels. This makes the error propagation and the consideration in an appropriate stochastic model a challenging process. Consequently, mathematically modeling the uncertainty for the Multilevel method is not optimal, and for large data sets the process is not computationally practical.

In order to solve this issue, a non-parametric approach based on the bootstrapping method is adopted to approximate the sampling distribution of the estimated RGM. Bootstrapping is a computer-intensive method, which can be used to obtain the sampling distribution of an estimate. It was first introduced by Efron et al. [39,40]. The method is based on intensive resampling from a limited existing sample and generating new samples. Using the information from all samples, one can derive the bootstrap sampling distribution. The standard error or confidence interval of an estimate can be derived based on the bootstrap sampling distribution. However, in terms of PSI observations and approximation surfaces, this non-parametric approach provides the uncertainty of the approximated surface. The uncertainty will mainly represent the quality of the model, reflecting the general noise and data gaps.

The rest of the paper is organized as follows: Section 2 gives an overview of the data set that is used in this paper. Section 3 provides a detailed explanation of the implemented methodologies, including the basics of the surface-based modeling method and an overview of the implemented bootstrapping approach. In Section 4, the computational results of applying the above-mentioned methodologies on the data set of interest are analysed and evaluated. The main outputs of the research, along with the strengths and limitations of the methods, are discussed in Section 5. Section 6 concludes and provides a discussion on the characteristics of the developed method, and possible opportunities are presented.

2. Data

Deformation of the Earth's surface can be caused by various geological processes or anthropogenic measures. Due to its high temporal and spatial resolution, radar interferometry provides valuable data for detecting areas influenced by ground movements. The analyzed motions in the area of Hanover are based on SAR data from the Sentinel-1 mission, which is part of the European Space Agency (ESA) Copernicus Earth observation program [41]. The identical radar satellites Sentinel-1A and Sentinel-1B were respectively launched in April 2014 and April 2016, and offer a revisiting time of 6 days on a shared orbit plane. The radar satellites operating in C-band have a spatial resolution of $5\text{ m} \times 20\text{ m}$ in Interferometric Swath mode and scan the Earth's surface over a width of approximately 250 km. The data set for this paper provided by the BGR was generated by using PSI-WAP (Wide-Area-Product) processing [42], and contains 319226 PSI velocities. To mitigate possible large-scale errors, such as residual orbital or atmospheric errors, the PSI-WAP analysis includes independent velocities from GNSS reference stations for calibration. In the color-coded points in Figure 1, the area with ground movement caused by salt mining in the west of Hanover near Wunstorf is clearly visible. Besides this, the clustering characteristic of PSI information in urban areas and the data gaps in rural regions become apparent. The presented data material originates from an ascending satellite orbit, which covers an acquisition period from 13.10.2014 to 01.04.2018. Overall, the PSI processing contains 138 SAR images, from which the acquisition of 20.09.2016 was selected as a master scene. The derived velocities were determined in the line of sight (LOS) of the satellite and projected vertically by assuming no horizontal displacement. Horizontal displacements, especially in local ground motion areas, may lead to systematic errors of derived height changes if neglected. To separate the LOS-movement into vertical and horizontal components, a combined solution of data from ascending and descending radar satellites is necessary [43], which is out of the scope of the current paper.

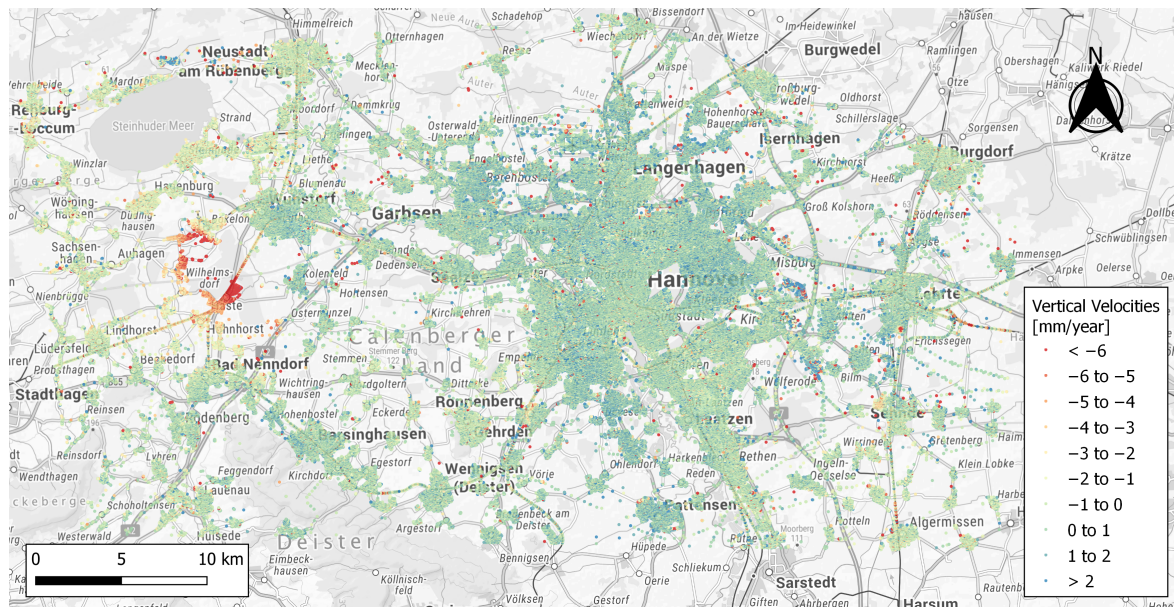


Figure 1. Provided velocity information in the Hanover area by PSI processing.

The provided PSI information is corrupted by a high level of measurement errors. The measurement errors can be divided into two parts: noise and outliers. The noise in the data expresses the precision of the measured samples. By considering prior knowledge about the performance of the measurement system, this can be considered in the surface modeling process.

The second type of errors, outliers, are those observations that do not follow the general behavior of the neighboring points. The existing outliers can be caused by various influencing factors, such as insufficient state modeling of the unknowns in PSI processing. In addition, very local displacements (e.g., subsidence of new buildings) can also lead to anomalies, which in practice do not represent the ground motions in wider areas. Before any further processing and interpretation of the PSI velocities, the outliers have to be eliminated from the data. Those outliers which are due to very local displacements in a short period of time can usually be detected via a temporal outlier detection process [1] (Section 2.1). The rest of the spatial anomalies are to be detected in spatial outlier detection, which is the main focus in this research (Section 3.1).

2.1. Temporal Outlier Detection

The existing outliers in the time series of the scatters can be caused by local displacements in a short period of time. Hence, the time series of the height changes of the persistent scatterer were analyzed first, since they show varying quality levels. In order to identify time series with high measurement noise, a temporal outlier detection approach with subsequent elimination is adopted [1]. For this purpose, the time series of the PSI points are de-trended (by using a linear regression model) and the remaining residuals serve as a measure for the variability. If the standard deviation of the de-trended time series exceeds the defined experimental threshold of 6 mm, the scatterer is considered as an outlier and excluded from further processing.

Even after temporal filtering, the PSI velocities still show high spatial variability due to different movement behaviors of neighboring scatterers. Therefore, to remove such high-frequency outliers from the data set, a spatial outlier filtering has to be performed. Details about the adapted method is explained in Section 3.1.

3. Methodology

Detailed explanation of the methodologies adopted to model the PSI data are presented in the following section. Figure 2 presents a flowchart of the main steps and framework of the whole process.

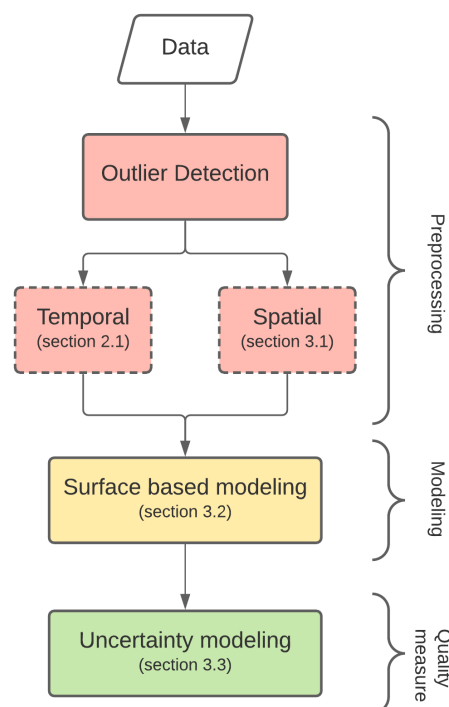


Figure 2. Flowchart of the main methodologies adopted.

3.1. Spatial Outlier Detection: Data Adaptive Outlier Detection

Some observations that might deviate from the global or local distribution of the whole data set: As described in Section 2, the PSI velocities show high spatial variability due to different movement behaviors of the neighboring scatterers. This behavior might represent individual object movements, which does not necessarily represent the global ground movement in the region of interest. These anomalies should be detected and eliminated before modeling the RGM. A data-adaptive algorithm is proposed to process the data and identify the outliers. The outliers will be identified based on their deviation or distance to a fitted model. The model is based on least squares minimization, which estimates a HB-splines surface to approximate the data. The chosen method is based on MBA that is described with details in Section 3.2.

The aim is to assess the distance of the observations to the approximated model. The observations with the highest deviation are more suspected to be outliers. However, two issues should be considered: firstly, if the model is not able to detect the local behavior of the data, or in other words, the model has some smoothing effect, some correct data may be misclassified as outliers. More precisely, some large deviations may be detected as a result due to the low complexity of the model. The second issue is the masking effect of the outliers, meaning that if there are extremely large outliers in a neighborhood, it may affect the model estimation. Consequently, the estimated model will be shifted toward the outliers and some correct observations might be misclassified as outliers, or some genuine outliers may not even be detected.

In order to mitigate these challenges, the process of detecting outliers is broken down into a few iterations. At every iteration, we model the data. Then, the deviations of the data to the model are calculated. The estimation of the model is based on least squares. Therefore, the assumption is that the residuals, or the deviations to the fitted model, are normally distributed. Considering the distribution of the residuals, those data points with residuals larger than a threshold are identified as outliers. The threshold for distinguishing between outliers and clean data is defined as a multiplication of the residuals standard deviation (σ_r) by a factor (T). In this paper, based on a sensitivity analysis, T is chosen to be 3, and the process of choosing this parameter will be explained in more detail in the following. Then, the detected outliers are eliminated, and the remaining data will be processed in the next iterations. The iterations will be terminated when the distribution of the residuals is close to the expected noise of the data set (Algorithm 1). The reason for this criterion is that the goal is detecting outliers, avoiding over-fitting the data, and modeling the noise. An overview of the adopted symbols in the Algorithm is presented in Table A1 (Appendix A).

Algorithm 1: Outlier detection algorithm.

```

1 Input: observations  $P = [x \ y \ z]$ ,  $\Phi = \{\Phi^1, \Phi^2, \dots, \Phi^H\}$ , expected noise in data  $\sigma_n$ , multiplier  $T$ 
2 Output: cleaned observations  $P'$ , outliers  $O$ 
3 Initialization:
4  $O = []$ 
5  $i \leftarrow 1$ 
6 while  $\sigma_r > \sigma_n$  do
7   compute  $\Phi^i$  from  $P$  (see Section 3.2)
8   estimate  $f(x, y)$  (see Section 3.2)
9   estimate residuals ( $r$ ):  $r = f(x, y) - z$ 
10   $\sigma_r :=$  standard deviation of residuals
11   $O^i :=$  points with residuals larger than  $T \cdot \sigma_r$ 
12   $P' :=$  points with residuals less than  $T \cdot \sigma_r$ 
13   $i \leftarrow i + 1$ 
14   $O = [O; O^i]$ 
15   $P = P'$ 
16  check criterion: compare  $\sigma_r$  and  $\sigma_n$ 
17 return  $P', O$ 

```

In the first iteration, a coarse global model Φ^1 is used to approximate the observations P . It will result in a rough approximation of the data. However, for choosing the initial model, a minimum complexity should be considered. A very simple model would result in assigning normal observations to outliers O , which could be avoided by taking into consideration prior knowledge about data behavior. In each iteration, the complexity of the model increases. Increasing the complexity of the models from one iteration to the next will help to gradually take the smoothing effect of the approximation into account.

In order to assess the accuracy of the proposed method, the outputs are compared with reference data in which the genuine outliers are already known. For this purpose, a reference data set is simulated. The simulated data are a point cloud with three components. Only the z-component is stochastic, while the x- and y-components are assumed to be deterministic. The simulated data set consists of three parts: trend, noise and outliers. The noise is generated from a Gaussian distribution with zero mean and a standard deviation of 0.05 m. In addition, the outliers are randomly generated from a Chi-square distribution with zero mean and standard deviation of 0.5 m. The simulated data represent a scenario in which the measured data contain noise, as well as large outliers. A realization of the simulated reference data is illustrated with different parts in Figure 3. To ensure the functionality and performance of the algorithm, it is tested in a Monte-Carlo (MC) simulation. In each MC run, a new set of noise and outliers are generated.

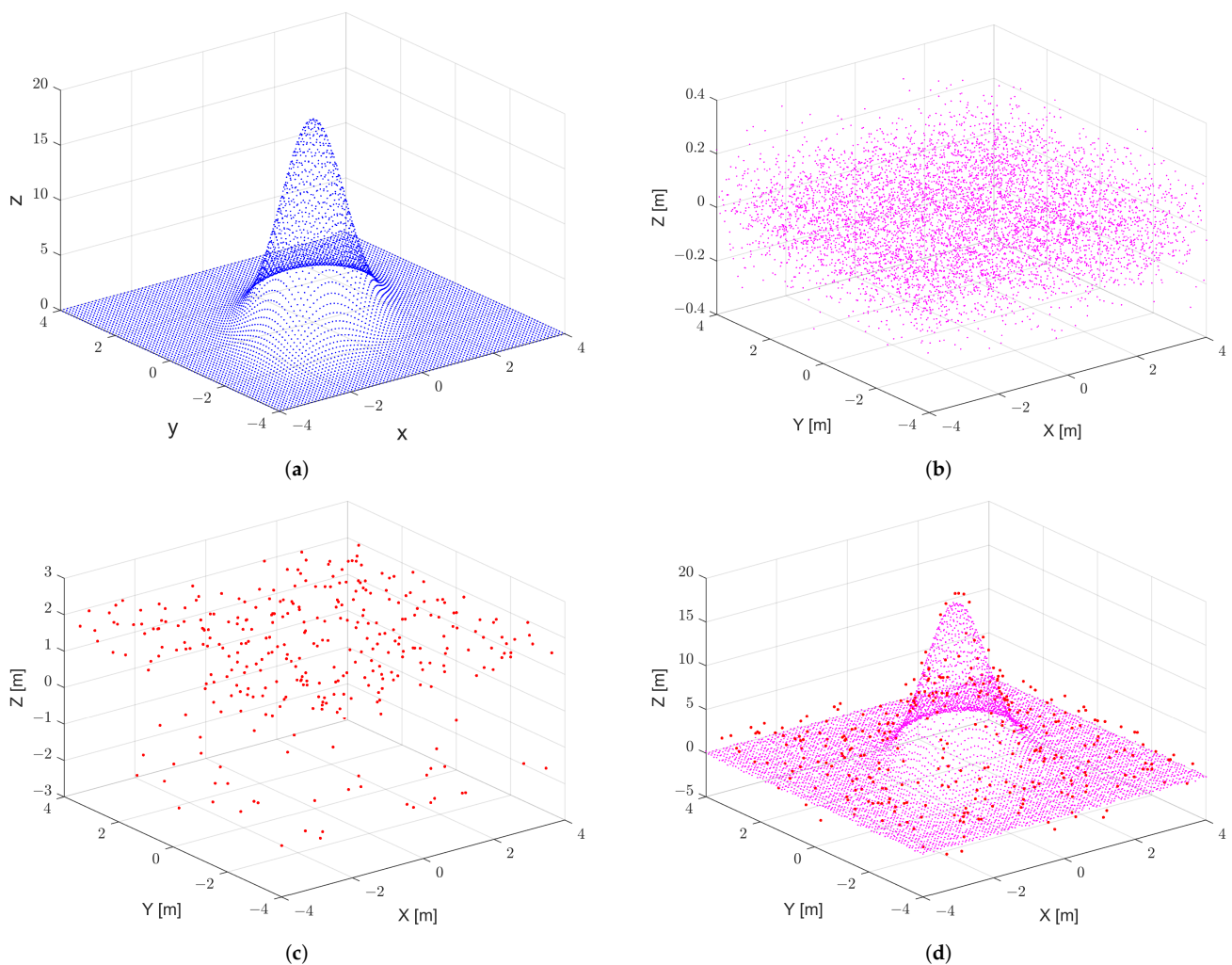


Figure 3. One realization of the simulated reference data. (a) Trend. (b) Noise. (c) Outliers. (d) Trend + Noise + Outliers.

The algorithm can be seen as a binary classifier that categorizes the points into inliers and outliers. The two outcomes of the classifier can be positive (outlier) and negative (inlier). The results can be expressed in a two-by-two confusion matrix (Table 1). True Negative (TN) and True Positive (TP) present the outcomes in which an actual inlier and an actual outlier are correctly predicted, respectively. False Negative (FN) and False Positive (FP) represent the cases where an instance is assigned to the wrong class. To assess the performance of the algorithm, four measures of precision, recall, the F_1 -score, and accuracy are used, which are calculated based on the following formulas (Equations (1)–(4)).

Table 1. Confusion matrix.

		Actual	
		Inliers /Negative	Outliers/Positive
Predicted	Inliers /Negative	True Negative (TN)	False Negative (FN)
	Outliers/Positive	False Positive (FP)	True Positive (TP)

$$\text{precision} = \frac{\text{Outliers correctly classified (TP)}}{\text{Total outliers classified (TP+FP)}} \quad (1)$$

$$\text{recall} = \frac{\text{Outliers correctly classified (TP)}}{\text{Actual Outliers (TP + FN)}} \quad (2)$$

$$F_1\text{-score} = \frac{1}{\frac{1}{\text{precision}} + \frac{1}{\text{recall}}} \quad (3)$$

$$\text{accuracy} = \frac{\text{TP} + \text{TN}}{\text{TP} + \text{TN} + \text{FP} + \text{FN}} \quad (4)$$

The results of the algorithm for different percentages of outliers and noise levels are presented in Table 2. Each measure is the median of all calculated values for 1000 MC runs. The whole simulated data set consists of 6561 points, and in the three scenarios, the generated outliers are 5%, 10% and 15% of the data. The level of noise also varies for three cases, and it shows the standard deviation of the Gaussian distribution from which the noise is generated. For noise with $\sigma_n = 0.05$ m, by considering 5% outliers, precision is more than 90%. This means that the ratio of the correctly classified outliers is high. Recall or sensitivity shows the ratio of detected outliers to the actual outliers. A recall of 1 means that all the outliers are detected. However, some inliers are also classified as outliers (here the median is 34). Such wrong classifications are best expressed by a F_1 -score, which is the harmonic mean of precision and recall. For 10% of outliers, the algorithm still performs well; however, this is no longer the case for 15% of outliers. Although with high percentages of outliers the precision is still good, the sensitivity of the algorithm is decreased. Such an effect can be improved by optimizing the selected criteria for eliminating the outliers in each step, which is not the focus of the current paper. Furthermore, by increasing the noise level, the sensitivity is affected. This is more critical when the noise level is close to the outliers' distribution; meaning with a high level of noise, it is difficult to distinguish between the noise and outliers.

Table 2. Accuracy measures of the classification into outliers and inliers for simulated data for different scenarios (each measure is the median of 1000 MC runs).

Noise Level (σ_n)	0.05 m			0.1 m			0.5 m		
Outlier Percentage (O_p)	5%	10%	15%	5%	10%	15%	5%	10%	15%
TN	6199	5862	5529	6206	5859	5539	6215	5900	5575
FN	0	0	483	0	0	578	189	573	938
FP	34	43	48	27	46	38	18	5	2
TP	328	656	501	328	656	406	139	83	46
Precision	0.91	0.94	0.91	0.92	0.93	0.91	0.89	0.94	0.96
Recall	1	1	0.51	1	1	0.41	0.42	0.12	0.05
Accuracy	0.99	0.99	0.92	0.99	0.99	0.91	0.97	0.91	0.86
F1-score	0.95	0.97	0.65	0.96	0.96	0.57	0.57	0.22	0.09

To choose a suitable threshold for detecting outliers in each iteration of the outlier detection algorithm, we performed a sensitivity analysis. The value of the threshold is increased incrementally by changing the multiplier T between 1.5 and 5. The performance of the algorithm with respect to different threshold values in the range of $[1.5\sigma_r, 5\sigma_r]$ is illustrated in Figure 4, by means of the four mentioned parameters: precision, recall, accuracy and F_1 -score. In Figure 4, the results related to the three mentioned scenarios and the different outlier percentages are presented. The best performance of the algorithm occurs when factor T is in the range of $[2.8, 3.5]$, for the first two scenarios where σ_n is 0.05 and 0.1. The optimal value of the factor T is also sensitive to the outlier percentage. For lower percentages, higher T values would suffice, and where more outliers are included in the data, smaller values perform better. As explained previously, the last scenario ($\sigma_n = 0.5$) does not perform well even with different T values. The reason is the high range of noise, which makes it difficult for the algorithm to distinguish between noise and outliers. In this paper, for the factor T , the value of 3 is chosen and used.

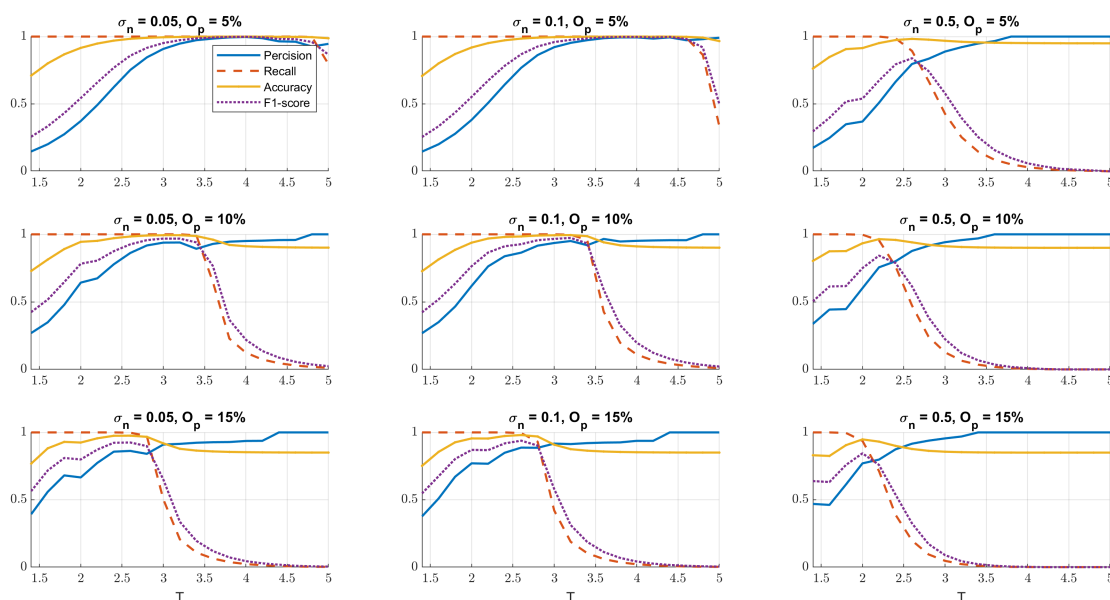


Figure 4. Results of sensitivity analysis; performance of the outlier detection algorithm with respect to different values of the chosen threshold.

3.2. Multilevel B-Spline Approximation (MBA)

According to Section 2, the PSI observations of interest here represent a large area. The 3D point cloud of PSI observations can be described as scattered data, since only vertical velocities are considered. The data set contains a high level of noise, and due to the clustering characteristics of PSI observations, especially in urban areas, the data set is irregularly distributed. This varying density of the point cloud causes large areas with very low density or no observation (data gap). The scattered data set does not provide information on the connectivity between the points, and considering the mentioned characteristics of the data, the global behavior is not visible. Therefore, it is important to understand the underlying pattern in the data. By finding a suitable mathematical model that describes the underlying function, the noise in the data can be eliminated and a prediction surface for the data gaps derived, and as a result, the global behavior of the data set will be uncovered.

In conversion from discrete points to a continuous surface, a deterministic technique based on free-form surfaces is used [44]. The MBA method is an approximation method based on hierarchical tensor product B-spline surfaces. This method was first developed in the 1990s for specific image-processing applications, such as image morphing [45,46]. Lee et al. [29] introduced a modified version of this approach that can handle scattered data. The B-spline surface is defined by a control lattice $\Phi_{m,n}$ that contains $(m+3) \times (n+3)$ control points. If we assume $\Phi_{m,n}$ is overlaid on the domain $\Omega = \{(x, y) | 0 \leq x < m, 0 \leq y < n\}$, any control point ϕ_{ij} on the lattice $\Phi_{m,n}$ overlaps with the integer values of Ω . The B-splines surface f is defined as a linear combination of uniform bicubic basis functions ($B_k(s), B_l(t)$) and control points of a control lattice Φ , wherein $i = \lfloor x \rfloor - 1, j = \lfloor y \rfloor - 1, s = x - \lfloor x \rfloor, t = y - \lfloor y \rfloor$.

$$f(x, y) = \sum_{k=0}^3 \sum_{l=0}^3 B_k(s) B_l(t) \phi_{(i+k)(j+l)}. \quad (5)$$

The uniform cubic basis functions $B_k(s)$ for $0 \leq s < 1$ are defined as follows,

$$\begin{aligned} B_0(s) &= \frac{(1-s)^3}{6}, \\ B_1(s) &= \frac{(3s^3 - 6s^2 + 4)}{6}, \\ B_2(s) &= \frac{(-3s^3 + 3s^2 + 3s + 1)}{6}, \\ B_3(s) &= \frac{s^3}{6}. \end{aligned} \quad (6)$$

Similarly, the basis functions $B_l(t)$ are calculated. Let $P_{ij} = \{(x_c, y_c, z_c) \in P | i - 2 \leq x_c < i + 2, j - 2 \leq y_c < j + 2\}$ be the proximity data points of each control point. The proximity data are those points that lie in the 4×4 neighborhood of a control point ϕ . For each point P_c in the proximity data set of a control point, one solution can be derived ϕ_c . The unique solution ϕ_{ij} for a control point is derived from minimizing the error term $(w_c \phi_{ij} - w_c \phi_c)$ for all points, wherein $w_c = B_k(s) B_l(t), k = (i+1) - \lfloor x_c \rfloor, l = (j+1) - \lfloor y_c \rfloor, s = x_c - \lfloor x_c \rfloor, t = y_c - \lfloor y_c \rfloor$. The minimization is solved by means of a Least Squares method, and the final solution is as follows:

$$\phi_{ij} = \frac{\sum_c w_c^2 \phi_c}{\sum_c w_c^2}, \quad (7)$$

wherein $\phi_c = \frac{w_c z_c}{\sum_{a=0}^3 \sum_{b=0}^3 w_{ab}^2}$. It should be noted that when the proximity data set is empty, it implies that ϕ_{ij} does not influence the B-splines surface function (Equation (5)) and therefore, any value can be assigned to the aforementioned control point. In this case, here a value of zero is assigned to ϕ_{ij} .

In their proposed algorithm for MBA approximation, Lee et al. [29] used a hierarchy of control lattices to generate a sequence of f_k . The sum of all B-splines surfaces in the hierarchy approximates the final desired surface. The approximation starts with a rough estimation, and the resolution of the control lattices increases in each step. For approximation, at the first step, a hierarchy of control lattices $\Phi_0, \Phi_1, \dots, \Phi_h$ are defined, where the first control lattice is Φ_0 , and the lowest number of control points is the coarsest one. On the other hand, the last control lattice, Φ_h is the finest control-point lattice, which contains the highest resolution of control points. The approximation process starts with the coarsest control-point lattice (Φ_0). Afterwards, by using the deviation of the estimated function to the original observations $\Delta^1 z$ based on (Φ_0), the control lattice of the next level is estimated. Such a process should continue until the last control lattice is estimated. In general, at each level k , for estimating the control lattices, the function f_k is calculated based on $\Delta^k z_c$.

$$\Delta^k z = z - \sum_{i=0}^{k-1} f_i(x, y) = \Delta^{k-1} z - f_{k-1}(x, y) \quad (8)$$

$$\Delta^0 z = 0 \quad (9)$$

The final approximation function is defined as the sum of functions in the hierarchy as follows,

$$f(x, y) = \sum_{i=0}^{k-1} f_i(x, y). \quad (10)$$

As mentioned, the PSI data is a large data set that also contains large data gaps. These gaps in the data not only introduce uncertainty to the modeled surface, but also create numerical instability. The characteristics of MBA make it suitable to model the PSI data. The proposed MBA algorithm by Lee et al. [29] is computationally efficient and the method can easily handle large data sets. The model is numerically stable because in the estimation of the unknowns, no inversion is required, and in combination with the regularization option in the function, the method is powerful in dealing with data gaps.

3.3. Bootstrapping

The final approximated model is influenced by different elements, such as measurement error, data gaps and the complexity of the chosen model. Therefore, it is important for a user to have a measure of quality for the approximated surface. Based on the explained method in Section 3.2, the approximated model based on MBA in each level is derived with least squares minimization. Therefore, mathematically, a measure of uncertainty for the model can be derived based on the precision of the observations. However, the final model in MBA consists of more than one level. The levels are approximated sequentially based on the previous ones. This creates a highly mathematical correlation between all layers. This makes error propagation a challenging process. Doing so makes the process computationally expensive and impractical in cases where there are large data sets. To overcome this problem, we have adopted a non-parametric method called “bootstrapping”.

Bootstrap is a computationally intensive method, which was first formulated by Efron et al. (e.g., [47,48]) to simulate a statistic distribution. This method provides the possibility of inference from an existing sample with a limited size and no information about the data distribution. The idea is to intensively resample from the existing samples to generate new ones. The new samples are called “bootstrap samples”. Afterwards, information from the empirical distribution of each bootstrap sample could be extracted. Combining the information from all bootstrap samples will provide the possibility to infer the distribution of the desired statistics related to the main population. Here, the goal is to get information on the distribution of a predicted point through bootstrapping. The variations of the predicted point, or in other words, of the model at a given location, need to be investigated by applying different bootstrap samples. The variations will result in a histogram showing the distribution of the predicted point. From this distribution, we

can describe the standard deviation and confidence interval of the predicted surface at a specific position.

In the first step of calculating the standard deviation σ of the approximated surface based on this method, the bootstrap samples (P^*) should be formed. A bootstrap sample is generated from the original observations (P). Any point in the bootstrap sample is drawn randomly and with equal probability from the original sample. In practice, the size of the original sample may be large, and it might not be possible to enumerate all possible bootstrap samples. Instead, a large number (B) of bootstrap samples are independently drawn from the original sample.

In the scope of this paper, the goal is to get the standard deviation of the approximated surface based on the original PSI observations P at a desired position. Based on each bootstrap sample, a surface is approximated, which leads to available predictions at the desired position from all bootstrap samples at the end (P_{pred}^{*i}). This will represent the possible variations of the prediction and its distribution. Based on the distribution, the related bootstrap standard deviation ($\sigma_{Bootstrap}$) can be calculated as follows,

$$\sigma_{Bootstrap} = \sqrt{\frac{\sum_{i=1}^B (P_{pred}^{*i} - P_{pred}^*)^2}{(B-1)}}, \text{ with } P_{pred}^* = \frac{\sum_{i=1}^B P_{pred}^{*i}}{B}, \quad (11)$$

wherein P_{pred}^* represents the mean of the bootstrap predictions at the desired position.

A confidence interval (CI) of the predicted surface can also be obtained non-parametrically. For a specific significance level of α , a $100(1 - 2\alpha)\%$ CI can be computed based on the sorted predicted values from the smallest to the largest [49,50]. The lower and upper bound of the CI are the $(B+1)\alpha$ th and $(B+1)(1-\alpha)$ th values, respectively. In the case of non-integer numbers, the nearest integer value is selected. Figure 5 illustrates the explained bootstrapping algorithm which is implemented (see Algorithm 2). An overview of the adopted symbols in the Algorithm is presented in Table A1.

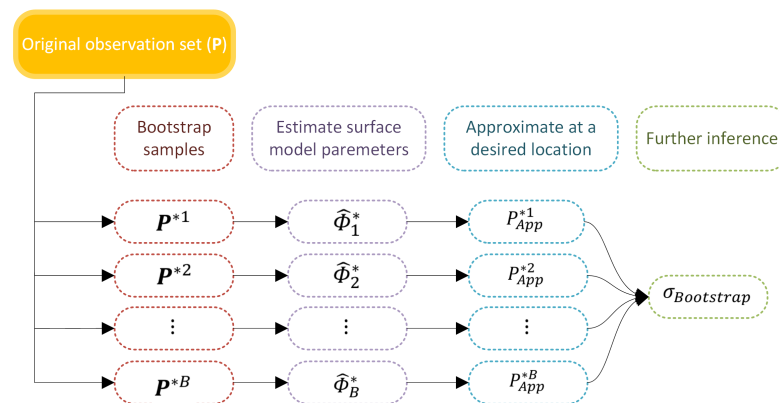


Figure 5. Overview of the implemented bootstrapping algorithm.

As a result, point-wise standard errors can be derived. We can get information on possible variability of the prediction. The bootstrapping algorithm does not require theoretical calculations and provides information even for complicated problems. It should be noted that the dispersion of the distribution related to a predicted point is dependent on the observations, as well as the complexity of the modeled surface. Additionally, in areas with less observations, the distribution will be stretched. Moreover, if the chosen model is over-fitting the data, it leads to an increase in the uncertainty range.

Algorithm 2: Bootstrap Algorithm.

```

1 Input: observations ( $P$ )
2 Output: distribution of prediction  $D$ ; bootstrap standard deviation ( $\sigma_{Bootstrap}$ ), 95% confidence interval (CI)
3 for  $i = 1:B$  do
4     generate bootstrap sample ( $P^{*i}$ ) from ( $P$ )
5     approximate the model ( $\Phi^{*i}$ ) based on  $P^{*i}$ 
6     make prediction ( $P_{pred}^{*i}$ ) at the desired location based on  $\Phi^{*i}$ 
7     let distribution of predictions  $D := \{P_{pred}^{*1}, P_{pred}^{*2}, \dots, P_{pred}^{*i}\}$ 
8 Compute 95% CI of  $D$ 
9 Compute  $\sigma_{Bootstrap}$  of  $D$  (Equation (11))

```

4. Results

This section entails the results of applying the explained methods from Section 3 on the data set of interest (Section 2). In the first step, the data are pre-processed (Section 4.1) by using the proposed outlier detection algorithm (Section 3.1). After eliminating the outliers, in Section 4.2, the observations are modeled as a continuous surface according to the explained surface approximation technique in Section 3.2. At the end in Section 4.3, 95% CIs are derived for the approximated surface based on the bootstrapping method (Section 3.3).

4.1. Pre-Processing of Data

The real data, introduced in Section 2, are first processed for spatial outliers based on Algorithm 1. The data set contains 301,386 observations. After running the algorithm, 15,201 outliers from 301,386 data points are detected. The process takes five iterations. The initial model starts with two levels $\Phi^1\{\Phi_{10,5}, \Phi_{20,10}\}$ and in each iteration, one layer is added to the control lattice hierarchy in such a way that the next layer has five more control points in each direction. The noise level in the data are not known, and therefore based on the dispersion of the data around zero, a suitable noise level is chosen as a stop criterion for the algorithm. Since the data are not normally distributed and also contain outliers, two-thirds of the standard deviation is used. In Figure 6, the histogram of residuals from different iterations is illustrated. The improvement in the shape of the histogram of the residuals from one iteration to the other could be seen. The final histogram is still not exactly normally distributed, but it is symmetric and is centered around zero. Figure 7 illustrates the detected outliers and shows reduction of noise in the observations.

The genuine outliers are not known in this case, and therefore, to evaluate the accuracy of the proposed algorithm, we try a comparison to a similar study. This data set has been processed by Brockmeyer et al. [1]. They used a local neighborhood analysis to identify the outliers. By comparing the individual PSI velocities with the associated neighborhood functions, spatial variations are detected as outliers with a given probability of error [1]. As a result of the conducted outlier detection, 15,609 PSI velocities were detected as outliers. This method has two disadvantages: firstly, it only compares the points locally, and secondly, it requires a high computation time. Because each point is tested individually, it therefore becomes even more challenging in large data sets. The output of our algorithm is compared with results of [1], which are shown in Table 3. The results show high compatibility of the estimations from both algorithms. The precision and accuracy is high in comparison to recall, which means that the algorithm has classified some of the outliers from [1] as inliers.

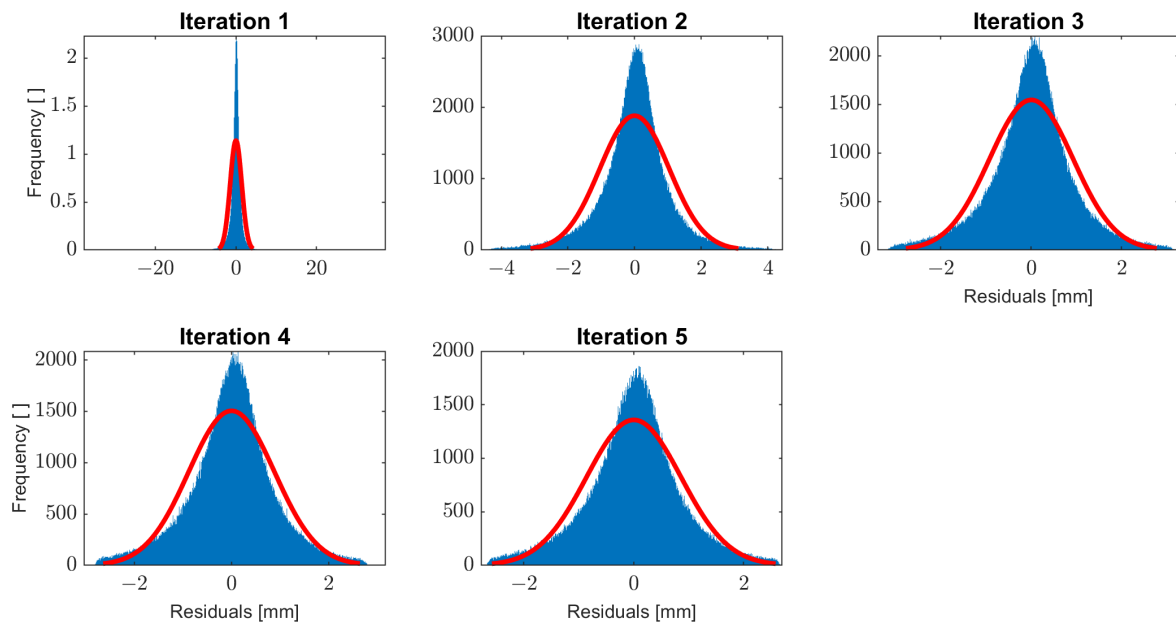


Figure 6. Histogram of residuals; the red lines shows the best-fitted normal distribution to the residuals at each iteration in the outlier detection algorithm.

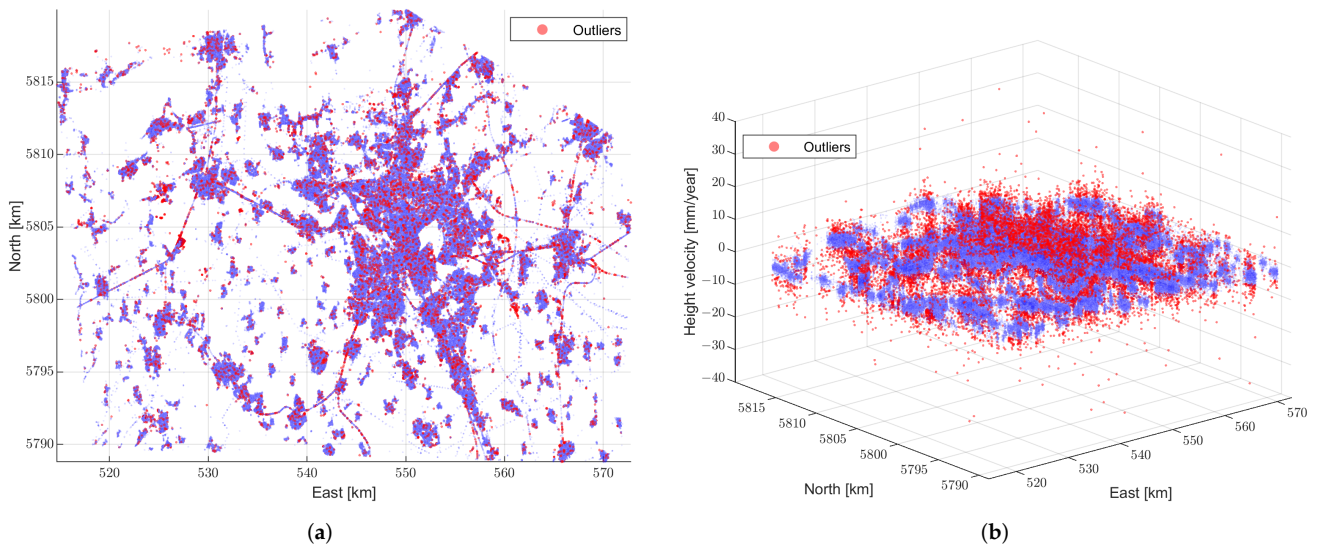


Figure 7. Detected outliers (red points) and the clean observations (blue points). (a) 2D view. (b) 3D view.

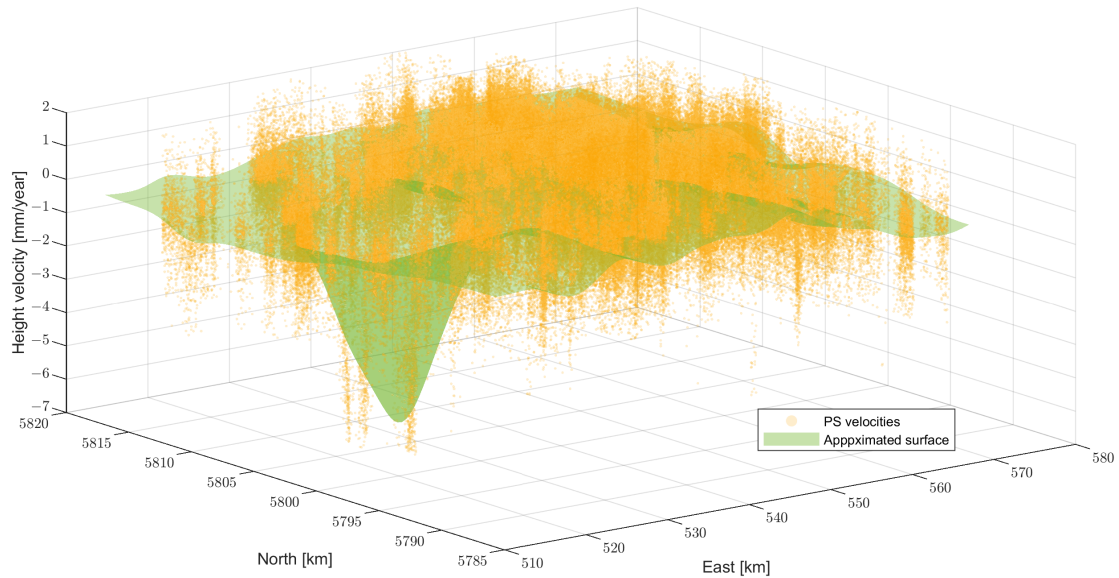
Table 3. Comparison of the proposed algorithm with the results from [1].

Accuracy Measure	Precision	Recall	Accuracy	F_1 -Score
Value	0.93	0.89	0.99	0.91

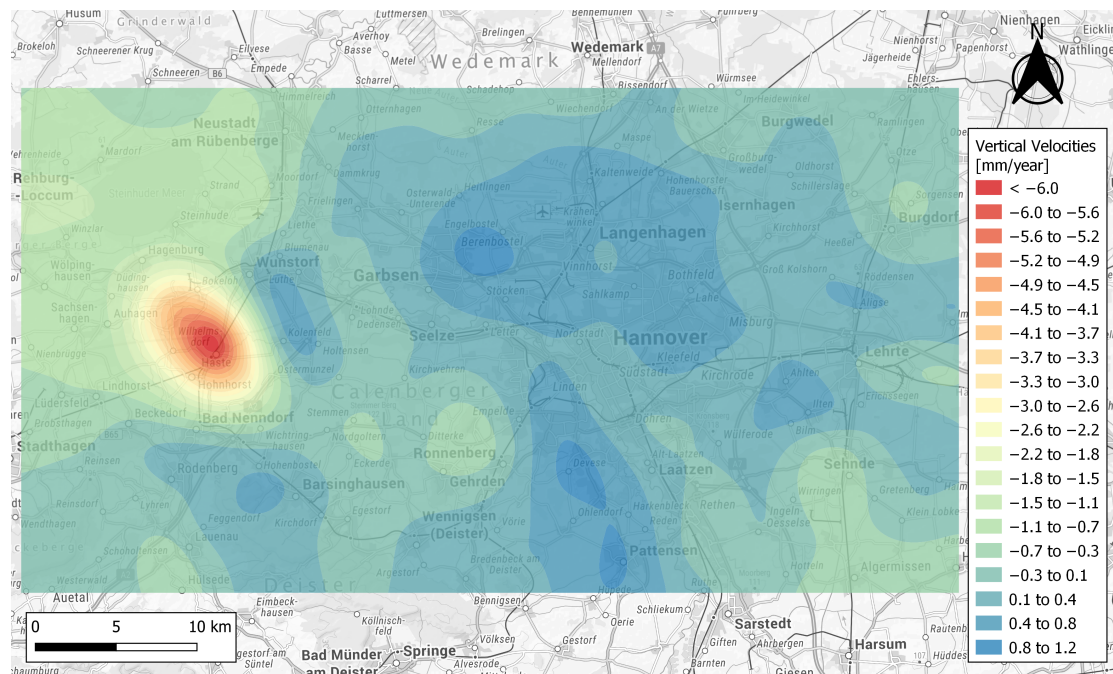
4.2. Approximation of RGM

The next step after pre-processing the data and eliminating the outliers is to mathematically model the height velocities followed by approximating a continuous surface, which represents the RGM in the area of Hanover. The RGM is approximated based on the MBA method (Section 3.2). Based on the nature of the data set and prior information of the general ground behavior of the region, a control lattice hierarchy of three levels

$\Phi \{ \Phi_{10,5}, \Phi_{20,10}, \Phi_{25,15} \}$ is used. Figure 8a illustrates the approximated surface along with the observed height velocities. In more detail, the approximated RGM is presented in Figure 8b as a color-coded map. Aside from local movements (in the range of $(-2, 1)$ [mm/year]) to the Earth's surface, a large movement up to -6 [mm/year] is observed in the left side (area of Wunstorf).



(a) 3D view



(b) 2D view (heat map)

Figure 8. Approximated RGM of Hanover based on PSI observations: (a) 3D view of the approximated surface and the observations, (b) heat map of the RGM.

4.3. Confidence Interval

Even after pre-processing and eliminating the outliers, the remaining PSI velocities contain high levels of noise. Additionally, spatial distribution of the velocities is non-homogeneous, and there are large areas with sparse observations (Figure 7a). This introduces a high level of uncertainty to the approximated RGM model (Section 4.2). To derive an uncertainty measure that best describes these effects on the approximated model, the bootstrapping method is implemented in accordance with Section 3.3.

As described in Section 3.3, at first, the bootstrap samples are generated. The observation sample after eliminating the outliers still consists of 286,185 points; therefore, practically all the $286,185^{286,185}$ possible samples cannot be formed. Instead, a large number of bootstrap samples ($B = 1000$) with equal probability is drawn from the observations. Afterwards, for each bootstrap sample, the RGM is modeled.

To assess the quality of the approximated model, the difference between the PSI velocity and the predicted value can be used as an error measure. These differences or residuals are calculated for all the points in the observation set, over all approximated models related to the bootstrap samples (P_{pred}^{*i}). The results for all residuals ($1000 \times 286,185$) are illustrated in Figure 9. The histogram shows that the residuals are symmetrically distributed. However, there is a number of large deviations (around 20 [mm/year]) related to a specific area in the observations where sharp local deformations have been observed, which was not detected by the adopted model.

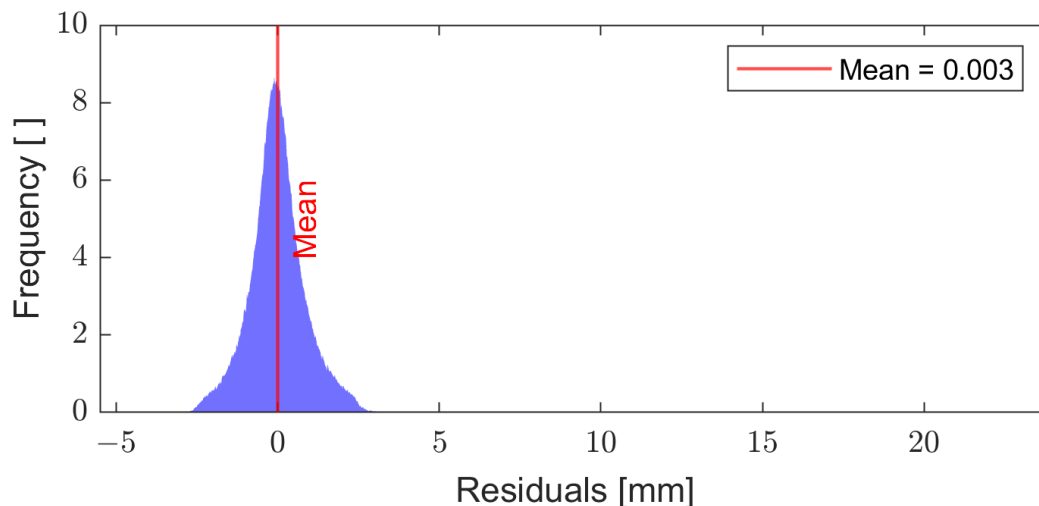


Figure 9. Histogram of approximation error (residuals) for all points and all bootstrap samples. Residuals are defined as the difference between approximation and the observation.

In more detail, the variations of predictions (P_{pred}^{*i}) through all bootstrapping iterations for 10 arbitrary points are assessed. The 2D view of the location of these 10 chosen points along with the histograms are shown in Figure 10. Histograms show less variations in areas with more observations. The spread of the histograms is also affected by the spatial distribution of neighboring points. This effect can be seen, for example, in the difference in histogram for point 1 and point 6. Point 1 is located in an area with many observations in the neighborhood. On the contrary, point 6 is in a sparse area. Such a neighbourhood effect is directly reflected in the spread of the derived histograms and the corresponding bootstrap standard deviations (σ_b for point 1 and 6 is 0.008 and 0.04 [mm/year], respectively). The histogram of observations for the points individually is not symmetrically distributed in all cases; however, the histogram of all the points for the whole region represents a symmetric distribution (see Figure 9).

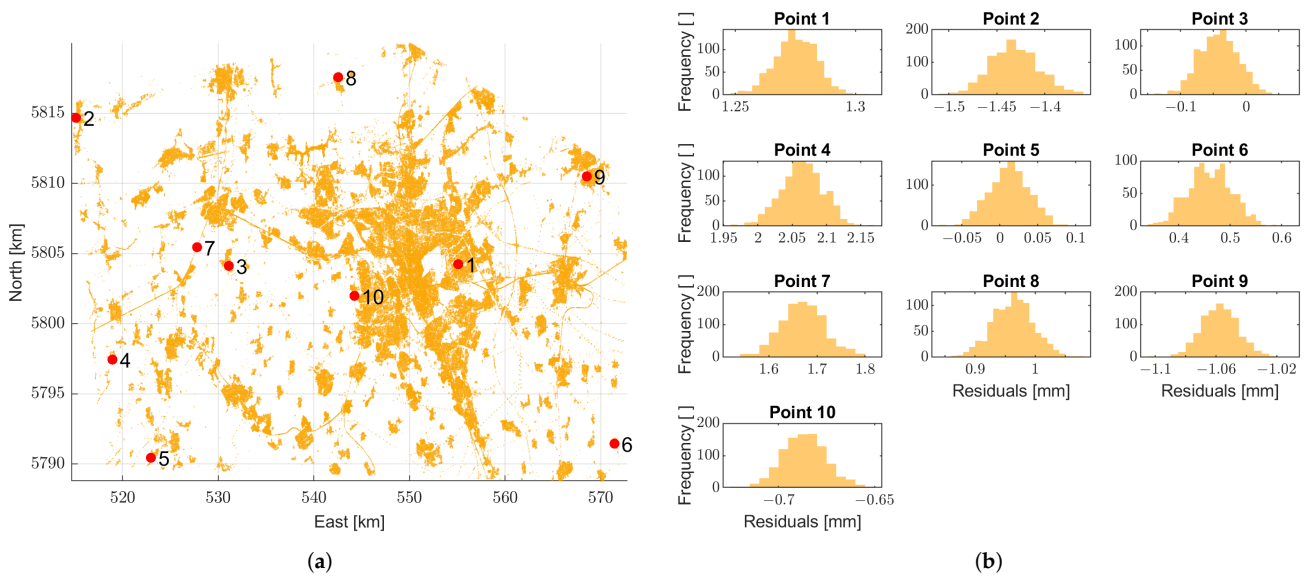


Figure 10. Histogram of predicted value based on all bootstrap samples in 10 arbitrary points. (a) Observations and 10 chosen points (red). (b) Histograms.

Based on the performed bootstrapping process, a 95% confidence region can be obtained for the whole area. The CI is calculated from the quantiles of the bootstrap predictions. In Figure 11, the range of the CIs is represented as a color-coded surface. The range is derived based on the difference between the lower and upper bounds of the 95% percentile interval. For the whole area, the lengths of the CIs are between 0.01–0.4 [mm/year]. The minimum and maximum bootstrap standard deviations (σ_b) for the whole region is 0.003 [mm/year] and 0.13 [mm/year], respectively.

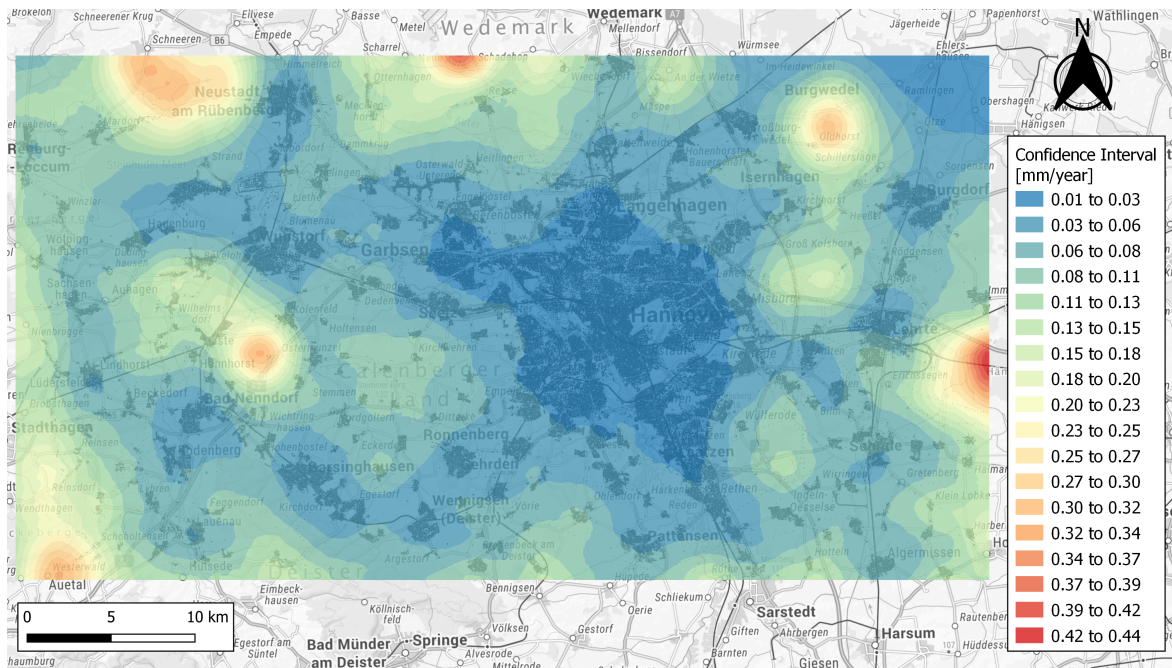


Figure 11. Heat map of the 95% percentile interval of the approximated RGM. The range of the CIs are color-coded. The black points represent the PSI observations.

The range of the CI of the approximation highly depends on spatial distribution of the points. In the areas where less observations are available, there will respectively be less observations in the bootstrapping sample, which directly affects the model. As a result, the range of the CI in such regions increases automatically. In a closer look, such an effect can be seen for example in two selected lines that are specified in Figure 12. In Figure 12a, the position of the observations and the lines of interest are presented. Line 1 is situated in the edge, and less observations are available in its neighbouring area. On the other hand, line 2, which is closer to the middle region, is in an area with more observations. It is expected that in areas with less observations, the approximated model is more uncertain and shows higher variability in the distribution of prediction from bootstrap samples. This can be observed in Figure 13. The CI of line 1 (see Figure 13a) shows that the approximated model towards the edge of the area is highly uncertain, as expected. In contrast, the interval is relatively small for line 2. The confidence bands describe the uncertainty of the approximated model in Section 4.2, where all observations are used to model RGM. In Figure 13, the continuous line represents the mentioned approximated model, and the dashed line is the median of the approximations based on the bootstrap samples. The median lies mostly over the approximated model.

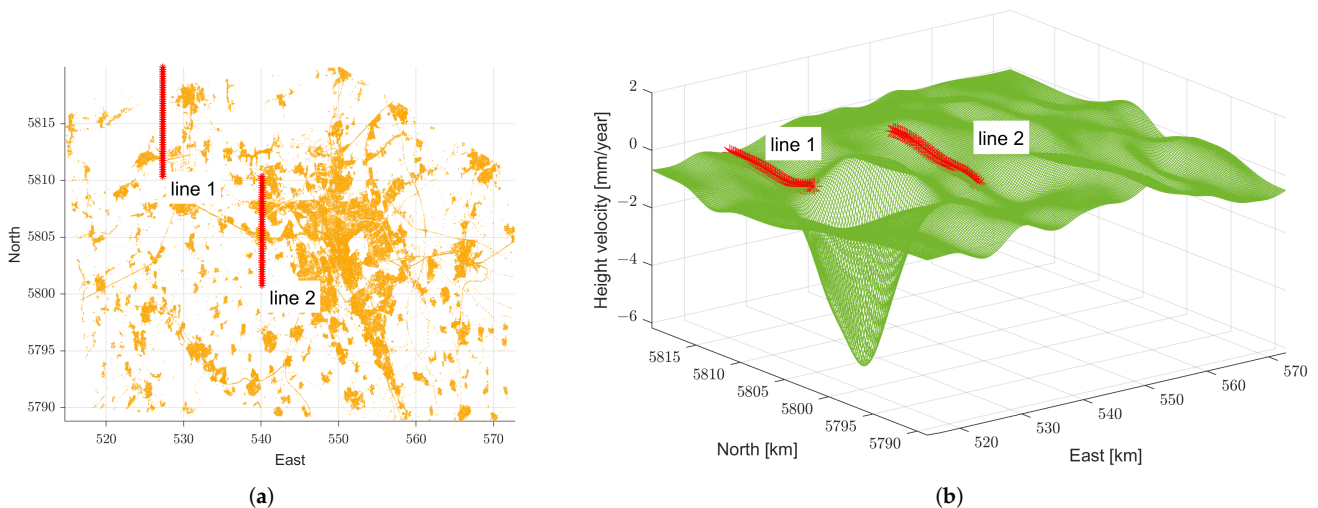


Figure 12. The two selected lines to observe the CI. (a) Observations (2D view). (b) Approximated surface (Figure 8) (3D view).

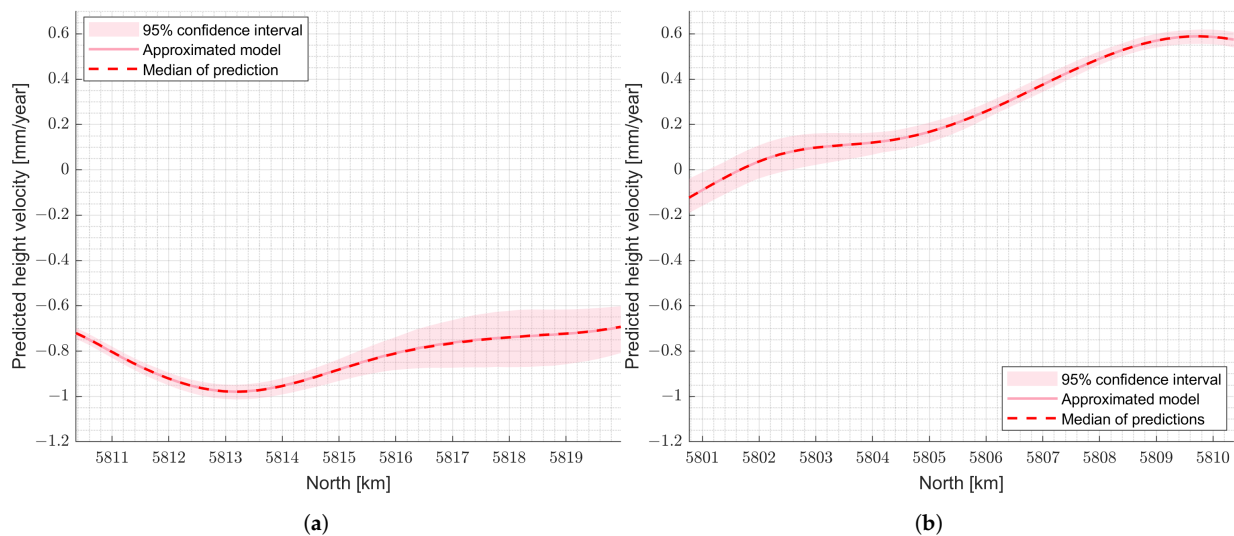


Figure 13. CIs for lines 1 and 2 in Figure 12. (a) Line 1. (b) Line 2.

As explained, the CIs (see Figures 11 and 13) describe the uncertainty of the approximated model by considering all the observations for the chosen control lattice hierarchy in Section 4.2. However, the range of the interval depends also on the complexity of the chosen model. This effect can be seen in Figure 14. The estimated CI for the two lines are calculated for two different models with the following control lattice hierarchy for the two models: $\Phi_1\{\Phi_{10,5}, \Phi_{20,10}, \Phi_{25,15}\}$ and $\Phi_2\{\Phi_{10,5}, \Phi_{20,10}, \Phi_{25,15}, \Phi_{30,20}, \Phi_{35,25}, \Phi_{40,30}\}$.

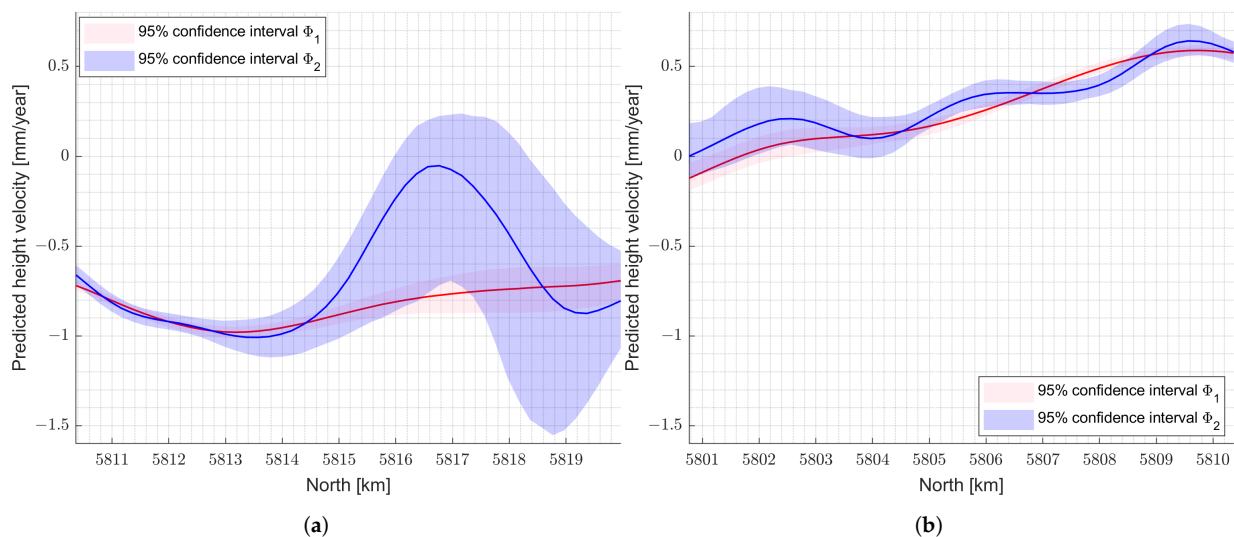


Figure 14. CI from models with different complexities for the two lines in Figure 12. (a) Line 1. (b) Line 2.

5. Discussion

The proposed spatial outlier detection algorithm shows compatible results to the study by Brockmeyer et al. [1]. Since the ground truth behind the distribution of the outliers in the real data is not known, it is not possible to evaluate these results more comprehensively. The algorithm not only considers both local and global behavior of the data, but the iterative process of the algorithm also helps to detect the anomalies more precisely. By fitting a surface to the data in each iteration, the nature of the data which represents a surface is taken into account. This makes the approach especially suitable for these kinds of applications. The performance of the algorithm will be improved by having some prior knowledge of the data set. For example, information regarding the minimum noise level and rough expected RGM would help to decide on the complexity of the models for the first and last iterations.

The MBA approach showed computational efficiency and numerical stability in dealing with the real data set. Therefore, it is possible to choose a very complex model with a high number of control points and many levels; however, the approximation of the data based on the MBA approach is very sensitive to complexity of the chosen model. To avoid over- or under-fitting the data, an appropriate control lattice hierarchy could be selected based on the type of dataset and the prior information about the general ground behavior of the region.

The calculated confidence bounds describe the quality of the model very well. The effect of data gaps and noise is directly reflected on the range of the CIs. In this research, the CIs are determined based on the quantiles; however, an improved interval or the 'bias-corrected- BC_a' ' could also be calculated [47].

The range of the CIs is also influenced by the complexity of the model. Increasing the complexity increases the uncertainty range of the approximation. This is particularly important when there is a risk of over- or under-fitting the data or, in other words, the model selection problem. The information from the CIs and standard deviations of the bootstraps can be helpful in finding the most appropriate model for a given data set. This could lead

to a solution to solve the model selection problem in similar situations. In the present work, the initial model selected is based on the prior information of the global movement in the region. The model selection concept is not the focus of the current paper.

In practice, the output of this process will help to detect areas affected by movement. By considering the additional information on the uncertainty of the model (CIs), the user can optimally pinpoint areas where new measurements by a more accurate geodetic technique are necessary to update the spatial reference system. Having a reliable mathematical model not only helps to better understand the general behavior of the data, but also provides the opportunity to keep track of any changes of the surface more efficiently, for example by statistical testing. Additionally, the outputs of the outlier detection algorithm can be used to detect the movements of individual objects. These anomalies might represent very local changes that do not affect modeling RGM. However, this information can be of high interest in monitoring infrastructure or other monitoring applications.

6. Conclusions

In this paper, processing and modeling PSI observations related to the area of Hanover, Germany were discussed. The goal is to precisely model RGM as a continuous surface that enables the user to predict movements at positions where no measurements are available. The contribution of the current paper consists of three main parts: pre-processing of data, modeling and CIs for the model.

For pre-processing the data, a data-adaptive outlier detection algorithm is proposed. The process considers both global and local behavior of the data. The algorithm is an iterative process in which a model is fitted to the data and in each iteration, the largest deviation to the model is globally detected. The proposed algorithm is tested in a MC simulation for different reference data sets. Results show promising performance in detecting outliers with an accuracy of 0.95 and F_1 -score of at least 0.95 for data sets containing up to 10% of outliers. Moreover, the algorithm detects around 5% of outliers in the PSI observations. The proposed methodology is not adopted for outliers of more than 10%, which is due to the criteria for recognizing outliers within the algorithm. This aspect could be improved by optimizing criterion selection, which was not within the scope of the current paper. However, in the next steps, we plan to develop an approach to find the optimal criteria based on individual data sets. For the real data set, 5% of outliers is detected.

The modeled RGM, based on MBA, shows mostly small movements in the area. A large movement area is also detected with up to -6 [mm/year]. The method helps to overcome the challenges in modeling PSI observations, which are mainly the large number of observations and irregular distribution of points. The method is computationally efficient and can numerically handle data gaps. However, it is difficult to model the correlation between different levels, and especially due to the large amount of data, parametrical modeling of uncertainty is not practical. Therefore, the uncertainty of the model is derived from the non-parametric method of bootstrapping. As a result, a CI is estimated for the approximated surface. The CI for the whole area has a range between 0.01–0.4 [mm/year].

The derived CIs reflect the sources of uncertainty in the model. An important source is caused by data gaps in the PSI observation. Additionally, high local variations or noise of the data affect the confidence bands. If the chosen model is not suitable for the data set, the range of the CIs will also increase, which in turn leads to a higher level of uncertainty in the model. Therefore, model selection is an essential step, which directly affects the confidence bands. In the future, we will investigate ways of using the information about the CIs to solve the model selection problem.

Overall, we provided a pipeline for modeling RGMs based on PSI observations including a series of steps. The steps have been designed to consider the nature of the data and the general movement they represent. Although the PSI data provide a large amount of information, the data are contaminated by high levels of noise and outliers besides the irregular distribution of the data, which is challenging to model. The main steps of

preprocessing, modeling and quality assurance are done by temporal outlier detection, spatial outlier detection, MBA and bootstrapping methods, respectively.

The combination of a mathematical model of the RGM and the quality measure of the model (CIs) helps the user in identifying the critical locations for updating the spatial reference system. The output of this research could be of high interest for monitoring purposes. Having a mathematical model of the RGM and tracking any changes to the model in time will give the possibility of statistically testing any significant changes to the region in a systematic way. The detected outliers in the spatial outlier detection step may carry important information of very local changes to important infrastructures or buildings.

Author Contributions: Conceptualization, B.M., M.B., I.N., C.-H.J. and H.A.; methodology, B.M., M.B. and H.A.; software, B.M.; formal analysis, B.M.; investigation, B.M., M.B., I.N., C.-H.J. and H.A.; writing—original draft preparation, B.M., M.B., I.N., C.-H.J. and H.A.; writing—review and editing, B.M., M.B., I.N., C.-H.J. and H.A.; visualization, B.M., M.B.; supervision, H.A., C.-H.J. and I.N. All authors have read and agreed to the published version of the manuscript.

Funding: The publication of this article was funded by the Open Access Fund of the Leibniz Universität Hannover.

Institutional Review Board Statement: Not applicable.

Informed Consent Statement: Not applicable.

Acknowledgments: We are extremely grateful to the Federal Institute for Geo-sciences and Natural Resources (BGR) for providing the PSI-dataset, which has enabled the presented research. We also appreciate the reviewers insightful comments that improved this manuscript.

Conflicts of Interest: The authors declare no conflict of interest.

Abbreviations

The following abbreviations are used in this manuscript:

BGR	Federal Institute for Geo-sciences and Natural Resources
CI	confidence interval
ESA	European Space Agency
GNSS	Global Navigation Satellite System
HB-Splines	Hierarchical B-splines
InSAR	Interferometric Synthetic Aperture Radar
LOF	Local Outlier Factor
LOS	Line of Sight
MBA	Multilevel B-spline Approximation
MC	Monte-Carlo
PS	Persistent Scatterer
PSI	Persistent Scatterer Interferometry
PSI-WAP	PSI Wide-Area-Product
RGM	Regional Ground Movement
SAR	Synthetic Aperture Radar

Appendix A

Table A1. Overview of the used symbols in Algorithms 1 and 2.

Symbol	Description	Algorithm
P	observations	Algorithms 1 and 2
P'	cleaned observations	Algorithm 1
O	outliers	Algorithm 1
r	residuals	Algorithm 1
P^*	bootstrap sample	Algorithm 2
P_{pred}^i	predicted value based on Φ^*	Algorithm 2
Φ	control lattice hierarchy	Algorithm 1
Φ^*	control lattice hierarchy based on P^*	Algorithm 1
T	multiplier	Algorithm 1
σ_r	residuals standard deviation	Algorithm 1
σ_n	expected noise in the data	Algorithm 1
$\sigma_{Bootstrap}$	bootstrap standard deviation	Algorithm 2
95% CI	95% confidence interval	Algorithm 2
D	distribution of predictions	Algorithm 2
i	counter	Algorithms 1 and 2

References

- Brockmeyer, M.; Schnack, C.; Jahn, C.H. Datenanalyse und flächenhafte Modellierung der PSI-Informationen des BodenBewegungsdienst Deutschlands für die Landesfläche Niedersachsens. *Zfv-Z. Geod. Sie Geoinf. Landmanag.* **2020**, *3*, 154–167.
- Li, Z.W.; Yang, Z.F.; Zhu, J.J.; Hu, J.; Wang, Y.J.; Li, P.X.; Chen, G.L. Retrieving three-dimensional displacement fields of mining areas from a single InSAR pair. *J. Geod.* **2015**, *89*, 17–32. [\[CrossRef\]](#)
- Shamshiri, R.; Motagh, M.; Baes, M.; Sharifi, M.A. Deformation analysis of the Lake Urmia causeway (LUC) embankments in northwest Iran: Insights from multi-sensor interferometry synthetic aperture radar (InSAR) data and finite element modeling (FEM). *J. Geod.* **2014**, *88*, 1171–1185. [\[CrossRef\]](#)
- Harmening, C.; Neuner, H. A spatio-temporal deformation model for laser scanning point clouds. *J. Geod.* **2020**, *94*, 26. [\[CrossRef\]](#)
- Ferretti, A.; Prati, C.; Rocca, F. Permanent scatterers in SAR interferometry. *IEEE Trans. Geosci. Remote Sens.* **2001**, *39*, 8–20. [\[CrossRef\]](#)
- Lubitz, C.; Motagh, M.; Wetzel, H.U.; Anderssohn, J. TerraSAR-X Time series uplift monitoring in Staufen, South-West Germany. In Proceedings of the 2012 IEEE International Geoscience and Remote Sensing Symposium, Munich, Germany, 22–27 July 2012; pp. 1306–1309.
- Hooper, A. A multi-temporal InSAR method incorporating both persistent scatterer and small baseline approaches. *Geophys. Res. Lett.* **2008**, *35*. [\[CrossRef\]](#)
- Anderssohn, J.; Motagh, M.; Walter, T.R.; Rosenau, M.; Kaufmann, H.; Oncken, O. Surface deformation time series and source modeling for a volcanic complex system based on satellite wide swath and image mode interferometry: The Lazufre system, central Andes. *Remote Sens. Environ.* **2009**, *113*, 2062–2075. [\[CrossRef\]](#)
- Hawkins, D.M. *Identification of Outliers*; Springer: Berlin/Heidelberg, Germany, 1980; Volume 11.
- Barnett, V.; Lewis, T. *Outliers in Statistical Data*; Wiley: Washington, DC, USA, 1984.
- Papadimitriou, S.; Kitagawa, H.; Gibbons, P.B.; Faloutsos, C. Loci: Fast outlier detection using the local correlation integral. In Proceedings of the 19th International Conference on data Engineering (Cat. No. 03CH37405), Bangalore, India, 5–8 March 2003; pp. 315–326.
- Knorr, E.M.; Ng, R.T.; Tucakov, V. Distance-based outliers: Algorithms and applications. *VLDB J.* **2000**, *8*, 237–253. [\[CrossRef\]](#)
- Shen, J.; Liu, J.; Zhao, R.; Lin, X. A kd-tree-based outlier detection method for airborne LiDAR point clouds. In Proceedings of the 2011 International Symposium on Image and Data Fusion, Tengchong, China, 9–11 August 2011; pp. 1–4.
- Breunig, M.M.; Kriegel, H.P.; Ng, R.T.; Sander, J. LOF: Identifying density-based local outliers. In Proceedings of the 2000 ACM SIGMOD International Conference on Management of Data, Dallas, TX, USA, 16–18 May 2000; pp. 93–104.
- Jain, A.K.; Murty, M.N.; Flynn, P.J. Data clustering: A review. *ACM Comput. Surv. (CSUR)* **1999**, *31*, 264–323. [\[CrossRef\]](#)
- Sotoodeh, S. Hierarchical clustered outlier detection in laser scanner point clouds. *Int. Arch. Photogramm. Remote Sens. Spat. Inf. Sci.* **2007**, *36*, 383–388.
- Arge, L.; Larsen, K.G.; Mølhave, T.; van Walderveen, F. Cleaning massive sonar point clouds. In Proceedings of the 18th SIGSPATIAL International Conference on Advances in Geographic Information Systems, San Jose, CA, USA, 2–5 November 2010; pp. 152–161.
- Rasmussen, C.; Williams, C. *Gaussian Processes for Machine Learning*; MIT Press: Cambridge, MA, USA, 2006; Volume 1.
- Johnson, T.; Kwok, I.; Ng, R.T. Fast Computation of 2-Dimensional Depth Contours. In Proceedings of the KDD, New York, NY, USA, 27–31 August 1998; pp. 224–228.

20. Tobler, W.R. A computer movie simulating urban growth in the Detroit region. *Econ. Geogr.* **1970**, *46*, 234–240. [[CrossRef](#)]
21. Haslett, J.; Bradley, R.; Craig, P.; Unwin, A.; Wills, G. Dynamic graphics for exploring spatial data with application to locating global and local anomalies. *Am. Stat.* **1991**, *45*, 234–242.
22. Pannatier, Y. *VARIOWIN: Software for Spatial Data Analysis in 2D*; Springer Science & Business Media: Berlin/Heidelberg, Germany, 2012.
23. Haining, R. *Spatial Data Analysis in the Social and Environmental Sciences*; Cambridge University Press: Cambridge, UK, 1993.
24. Anselin, L. Local indicators of spatial association—LISA. *Geogr. Anal.* **1995**, *27*, 93–115. [[CrossRef](#)]
25. Liu, H.; Jezek, K.C.; O’Kelly, M.E. Detecting outliers in irregularly distributed spatial data sets by locally adaptive and robust statistical analysis and GIS. *Int. J. Geogr. Inf. Sci.* **2001**, *15*, 721–741. [[CrossRef](#)]
26. Lu, C.T.; Chen, D.; Kou, Y. Algorithms for spatial outlier detection. In Proceedings of the Third IEEE International Conference on Data Mining, Melbourne, FL, USA, 22 November 2003; pp. 597–600.
27. Chen, D.; Lu, C.T.; Kou, Y.; Chen, F. On detecting spatial outliers. *Geoinformatica* **2008**, *12*, 455–475. [[CrossRef](#)]
28. Franke, R.; Nielson, G.M. Scattered data interpolation and applications: A tutorial and survey. In *Geometric Modeling*; Springer: Berlin/Heidelberg, Germany, 1991; pp. 131–160.
29. Lee, S.; Wolberg, G.; Shin, S.Y. Scattered data interpolation with multilevel B-splines. *IEEE Trans. Vis. Comput. Graph.* **1997**, *3*, 228–244. [[CrossRef](#)]
30. Schabenberger, O.; Gotway, C.A. *Statistical Methods for Spatial Data Analysis*; CRC Press: Boca Raton, FL, USA, 2017.
31. Piegl, L.; Tiller, W. *The NURBS Book*, 2nd ed.; Springer: Berlin/Heidelberg, Germany, 1997.
32. Bureick, J.; Alkhatib, H.; Neumann, I. Robust spatial approximation of laser scanner point clouds by means of free-form curve approaches in deformation analysis. *J. Appl. Geod.* **2016**, *10*, 27–35. [[CrossRef](#)]
33. Straub, C. Recent Crustal Deformation and Strain Accumulation in the Marmara Sea Region, NW Anatolia, Inferred from GPS Measurements. Ph.D. Thesis, ETH Zurich, Zurich, Switzerland, 1996.
34. Montero, J.; Delfiner, P.; Mateu, J. *Spatial and Spatio-Temporal Geostatistical Modeling and Kriging*, 1st ed.; John Wiley and Sons: Chichester, UK, 2015.
35. Mohammadiojdan, B.; Alkhatib, H.; Brockmeyer, M.; Jahn, C.H.; Neumann, I. Surface Based Modelling of Ground Motion Areas in Lower Saxony. *Geomonitring* **2020**, 107–122. [[CrossRef](#)]
36. Forsey, D.R.; Bartels, R.H. Hierarchical B-spline refinement. *ACM Siggraph Comput. Graph.* **1988**, *22*, 205–212. [[CrossRef](#)]
37. Forsey, D.R.; Bartels, R.H. Tensor products and hierarchical fitting. In *Curves and Surfaces in Computer Vision and Graphics II*; International Society for Optics and Photonics: Bellingham, WA, USA, 1992; Volume 1610, pp. 88–96.
38. Forsey, D.R.; Bartels, R.H. Surface fitting with hierarchical splines. *ACM Trans. Graph.* **1995**, *14*, 134–161. [[CrossRef](#)]
39. Efron, B. Censored data and the bootstrap. *J. Am. Stat. Assoc.* **1981**, *76*, 312–319. [[CrossRef](#)]
40. Efron, B.; Tibshirani, R.J. *An Introduction to the Bootstrap*; CRC Press: Boca Raton, FL, USA, 1994.
41. European Space Agency. Sentinel-1. 2020. Available online: <https://sentinel.esa.int/web/sentinel/missions/sentinel-1> (accessed on 1 September 2020).
42. Kalia, A.; Frei, M.; Lege, T. A Copernicus downstream-service for the nationwide monitoring of surface displacements in Germany. *Remote Sens. Environ.* **2017**, *202*, 234–249. [[CrossRef](#)]
43. Yin, X. Einflüsse Geometrischer Radar-Aufnahmekonstellationen auf die Qualität der Kombinativ Berechneten Bodenbewegungskomponenten. Ph.D. Thesis, Universität Clausthal, Clausthal-Zellerfeld, Germany, 2020.
44. Piegl, L.; Tiller, W. *The NURBS Book*; Springer Science & Business Media: Berlin/Heidelberg, Germany, 1996.
45. Lee, S.Y.; Chwa, K.Y.; Shin, S.Y.; Wolberg, G. Image metamorphosis using snakes and free-form deformations. In Proceedings of the SIGGRAPH, Los Angeles, CA, USA, 6–11 August 1995; Volume 95, pp. 439–448.
46. Lee, S.; Wolberg, G.; Chwa, K.Y.; Shin, S.Y. Image metamorphosis with scattered feature constraints. *IEEE Trans. Vis. Comput. Graph.* **1996**, *2*, 337–354.
47. Tibshirani, R.J.; Efron, B. An introduction to the bootstrap. *Monogr. Stat. Appl. Probab.* **1993**, *57*, 1–436.
48. Efron, B.; Hastie, T. *Computer Age Statistical Inference: Algorithms, Evidence, and Data Science*; Institute of Mathematical Statistics Monographs: New York, NY, USA; Cambridge University Press: Cambridge, UK, 2016.
49. Alkhatib, H.; Neumann, I.; Kutterer, H. Uncertainty modeling of random and systematic errors by means of Monte Carlo and fuzzy techniques. *J. Appl. Geod.* **2009**, *3*, 67–79. [[CrossRef](#)]
50. Alkhatib, H.; Kargoll, B.; Paffenholz, J.A. Further results on a robust multivariate time series analysis in nonlinear models with autoregressive and t-distributed errors. In Proceedings of the International Work-Conference on Time Series Analysis, Granada, Spain, 19–21 September 2017; pp. 25–38.

Robust algorithm for automatic surface-based outlier detection in MBES point clouds

Bahareh Mohammadivojdan^a, Felix Lorenz^b, Thomas Artz^b, Robert Weiß^b, Frederic Hake^a, Yazan Alkhatib^a, Ingo Neumann^a, and Hamza Alkhatib^a

^aGeodetic Institute, Leibniz University Hannover, Hannover, Germany; ^bFederal Institute of Hydrology, Koblenz, Germany

ABSTRACT

Bathymetric multibeam echosounder systems (MBES) provide high-resolution mapping of underwater topography but are highly susceptible to errors due to harsh environmental conditions and the measurement process. Traditionally, manual post-processing is required to ensure data quality, a time-consuming, expensive, and subjective task. To address this issue, we propose a surface-based algorithm for pre-processing and cleaning MBES data that reduces manual intervention and improves consistency. A surface-based algorithm models the underwater topography as a surface instead of processing individual points. By assuming a continuous surface for underwater geometry, the algorithm easily identifies observations that deviate significantly from this model. The method combines a hierarchical B-spline surface with iterative robust estimation to automate data cleaning. Preliminary results on example datasets show a balanced outlier detection accuracy of 0.99, with manual processing time reduced from 2 days to just 30 min.

ARTICLE HISTORY

Received 17 July 2024
Accepted 18 September 2024

KEYWORDS

Outliers; MBES; robust estimator; surface model

Introduction

Digital bathymetric models (DBMs) are invaluable sources across a spectrum of applications, thanks to advancements of various methodologies, such as range-based acoustic systems like Single Beam Echo Sounder (SBES), Multibeam Echo Sounder (MBES), and Lidar methods. These technologies enable the acquisition of high-resolution maps of underwater regions, essential for sensitive applications, like navigation safety, and deformation monitoring across different epochs. However, MBES data are usually contaminated by numerous errors due to the challenging underwater conditions and the dynamic nature of MBES measurement systems.

CONTACT Bahareh Mohammadivojdan  mohammadivojdan@gih.uni-hannover.de  Geodetic Institute, Leibniz University, Hannover, Germany.

© 2024 The Author(s). Published by Informa UK Limited, trading as Taylor & Francis Group
This is an Open Access article distributed under the terms of the Creative Commons Attribution License (<http://creativecommons.org/licenses/by/4.0/>), which permits unrestricted use, distribution, and reproduction in any medium, provided the original work is properly cited. The terms on which this article has been published allow the posting of the Accepted Manuscript in a repository by the author(s) or with their consent.

These measurement errors typically originate from various sources, including the measurement platform, sensors, environmental factors, synchronization issues, and sensor calibration (Hare, Eakins, and Amante 2011). The presence of erroneous measurements reduces the likelihood of deriving a reliable DBM and results in discrepancies between the actual underwater topography and the model. To obtain a reliable model, errors should be eliminated in the initial data processing steps. This is as crucial as a suitable model selection for computing the most accurate DBM. Identifying errors in underwater data is therefore not easy. Due to the lack of information about the true geometry and the dynamic nature of the underwater environment, this task usually depends on expert knowledge and objective judgment, which is costly considering the dimension and size of the data sets. However, the International Hydrographic Organization (IHO) S-44 standard (IHO S-4444 2022) only recommends the adaptation of a well-documented automated processing tool. However, it also requires that the final results be carefully checked by a trained hydrographer, a step that, while essential, remains time consuming and costly.

Measurement errors can be categorized into three types: noise, systematic errors, and outliers. Noise primarily originates from the sensors and reflects the precision of the measured samples. By considering prior knowledge about the sensor performance, these types of errors can be statistically modeled. Systematic deviations, the second source of error, is linked to the measurement system and procedure. These errors become more prominent and detectable in fusing measurements from different measurement platforms of a common region. Some systematic errors can be mitigated by adopting different strategies such as sensor and platform calibration, using target points, or conducting repeated measurements in opposite directions. Outliers, the third type of error, are measurements that do not accurately represent the geometry of interest and usually deviate from the general behavior of the neighboring points. Outliers originate from the measurement process due to various reasons, such as multiple acoustic reflection paths, adverse weather conditions, and obstacles (Le Deunf et al. 2020).

While the potential impact of systematic errors and noise should be recognized, in this research, presence of noise is considered but the focus is on outliers and we assume that appropriate measures have been taken to minimize the other influencing factors. Our research aims to design an algorithm for an automatic and reliable data cleaning process, with the goal of efficiently reducing manual inspection and processing time. In this practical application, we evaluate the performance and efficiency of our proposed algorithm. Furthermore, we have tested our algorithm against other methods to highlight the strengths and identify potential weaknesses of our algorithm relative to established techniques.

Outlier Detection & Bathymetric Data

Outlier detection is a recognized research problem having had many studies dedicated to this topic. An outlier is defined as an observation that significantly deviates from others (Hawkins 1980). It might belong to the tails of the distribution of the main body or raise suspicion that it was generated by a different mechanism. This suggests that more than one individual distribution may exist in the data (Hawkins 1980; Davies and Gather 1993). Various techniques have been developed to address this problem. Detecting outliers can be seen as a binary classification problem, and finding a suitable approach depends on the inherent characteristics of the data, outlier type, and whether the method employs supervised or unsupervised learning (Chandola, Banerjee, and Kumar 2009). In most of these techniques, the classified outliers are eliminated, and the remaining data provide a clean base for further modeling. Another way to deal with the presence of outliers is to use approaches such as robust estimators, where outliers are not eliminated but down-weighted to minimize their impact on the final model. Bathymetric data points sampled from the underwater topography are considered as spatial data. When choosing the outlier detection method, it is important to consider that the type of learning employed is limited by the lack of known labels and the true geometry of the underwater area, making supervised learning more challenging. Therefore, the majority of bathymetric research tends towards unsupervised algorithms. However, there are a few cases where supervised learning has been used in this context (Stephens et al. 2020; Long, Zhang, and Zhao 2023).

Le Deunf et al. (2020) divides the related unsupervised outlier detection techniques into two categories: data-oriented and surface-oriented. Data-oriented techniques work directly on the data points, such as distance-based, density-based, clustering-based, and distribution-based methods (Papadimitriou et al. 2003). Distance-based approaches define an outlier as a point from which a certain portion of the neighboring data has a distance more than a specific threshold (Knorr, Ng, and Tucakov 2000; Shen et al. 2011; Arge et al. 2010). However, distance-based approaches can lead to problems with non-homogeneously distributed data. Similarly, density-based methods analyze the data distribution density (Yang et al. 2007, Sedaghat, Hersey, and McGuire 2013). In clustering-based methods, data points not assigned to any cluster are labeled as outliers (Du, Wells, and Mayer 1996; Jain, Murty, and Flynn 1999; Kammerer et al. 2001; Sotoodeh 2007). Distribution-based approaches focus on the majority and identify outliers as points that deviate from this distribution (Hawkins 1980, Barnett and Lewis 1984).

Surface-oriented approaches for outlier detection are based on modeling the underwater topography and identifying observations that deviate

significantly from this model. These methods require a mathematical model that accurately represents the topography of the study area. By selecting an appropriate model that fits the specific characteristics of the underwater region and the available data, it can be used as a reference against which observations can be compared. Establishing a reliable method for estimating the base model is crucial for the effectiveness of these techniques. The choice between using global surface or local surface functions depends on several factors, including the complexity of the underwater geometry, data characteristics such as size and distribution, and the ability of the surface model to adapt to changes in the underwater topography. Local surface approximations offer more flexibility by allowing the use of various functions adaptable to varying geometries (Lu et al. 2010; Debese, Moitié, and Seube 2012; Rezvani, Sabbagh, and Ardalan 2015). The drawback is focusing on local structures, which makes the model more vulnerable to clusters of outliers. For a global approximation of the surface, Arnold and Shaw (1993), Bjørke and Nilsen (2009) and Mohammadivojdan et al. (2021) use a coarse-to-fine strategies in building the surface. Bisquay et al. (1998) and Bottelier et al. (2005) use Kriging to interpolate the underwater geometry. One effective solution to reduce the impact of outliers is to use robust estimators and trimming techniques (Lu et al. 2010, Bottelier et al. 2005, Debese and Bisquay 1999; Debese, Moitié, and Seube 2012; Huang et al. 2020; Lorenz et al. 2021). Some of these methods are based on lower-degree local functions. They are not reproducible for other data sets and require substantial parameter tuning. Ultimately, manual inspection would be unavoidable. To summarize, data-oriented methods are highly sensitive to chosen hyperparameters and are not reproducible across different data sets. If not chosen wisely, one could risk error of Types I and Type II (overestimation or underestimation of outliers, respectively). Errors in navigation applications are critical, with serious consequences even for Type II errors, as any point could represent an obstacle that might endanger vessels.

The mentioned surface-oriented approaches model the surface either at each point locally or in a predefined neighborhood based on a polynomial function. These methods will be affected by clusters of outliers. A global surface can be effective for detecting outliers; however, they can be limited in regions with complex topography, gaps, or even low density of data. The accuracy of the base model heavily influences the detection of outliers, so ensuring a robust and accurate model estimation is crucial. The current research builds on the foundational work of Mohammadivojdan et al. (2021), who developed a regional ground movement detection methodology by analyzing and modeling Persistent Scatterer Interferometry (PSI) observations. Their approach used a hierarchical data trimming procedure to

detect outliers within datasets representing a surface. The insights and methodologies from their research provide a critical bridge to the current approach. In the previous work, Mohammadivojdan et al. (2021) focused on using a global surface model and iterative distribution trimming to eliminate outliers for complex geometries. However, in the presence of outlier clusters, particularly those connected to the main body, it may not provide the most optimal results. This limitation is due to the masking effect, which introduces a bias into the surface model, resulting in over-fitting. To model MBES data, considering the specific challenges posed by high-density, high-noise, nonhomogeneous data, we required a model that can adapt to varying topographies similar to underwater geometry.

The Multilevel B-spline surface (MBA) model by Lee, Wolberg, and Shin (1997) is a suitable solution. To detect outliers, we integrate an iterative robust estimation in the modeling process. However, due to the unpredictable nature of the data, the lack of information about the proportion of outliers, and the fact that these data have a nonhomogeneous distribution, several challenges arise. A robust estimator alone may not guarantee a perfect solution. Thus, it is necessary to remove as many corrupted observations as possible in advance. To achieve this, we propose an iterative approach where each iteration incrementally detects outliers, leading to a step-by-step improvement of the outlier detection process. In other words, we adapt the iterative trimming suggested by Mohammadivojdan et al. (2021) and combine it with a robust estimator.

Our proposed surface-based data pre-processing and cleaning algorithm performs automatically and is not sensitive to the chosen hyperparameters. This minimizes the need for manual intervention in the process. We test and evaluate the performance of our algorithm using real data (Section “Data Acquisition”). We also compare the results with a few common unsupervised methods (see Section “Results and Comparison”). Our descriptive definition of different types of outliers in MBES data is presented in Section “Outlier Types”. The detailed methodology is described in Section “Methodology”. Section “Experiment and Analysis” presents the results and describes the application of the developed methodology in an experiment setting.

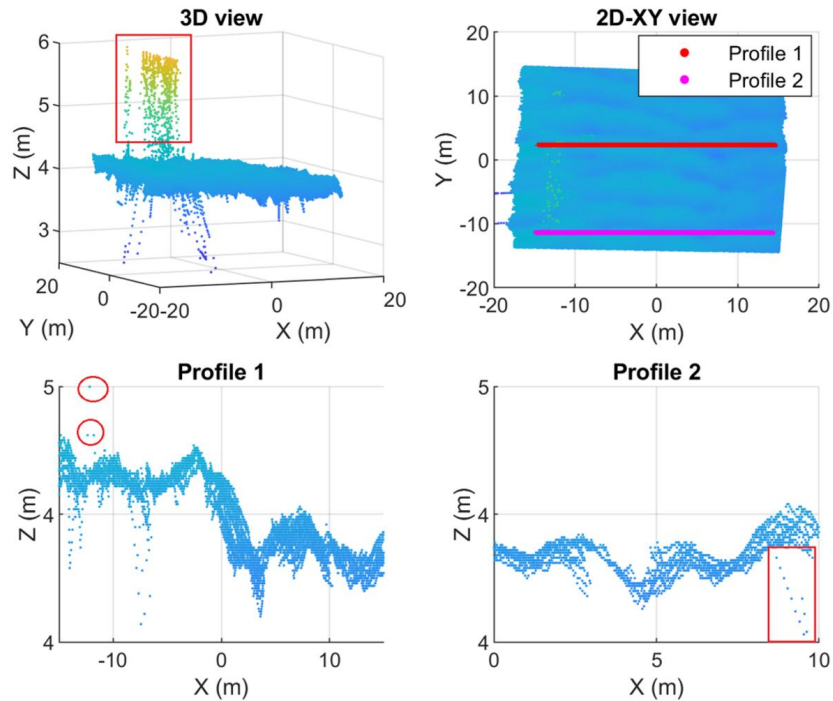
Outlier Types

Despite recent advances in MBES technology, error management and uncertainty quantification in this complex environment remain challenging. Various factors contribute to outliers in hydrographic data, and distinguishing them from real features is often difficult. Errors can originate from the platform (e.g. sensor malfunction, transducer head bubbles, multiple

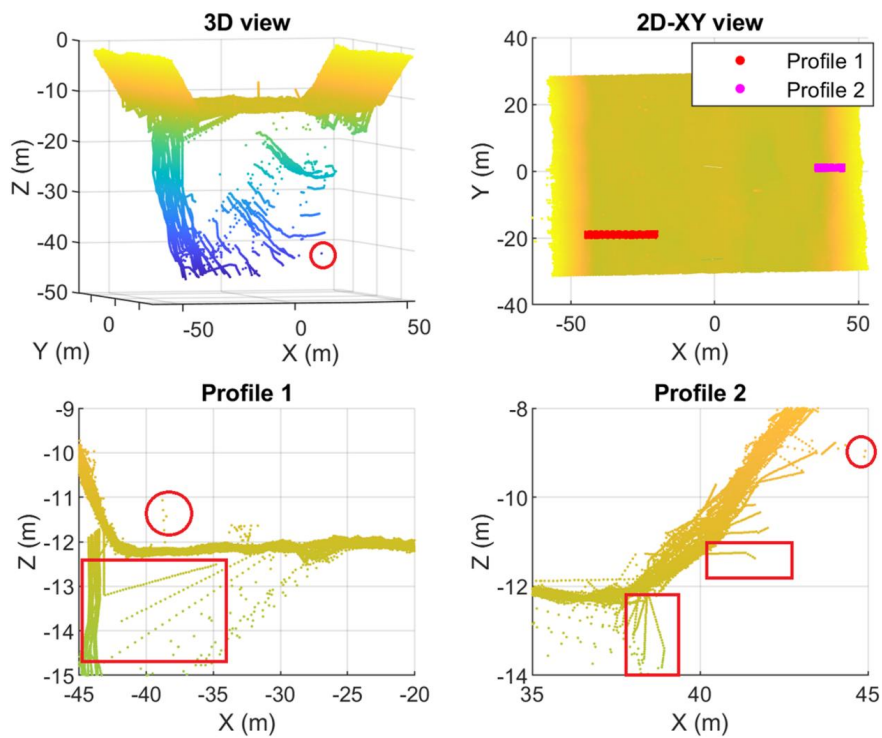
acoustics, etc.) or the environment (obstacles such as fish, algae, adverse weather conditions, etc.) (Le Deunf et al. 2020). Generally, outliers are identified as soundings that exhibit significant deviation from the smooth and continuous structure of the water bed. Based on the density and position of outliers relative to the main body of data, we can distinguish different scenarios. Le Deunf et al. (2020) and Yang et al. (2022) adopt similar methods for classifying different outlier types in MBES data. Figure 1 illustrates two example areas measured by MBES (1a, 1b). For each area, a 3D view and two profiles are presented. The locations of the profiles are shown in the ‘2D-XY view’ part of the figures. Depending on the nature of the error, we can distinguish between the following cases:

1. Isolated events: Outliers may appear as isolated occurrences that deviate significantly from the surrounding data. They can be caused by measurement errors or other factors (examples are indicated by circles in Figure 1a (profile 1) and 1b (3D view, profile 1 and profile 2)). Detecting these outliers becomes particularly challenging when they are close to the main body of data.
2. Clusters: Outliers may form distinct patterns or structures in the data, appearing as clusters, streaks, or bands. These clusters may be connected to or distant from the main body of data (examples are highlighted by rectangles in Figure 1a 3D view and 1b (profile 1 and profile 2)).

A clear mathematical definition of outliers facilitates their efficient detection. For instance, they can be defined as observations belonging to a distribution different from that of the main body of data. We consider points belonging to the main body as normal points, while any point that does not belong to it is considered an outlier. This could be any observation representing a genuine error induced by the measurement process or even reflection from an object, not part of the main body, such as a plant. However, this definition may not suffice in some cases to differentiate outliers from real features. Therefore, to ensure a reliable cleaning process, the topography of the area and the characteristics of the measurement process should always be considered. The representation of any structure in the data and the performance of the detection method are affected by the measurement density, or more precisely, the horizontal and vertical resolution of the MBES observation. As mentioned earlier, the specific shapes and characteristics of outliers may vary depending on the survey methodology, measurement system, and environmental conditions. To distinguish true features from outliers, additional information such as metadata, survey reports, and knowledge from previous surveys can also be considered. The



(a) Example area 1



(b) Example area 2

Figure 1. Demonstration of two defined outlier types: isolated events and clusters. Both example area 1 and 2 are illustrated in 3D, 2D, and 2 random profile views. Examples of isolated events and clusters are indicated by circles and rectangles, respectively.

mathematical definition of outliers used for further processing is explained in Section “Outlier definition”.

Methodology

The algorithm proposed here is formulated under the fundamental assumption that the domain of interest, the underwater terrain, can be represented as a continuous surface. Any data point that deviates substantially from this hypothesis would be considered a possible outlier. Therefore, we require a mathematical surface model. The steps to estimate surface parameters are outlined in Section “Surface parameter estimation”. To address the challenges of outliers and clusters of outliers, we propose a surface-based algorithm based on robust parameter estimation with additional steps to mitigate these concerns (Section “Iterated re-weighted parameter estimation”).

Surface Parameter Estimation

There are usually many structures in the underwater topography. These structures may not be very prominent relative to the overall dimension of the area under study, but they should be captured to understand the underwater structure and distinguish between outliers and real features. The goal of capturing underwater structures (and distinguishing real features from outliers) could also be aligned with achieving the appropriate level of confidence according to IHO’s Category Zones of Confidence (CATZOC) standards (IHO S-6767 2020). A B-spline surface is a powerful tool for modeling such structures. Considering the characteristics of the MBES data, such as high resolution, large data volume, and possible gaps, we use a 2.5-dimensional (2.5D) surface model to mitigate computational burden. In 2.5D, for a point (x_0, y_0, z_0) belonging to the surface,

$$z_0 = f(x_0, y_0). \quad (1)$$

We adapted the method of Multilevel B-spline Approximation (MBA) by Lee, Wolberg, and Shin (1997) to represent the main body and build the DBM. MBA constricts a hierarchy of 2.5 D surfaces and can efficiently handle large amounts of data.

Surface Approximation

The MBA method is based on hierarchical tensor product B-spline surfaces. Lee, Wolberg, and Shin (1997) introduced the MBA algorithm to model scattered data. The B-spline surface is defined by a control lattice $\Phi_{m,n}$ that contains $(m + 3) \times (n + 3)$ control points, where m and n define model complexity in x and y directions, respectively. If we assume $\Phi_{m,n}$ is

overlaid on the domain $\Omega = \{(x, y) | 0 \leq x < m, 0 \leq y < n\}$, all control points in $\Phi_{m,n}(\phi_{ij})$ appear on the integer intersections of Ω .

Any point on the B-spline surface $(x_0, y_0, f(x_0, y_0))$ would be a linear combination of uniform bicubic basis functions B_k, B_l and its surrounding control points ϕ .

$$f(x_0, y_0) = \sum_{k=0}^3 \sum_{l=0}^3 B_k(s)B_l(t)\phi_{(i+k)(j+l)} = w_c\phi_{ij}, \quad (2)$$

Where $i = \lfloor x_0 \rfloor - 1, j = \lfloor y_0 \rfloor - 1, s = x_0 - \lfloor x_0 \rfloor, t = y_0 - \lfloor y_0 \rfloor$. The uniform cubic basis functions $B_k(s)$ and similarly $B_l(t)$ for $0 \leq s < 1$ are defined as follows:

$$\begin{aligned} B_0(s) &= \frac{(1-s)^3}{6}, \\ B_1(s) &= \frac{(3s^3 - 6s^2 + 4)}{6}, \\ B_2(s) &= \frac{(-3s^3 + 3s^2 + 3s + 1)}{6}, \\ B_3(s) &= \frac{s^3}{6}. \end{aligned} \quad (3)$$

To approximate the surface $f(x, y)$, the unknown elements of $\Phi_{m,n}$ must be solved. This problem is formulated as a linear Gauss-Markov model (GMM) Equation (4) in which, \mathbf{z} is the observation vector and \mathbf{v} is the residual vector. \mathbf{A} and ϕ represent the full ranked design matrix and the unknown parameter vector, respectively.

$$\mathbf{z} + \mathbf{v} = \mathbf{A}\phi \quad (4)$$

The solution to the GMM can be derived by minimizing the sum of the squared residuals, or in other words, Least squares (LS). This is formulated as $\min\{\mathbf{v}^T\mathbf{v}\}$. Here, observations are assumed to be equally weighted and uncorrelated. The final estimated solution $\hat{\phi}$ can be obtained by differentiating the term $\mathbf{v}^T\mathbf{v}$ with respect to the unknown parameters ϕ . The result is according to Equation (5)

$$\hat{\phi} = (\mathbf{A}^T\mathbf{A})^{-1}\mathbf{A}^T\mathbf{z} \quad (5)$$

According to Equation (2), each control point ϕ_{ij} is influenced by points in its 4×4 neighborhood, the so-called proximity points. Let c represent the proximity points. If we only construct the design matrix for solving one control point, the design matrix would be,

$$\mathbf{A}_{ij} = \left[\begin{array}{ccc} \sum_{a=0}^3 \sum_{b=0}^3 \frac{w_{ab}^2}{w_1} & \dots & \sum_{a=0}^3 \sum_{b=0}^3 \frac{w_{ab}^2}{w_c} \end{array} \right]^T \quad (6)$$

where, $w_c = B_k(s)B_l(t)$. Similarly, for one control point ϕ_{ij} the estimation would be

$$\hat{\phi}_{ij} = \frac{\sum_c w_c^2 \phi_c}{\sum_c w_c^2}, \quad (7)$$

If the proximity data set is empty, ϕ_{ij} could not be solved. As the ϕ_{ij} will not affect the calculation of main function Equation (2), for regularization measures any value can be assigned to the control point. In such cases, a value of zero is assigned to ϕ_{ij} . However, LS does not directly estimate σ_0^2 (Benning 2011, 144). Therefore, the updated residuals $\hat{\mathbf{v}}$ and a posteriori variance factor $\hat{\sigma}_0^2$ are estimated based on the LS estimation for ϕ .

$$\hat{\mathbf{v}} = \mathbf{A}\hat{\phi} - \mathbf{z} \quad (8)$$

$$\hat{\sigma}_0^2 = \frac{\hat{\mathbf{v}}^T \hat{\mathbf{v}}}{N - M} \quad (9)$$

The difference between N (number of observations) and M (number of parameters) represents the degree of freedom where M is the sum of all control points across all levels.

Surface Hierarchy

To increase the accuracy of the estimation while ensuring the smoothness of the surface, Lee, Wolberg, and Shin (1997) suggest continuing the approximation of the surface function f for the residuals of the estimation with a denser control point lattice. By using a hierarchy of control lattices, a sequence of $f_k < sub > < /sub >$ is generated whose sum approaches the final desired surface. The approximation starts with a rough estimation and the resolution of the control lattices increases in each step. If a hierarchy of control lattices $\Phi_0, \Phi_1, \dots, \Phi_h$ is defined, for the k^{th} level of the hierarchy, the updated observations $\Delta^k \mathbf{z}$ are calculated according to Equation (10), (note that $\Delta^0 \mathbf{z} = 0$).

$$\Delta^k \mathbf{z} = \mathbf{z} - \sum_{i=0}^{k-1} f_i(x, y) = \Delta^{k-1} \mathbf{z} - f_{k-1}(x, y). \quad (10)$$

The final approximation function is defined as the sum of functions f_k from the coarsest lattice Φ_0 to the finest lattice Φ_h .

$$f(x, y) = \sum_{k=0}^h f_k(x, y) \quad (11)$$

At each level of the MBA algorithm, a fixed control lattice is introduced and only the z -direction estimation is performed. The proximity area of each control point is fixed and limited, so it can be calculated at each position where basis functions are influencing the estimation. These features make the algorithm relatively simple compared to general B-spline surface

approximation techniques (Piegl and Tiller 1997) with full 3D estimation of a surface. In MBA, parameterization is limited, and hierarchical estimation compensates for the simplifications, significantly improving the estimated surface. The initial coarse control grid forms a central region covering all data points, making it easy to assign values to areas with data gaps. The gradual refinement of the control points as we move from one level to the next significantly improves the accuracy of the approximation throughout the process. The MBA algorithm requires the user to define two key parameters: the density of the coarsest control lattice and the number of hierarchy levels. The choice of these parameters is crucial to achieving an optimal solution. If the initial grid is not sufficiently coarse, this can result in a non-smooth approximation surface where each data point has only a localized effect on the estimate. Prior knowledge on the object could help on deciding on a suitable initial grid. The user can influence the approximation process by setting stopping criteria. For example, to avoid overfitting, this criterion can be chosen based on the point density and noise level in the data.

Iterated Re-Weighted Parameter Estimation

When outliers contaminate observations, the distribution of the observations is affected. This change could severely compromise the accuracy of the approximated model parameters. The ground truth about the underlying function is unknown in our modeling process. We utilize a model to approximate the representation of the underlying function, rather than assuming it is an exact depiction. Therefore, it is important that the estimator performs efficiently and stably, and does not break down due to large deviations. Simple terms, it should remain unaffected by minor deviations from the main population; these are the features of a robust estimator according to Huber and Ronchetti (2009).

Parameter estimation in Section “Surface parameter estimation” is based on minimizing the sum of squared (LS), which is highly sensitive to outliers. One possible approach is to apply tests for outliers; however, in our case, it is not efficient due to the high percentage of outliers. Another solution could be to emphasize or de-emphasize certain observations by using weights. This can be achieved by adapting a robust Maximum likelihood estimator (M-estimator).

Outlier Definition

To select and understand an estimator and its influence function, the first step is to define our interpretation and assumptions regarding outliers. In GMM the assumption is that the measurement error of observations (and

therefore the observations) are normally distributed. In practice, observations may be contaminated with outliers, whose presence can potentially affect or nullify the hypothesis of normal distribution. One of the most commonly assumed models is that the majority of the observations belong to the main distribution $F_G(\cdot)$ and a small proportion ϵ of the observations come from the outlier distribution $F_o(\cdot)$ (Huber and Ronchetti 2009, 2). By these definitions, the distribution of the random deviations containing outliers can be realized by extending the distribution assumption to

$$F_\epsilon(e) = (1 - \epsilon)F_G(e) + \epsilon F_o(e) \quad \epsilon \leq 1, \quad (12)$$

where we consider the variable ϵ as the outlier percentage in this context.

Robust Estimator

Considering Equation (12), one may inquire about the extent to which the outlier distribution affects the final estimation. To address this issue the influence function (*IF*) obtained from Huber and Ronchetti (2009) can be employed. *IF* represents the impact of a single observation on the parameter estimation. For an estimator s :

$$IF(e_i, s(\cdot), F_\epsilon) = \lim_{\epsilon \rightarrow 0} \frac{s(F_\epsilon) - s(F_G)}{\epsilon} \quad (13)$$

As described, the LS estimator is not robust because the loss function is quadratic, resulting in a linear influence function. The effect of large residuals will increase linearly. To mitigate the impact of large residuals, a function that doesn't increase as rapidly is preferred. Here we adapted the Huber Estimator (Robust Statistics), in which the loss function of larger residuals is defined linearly, and their influence is bounded to a constant value. Huber (1964) suggests constructing the loss function by combining two different distribution families, assuming outliers from Equation (12). According to Huber and Ronchetti (2009, 75), the simplest way to construct a robust M-estimator is to combine the loss function of the normal distribution and Laplace distribution in accordance to the following function, namely Huber estimator:

$$\rho_\xi(v_i) = \begin{cases} \frac{1}{2} v_i^2 & \text{for } |v_i| < \xi \\ \xi|v_i| - \frac{1}{2}\xi^2 & \text{for } |v_i| \geq \xi \end{cases}, \quad (14)$$

The choice of the constant ξ , also called the Huber constant, depends on the outlier proportion ϵ in the observations (Huber and Ronchetti 2009, 85).

Considering Eq. (13), the influence function of ρ will be:

$$\Psi_{\xi}(v_i) = \frac{\partial \rho_{\xi}(v_i)}{\partial v_i} = \begin{cases} v_i & \text{for } |v_i| < \xi \\ \xi \cdot \text{sign}(v_i) & \text{for } |v_i| \geq \xi \end{cases}, \quad (15)$$

To estimate the unknown parameters ϕ for the linear functional model from Equation (4) and chosen loss function $\rho(\cdot)$, the approach described by Koch (1999) can be used. In this approach, a weight matrix \mathbf{P} is determined to represent the loss function. The weights of the individual observations z_i follow from the Ψ function and the relation

$$p_i = \frac{\Psi(v_i/\sigma)}{(v_i/\sigma)}, \quad (16)$$

which gives the diagonal weighting matrix P . Since the loss function is generally derived from the standardized family of distributions with $\sigma = 1$, the improvements in Equation (16) must be divided by the associated σ . In the Huber estimator, in addition to $\hat{\phi}$ and $\hat{\sigma}_0^2$ the unknown weights $\hat{p}_{i;\xi}$ will also be estimated. By adding weights to Equation (5), the $\hat{\phi}$ can then be estimated in accordance with Equation (17).

$$\hat{\phi} = (\mathbf{A}^T \mathbf{P} \mathbf{A})^{-1} \mathbf{A}^T \mathbf{P} \mathbf{z} \quad (17)$$

Due to the dependence of the residuals \hat{v} and the variance factor $\hat{\sigma}_0^2$ on the estimated parameters $\hat{\phi}$, the solution of the M-estimators is obtained iteratively.

Iterative Estimation of Parameters

The iterative process allows convergence to an optimal solution. This process is referred to as Iterative Reweighted Least Squares (IRLS), which was first introduced by Lawson (1961) with a focus on weighted l_p -norm solutions. This basic concept has undergone several iterations in various fields, with varying degrees of success (Björck 1996, Burrus and Barreto 1992; Burrus, Barreto, and Selesnick 1994; Vargas and Burrus 2012). Cline (1972) proved that this algorithm has, in principle, a linear convergence rate.

The algorithm starts with unity weighting $P = I$, solves for the initial parameters $\hat{\phi}$ with Equation (17). By calculating the updated residuals (Equation (8)) new weights $\hat{p}_{i;\xi}$ and variance factor $\hat{\sigma}_0^2$ can be calculated. This new weight matrix is then used to estimate the parameters $\hat{\phi}$ in the next iteration. It should be noted that combining the normal and Laplace distributions will not give a realistic estimation of $\hat{\sigma}_0^2$ using Equation (9). Huber and Ronchetti (2009) provides detailed information on how to calculate robust variance in such cases. The stopping criterion here determines when the iterative process of refining the parameter estimates can be

terminated. As the stop criterion we consider the algorithm stops when the change in estimated residuals between successive iterations falls below a predefined threshold Equation (18)

$$\left| \sigma_{\hat{v}}^{(c+1)} - \sigma_{\hat{v}}^{(c)} \right| < \theta \quad (18)$$

where $\sigma_{\hat{v}}^{(c+1)}$ is the standard deviation of the residuals in iteration $(c + 1)$ and θ is a small positive value (e.g., 10^{-6}) representing the tolerance level for convergence and k refers to the iteration number in the IRLS algorithm.

Trimming

After determining the optimal weights and parameters, outliers are identified as those observations with deviations exceeding a pre-defined threshold in the distribution of residuals/errors, allowing them to be trimmed from the dataset. However, some limitations do not guarantee a robust estimation; the methods described in the literature and adapted for this study are designed to work well with small deviations from a given model (Rousseeuw 1987, Massey 1951). This entails two major constraints: first, the assumption of a predefined model, and second, a defined sense of what constitutes a ‘small’ deviation. If the presumed model is not accurate and/or the level of contamination with outliers is significant, this would lead to a phenomenon called masking, where multiple outliers exist, but their presence is masked because they are part of a cluster making them difficult to detect.

In this application, the actual model of the data and the precise level of contamination are unknown. To mitigate these effects and increase the likelihood of detecting masked outliers, the estimation of surface parameters using IRLS is carried out iteratively. In each iteration, the algorithm examines the error distribution. Based on the assumed contamination level, a confidence interval (CI) is constructed and the probability density function (PDF) of the error distribution is trimmed. The observations that fall within the CI go through another iteration of IRLS. In this iterative process, the error distributions will converge and the algorithm stops. The convergence test involves checking for equality in the PDF of errors among subsequent iterations. This is achieved by utilizing the Kolmogorov-Smirnov test. The Kolmogorov-Smirnov statistic calculates the maximum absolute difference between two cumulative distribution functions (Massey 1951). Figure 2 illustrates the overall algorithm of the mentioned steps. The proposed algorithm consists of two main blocks: IRLS of surface parameters and iterative trimming. From this point forward, this algorithm is referred to as Iterative Estimation of Surface Parameters (IESP).

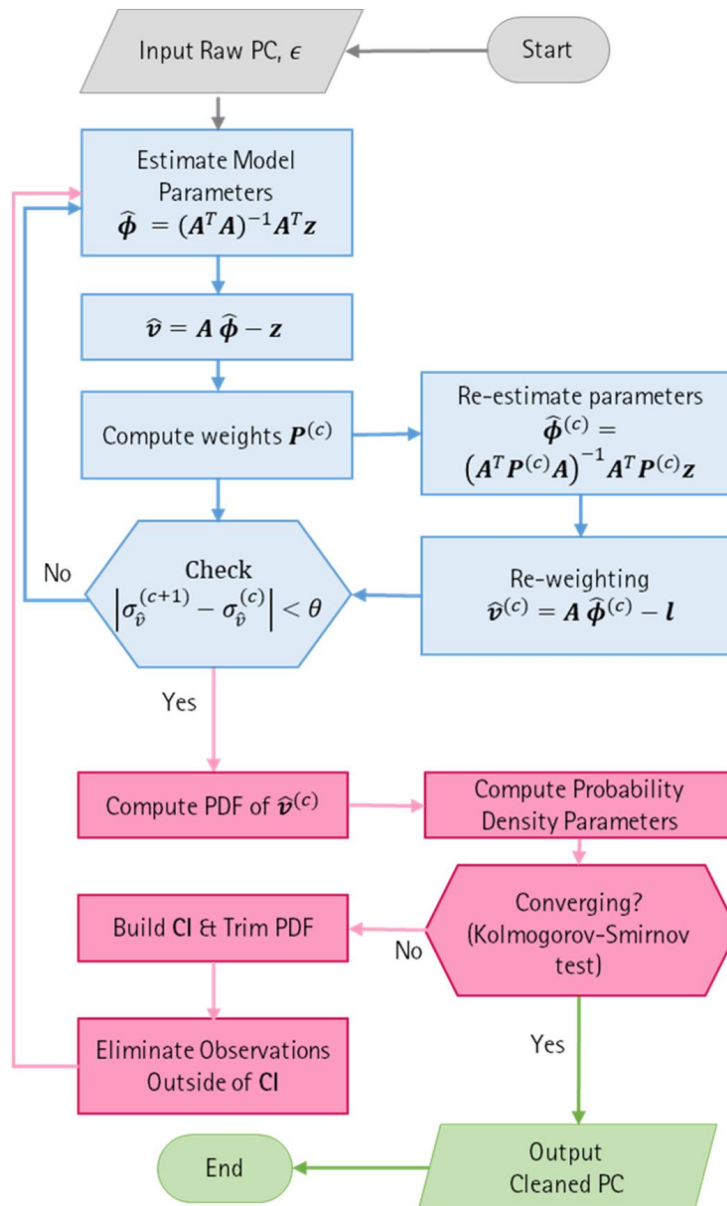


Figure 2. Flowchart of the proposed algorithm for outlier detection; iterative estimation of surface parameters (IESP).

Experiment and Analysis

In an experiment, the performance of IESP is evaluated and compared with other methods. The study area in the experiment is the Kiel Canal in Germany. Details of the data acquisition process and analysis results are given in Sections “Data Acquisition” and “Implementing IESP” respectively.

Data Acquisition

The Kiel Canal is a man-made waterway. In the analyzed area, a 100 m segment, the canal comprises both flat parts and areas structured by small

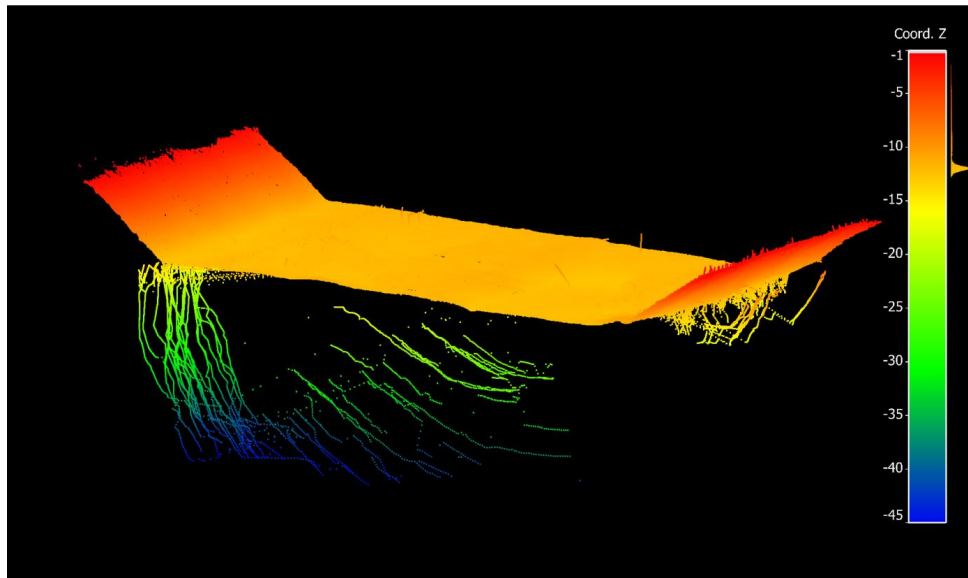


Figure 3. Visualization of 100 m segment of raw soundings, representing the underwater topography of the Kiel Canal. All points are color-coded according to depth values.

sediment dunes. Typically, the riverbed consists of rock, silt, and gravel. The canal's boundaries include stone banks under bridges (recognizable by the canal rejuvenation in the test data) and sand banks, where the outer areas are enclosed by vertical sheet piling. The water depth ranges up to 11 m around the center of the canal in the test area.

The German Federal Waterways and Shipping Administration (WSV) conducted the measurement in 2019 (Elbe-North Sea (Tönning) Waterways and Shipping Office). To capture the area a dual-head system, two Kongsberg Maritime multibeam echosounders EM2040C were used. An integrated navigation system (INS) consisting of a Sea-path 300+, and a motion reference unit (MRU 5+) was employed to track the vessels' motion, with positioning done in precise differential global navigation satellite system (PDGNSS) mode. The multibeam echosounders operated in equidistant mode, with each ping resulting in 256 beams forming angularly equidistant bottom points. In that measurement, visualized in Figure 3, a swath has a typical point spacing of 0.4 m along the track and 0.06 m in across the track. Due to overlapping measurement swaths, a point density of around 45 points per square meter can be achieved. Besides measurement noise from all used sensors, outliers also occur in the form of measurement errors. Two main types of measurement errors were observed: first, in the middle section a linear stripe-like chain of points starting from the ground and pointing upwards (which can be tilted), and second, a ping-wise deflection below the real canal bed, mainly present on the sides. These measurement errors are dense in space and can be near valid points, making it challenging to distinguish between valid points and outliers.

Outliers even occur in topographical structured areas, amplifying the difficulty of outlier detection.

On a small scale, systematic errors on the outer areas of each measurement swath are visible, especially where neighboring swathes overlap. The overall quality of the measurement is good, with no significant systematic errors due to the sensor calibration. Large areas without significant systematic errors exist, and the measurement noise is within a typical range. However, obvious clusters of errors as depicted in [Figure 1b](#) being an issue to various echosounder manufacturers occur at a few scattered locations and cannot be explained. The selected data set provides an ideal experiment due to its diverse underwater environment geometries and a variety of outlier types, including isolated events and clusters, either due to measurement failure (e.g. false pings) or contextual errors. Morphologically, the area encompasses regions with moderate to abrupt changes in slope. This presents a challenge in modeling and indicates that many measurements with unfavorable beam angles had to be included to cover the entire area. This diversity underscores the complexity of applying a single methodology for outlier detection without risking over-fitting or excluding valid observations.

Implementing IESP

First, we focused on the analysis of a small sample section of the point cloud data set, with particular attention to error distribution and model fitting. For this section, the error distribution over different iterations are visualized ([Figure 4](#)). In the IESP algorithm, two hyperparameters need to be considered: the complexity of the surface model and the percentage of outliers (ϵ). For hydrographic data, which often lack sufficient prior information on these points, model complexity can be informed by existing DBMs or determined based on the density of observations and the noise level within the data. This information helps to avoid overfitting. The MBA function approximates a smooth global surface, and its hierarchical characteristics also allow for modeling small variations of the surface. Due to these characteristics, the IESP algorithm is robust to variations in (ϵ). Aside from the main assumption of small contamination levels, slight changes in (ϵ) should not affect the outlier detection process significantly. If the chosen (ϵ) is small, it will increase the number of iterations and computation time. However, a higher (ϵ) may lead to overfitting the noise. In this case, we assume a contamination level of 3% with outliers. This means outlier trimming is guided by the 97% CIs of the PDF at each iteration, where the PDF of the empirical distribution of the errors is approximated. Assuming a normal distribution of errors, the squared errors are expected

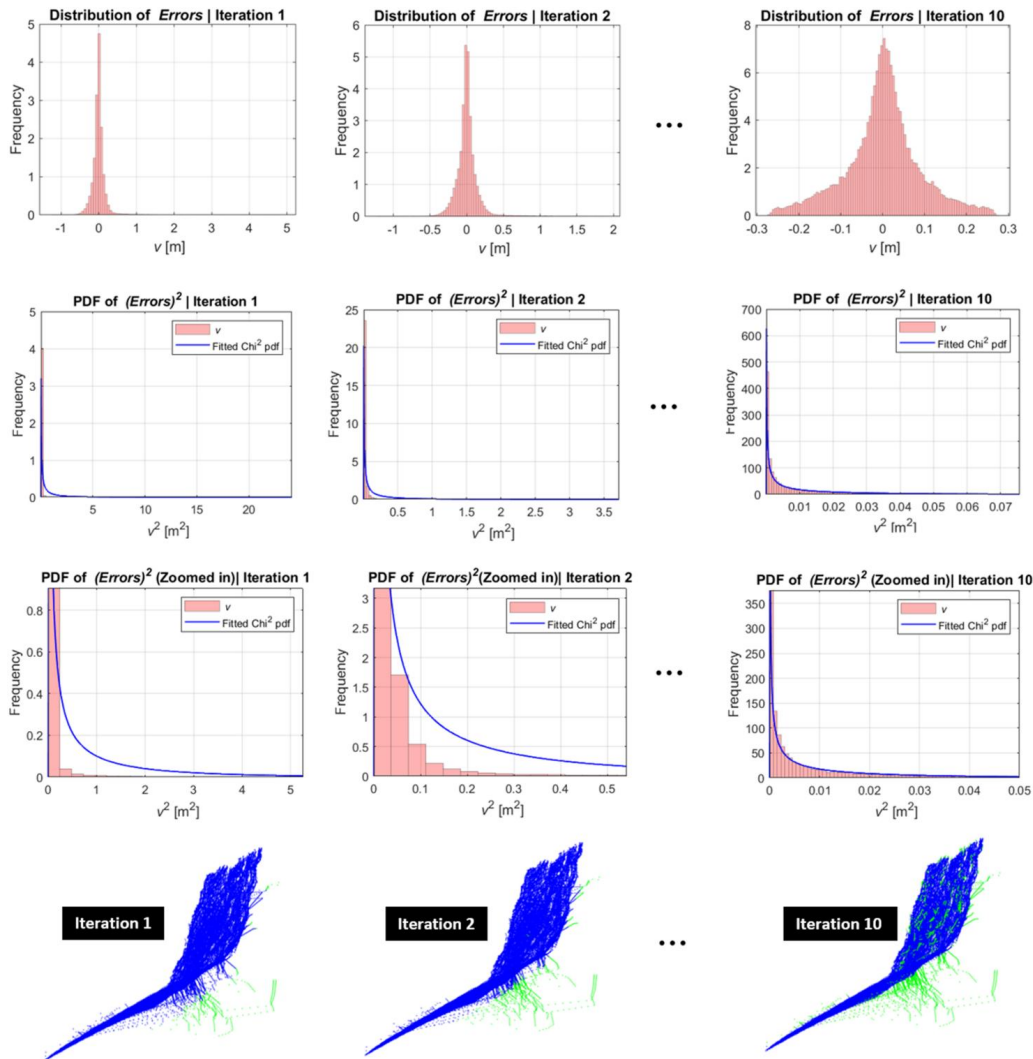


Figure 4. Details of different iterations on a section of the Kiel canal data. First row shows the histogram of residuals in each iteration. Second row shows histogram of squared residuals along with the fitted PDF. Third row illustrates zoomed-in view of the fitted PDF. Fourth row shows 3D visualization of the points (green points illustrate the detected outliers in each step).

to follow a χ^2 -distribution. Parameters such as degrees of freedom (dof), location, and scale for this distribution are determined using Scipy's statistics modules, a package of open-source Python libraries (Virtanen et al. 2020). The iterative process of the IESP algorithm is designed to stop when the parameters of the χ^2 -distributions converge from one iteration to the next, ensuring stability and accuracy in the model's performance. A critical aspect of our methodology is addressing the challenge posed by significantly large errors. These large errors can adversely affect the fitting of a proper PDF to the residuals, thereby compromising the accuracy of the confidence intervals. To circumvent this problem, we take an initial data preprocessing step, which can be accomplished using simple algorithms such as RANSAC (Fischler and Bolles 1981) to identify and flag these

extreme points. In our case, we set a substantial deviation of 5 to 10 times the standard deviation of the overall data, beyond which points are immediately classified as outliers. This large value makes the numerical computations easier while being consistent with our assumption of 97% CI, ensuring that eliminated points do not belong within the chosen CI. This step significantly contributes to a more efficient and smoother iterative process, ensuring the robustness and reliability of our model fitting and subsequent analysis. These steps are illustrated in [Figure 4](#) for the sample data sets. The IESP detected outliers in 10 iterations. The first row shows the distribution of the residuals from iteration 1 to 10. The second row depicts the distribution of the squared values of the residuals along with the fitted χ^2 -PDF. In the distributions, few large residuals exist. To better visually assess the fit, the third row illustrates a zoomed-in version of the second row. In the next step, the 97% CI is built based on the parameters of the PDF. Those points that do not belong to the defined CI are trimmed out as outliers. The detected outliers are depicted as green in the fourth row of [Figure 4](#). In each iteration, the number of detected outliers will increase.

The example in [Figure 4](#) illustrates the functionality of the proposed algorithm, although it has some limitations under certain conditions. In particular, in areas with sharp slopes, low point density, and high contamination, the model occasionally fails to detect all outliers or detects too many, resulting in data gaps. The underlying problem stems from the chosen surface model, MBA, which is essentially a 2.5D function rather than a full 3D model. This 2.5D approach was chosen for its efficiency in modeling high density data; however, it introduces limitations in the accurate calculation of optimal weights in the IRLS algorithm. Specifically, weight calculations are based on residuals or error values in the z-direction, which can lead to inaccuracies, especially in sloped regions. A more effective measure would be to use the shortest distance between the surface and the observations. Our observations suggest that basing the weights on the shortest distance yields better results. A visual comparison of the performance of different versions of the IESP algorithm is shown in [Figure 5](#). This figure shows the results when the IESP algorithm uses two different methods for calculating deviations: IESP.v1, which uses residuals, and IESP.v2, which uses the shortest distances. This color-coded representation effectively illustrates how each version operates under different outlier detection criteria and their impact on outlier identification. In this comparison, blue dots represent clean data points that both versions jointly identified as not outliers, indicating agreement on these classifications. Red points are exclusively identified as outliers by IESP.v1, highlighting that the residual-based method may be sensitive to gaps and slopes. Green points are exclusively identified as outliers by IESP.v2, indicating that the use of the shortest

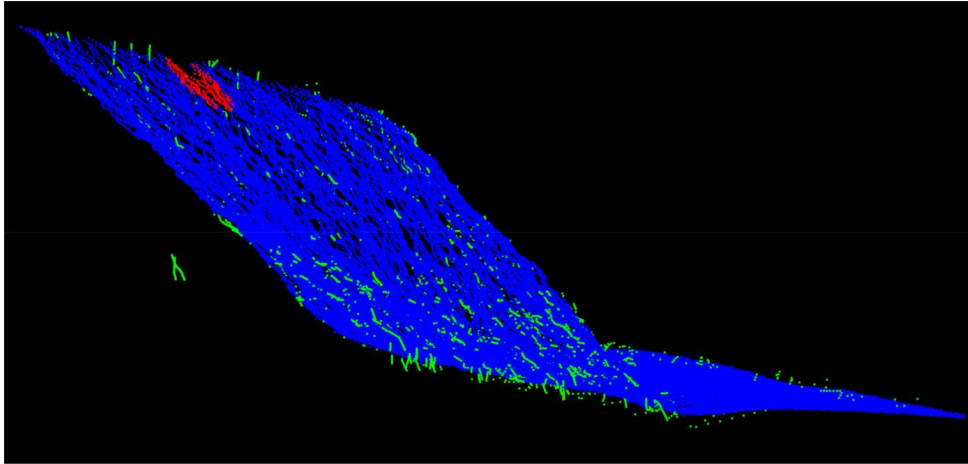


Figure 5. Example of a comparison between detected outliers by IESP.v1 and IESP.v2; blue points are commonly detected clean points. Red present those points that are only detected as an outlier by IESP.v1. Green points show detected outliers only by IESP.v2.

distance increases the robustness of the algorithms given the nature of the data. This version can effectively detect small artifacts near the surface and directional changes in the geometry. The new weights increase the robustness of the algorithm and reduce the sensitivity to parameters. Our weight calculations are based on the shortest distance.

Results and Comparison

To evaluate the performance of the proposed algorithm, a significant challenge is the knowledge gap regarding the true underwater geometry. Traditionally, bathymetric data sets are manually labeled by hydrographers. These labels are not flawless and rely on human judgment, especially when reflections from obstacles or minor surface variations occur. However, manual labels serve as a working ground truth in our analysis. To evaluate the effectiveness of our method, we compared the results of IESP to three other methods. One approach developed at the Federal Institute of Hydrology (BfG) is an applied strategy used in practice for instance in use by organizations such as WSV, which we refer to as Method 1.

In addition, two density-based clustering algorithms, namely Local Outlier Factor (LOF) and Density-Based Spatial Clustering of Applications with Noise (DBSCAN), are adapted. The cleaning approach by BfG combines analytical and manual labeling processes. The analytical part, applied in the first step, as described in Lorenz et al. (2021), uses carefully chosen parameters to eliminate the vast majority of outliers distant from the riverbed. An important aspect of this step is ensuring that no measurement point representing the riverbed is considered an outlier. In the second step, the remaining outliers are labeled by hand. Points labeled as outliers in the

first step that could be part of the riverbed or structures on it, such as small stones, are recovered (i.e., labeled as valid points). LOF, proposed by Breunig et al. (2000), identifies outliers based on the local density of a point in comparison to the local density of its neighboring points. DBSCAN (Ester et al. 1996) builds up clusters around each point based on a specified radius and a minimum number of neighbors. Any point that is at the end left without a cluster, would be considered as outlier.

In adapting each of these approaches to this particular data set, the selection of appropriate hyperparameters is a critical step. Specifically, for LOF, key hyperparameters include the number of neighbors and the degree of contamination. A major challenge is the management of outlier clusters. With too few neighbors, these clusters may be misidentified as normal data points. Conversely, a large neighborhood parameter can cause minor data deviations to be misidentified as outliers. This problem arises from variations in parameter levels. For our study, the LOF was configured with a minimum neighborhood size of approximately 800 points and a contamination level of 2%. This configuration helps maintain the structural integrity of the data by preventing holes and preserving homogeneity that could be compromised with a smaller neighborhood size. In the case of DBSCAN, choosing the right parameters is just as important, but the method offers more flexibility. After extensive empirical testing, we selected a radius of 0.3 and a minimum core point number of four for the DBSCAN algorithm. For our algorithm, a contamination level of 3% was determined to be optimal based on systematic experimentation. It is important to note that, although a higher contamination level increases noise detection, it does not compromise the integrity of the surface data.

For detailed visualization and analysis, these results are focused on the middle section of the Kiel Canal. This specific selection allows us to demonstrate the analytical results in a clear, structured manner. Results are presented as point clouds in Figures 6 through 10, where green points represent detected outliers and blue points represent clean data. These figures also include ground truth derived from manual editing, recognizing that even this ground truth is subjective. In the 2D (XY) plane view of Figure 6, it is noticeable that LOF tends to misidentify edges as outliers, a phenomenon that is also slightly evident in Method 1's results, despite hyperparameter optimization. The 3D view in Figure 7 shows that larger outlier clusters are primarily detected by IESP,

Method 1, and DBSCAN, but LOF struggles with such clusters due to its sensitivity to hyperparameter choices.

A detailed analysis of Figure 8, specifically in the x-direction profile views (perpendicular to ship movement) and focusing on the transition from the flat to the sloped parts of the riverbed, reveals inconsistencies that

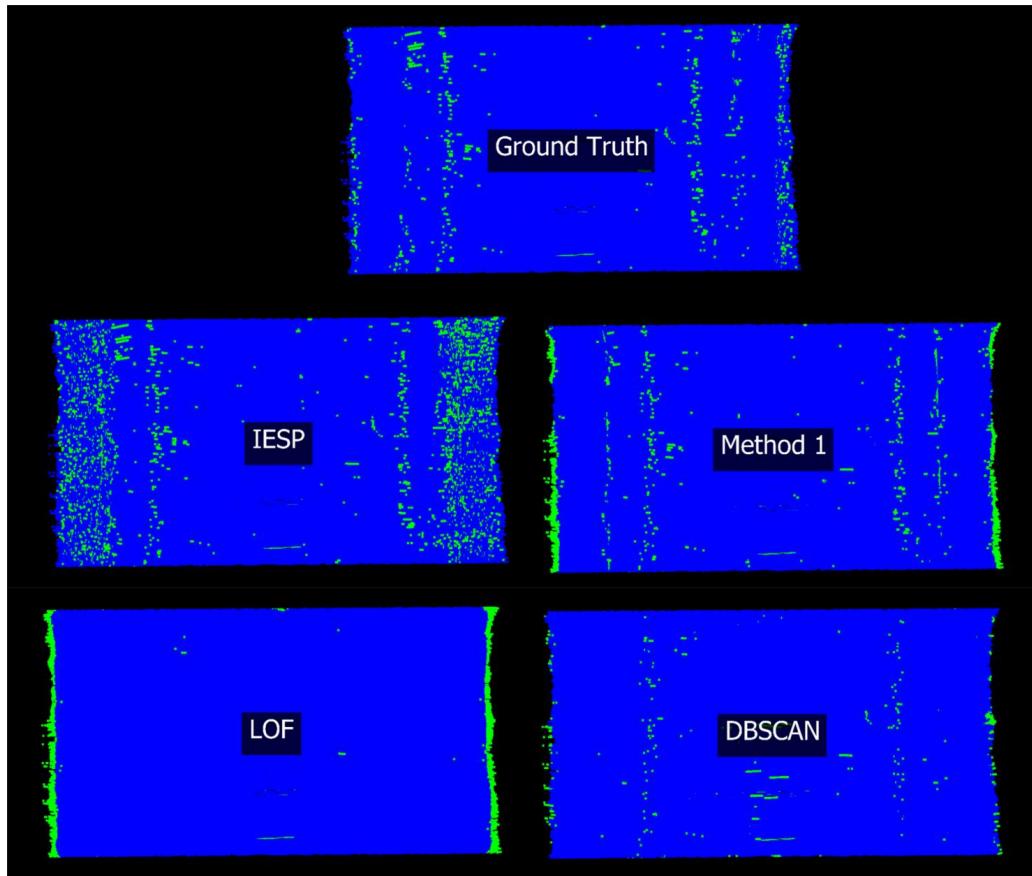


Figure 6. 2D (XY) plane view of the results. Green points represent detected outliers and blue points represent clean data.

are challenging for clustering algorithms such as LOF and DBSCAN to detect. The reason is the nonhomogeneous distribution of the data. The measurement setup results in high sampling rate in the x-direction and low density in the y-direction (along the movement). These outliers are also visible in [Figure 9](#), where Method 1's methodology fails to detect near-surface defects, unlike IESP, which effectively detects subtle surface discrepancies. In addition, [Figure 10](#), shows a cross-profile of multibeam data in the y-direction (perpendicular to ship movement), highlighting the challenge of detecting small to large clusters of outliers. IESP shows proficiency in identifying these inconsistencies. Similarly, Method 1's approach struggles with the outliers closest to the surface. For DBSCAN and LOF, very close clusters to the surface raise similar problems as mentioned before.

To quantitatively compare performance, we use a confusion or error matrix consisting of true positives (TP), true negatives (TN), false positives (FP), and false negatives (FN), where 'positive' indicates an outlier. Calculated performance metrics include precision, recall, accuracy, F1 score, balanced accuracy, and Matthews correlation coefficient (MCC). These metrics are calculated in accordance with [Table 1](#).

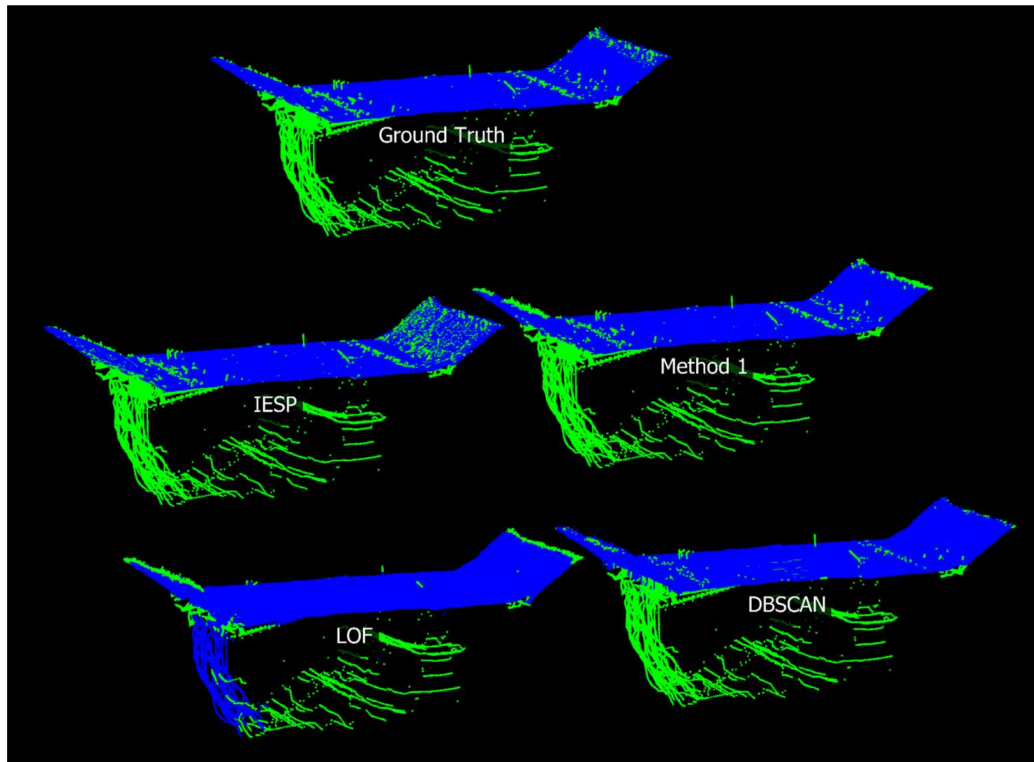


Figure 7. 3D view of the results. Green points represent detected outliers and blue points represent clean data.

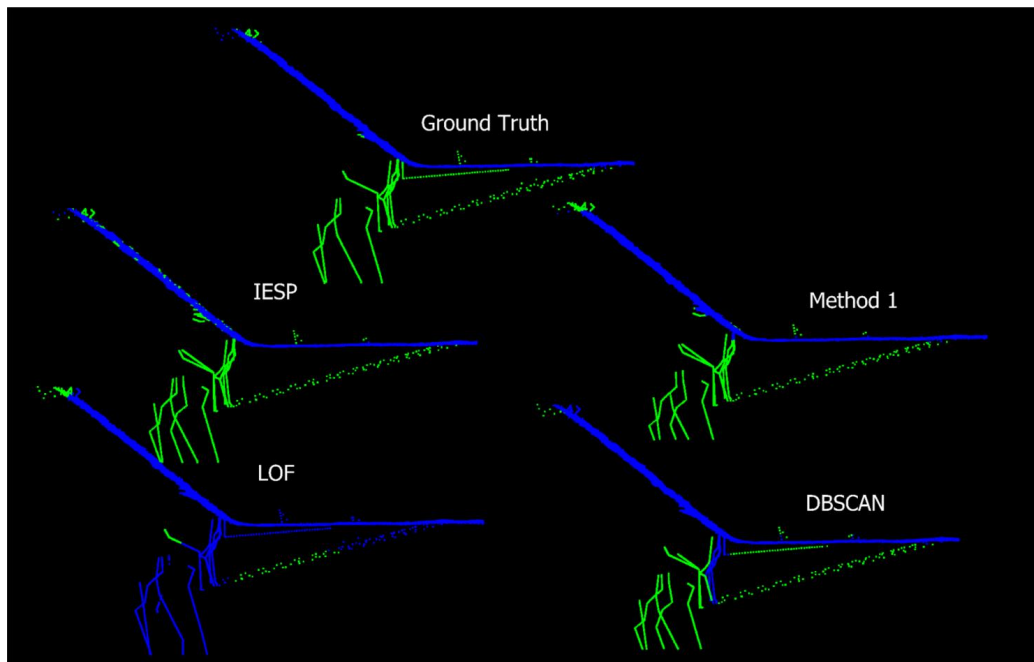


Figure 8. Zoomed area, profiled views in the x-direction (perpendicular to ship movement). Green points represent detected outliers and blue points represent clean data.

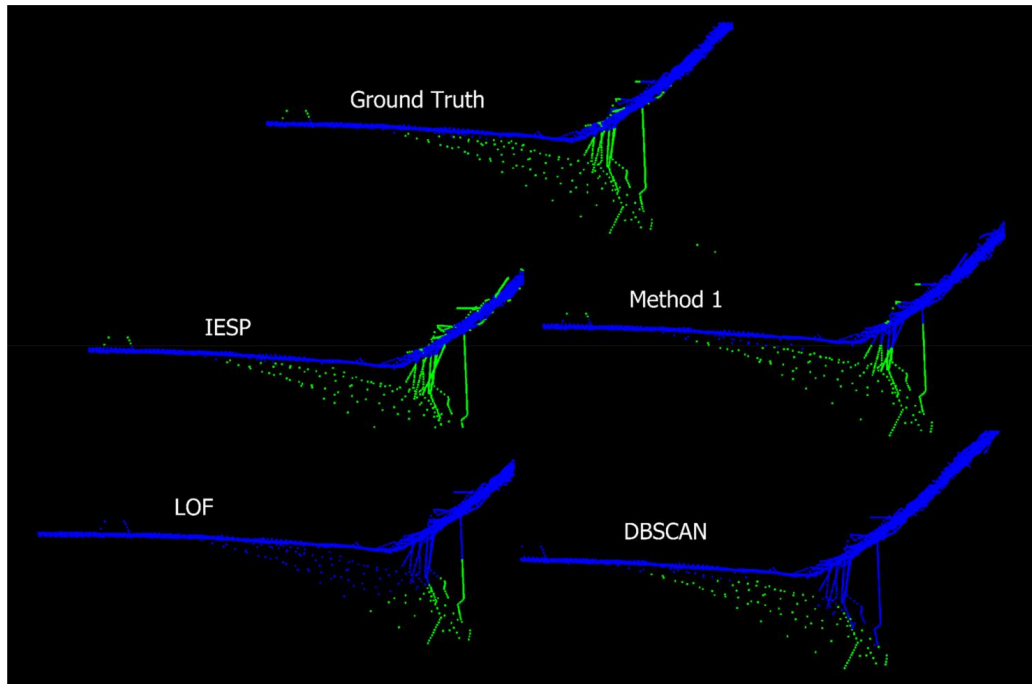


Figure 9. Zoomed area, profiled views in the x-direction (ship movement). Green points represent detected outliers and blue points represent clean data.

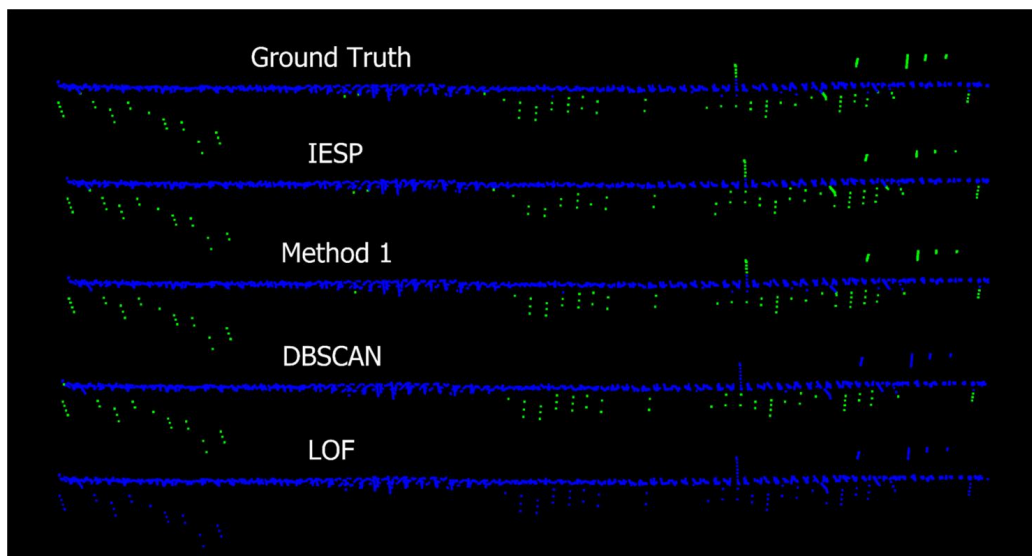


Figure 10. A cross-profile of point clouds in the y-direction (ship movement). Green points represent detected outliers and blue points represent clean data.

Table 2 contains the analytical results for the sample data. When evaluating the performance of outlier detection methods, we must consider several aspects to ensure reliability. Critical to our evaluation is minimizing the miss rate, which reflects the ability to eliminate as many outliers as possible. In this context, Type II errors are particularly detrimental because

Table 1. Performance metrics based on confusion matrix elements; true positives (TP), true negatives (TN), false positives (FP), and false negatives (FN).

Performance Metric	Formula
Precision	$\frac{TP}{TP+FP}$
Accuracy	$\frac{TP+TN}{TP+FN+FP+TN}$
Recall	$\frac{TP}{TP+FN}$
True Positive Rate (TPR)	$\frac{TP}{TP+FN}$
True Negative Rate (TNR)	$\frac{TN}{FP+TN}$
F1-Score	$\frac{2TP}{2TP + FP+FN}$
Balanced accuracy	$\frac{TPR+TNR}{2}$
MCC	$\frac{TP \times TN - FP \times FN}{\sqrt{(TP+FP)(TP+FN)(TN+FP)(TN+FN)}}$

Table 2. Results of analysis of outlier detection algorithms on the Kiel Canal data, calculated based on Table 1.

Metric	Method 1	IESP	LOF	DBSCAN
TN	445502	435636	444634	447233
FN	4332	53	19994	9181
FP	2347	12213	3215	616
TP	21930	26209	6268	17081
Precision	0.9	0.68	0.62	0.97
Recall/TPR	0.84	1	0.24	0.65
Accuracy	0.99	0.97	0.95	0.98
F1-score	0.87	0.81	0.35	0.78
Balanced Accuracy	0.92	0.99	0.62	0.83
MCC	0.86	0.81	0.38	0.78

they represent undetected outliers. Also, very important is maintaining a low drop-out rate to preserve the point density of the data set. Additionally, the efficiency of an algorithm is assessed by its level of automation and its ability to minimize the necessity for manual, visual inspection. This evaluation extends beyond computational speed to include the intelligent design of the algorithm for autonomous task performance, thereby reducing analysis time and accelerating the detection process. Key criteria—such as miss rate, false positive rate, and automation efficiency—are crucial in determining the effectiveness of an outlier detection algorithm.

The evaluation of IESP in comparison to others has shown promising results. In particular, IESP has the lowest FN, indicating a minimal occurrence of undetected outliers, while LOF has the highest FN rate. Correspondingly, IESP achieves the highest TP. These conclusions are particularly reflected in the recall metric, with our algorithm achieving a perfect recall of 1, meaning that it successfully identified all true outliers. LOF's recall is 0.24, highlighting its relatively poor performance in detecting true outliers. The high recall of IESP is further validated by Method 1's recall of 0.84.

The evaluation of IESP in comparison to others has shown promising results. In particular, IESP has the lowest FN, indicating a minimal occurrence of undetected outliers, while LOF has the highest FN rate. Correspondingly, IESP achieves the highest TP. These conclusions are particularly reflected in the recall metric, with our algorithm achieving a perfect recall of 1, meaning that it successfully identified all true outliers. LOF's recall is 0.24, highlighting its relatively poor performance in detecting true outliers. The high recall of IESP is further validated by Method 1's recall of 0.84. These results support the earlier discussions and confirm that IESP not only effectively identifies the vast majority of outliers, but also maintains a higher recall, or less FNs. IESP's precision is 0.68, signifying a higher detection rate of outliers compared to true labels, and a recall of 1, indicating almost all true outliers are identified. DBSCAN and BfG show high precision, but LOF falls short, failing to detect many outliers and mislabeling non-outliers. The higher false positive (FP) rate in IESP may indeed be influenced by the choice of hyperparameters, particularly the assumed level of data contamination due to the absence of precise contamination information. Despite this, IESP remains robust under higher contamination assumptions, as this primarily leads to more data being cleaned and the surface smoothed, without compromising the integrity of the dataset. While some FPs may not represent true outliers, distinguishing between them and valid data points can be difficult, even for a trained observer. Additionally, manual cleaning is not only time-consuming but often fails to detect all outliers, further highlighting the limitations of human intervention. For binary classification one good measure is F1-score, higher values indicated smaller values in both FP and FN. However, given the imbalanced nature of the dataset—where only about 6% are labeled as outliers—it is crucial to focus on the metrics that accurately reflect this disproportion. For instance, MCC provides a balanced measure to evaluate the quality of the classification even if the classes are imbalanced (Matthews 1975). MCC is a correlation coefficient ranging between -1 and $+1$, and a coefficient of $+1$ represents a perfect prediction. Method 1 stands out with a balanced accuracy of 0.92 and a high MCC, suggesting a strong correlation between predictions and ground truth. In contrast, Method 1, while precise, struggles with a higher rate of FP and a significant number of FN, critical in contexts where missing outliers is a major concern.

The algorithms discussed in this article are implemented in MATLAB and Python and run on a single-core PC with a 3.60 GHz CPU and 64 GB of RAM. The implementations of the LOF and DBSCAN algorithms are derived from the open-source libraries provided by Scikit-learn (Pedregosa et al. 2011). We observed a significant variation in the processing times of

Table 3. Comparative performance of the four outlier detection approaches: This table presents the results of the comparative performance of the four outlier detection approaches-IESP, Method 1, DBSCAN, and LOF-on the example dataset. The comparison includes key characteristics such as algorithm type, degree of automation, computational speed, performance results, strengths, and limitations.

Approach	Algorithm Type	Degree of Automation	Computational Speed	Performance Results	Description
IESP	Surface-based	High	Moderate	High	*Adaptable to non-homogeneous distribution *Handles noise well *Computationally intensive
Method 1	Distribution-based Manual labeling	Low	Low	High	*Requires manual labeling *Due to manual nature produces subjective results *Reliable results can be achieved by an experienced operator
DBSCAN	Density-based	Moderate	High	Moderate	*Extremely time consuming *Handles noise well *Requires significant Parameter tuning *Can struggle with outlier clusters
LOF	Density-based	Moderate	High	Low	*Sensitive to non-homogeneous distribution *Requires significant Parameter tuning *Captures local density variations *Struggles with outlier clusters *Sensitive to non-homogeneous distribution

the different algorithms tested. DBSCAN was the fastest, taking about 10 s, while LOF took about 3 min. The IESP took about 30 min and the processing time of Method 1 was extended to 1-2 days, influenced by manual processing interventions. It is important to emphasize that computation time does not directly reflect the overall quality or effectiveness of the algorithms' performance. While IESP's current processing time of 30 min is effective for offline analysis, it may pose a challenge for real-time shipboard processing. The present implementation does not yet take advantage of multi-core processing or GPU acceleration, both of which could significantly reduce runtime and enhance the algorithm's suitability for real-time applications in the future.

The comparative performance of the four outlier detection approaches is summarized in Table 3. This table presents the results of the comparative performance of the four outlier detection approaches-IESP, Method 1, DBSCAN, and LOF on the example dataset. The comparison includes key characteristics such as algorithm type, degree of automation, computational speed, performance results, strengths, and limitations.

Conclusion

In this article, we present a novel outlier detection algorithm based on robust statistical estimators, designed to handle challenging data

characteristics, such as outliers and nonhomogeneous distribution. Our algorithm operates under the assumption that a sampled point cloud from an underwater environment approximates a continuous surface. Through an iterative process of robust estimation, we compute surface parameters that inform our detection mechanism. Benchmarking against real-world data demonstrates that IESP outperforms established methods such as Method 1, LOF, and DBSCAN. The effectiveness of our algorithm is evaluated using several metrics, including miss rate, failure rate, and automation efficiency. The efficiency of applying MBES data extends beyond computational speed, encompassing the degree of the algorithm's automation and its ability to minimize manual, visual inspection. This autonomous operation significantly reduces analysis time and accelerates the outlier detection process.

Despite its slower operating speed compared to other methods - a facet that will require future improvements - our algorithm's design necessitates minimal hyperparameter tuning, primarily focusing on the contamination level. This streamlined approach contrasts sharply with the labor-intensive process typically employed, highlighting our algorithm's advantage in automation and reduced reliance on manual intervention. A key challenge remains the limited availability of accurate ground truth labels. Even meticulously hand-edited labels are subject to subjective errors, complicating the validation process. Future steps include testing the algorithm on additional data sets to further validate its robustness and reliability. The primary aim of our research was to develop a method to eliminate outliers from echosounder measurements, thereby reducing manual tasks in hydrographic data processing. Transferring the research procedures to the practical work of the WSV will be a future task of BfG, aiming to improve efficiencies and deliver products to users with higher frequencies.

This algorithm and methodology can be applied to any point cloud data that can be represented as a surface, including data from sidescan sonar, single-beam sonar, and LiDAR point clouds. While the core principles remain consistent, variations in measurement processes—such as resolution, noise, and sampling density—may require tuning of the hyperparameters to ensure optimal performance. These adjustments will help maintain the robustness of the methodology across different data acquisition technologies.

Acknowledgements

We would like to express our gratitude to the German Federal Waterways and Shipping Agency Elbe-North Sea (Tönning) for providing the survey data.

Disclosure statement

No potential conflict of interest was reported by the author(s).

Funding

This work was supported by the Federal Ministry for Digital and Transport.

Data Availability Statement

The authors are not allowed to publish the data sets.

References

- Arge, Lars, Kasper Green Larsen, Thomas Mølhave, and Freek van Walderveen. 2010. "Cleaning Massive Sonar Point Clouds." *Proceedings of the 18th SIGSPATIAL International Conference on Advances in Geographic Information Systems*, ACM-GIS, San Jose California, ACM, 152–161.
- Arnold, James, and Scott Shaw. 1993. "A Surface Weaving Approach to Multibeam Depth Estimation." *Proceedings of OCEANS'93*, pp II–95. IEEE.
- Barnett, Vic, and Toby Lewis. 1984. *Outliers in Statistical Data*. John Wiley & Sons. ISBN: 0471905070.
- Benning, W. 2011. *Statistik in Geodäsie, Geoinformation und Bauwesen*. 4. Aufl. Berlin, Offenbach: Wichmann.
- Bisquay, H., X. Freulon, C. de Fouquet, and C. Lajaunie. 1998. "Multibeam Data Cleaning for Hydrography Using Geostatistics." IEEE Oceanic Engineering Society. OCEANS'98. Conference Proceedings (Cat. No.98CH36259). IEEE. 1135–1143. <https://doi.org/10.1109/OCEANS.1998.724413>
- Björck, Åke. 1996. *Numerical Methods for Least Squares Problems*. Vol. 51. Philadelphia, PA: Society for Industrial and Applied Mathematics. <https://doi.org/10.1137/1.9781611971484>
- Bjørke Jan T., and Stein Nilsen. 2009. "Fast Trend Extraction and Identification of Spikes in Bathymetric Data." *Computers & Geosciences* 35 (6): 1061–1071. <https://doi.org/10.1016/j.cageo.2008.05.009>
- Bottelier, P., C. Briese, N. Hennis, R. Lindenbergh, and N. Pfeifer. 2005. "Distinguishing Features from Outliers in Automatic Kriging-Based Filtering of MBES Data: A Comparative Study." In *Geostatistics for Environmental Applications*, edited by Philippe Renard and Hélène Demougeot-Renard, 403–414. Berlin and Heidelberg: Springer. https://doi.org/10.1007/3-540-26535-x_34
- Breunig, Markus M., Hans-Peter Kriegel, Raymond T. Ng, and Jörg Sander. 2000. "LOF: Identifying Density-Based Local Outliers." *Proceedings of the 2000 ACM SIGMOD International Conference on Management of Data*, Dallas, TX, USA. 93–104.
- Burrus, C. S., and J. A. Barreto. 1992. "Least p-Power Error Design of FIR Filters." 1992 IEEE International Symposium on Circuits and Systems, 3–6 May. New York: IEEE, 545–548. <https://doi.org/10.1109/ISCAS.1992.230134>
- Burrus, C. S., J. A. Barreto, and I. W. Selesnick. 1994. "Iterative Reweighted Least-Squares Design of FIR Filters." *IEEE Transactions on Signal Processing* 42 (11): 2926–2936. <https://doi.org/10.1109/78.330353>
- Chandola, Varun, Arindam Banerjee, and Vipin Kumar. 2009. "Anomaly Detection." *ACM Computing Surveys* 41 (3): 1–58. <https://doi.org/10.1145/1541880.1541882>
- Cline, A. K. 1972. "Rate of Convergence of Lawson's Algorithm." *Mathematics of Computation* 26 (117): 167. <https://doi.org/10.2307/2004726>

- Davies, Laurie, and Ursula Gather. 1993. "The Identification of Multiple Outliers." *Journal of the American Statistical Association* 88 (423): 782–792. <https://doi.org/10.1080/01621459.1993.10476339>
- Debes, N., and H. Bisquay. 1999. "Automatic Detection of Punctual Errors in Multibeam Data Using a Robust Estimator." *The International Hydrographic Review*. 76: 49–63.
- Debes, Nathalie, Rodéric Moitié, and Nicolas Seube. 2012. "Multibeam Echosounder Data Cleaning through a Hierarchic Adaptive and Robust Local Surfacing." *Computers & Geosciences* 46: 330–339. <https://doi.org/10.1016/j.cageo.2012.01.012>
- Du, Z., D. Wells, and L. Mayer. 1996. "An Approach to Automatic Detection of Outliers in Multibeam Echo Sounding Data." *Oceanographic Literature Review* 7: 737.
- Ester, Martin, Hans-Peter Kriegel, Jörg Sander, and Xiaowei Xu. and others. 1996. "A Density-Based Algorithm for Discovering Clusters in Large Spatial Databases with Noise." *Proceedings of the Second International Conference on Knowledge Discovery and Data Mining (KDD-96)*, 226–231.
- Fischler, Martin A., and Robert C. Bolles. 1981. "Random Sample Consensus." *Communications of the ACM* 24 (6): 381–395. <https://doi.org/10.1145/358669.358692>
- Hare, Rob, Barry Eakins, and C. J. T. I. H. R. Amante. 2011. "Modelling Bathymetric Uncertainty." *The International Hydrographic Review*. 6: 31–42.
- Hawkins, Douglas M. 1980. *Identification of Outliers*. Vol. 11. Heidelberg: Springer.
- Huang, Xianyuan, Chenhu Huang, Guojun Zhai, Xiuping Lu, Guorui Xiao, Lifan Sui, and Kailiang Deng. 2020. "Data Processing Method of Multibeam Bathymetry Based on Sparse Weighted LS-SVM Machine Algorithm." *IEEE Journal of Oceanic Engineering* 45 (4): 1538–1551. <https://doi.org/10.1109/JOE.2019.2921429>
- Huber, P. J. 1964. "Robust Estimation of a Location Parameter." *The Annals of Mathematical Statistics* 35 (1): 73–101. <https://doi.org/10.1214/aoms/1177703732>
- Huber, P. J., and E. M. Ronchetti. 2009. *Robust Statistics*. 2nd ed. Hoboken, NJ: Wiley.
- IHO S-44. 2022. *Standards for Hydrographic Surveys S-44*. Monaco: International Hydrographic Organization.
- IHO S-67. 2020. *Mariners' Guide to Accuracy of Electronic Navigational Charts (ENC)*. Monaco: International Hydrographic Organization.
- Jain, Anil K., M. Narasimha Murty, and Patrick J. Flynn. 1999. "Data Clustering: A Review." *ACM Computing Surveys* 31 (3): 264–323. <https://doi.org/10.1145/331499.331504>
- Kammerer, E., D. Charlot, S. Guillaudeux, and P. Michaux. 2001. "Comparative Study of Shallow Water Multibeam Imagery for Cleaning Bathymetry Sounding Errors." MTS/IEEE Oceans 2001. An Ocean Odyssey. Conference Proceedings (IEEE Cat. No.01CH37295). Marine Technol. Soc. 2124–2128. <https://doi.org/10.1109/OCEANS.2001.968327>
- Knorr, Edwin M., Raymond T. Ng, and Vladimir Tucakov. 2000. "Distance-Based Outliers: Algorithms and Applications." *The VLDB Journal The International Journal on Very Large Data Bases* 8 (3–4): 237–253. <https://doi.org/10.1007/s007780050006>
- Koch, K. R. 1999. *Parameter Estimation and Hypothesis Testing in Linear Models*, 2nd Ed. Berlin: Springer.
- Lawson, C. L. 1961. "Contribution to the Theory of Linear Least Maximum Approximation." PhD diss., Univ. Calif.
- Le Deunf, Julian, Nathalie Debes, Thierry Schmitt, and Romain Billot. 2020. "A Review of Data Cleaning Approaches in a Hydrographic Framework with a Focus on Bathymetric Multibeam Echosounder Datasets." *Geosciences* 10 (7): 254. <https://doi.org/10.3390/geosciences10070254>

- Lee, Seungyong, George Wolberg, and Sung Yong Shin. 1997. "Scattered Data Interpolation with Multilevel B-Splines." *IEEE Transactions on Visualization and Computer Graphics* 3 (3): 228–244. <https://doi.org/10.1109/2945.620490>
- Long, Jiawei, Hongmei Zhang, and Jianhu Zhao. 2023. "A Comprehensive Deep Learning-Based Outlier Removal Method for Multibeam Bathymetric Point Cloud." *IEEE Transactions on Geoscience and Remote Sensing* 61: 1–22. <https://doi.org/10.1109/TGRS.2023.3242095>
- Lorenz, Felix, Thomas Artz, Thomas Brüggemann, Julius Reich, Robert Weiß, and Axel Winterscheid. 2021. "Simulation-Based Evaluation of Hydrographic Data Analysis for Dune Tracking on the River Rhine." *PGF – Journal of Photogrammetry, Remote Sensing and Geoinformation Science* 89 (2): 111–120. <https://doi.org/10.1007/s41064-021-00145-0>
- Lu, Dan, Haisen Li, Yukuo Wei, and Tian Zhou. 2010. "Automatic Outlier Detection in Multibeam Bathymetric Data Using Robust LTS Estimation." 2010 3rd International Congress on Image and Signal Processing (CISP 2010), edited by Zheng-Hua Tan. Piscataway, NJ, IEEE, 4032–4036. <https://doi.org/10.1109/CISP.2010.5648184>
- Massey, Jr, Frank J. 1951. "The Kolmogorov-Smirnov Test for Goodness of Fit." *Journal of the American Statistical Association* 46 (253): 68–78. <https://doi.org/10.2307/2280095>
- Matthews, B. W. 1975. "Comparison of the Predicted and Observed Secondary Structure of T4 Phage Lysozyme." *Biochimica et Biophysica Acta* 405 (2): 442–451. [https://doi.org/10.1016/0005-2795\(75\)90109-9](https://doi.org/10.1016/0005-2795(75)90109-9)
- Mohammadivojdan, Bahareh, Marco Brockmeyer, Cord-Hinrich Jahn, Ingo Neumann, and Hamza Alkhatib. 2021. "Regional Ground Movement Detection by Analysis and Modeling PSI Observations." *Remote Sensing* 13 (12): 2246. <https://doi.org/10.3390/rs13122246>
- Papadimitriou, Spiros, Hiroyuki Kitagawa, Phillip B. Gibbons, and Christos Faloutsos. 2003. "LocI: Fast Outlier Detection Using the Local Correlation Integral." Proceedings 19th international conference on data engineering (Cat. No. 03CH37405), 315–326.
- Pedregosa, F., G. Varoquaux, A. Gramfort, V. Michel, B. Thirion, O. Grisel, M. Blondel, et al. 2011. "Scikit-Learn: Machine Learning in Python." *Journal of Machine Learning Research* 12: 2825–2830.
- Piegl, L., and W. Tiller. 1997. *The NURBS Book*. 2. Berlin: Springer.
- Rezvani, Mohammad-Hadi, Abbas Sabbagh, and Alireza A. Ardan. 2015. "Robust Automatic Reduction of Multibeam Bathymetric Data Based on M-Estimators." *Marine Geodesy* 38 (4): 327–344. <https://doi.org/10.1080/01490419.2015.1053639>
- Rousseeuw, Peter J. 1987. *Robust Regression and Outlier Detection*. New York: Wiley. <https://doi.org/10.1002/0471725382>
- Sedaghat, Leela, John Hersey, and Michael P. McGuire. 2013. "Detecting Spatio-Temporal Outliers in Crowdsourced Bathymetry Data." Proceedings of the Second ACM SIGSPATIAL International Workshop on Crowdsourced and Volunteered Geographic Information, 55–62. <https://doi.org/10.1145/2534732.2534739>
- Shen, Jing, Jiping Liu, Rong Zhao, and Xiangguo Lin. 2011. "A kd-Tree-Based Outlier Detection Method for Airborne LiDAR Point Clouds." *2011 International Symposium on Image and Data Fusion*, 1–4.
- Sotoodeh, Soheil. 2007. "Hierarchical Clustered Outlier Detection in Laser Scanner Point Clouds." *International Archives of the Photogrammetry, Remote Sensing and Spatial Information Sciences (ISPRS)* 36: 383–388.
- Stephens, David, Andrew Smith, Thomas Redfern, Andrew Talbot, Andrew Lessnoff, and Kari Dempsey. 2020. "Using Three Dimensional Convolutional Neural Networks for

- Denoising Echosounder Point Cloud Data.” 2590-1974 5: 100016. <https://doi.org/10.1016/j.acags.2019.100016>
- Vargas, Ricardo A., and C. Sidney Burrus. 2012. “Iterative Design of L_p Digital Filters.” <http://arxiv.org/pdf/1207.4526v1>
- Virtanen, Pauli, Ralf Gommers, Travis E. Oliphant, Matt Haberland, Tyler Reddy, David Cournapeau, Evgeni Burovski, et al. 2020. “SciPy 1.0: Fundamental Algorithms for Scientific Computing in Python.” *Nature Methods* 17 (3): 261–272. <https://doi.org/10.1038/s41592-019-0686-2>
- Yang, Fanlin, Fangzheng Xu, Miao Fan, Xianhai Bu, Zejie Tu, and Xunpeng Yan. 2022. “An Intelligent Detection Method for Different Types of Outliers in Multibeam Bathymetric Point Cloud.” *IEEE Transactions on Geoscience and Remote Sensing* 60: 1–10. <https://doi.org/10.1109/TGRS.2022.3209344>
- Yang, Fanlin, Jiabiao Li, Fengyou Chu, and Ziyin Wu. 2007. “Automatic Detecting Outliers in Multibeam Sonar Based on Density of Points.” OCEANS 2007 - Europe. IEEE, 1–4. <https://doi.org/10.1109/OCEANSE.2007.4302202>



PEER-REVIEWED ARTICLE

Enhancing digital bathymetric models by advanced measurement uncertainty analysis

Authors

Bahareh Mohammadivojdan¹, Frederic Hake³, Felix Lorenz², Jan Ole Böllert¹, Robert Weiß², Thomas Artz², Ingo Neumann¹ and Hamza Alkhatib¹

Abstract

Accurate Digital Bathymetric Model (DBM)s are essential for ensuring safe navigation on waterways, yet they heavily depend on precise underwater measurements and robust modeling techniques. However, measurements taken in underwater environments are highly susceptible to uncertainties due to challenging environmental conditions and unknown underwater geometries, complicating the evaluation of both measurements and resulting models. This paper explores the impact of measurement uncertainty on DBM quality and presents a systematic pipeline for modeling these uncertainties to improve the reliability of resulting models. The methodology comprises of two primary stages. A detailed measurement uncertainty model is developed in the first stage based on error propagation principles. This model accounts for multiple uncertainty sources ranging from instrument accuracy to environmental influences. In the second stage, we implement a simulation-based approach to evaluate the influence of these uncertainties on the final DBM. To this end, we have developed a survey simulator that simulates a Multi-Beam Echo Sounder (MBES) system and generates realistic measurement uncertainties. The integration of these uncertainties as observation weights during the modeling process enhances model accuracy and reliability. The effectiveness and practicality of the proposed method are confirmed through validation in a controlled simulation environment with known geometry and uncertainties. The results underscore not only the technical benefits of incorporating measurement uncertainty in surface modeling but also highlight its critical importance in ensuring navigational safety through high-quality, reliable DBMs.

Keywords

DBM · surface model · MBES · uncertainty modelling · uncertainty budget

✉ Bahareh Mohammadivojdan · mohammadivojdan@gih.uni-hannover.de

¹ Leibniz University Hanover, Geodetic Institute, Hannover, Germany

² Federal Institute of Hydrology, Koblenz, Germany

³ Allsat GmbH, Hannover, Germany

⁴ Saxon State Ministry of Infrastructure and Regional Development, Dresden, Germany

Resumé

Des modèles numériques de bathymétrie (MNB) précis sont essentiels pour garantir la sécurité de la navigation sur les voies navigables, mais ils dépendent fortement de mesures sous-marines précises et de techniques de modélisation robustes. Cependant, les mesures prises dans des environnements sous-marins sont très sensibles aux incertitudes dues à des conditions environnementales difficiles et à des géométries sous-marines inconnues, ce qui complique l'évaluation des mesures et des modèles qui en résultent. Cet article explore l'impact de l'incertitude des mesures sur la qualité des MNB et présente un pipeline systématique pour modéliser ces incertitudes afin d'améliorer la fiabilité des modèles obtenus. La méthodologie comprend deux étapes principales. Dans un premier temps, un modèle détaillé d'incertitude de mesure est développé sur la base des principes de propagation des erreurs. Ce modèle tient compte de multiples sources d'incertitude, allant de la précision des instruments aux influences environnementales. Dans un deuxième temps, nous mettons en œuvre une approche basée sur la simulation pour évaluer l'influence de ces incertitudes sur le MNB final. À cette fin, nous avons développé un simulateur de levé qui simule un système de sondeur multifaisceaux (SMF) et génère des incertitudes de mesure réalistes. L'intégration de ces incertitudes sous forme de pondérations d'observation pendant le processus de modélisation améliore la précision et la fiabilité du modèle. L'efficacité et la praticité de la méthode proposée sont confirmées par une validation dans un environnement de simulation contrôlé avec une géométrie et des incertitudes connues. Les résultats soulignent non seulement les avantages techniques de l'intégration de l'incertitude de mesure dans la modélisation de surface, mais aussi son importance cruciale pour garantir la sécurité de la navigation grâce à des MNB fiables et de haute qualité.

Resumen

Los Modelos Batimétricos Digitales (DBM) precisos son esenciales para garantizar la seguridad de la navegación por las vías navegables, pero dependen mucho de la precisión de las mediciones submarinas y de la solidez de las técnicas de modelado. Sin embargo, las mediciones tomadas en entornos submarinos son muy susceptibles a las incertidumbres debidas a las difíciles condiciones ambientales y a las desconocidas geometrías submarinas, que complican la evaluación tanto de las mediciones como de los modelos resultantes. Este artículo explora el impacto de la incertidumbre de las mediciones en la calidad de los DBM y presenta una vía sistemática para modelar estas incertidumbres para mejorar la fiabilidad de los modelos resultantes. La metodología consta de dos fases principales. En la primera fase se desarrolla un modelo detallado de incertidumbre de las mediciones basado en los principios de propagación de errores. Este modelo tiene en cuenta múltiples fuentes de incertidumbre desde la precisión de los instrumentos hasta las influencias ambientales. En la segunda etapa, implementamos un enfoque basado en simulaciones para evaluar la influencia de estas incertidumbres en el DBM final. Para ello, hemos desarrollado un simulador de levantamientos que simula un sistema de Ecosonda Multihaz (MBES) y genera incertidumbres de medición realistas. La integración de estas incertidumbres como confianza de las observaciones durante el proceso de modelado mejora la precisión y fiabilidad del modelo. La efectividad y viabilidad del método propuesto se confirman mediante la validación en un entorno de simulación controlado con geometría e incertidumbres conocidas. Los resultados subrayan no sólo los beneficios técnicos de incorporar la incertidumbre de las mediciones en el modelado de superficies, sino también su importancia crítica para garantizar la seguridad de la navegación mediante DBM de alta calidad y fiables.



1 Introduction

Accurate and reliable DBMs are needed for safe navigation in waterways. This is especially important for Germany— a leading global economic and export nation that relies heavily on its inland and maritime shipping routes to connect industrial hubs to seaports and ensure access to international markets. Its waterways, which connect the North and Baltic Seas and are central to Europe, are vital to the European waterway network, supporting trade and transport safety (BFG, 2013). Nowadays, with the capabilities of sonar-based systems such as MBES, it is possible to sample underwater topography in high spatial resolution and density. These systems measure both location and depth, generating Point Cloud (PC) comprising millions of points in a short time. Although high-resolution measurements are associated with greater detail and raise expectations regarding the detection of fine structures and higher accuracy, assumptions about the precision of such data can be misleading, as each measurement is subject to both vertical and horizontal uncertainties. The International Hydrographic Organization (IHO) provides guidelines to ensure safety and guarantee a minimum level of accuracy for users in order to standardize the quality of DBMs (IHO, 2022).

To create DBMs, we rely on raw measurements from which outliers have been removed. However, this process makes it difficult to produce a high-quality DBM because the source data are not always as accurate as required. Bathymetric measurement uncertainty depends on both the survey system and survey conditions. A survey system is, in essence, a multi-sensor system composed of several sensors (e.g., MBES, IMU, GNSS, etc.). The error budget is influenced by various factors related to the system and measurement set up (e.g. sensor installation, georeferencing, measurement track, speed, etc.) Hare et al. (2011). Additionally, further inaccuracies may be introduced during the modeling process itself, for example due to model approximation errors, limitations in the chosen surface representation, or the presence of noise and outliers in the input data. This raises two questions: if we closely examine the measurement process and its surrounding conditions, can we quantify these inaccuracies or estimate the uncertainties involved? And how might this information enhance the final model?

1.1 Uncertainty of bathymetry surveys

A realistic estimate of the measurement uncertainties is crucial for evaluating their impact on final products, such as DBM. This information is invaluable not only for assessing model quality but also for applications such as measurement planning and bridge risk management (Eakins & Taylor, 2010; Hare et al., 2011). Extensive research has focused on detecting and modeling the source of errors in bathymetric surveys. For example, Hare (1995) developed an algorithm to predict the uncertainty of bathymetry surveys by

considering various influencing factors. He accounted for the total depth error by including errors from the sounder system, roll, pitch, heave, refraction, dynamic draught, and water level. Moreover, the total error budget should also incorporate errors from the positioning system, relative transducer-sounding position, heading, and the relative antenna-transducer position (Hare, 1995). Today Precise Differential Global Positioning System (PDGPS) are used for positioning, which replaces the errors associated with dynamic draught and water level with the uncertainty of the GNSS solution. The law of propagation of variances can be applied to integrate different sources of uncertainty and derive estimates of Total Propagated Uncertainty (TPU), separating it into a vertical component – Total Vertical Uncertainty (TVU) – and a horizontal component – Total Horizontal Uncertainty (THU) (Hare, 1995; Hare et al., 2011). However, it is important to note that position and depth errors should not be considered as inherently coupled. In complex underwater environments, especially in areas with abrupt morphological changes, even small horizontal deviations can cause significant apparent depth discrepancies. Thus, while the TPU model provides an overall estimate of uncertainty, it does not fully account for morphology-driven effects. Therefore, in addition to considering the combined TPU, a separate and independent assessment of TVU and THU is necessary to properly characterize the measurement uncertainties. Many researchers have contributed to this model to account for more error sources e.g. doppler frequency shift, baseline decorrelation when using frequency modulated pulse (Haji Mohammadloo et al., 2018, 2019). The quality of uncertainty model, was researched by (Haji Mohammadloo et al., 2018; Tengku Ali et al., 2022; Abubakar & Poerbandono, 2023). However, due to lack of ground truth on underwater geometry, validation of the quality of the developed models still remains under-researched.

1.2 Modeling and quality of DBM

The accuracy of the DBM depends on both the quality of the source data and the modeling technique employed. Since every measurement inherently carries some uncertainty, these uncertainties propagate into the final bathymetric model. The modeling approach can range from a simple grid-based representation to a complex 3D mathematical surface. Numerous studies have focused on spatial data modeling. Choosing the suitable modeling technique, depends on the characteristics of the PC such as its size, distribution, density and regularity. Although MBES PCs are typically dense, they are non-homogeneous and contain some gaps. Consequently, many modeling techniques are unable to handle large datasets with high variability and spatial gaps. In practice, simpler grid representations are frequently used for these data (Maune et al., 2007), where each cell is assigned a single value derived from various

interpolation techniques. Common methods include splines, kriging, nearest neighbor, minimum curvature, modified Shepard's method, Inverse Distance Weighting (IDW), Triangulated Irregular Network or artificial intelligence (Lorenz et al., 2021; Maune et al., 2007; Włodarczyk-Sielicka et al., 2016). Each method has its strength and is chosen based on the specific circumstances of the dataset (Yang et al., 2004; Rishikeshan et al., 2014). An appropriately chosen interpolation technique not only reduces computational cost by limiting mesh nodes to local neighborhoods, but can also mitigate the influence of measurement noise by averaging over multiple observations. This often results in smoother and more realistic surface representations. However, the accuracy of the final model remains sensitive to factors such as cell size, point density, topographic variability within each cell, and the interpolation strategy chosen. In addition, unlike hierarchical or global surface models that can incorporate broader spatial dependencies, grid-based approaches may be limited in their ability to capture complex structures if the local window is too restrictive.

A DBM can be derived based on global functions. For example, Bisquay et al. (1998) and Bottelier et al. (2005) use Kriging to interpolate the underwater geometry by exploiting the correlation among data points. However, this method is computationally expensive, and to achieve reliable estimates, the underlying trend in the data must be modeled separately (Mohammadijodan et al., 2020). Alternatively, a DBM can be derived based on a mathematical model, representing a continuous global surface— such as traditional polynomial surfaces or free-form surfaces, like B-splines and non-uniform rational B-splines (Piegl, 1997; Bureick et al., 2016). For a global surface approximation, Arnold & Shaw (1993), Bjørke & Nilsen (2009) and Mohammadijodan et al. (2021), employ a coarse-to-fine strategy in building the surface. A hierarchical surface model can overcome specific challenges posed by high-density, high-noise, and nonhomogeneous distribution of MBES measurements. In this context, Mohammadijodan et al. (2024) utilize a hierarchical B-spline surface model – namely, the Multilevel B-spline Approximation (MBA) model introduced by (Lee et al., 1997) – which adapts to varying topographies and efficiently handles data gaps.

Furthermore, various survey configurations and operational setups also impact the accuracy of DBMs. These setups influence point density and distribution, which in turn affect modeling error. Maleika (2013) investigated the influence of factors such as vessel speed, swath width, track configuration, and measurement density on model quality (Maleika et al., 2012). Since there is no ground truth on the underwater geometry, it is challenging to precisely estimate the DBM accuracy. To quantify the modeling error, several statistical approaches are available, including cross-validation, split-sample and jack-knifing, and

bootstrapping (Paquet, 2010; Erdogan, 2009; Mohammadijodan et al., 2021). These approaches evaluate the model's predictive performance by testing it on data that were not used during the estimation process, ensuring that the model generalizes well to new, unseen data. By partitioning the data into subsets or repeated resampling, these techniques estimate the variability and reliability of the model's predictions, providing a robust assessment of its accuracy and potential biases. However, it is important to note that in the absence of ground truth, both training and test subsets are affected by similar random noise characteristics inherent to MBES systems. As a result, while these methods can provide insight into the internal consistency and robustness of the model, they may not fully reflect the absolute modeling error, especially in high-noise environments.

1.3 Contribution

The objective of this study is to quantify the uncertainty of a DBM and explore how incorporating uncertainty information can improve their accuracy and reliability. We achieve this by developing a comprehensive uncertainty model that quantifies the uncertainties inherent in bathymetric measurements. We employ a Monte-Carlo-based approach for error propagation, which provides a computationally straightforward way to account for complex, non-linear relationships and non-standard probability distributions. Unlike classical error propagation methods, our approach avoids intricate mathematical derivations while still offering a detailed representation of the uncertainties affecting our measurements. This work focuses on creating a DBM from outlier-cleaned raw data using a mathematical surface, specifically employing the MBA approach. Our goal is to explore how uncertainty information can enhance this model. Our approach is to incorporate uncertainty data as weights within the adjustment process, to assess its impact on model quality. However, a major challenge is the lack of real-world cases with known ground truth; without precise knowledge of the true underwater geometry, it is difficult to definitively evaluate the model's accuracy. To overcome this, we developed a simulation environment that generates a known geometry based on a precise mathematical model representing the ground truth. Within this controlled environment, we simulate both the measurement process and its corresponding uncertainties. This setup allows us to obtain measurements that include uncertainties while retaining complete knowledge of the true geometry, thereby enabling a better understanding of how uncertainty affects the model.

Recognizing that a single simulation scenario is insufficient for drawing reliable conclusions, we conducted a comprehensive Monte-Carlo simulation experiment, repeating the entire process multiple times. In each iteration, both the geometry and the associated uncertainties are simulated, and two versions of the DBM are generated: one that incorporates

the uncertainty information to improve the model, and one that does not. This comparative approach enables us to evaluate the impact of incorporating uncertainty on the model's accuracy and reliability. Ultimately, we identify the optimal model and generate additional outputs – such as Confidence Intervals (CI) and uncertainty maps – that provide a clearer picture of the model's precision. This paper is organized in three parts. Part 1 describes the development of the uncertainty model and the hydrographic survey system used in our experiment, as well as the model's validation (Sections 2 and 3). Part 2 presents the survey simulator (Section 4). Part 3 details the data processing, modeling algorithm, the Monte-Carlo experiment, and the resulting analysis (Section 5).

2 Description of the uncertainty model

According to the Guide to the Expression of Uncertainty in Measurements (GUM), to estimate uncertainty of a measured value Y , we should establish the functional relationship between the target value Y and all the other quantities (X_1, X_2, \dots, X_N) contributing in the measurement process (ISO, 1995)

$$Y = f(X_1, X_2, \dots, X_N) \quad (1)$$

If the input variables are uncorrelated, the combined measurement uncertainty $u_c(Y)$ of a target quantity Y can be calculated from the standard uncertainties of the input quantities $u_i(X)$ as follows (Schwarz, 2020a):

$$u_c(Y) = \sqrt{\sum_{i=1}^n (c_i \cdot u(X_i))^2} \quad (2)$$

wherein,

c_i – Sensitivity coefficient, defined as $c_i = \partial f / \partial x_i$

$u(x_i)$ – Standard uncertainty of the input quantity x_i

n – Number of input quantities

The uncertainty u_c is propagated from the uncertainties of the inputs using a first-order Taylor series expansion (linear approximation). The sensitivity coefficient is derived from the partial derivative of the functional model ($Y=f(X)$) with respect to the input quantities, which indicates the effect of each input quantity on the final results. This represents the case where functional model is linear and no correlation is assumed between the input parameters.

The concept of GUM, defines a CI around a measured value called *expanded uncertainty*. The true value of the measurand is expected to lie within this interval. Mathematically, it is represented as:

$$U(Y) = k \cdot u(Y) \quad (3)$$

where k is the coverage factor, determined based on the desired Confidence Level (CL). Thus, the final measurement result can be expressed as:

$$Y \pm U(Y) \quad (4)$$

2.1 Establishing the measurement model

In this case, the measurement model is the solution of the coordinates in the target coordinate system. The goal is to derive the absolute coordinates of the waterbed from the raw measurement data collected by the installed sensors. This derivation occurs in multiple steps and is relative to different reference systems.

Step 1 – Deriving coordinates within Transducer coordinate system (T-Frame): Coordinates in the T-Frame are derived based on transducer measurements (range r , beam angle θ) as follows:

$$\begin{bmatrix} X_T \\ Y_T \\ Z_T \end{bmatrix} = \begin{bmatrix} 0 \\ r \cdot \sin(\theta) \\ -r \cdot \cos(\theta) \end{bmatrix} \quad (5)$$

Step 2 – Transforming into Ship's coordinate system (B-Frame): In the B-Frame, the X-axis runs along the ship's length (positive toward the bow), and the Z-axis points toward the zenith of the ship. The Y-axis corresponds to the port side direction. The origin of this coordinate frame is the ship's Center of Gravity (CoG). Coordinates in B-Frame are obtained by a 6DOF transformation: first, the coordinates in T-Frame are rotated based on mounting angles of the transducer with respect to the ship body frame (denoted by α , β , and γ), and then they are translated based on the coordinate difference between the transducer's reference point and the ship's CoG. This translations in XYZ(ΔX_{T-B} , ΔY_{T-B} , ΔZ_{T-B}) are determined in a vessel offset survey.

$$\begin{bmatrix} X_B \\ Y_B \\ Z_B \end{bmatrix} = \mathbf{R}(\alpha, \beta, \gamma) \cdot \begin{bmatrix} X_T \\ Y_T \\ Z_T \end{bmatrix} + \begin{bmatrix} \Delta X_{T-B} \\ \Delta Y_{T-B} \\ \Delta Z_{T-B} \end{bmatrix} \quad (6)$$

Step 3 – Transformation from B-Frame into the Local topocentric coordinate system (LL-Frame): Measurements from the Global Navigation Satellite System (GNSS) sensor are obtained in the LL-Frame, which has globally defined axes: The Y-axis points toward geographic north, and the Z-axis runs parallel to the plumb line, pointing toward the local zenith. The translation values in XYZ(ΔX_{B-LL} , ΔY_{B-LL} , ΔZ_{B-LL}), are based on the coordinate differences between the ship's CoG and reference point of the GNSS antenna. Due to the axis orientation in the UTM system, α_H is introduced, which results from the heading according to $\alpha_H = 90^\circ - H$. The rotation is based on the measured heading α_H , pitch P and roll R by Inertial Measurement Unit (IMU).

$$\begin{bmatrix} X_{LL} \\ Y_{LL} \\ Z_{LL} \end{bmatrix} = \mathbf{R}(\alpha_H, P, R) \cdot \begin{bmatrix} X_B \\ Y_B \\ Z_B \end{bmatrix} + \begin{bmatrix} \Delta X_{B-LL} \\ \Delta Y_{B-LL} \\ \Delta Z_{B-LL} \end{bmatrix} \quad (7)$$

Step 4 – Combining with GNSS Measurements: The final coordinates are obtained by combining the transformed coordinates in LL-Frame with the GNSS measurements

from the GNSS:

$$\begin{bmatrix} X \\ Y \\ Z \end{bmatrix}_{Final} = \begin{bmatrix} X_{LL} \\ Y_{LL} \\ Z_{LL} \end{bmatrix} + \begin{bmatrix} X_{GNSS} \\ Y_{GNSS} \\ Z_{GNSS} \end{bmatrix} \quad (8)$$

This generalized formulation describes the measurement system illustrated in Fig. 1 and applicable to different sensor types and fields of application.

2.2 Identifying influencing factors

Once the measurement model has been established, the next crucial step is to identify all elements that influence the accuracy of the final quantity. These factors arise from the sensors themselves – including their quality and the reliability of the source data – environmental conditions, and the definition of the chosen reference frames. In the case of an MBES, not only must uncertainties in measured range and angle be considered, but also indirect influences such as variations in sound speed at different depths, the transducer's opening angle, pulse length, beam bandwidth, and heave. In addition, the precise alignment of the sensors relative to one another and the careful definition of reference points play a vital role in ensuring accurate results. The main factors influencing bathymetric measurement uncertainty are illustrated in Fig. 2. For a deeper discussion of each uncertainty source, its overall impact, and the methodologies to quantify it, readers are referred to (Hare, 1995) and (Wirth, 2011).

2.3 Uncertainty estimation

With the measurement model established and the relevant influencing factors identified, the next step is to estimate the uncertainty of the target quantity via error propagation. Classical GUM propagation (refer to Eq. 2) involves computing the derivatives of the measurement model for all influencing parameters. However, because our measurement model is highly nonlinear, the classical approach is suboptimal. For complex systems, an alternative solution is to use Monte Carlo Method (MCM), as described in GUM (ISO, 1998). MCM offer several advantages: it overcomes the limitations of classical GUM propagation – which assumes small uncertainties and relies on a first-order Taylor expansion – and it accommodates any Probability Density Function (PDF) of input parameters, thereby extending the analysis beyond the constraints of normal distributions. The outcome of MCM is not just a standard uncertainty, it also gives a complete uncertainty distribution.

To estimate uncertainties using MCM, it is first necessary to identify the PDF corresponding to each influencing factor. MCM is based on performing a large number of simulated random experiments, and its validity is ensured when a sufficient number of trials are conducted. Typically, the number of samples ranges from 1,000 to 1,000,000 (e.g., $m = 100,000$ in Alkhatib et al. (2009) and $m = 1,000,000$ in

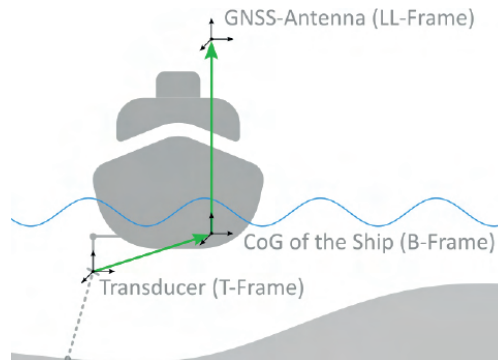


Fig. 1 Illustration of measurement system, sensors, and the defined coordinate frames.

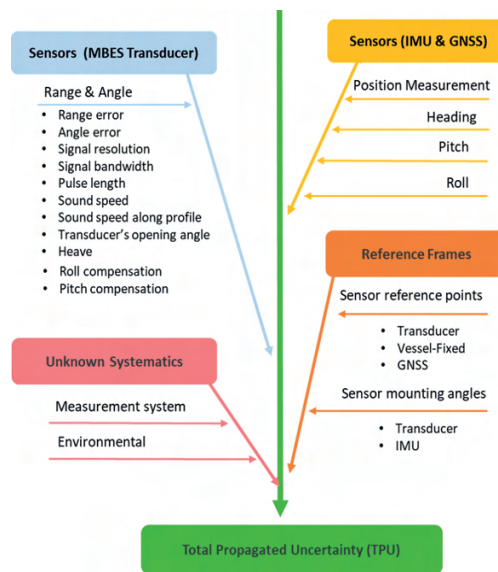


Fig. 2 The influencing factors on bathymetric measurement uncertainty.

Schwarz (2020b)). Due to its computational intensity, it is imperative to optimize the number of samples to achieve a balance between computational efficiency and result accuracy (ISO, 1998; Schwarz, 2020b).

The outcome of MCM is the PDF of the parameter of interest, which represents the combined measurement uncertainty. The three-dimensional expanded uncertainty, at a 95 % CL, is defined as the TPU. As specified by the IHO (2022), the TPU consists of two components: TVU and THU. The TVU is extended uncertainty in vertical dimension (σ_{Height}). Similarly, THU is a two-dimensional uncertainty for the North and East dimensions (σ_{North} , σ_{East}). For normally distributed, one and two-dimensional variables, The IHO defines an expansion factor of 1.96 and 2.45, respectively. Known systematic deviations U_c can also be incorporated. TVU is calculated as:

$$TVU = 1.96 \cdot \sqrt{\sigma_{Height}^2 + U_{sys.V}^2} \quad (9)$$

and THU is calculated as:

$$THU = 2.45 \cdot \sqrt{\sigma_{East}^2 + \sigma_{North}^2 + U_{sys.H}^2} \quad (10)$$

3 Validation of the uncertainty model

To assess the functionality of our model and validate its performance, we use real data. Although the systems and configurations of measurement instruments may vary across different vessels, their underlying principles remain similar. In this study, we focus on a specific measurement system – the Uwe Jens Lornsen (UJL; Fig. 3). We developed the measurement model for UJL according to Section 2.1, and for a specific measurement campaign, a complete uncertainty model is also established.

3.1 Details of the measurement system

The survey vessel UJL (Fig.3) is a survey vessel operated by the Elbe-North Sea (Tönning) Waterways and Shipping Office (WSA). Built in 1993, its primary tasks include monitoring and depth surveying of maritime navigation channels along the Schleswig-Holstein West Coast to ensure safe and efficient navigation. Additionally, UJL is used for surveying structures, harbors, and dredging areas. To perform these tasks, the UJL uses a Kongsberg EM2040C dual-head

multibeam echo-sounding system with two permanently installed transducers. For spatial referencing, a satellite-based positioning system – comprising PDGNSS with an integrated navigation sensor system (INS), including a Seapath 330+ and a motion reference unit (MRU 5+) – is used. The location of the sensors on UJL is shown in Fig. 4.

The primary sampling sensors used on UJL is MBES. Two MBES are mounted perpendicularly to the vessel, enabling a profile-based scanning of the seafloor. For efficient scanning, these two echo sounders are oriented along the port–Back Board side (BB) and Star Board side (STB) and tilted at 37° relative to the ship's baseline. In addition to the dual-head system, a third hydroacoustic sensor – a Single Beam Echo Sounder (SBES) – is used to measure the central depth at the vessel's nadir using various frequencies. Note that the SBES was used exclusively for navigation support and was not involved in the bathymetric data processing or experimental analysis.



Fig. 3 Image of survey vessel UJL (WSA, 2023).

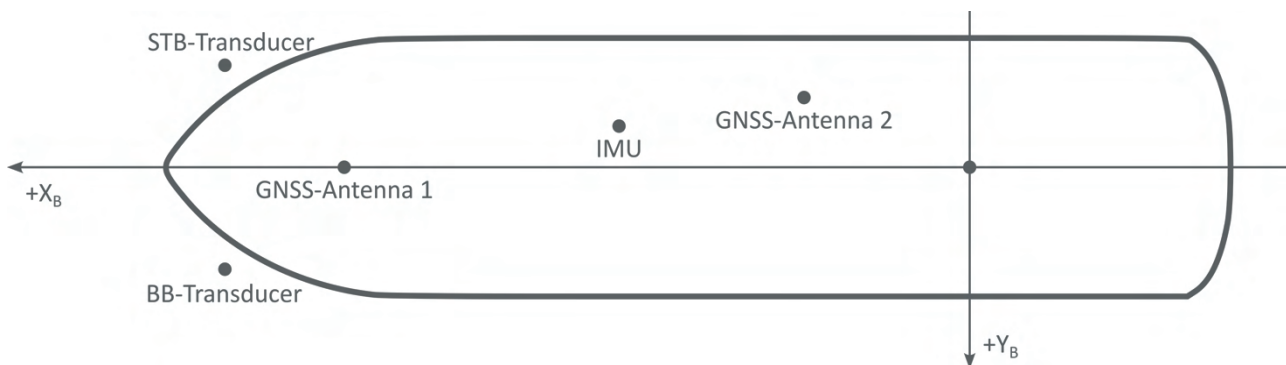


Fig. 4 Schematic layout of the sensor configuration on the UJL survey vessel.

The UJL was used in 2019 for a measurement campaign of the man-made Kiel Canal (Fig. 5), conducted by the Elbe Nordsee Waterways and Shipping Office (Tönning). A 300 m long measurement swath was used as test data. In the selected section of the campaign, both flat areas and structured regions characterized by small bed load transport bodies (dunes), embankments, and leaps across flow direction were observed. The riverbed in this area typically consists of rock, silt, and gravel; water depths reach up to 13 m. The 'equal angular' measurement mode produces 256 measurement points per ping, with an across-track distance of around 0.06 m near nadir and 0.4 m in the remote swath areas. Near the vessel's nadir, the point density is approximately 45 points per square meter, decreasing to 15 points per square meter in the outer regions. Based on the vessel's speed and the chosen sampling rate, the pings have a typical along track distance of 0.35 m.

The test area exhibits varying effects on the measurement uncertainty due to the combination of high-water depth with partly shallow areas characterized by sediment and partly sloping embankments. The geometry of the observation configuration changes significantly – for example, the measured distance, the angle of incidence, and consequently, the size of the measurement footprint varies considerably. Furthermore, different structures such as small dunes or leap areas provide distinct backscattering properties, each influencing the measurement uncertainty in a unique way.

3.2 Uncertainty model for UJL

All sensors deliver the raw data in their specific sensor coordinate frame. To retrieve a 3D PC in the target reference frame, the measurements must first be transformed to a consistent vessel reference frame and then to the target reference frame. Section 2.1 outlines the methodology for calculating the seafloor coordinates for a single transducer. Following this methodology, we establish the measurement model for UJL, where the target coordinate system here is ETRS89/DREF91 (realization 2016) with UTM projection.

A detailed list of the key parameters and their corresponding uncertainty values, as incorporated into our uncertainty modeling, is presented in Table 1. For those parameters marked with "e.g.", the listed values are representative examples from the dataset and are not treated as fixed. Instead, they are dynamically estimated per observation within the simulation, using established models such as the geometric range uncertainty model of Hare (1995) and Wirth (2011), which incorporate relevant factors like slant range, beam angle, and sound speed variability. For more details on each uncertainty source and the methods used to quantify them, readers are referred to Hare (1995) and Wirth (2011).

Here, we assume normal distribution for all parameters considered, as listed in Table 1. In this approach, input parameters are assumed to be

statistically uncorrelated. Nevertheless, correlations that naturally arise through the functional relationships between variables are implicitly captured by the Monte Carlo Simulation process. The different variations of the input parameters propagate through the nonlinear system model, and their mutual effects on the target variables (X, Y, Z coordinates) are reflected in the output's distribution. The uncertainties are calculated separately for each coordinate component, providing individual uncertainty values for the East, North, and Height components. Following the MCM, 1000 simulations were performed, resulting in 1000 solutions for each point and its East, North, and Height components. The PDF of one example measurement point's coordinate solutions is illustrated in Fig. 6 as an example. A normal distribution has been estimated for each component and shown with red lines in Fig. 6. The calculated coordinates align well with the Normal distribution curve, with no significant deviations observed. Therefore, we use standard deviation corresponding to a CL of 68 % to determine uncertainties of each component (σ_{East} , σ_{North} , σ_{Height}). These uncertainties are then used to calculate TPU values (Eqs. 9 and 10).

Fig. 7 illustrates the results of the MCM uncertainty calculation with 95 % CL for each measurement point. Here, uncertainties are expressed at a 95 % CL, in accordance with the definition of TPU (see Eqs. 9 and 10). The previously calculated standard uncertainties (at 68 % CL) are used as the basis for this propagation. Fig. 7a shows the height uncertainties for the first 100 profiles within the measurement swath, while Fig. 7b presents the horizontal uncertainties. These figures include measurements from both BB and STB transducers, with coordinates color coded according to their calculated TVU and THU. The color scale is provided in the legend. In the height component, uncertainties vary significantly within a single profile, ranging from 9 cm directly under the ship to 29 cm for the outer transducer beams. This variation aligns with the expectation that measurement uncertainty increases with greater measured distances and larger beam angles. Additionally, a slight increase in uncertainty is observed in the direct nadir area. This increase in TVU is mainly due to limitations in signal resolution. At nadir, where the acoustic path is shortest and perpendicular, pulse duration plays a dominant role in depth resolution. Similarly, horizontal uncertainty increases with distance from the vessel due to larger beam footprints and weaker signal returns at steeper angles. In outer swath areas, small errors in angle or range are amplified, leading to greater horizontal position uncertainty. However, the range of the horizontal uncertainty values differs considerably from that of the height uncertainties, varying from 0.55 m near the nadir to 1.28 m in the outer beams. This confirms that horizontal uncertainty is generally higher than height uncertainty.

Table 1 Uncertainty values and influencing parameters for MBES, IMU, and GNSS.

Influencing parameter	Value	Uncertainty symbol	Uncertainty value
Related to MBES			
Angle measurement θ	-	σ_θ	e.g. 0.002 deg
Range measurement error r	-	σ_r	e.g. 0.12 m
Sound speed along profile v_m	1469 m/s	σ_{vm}	0.123 m/s
Surface sound speed v_s	1468 m/s	σ_{vs}	0.048 m/s
Speed over ground v_{SOG}	2 m/s	σ_{vSOG}	0.101 m/s
Spatio-temporal variations of sound speed Δv	-	$\sigma_{\Delta v}$	0.01 m/s
Signal bandwidth	15 kHz	-	-
Pulse length Δt_{imp}	0.015 s	$\sigma_{\Delta t_{imp}}$	0.05 s
Definition of the ground	-	U	0.03 m
MBES Pitch compensation Pk	-	σ_{Pk}	0.11 deg
MBES Roll compensation Rk	-	σ_{Rk}	0.05 deg
Heave	-	-	0.05 m
Related to IMU & GNSS			
Heading α	-	σ_α	0.064 deg
Pitch P	-	σ_P	0.054 deg
Roll R	-	σ_R	0.054 deg
$X_{GNSS}, Y_{GNSS}, Z_{GNSS}$ (PDGNSS)	-	$(\sigma_x, \sigma_y, \sigma_z)_{PDGNSS}$	(0.005, 0.005, 0.013) m
X, Y, Z (Position)	-	$(\sigma_x, \sigma_y, \sigma_z)_{Pose}$	e.g. (0.143, 0.147, 0.014) m
Related to reference frames			
$\{X_0, Y_0, Z_0\}_{GNSS}$	-	$\sigma_{\{X_0, Y_0, Z_0\}_{GNSS}}$	0.005
$\{X_0, Y_0, Z_0\}_{Ship}$	-	$\sigma_{\{X_0, Y_0, Z_0\}_{Ship}}$	0
$\{X_0, Y_0, Z_0\}_{Transducer}$	-	$\sigma_{\{X_0, Y_0, Z_0\}_{Transducer}}$	0.005
Transducer mounting angles (α, β, γ)	-	$\sigma_{(\alpha, \beta, \gamma)_{Transducer}}$	(0.1, 0.1, 0.1) deg
IMU mounting angles	-	$\sigma_{Mount, Pitch}, \sigma_{Mount, Roll}$	0.02 deg

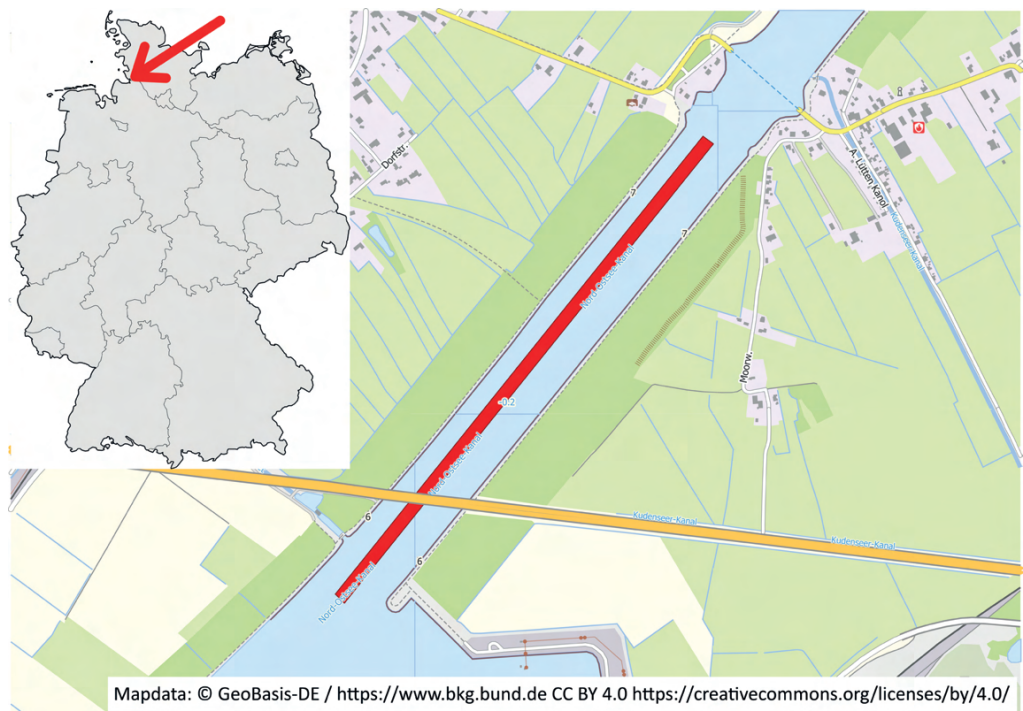


Fig. 5 Survey area of Kiel Canal. The 300 m long measurement swath used as test data.

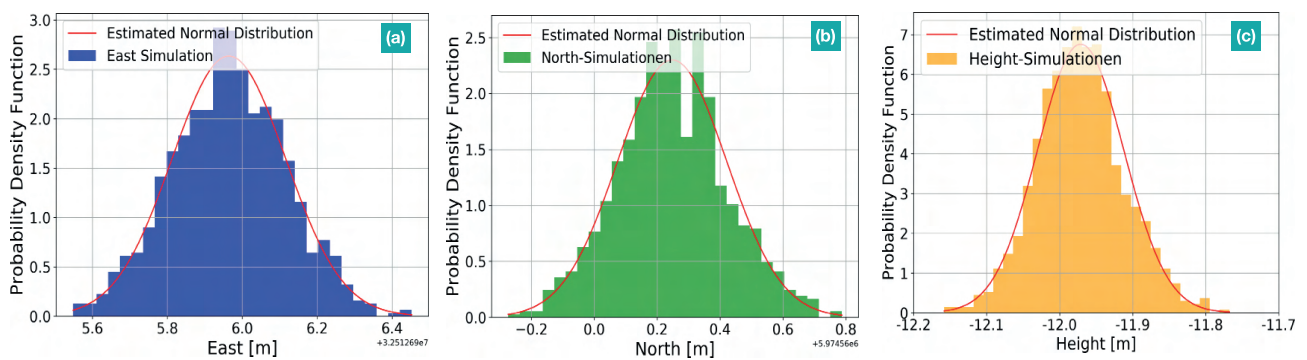


Fig. 6 PDF of East, North, and Height components for one point. The PDF results from 1000 MCM simulations. Red lines represent the fitted normal distribution.

3.3 Discussion of TPU modelling results

To validate the results of the uncertainty analysis, we compared our MCM results with those obtained using the classical GUM approach and those estimates from the commercial software QINSy (version 8.18.3; QPS, 2025), which is used as the data acquisition software on UJL. In this software, the offsets in the vessel frame and the measurement data from the sensors are converted into a 3D PC as projected points in the official reference frame. In addition, other attributes recorded by the sensors are included so that a TPU value per beam can also be determined and specified. The exact procedure for determining the TPU by QINSy is not known, but tests and comparisons suggest that the procedure is similar to the methods described in (Hare, 1995; Wirth, 2011). Nonetheless, it is presumed that QINSy's TPU estimations meet hydrographic standards and provides combined standard uncertainties with 95 % CL.

According to IHO, each survey must comply with a defined "maximum allowable uncertainty" for both vertical and horizontal measurements. For vertical uncertainties, permissible limits at a 95 % CL are computed based on depth-dependent b and depth-independent a parameters, as well as the actual depth d (Eq. 11). These parameters differ according to the survey order as described in IHO (2022). Furthermore, the S-44 standard defines maximum permissible horizontal uncertainties; for example, the maximum horizontal uncertainty THU_{max} allowed for Special Order surveys is set to 2 m (IHO, 2022).

$$TVU_{max} = \sqrt{a^2 + (b \cdot d)^2} \quad (11)$$

Fig. 8 presents the TVU of measurement points for a single representative profile to illustrate the structure and variation of the uncertainty with respect to beam angle relative to the ship's vertical axis (Fig. 8a) and lateral distance (Fig. 8b). While this profile is not intended to be statistically representative of the full dataset, it provides a clear example of the underlying trend. The plots compare solutions from the classical GUM approach, MCM, and QINSy. The uncertainties for BB and STB transducers are shown with similar color. Fig. 8 additionally illustrates the maximum

permissible vertical uncertainty TVU_{max} for the Special Order and Exclusive Order survey as defined by the IHO (2022), for a mean depth of 12 m. The uncertainties computed via MCM follow the expected pattern shown in Fig. 7a. As shown in Fig. 8a, TVU increases exponentially with respect to the beam angle, while Fig. 8b shows a more linear increase in TVU with lateral distance from the vessel. The lowest uncertainties occur at distances of 12–15 m from the ship, corresponding to beam angles of 48–53° from the ship's normal. This effect is primarily attributed to limitations in vertical resolution caused by pulse duration. The nadir beams, pointing directly downward, rely almost exclusively on the two-way travel time of the acoustic pulse to determine depth. Consequently, any uncertainty in echo detection, especially when longer pulse durations are used, directly translates into vertical measurement uncertainty. While side beams are more affected by geometric distortion due to effects such as decreasing signal intensity and increasing footprint resulting from beam divergence, nadir measurements are more sensitive to temporal resolution. Additionally, the nadir represents a transition zone between the BB and STB swaths. Here, overlapping beams from both swath edges – where positional and angular uncertainties are typically higher – may interact, compounding the overall uncertainty in this central region. While all three solutions exhibit similar trends, differences exist. The classical GUM approach does not capture the nadir effect seen in MCM results. Since both methods are based on measurement model described by Wirth (2011), only minor discrepancies are expected. These variations likely stem from differences in user-defined input parameters, highlighting their role in uncertainty analysis. Compared to QINSy's uncertainties, the relative variation aligns, but our uncertainty model appears to account for similar factors with differing absolute impacts. All three predicted uncertainties are below TVU_{max} for the Special Order survey. In Fig. 8, we observe that the outer-beam uncertainty of the BB transducer exceeds the Exclusive Order threshold defined by the IHO S-44 standard. According to S-44 standards, the TVU is expected to increase with water depth, following a depth-dependent model (IHO, 2022). However, the measurement campaign

analyzed in this study was conducted in a relatively uniform depth environment, with an average depth of approximately 13 meters. As a result, the data do not capture a wide range of depth-induced variability in TVU. Future work in more bathymetrically diverse areas may provide further insight into this relationship.

Fig. 9 presents estimated THU for the same profile measurement. It compares the results from MCM, GUM, and QINSy's THU values. The uncertainties for BB and STB transducers are shown with similar color. Fig. 9 also shows the maximum permissible horizontal uncertainty THU_{max} for the Special Order survey as defined by the IHO (2022), represented by the dotted line.

Compared to height uncertainty, horizontal uncertainty is substantially higher. The uncertainty profile also differs, showing no increased uncertainty in the nadir. The comparison across methods reveals

minimal differences between GUM and MCM results. To highlight this, Fig. 9b provides a close-up of the nadir region's uncertainty results. The MCM solution is noisier due to its reliance on simulation rather than linearization, as with the classical GUM method. Larger deviations appear in comparison with the QINSy solution. Particularly in this profile, in the nadir region, QINSy's uncertainty values are roughly 20 cm lower than those from GUM and MCM. Conversely, QINSy's uncertainty increases more significantly in the outer beams. In average the difference between our uncertainty model (both realizations MCM and GUM) and QINSy, along the profiles and for all the 3000 measured profiles, is around 17 cm. This suggests that positional uncertainty influences are modeled differently across methods, and further investigation into QINSy's calculation approach would be required to fully understand these discrepancies.

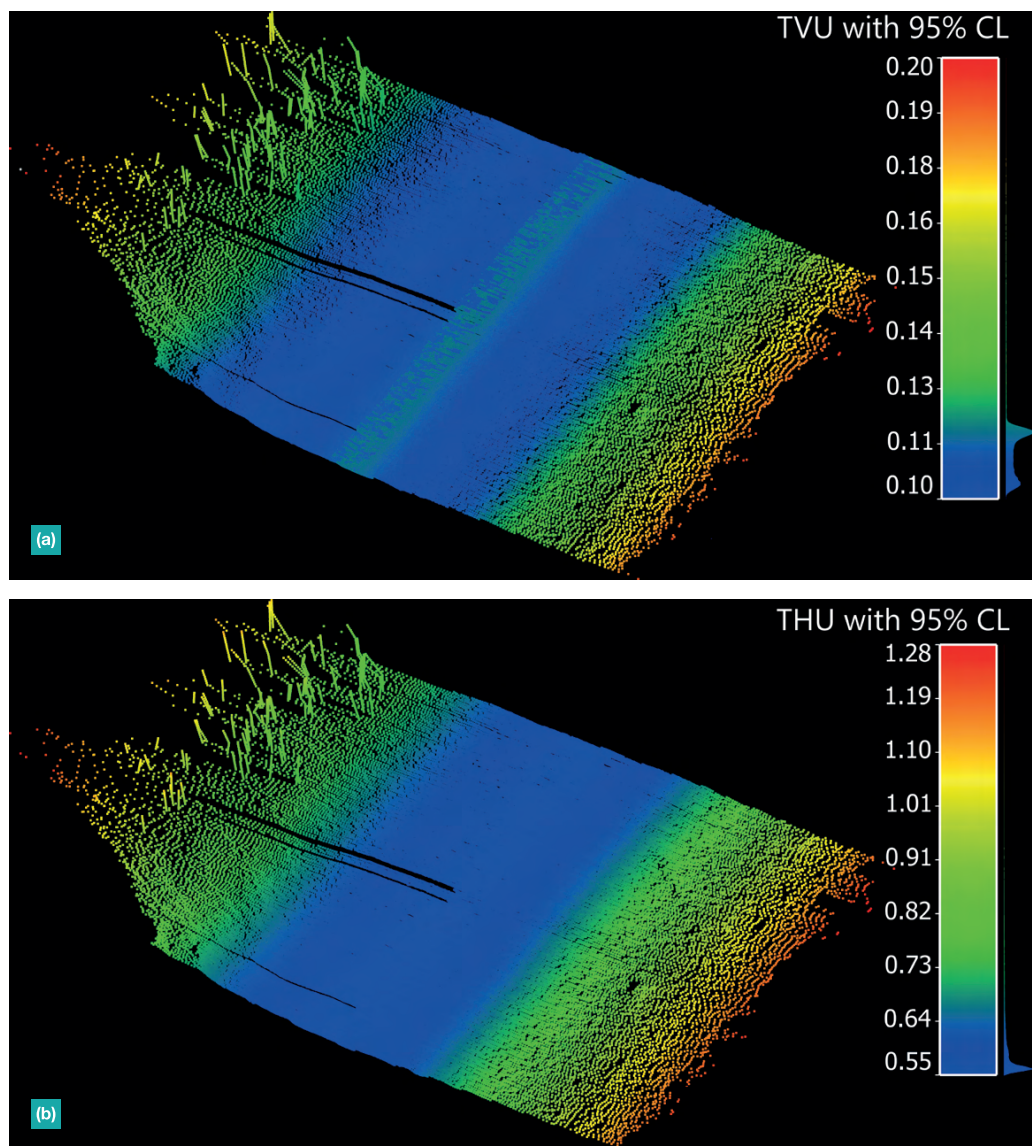


Fig. 7 The results of the MCM uncertainty estimation with 95 % CL for the first 100 profiles: (a) TVU of the first 100 profiles with CL of 95 %. (b) THU of the first 100 profiles with CL of 95 %.

All three predicted uncertainties remain below the THU_{max} threshold defined for Special Order surveys; however, at the swath boundaries, they exceed the stricter 1-meter limit specified for the Exclusive Order.

This research primarily focuses on uncertainty solutions derived from MCM. To assess the plausibility of the estimated TPU values, we analyze the overlap area where the BB and STB transducers record measurements simultaneously. This region offers a valuable opportunity to validate the model's accuracy. The two independent transducers measure the same physical surface in this region under slightly different conditions. Since the modeled uncertainty is expressed at the 95 % CI, we expect that, statistically, approximately 95 % of the measurements from one transducer should fall within the confidence interval predicted by the model using the measurements from the other transducer. Moreover, although the two transducers are internally similar, they are physically separate sensors with independent mounting setups. Small differences in mounting geometry, alignment, and calibration introduce slight variations between their measurements. This diversity further strengthens the validation, as it ensures that the comparison is not perfectly redundant but reflects realistic measurement variability. Fig. 10 presents the overlap area beneath the ship for one profile to evaluate height measurement uncertainty. The uncertainty, estimated using the MCM, is expressed as CI around the absolute height measurements. Fig. 10 demonstrates that a majority of the measurements from each transducer fall within the CI of the other. In Fig. 10a, 87.69 % of the BB transducer's readings align with the confidence bounds of the STB transducer, while in Fig. 10b, 87.48 % of the STB transducer's measurements fall within the BB transducer's CI. Although these percentages do not reach the expected 95 % threshold, they suggest that the overlap area is well-represented by repeated measurements. In just this one presented example, the sample size in the overlap region may not be sufficient to make definitive claims regarding the 95 % CL. We observed similar coverage for other profiles as well. Moreover, as the both transducers operate independently, their different setups could influence their measurements. Despite these factors, the observed overlap percentages provide reasonable validation of the estimated CIs.

The overlap area is also analyzed to assess position uncertainty. Since position uncertainty results from a quadratic combination of uncertainties in the East and North components, it is represented as a two-dimensional confidence region. Consequently, each measured point's uncertainty is expressed as a confidence ellipse. Fig. 11 illustrates the overlap area for position measurements, highlighting the confidence ellipses for points recorded by the BB. The semi-major and semi-minor axes correspond to East and North uncertainties, respectively, with no assumed correlation. As depicted, all STB transducer measurements fall within the

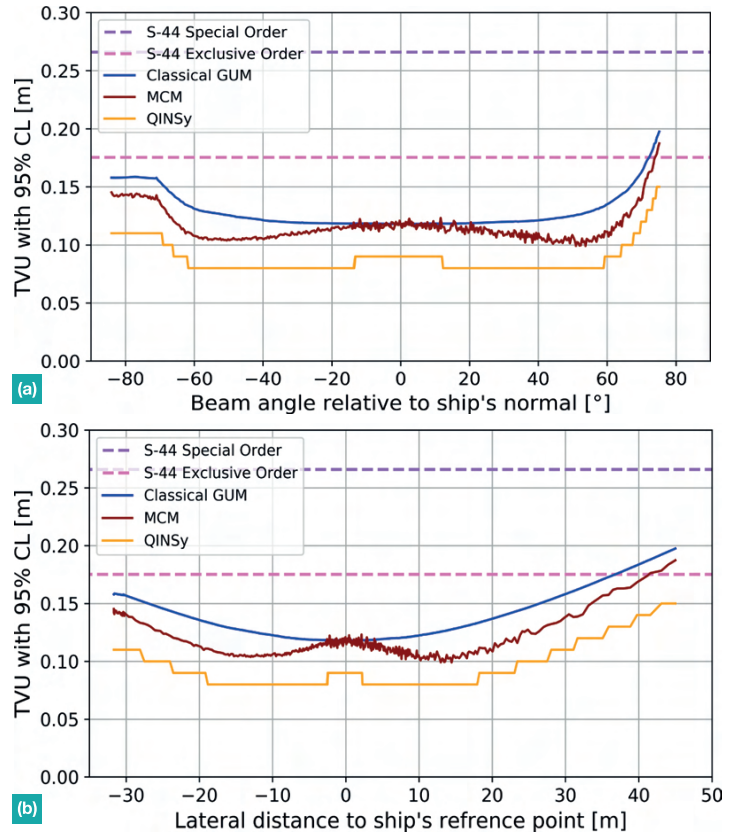


Fig. 8 Extended uncertainty in height for the first profile Measurement with 95 % CL (TVU): (a) TVU versus beam angle relative to ship's vertical. (b) TVU versus lateral distance from ship.

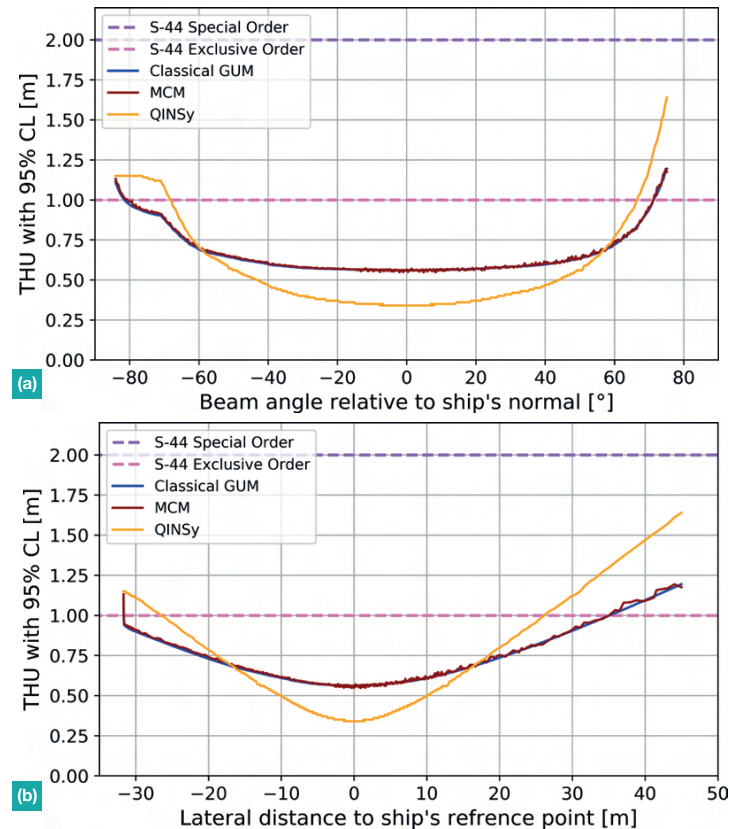


Fig. 9 Extended two-dimensional uncertainty for North and East dimensions of the first profile measurement with 95 % CL (THU): (a) THU versus beam angle relative to ship's vertical. (b) THU versus lateral distance from ship.

BB transducer's confidence ellipses. Unlike the height component, the 2D position measurements achieve a full 100 % overlap within their respective confidence ellipses. This result reinforces the reliability of the position uncertainty estimates obtained through MCM.

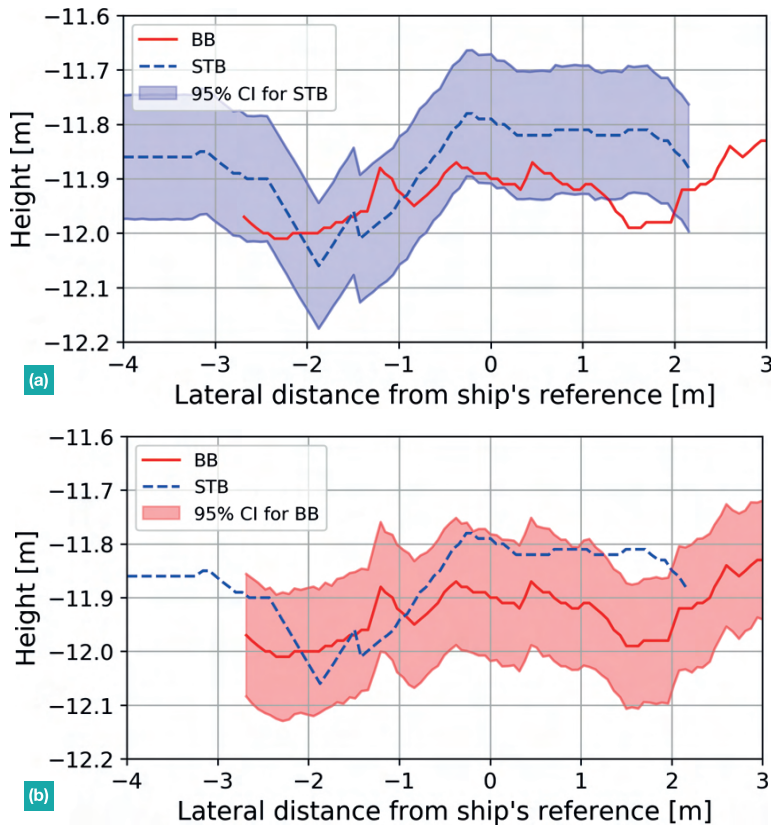


Fig. 10 Measured heights by STB and BB transducers versus their estimated 95 % CI in the overlapping measurement area beneath the ship. (a) CI of the STB transducer. (b) CI of the BB Transducer.

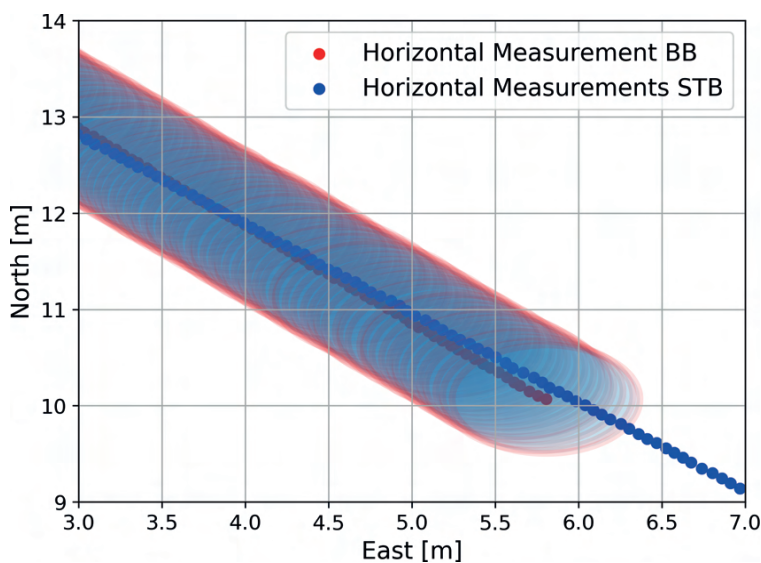


Fig. 11 Measured horizontal coordinates by STB and BB transducers with their corresponding confidence ellipses of overlapping measurement area beneath the ship. East and North are reduced for visualization.

It should be noted that there is no definitive ground truth for either the underwater geometry or the measurement uncertainty. Overall, the overlap analysis supports the validity of the developed uncertainty model. Comparisons with alternative methods further strengthen confidence in the reliability of the estimated TPU values. While systematic differences exist between models, their overall patterns remain consistent. Despite the observed systematic differences between uncertainty model and the commercial software, these deviations do not diminish the usefulness of our results. Since the primary goal of this analysis is to derive weights for the subsequent modeling step, the absolute magnitude of uncertainty is less critical than its relative distribution. The derived uncertainty values are used to construct normalized weights, directly informing the modeling process. Thus, these systematic variations will not negatively influence the outcomes in the second part of this paper. The weighting approach ensures that the subsequent analyses remain robust, as differences in the absolute uncertainty levels do not significantly affect our conclusions or the modeling accuracy presented in the later sections.

A potential empirical approach to characterizing measurement uncertainty in MBES systems would be to perform repeated high-density surveys over a flat and stable area, followed by the generation of a high-resolution averaged gridded surface. Deviations of individual measurements from this reference surface could then be used to estimate the distribution of random errors. Although not explored in the present study, such methods may provide valuable validation or calibration data for future uncertainty modeling.

A key approach to further evaluating this model is through simulation. In the next steps, we use the developed uncertainty model to simulate the ground truth, measurement process, and their corresponding uncertainties, assessing its applicability and reliability.

4 Survey simulator

A major drawback in estimating uncertainties for bathymetric measurements is the unknown geometry of the waterbed. A synthetic dataset is used in this study to overcome this issue. The main idea is to employ a mathematically defined surface to simulate realistic bathymetric measurements. The ground truth surface is defined based on MBA approach by Lee et al. (1997). Our MBA surface is constructed using a set of predefined hierarchical B-Spline functions and is exported as a 3D-PC with equidistant point spacing of 1 cm (Fig. 12).

The simulation environment is implemented in Python using standard libraries like NumPy (Harris et al., 2020) and PyVista (Sullivan & Kaszynski, 2019). Four steps are required to generate a realistic simulated 3D-PC of a waterbed:

1. Transform the generated 3D-PC into a mesh using Delaunay triangulation (Delaunay, 1934).
2. Compute Cartesian coordinates by intersecting

the beams of the echo sounder with the mesh of the waterbed using ray-tracing.

3. Calculate the range and beam angle between the sensor and intersected coordinates on the seabed.
4. Predict realistic uncertainties for the obtained coordinates by forward modeling based on the uncertainty model developed in Section 3, using the parameters described in Table 1.

After creating the original 3D point cloud with a resolution of approximately 1 cm, a Delaunay triangulation mesh with the same resolution (1 cm) was generated. The next step is to compute the coordinates of the simulated measurements on the waterbed. The measurement beams are generated according to the chosen sensor, with equidistant angular steps in the field of view of 120° , and the central beam is directed vertically downward. The environment is assumed to be uniform, and no refraction of the acoustic wave is considered, as is generally valid in shallow water areas. Therefore, each ray is treated as a straight line starting from the transducer in the direction of the beam. The intersection of the beam with the seabed surface is determined using ray-tracing; in cases of multiple intersections, the closest one is selected.

One drawback of using a triangulated mesh for the simulation is the occurrence of triangulation error, which is the difference between the generated ground truth surface and the meshed grid used for beam intersection. This error is intrinsic to the process of converting a smooth, continuous surface (the "ground truth") into a mesh made up of flat, polygonal facets. The error is most pronounced in regions with significant curvature, as the exported points in the triangulation are connected by planar triangles.

The magnitude of this error is influenced by several factors, including the curvature of the original surface, the density of the mesh, and the quality and arrangement of the triangles. In areas with high curvature, flat triangles struggle to capture the intricate details of the surface, resulting in larger errors. While the error can be mitigated by reducing point spacing (thereby increasing mesh density), this approach increases computational cost and memory usage. While the error can be mitigated, it remains present and must be considered in the analysis. The error in Z-direction was eliminated by recalculating the Z value at the determined XY location using the original B-Spline functions, ensuring that the simulated coordinates exactly follow the surface. The reprojection process eliminates XY triangulation errors by fixing the original X and Y coordinates and recomputing the Z value based on the true B-spline surface. Thus, only the Z-coordinate is corrected, and no residual XY positional error remains after reprojection. In addressing triangulation errors, recalculating the mesh coordinates using original surface functions, like B-Splines, offers a powerful method to enhance accuracy. This technique specifically targets errors in one or more dimensions by leveraging the precise mathematical

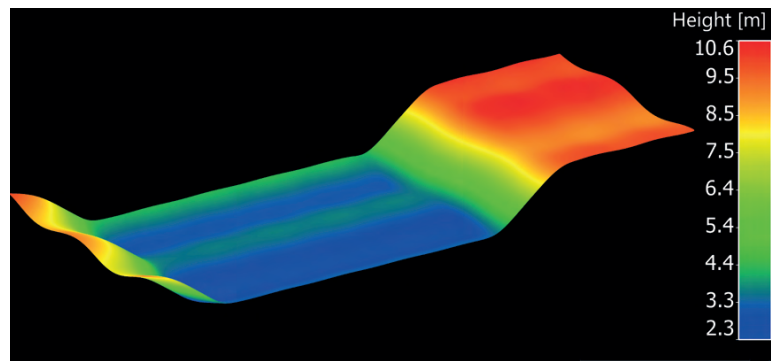


Fig. 12 Simulated geometry as a point cloud. The points are color-coded by the height in meter.

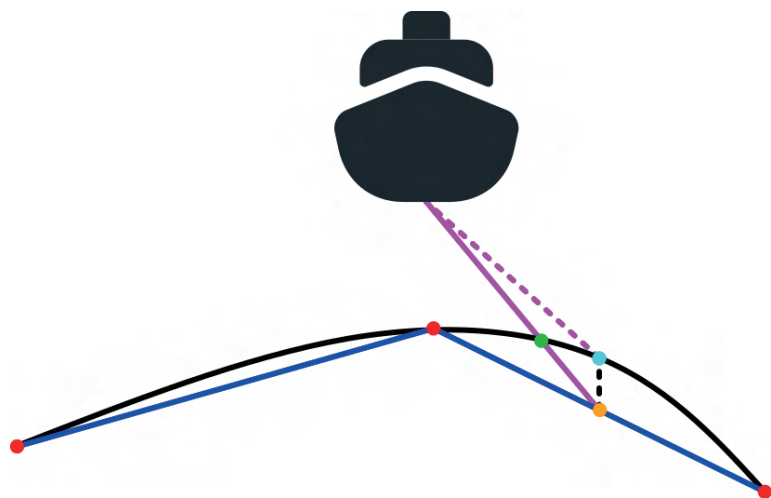


Fig. 13 Triangulation error due to discrepancies between the curved surface and the mesh. The simulated surface is shown in black, the exported point cloud in red dots, and the mesh from Delaunay triangulation in blue. The intersection of the beam (solid magenta line) with the mesh results in the orange point. The desired and true intersection with the surface is shown in green. To eliminate the error in the Z-direction, the orange point is projected onto the surface in the Z-direction and shown in cyan. Subsequently, the beam is recalculated to the new point, which is indicated by the dashed magenta line.

representation of the surface from which the mesh is derived. Subsequently, the range and beam angles are recalculated using the sensor's position, and uncertainties are then predicted. The triangulation error and the projection principle are illustrated in Fig. 13.

For the simulation in this study, a surface with dimensions of 80 m by 20 m and a total variation in Z-direction of 8 m is used. Four parallel trajectories are simulated to capture the entire area and to generate overlapping regions. The trajectories have an average height above the surface of 12 m above the surface and are spaced 20 m apart. The simulated surface and trajectories are shown in Fig. 14. A profile view of a random realization of the simulated measurements is shown in Fig. 15. The overall workflow of the algorithm is presented in Fig. 16.

After intersecting the beam pattern at every sensor position with the surface and recalculating the Z-value, the resulting beam angle and range readings are error-free. Realistic uncertainties are then added using the parameters and methods described

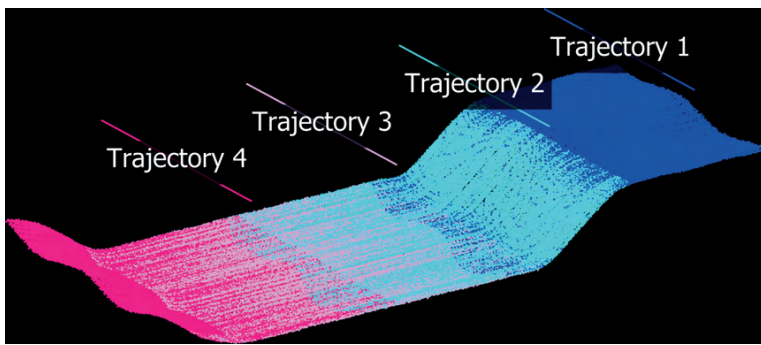


Fig. 14 Simulated measurements along with the four chosen trajectories for the vessel.

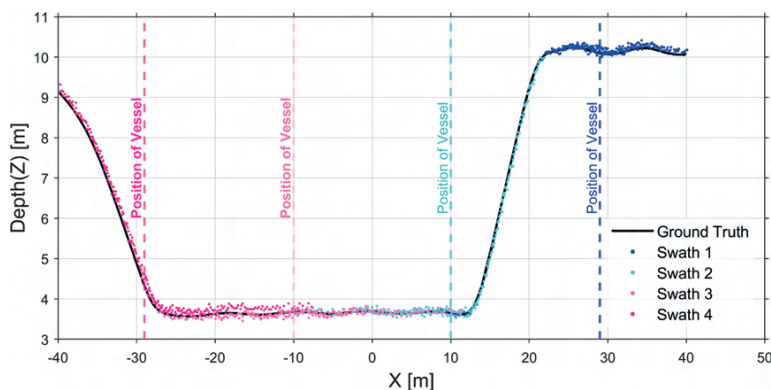


Fig. 15 Profile view of simulated measurements for one realization. The simulated measurements corresponding to different trajectories of the vessel are shown with different colors.

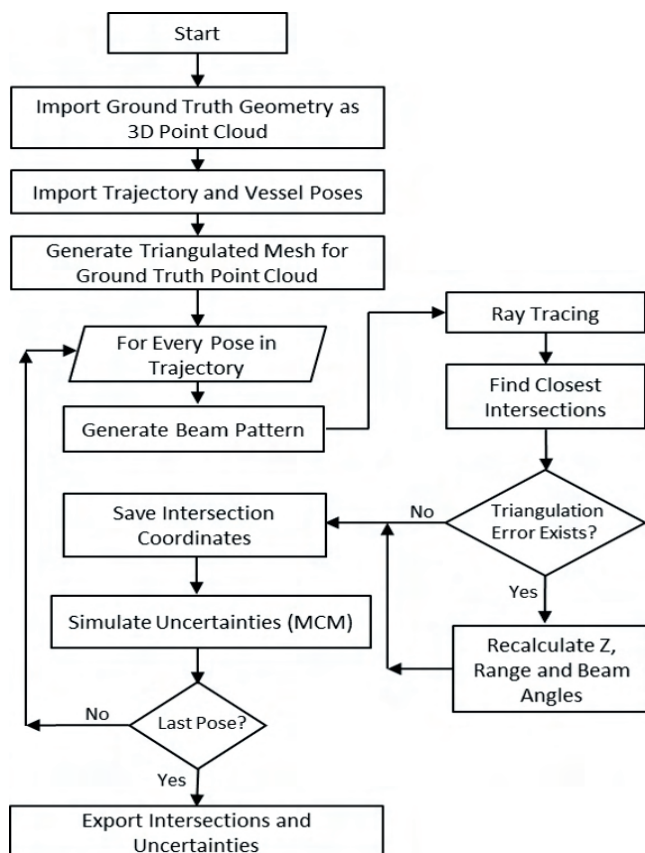


Fig. 16 General algorithm adopted in survey simulator.

in Section 3. This is performed within a Monte-Carlo simulation loop with 1,000 iterations, yielding 1,000 individual realizations for every simulated measurement. This approach facilitates a detailed analysis of the uncertainty budget, the distribution of the uncertainties, and the identification of specific ways to enhance model accuracy and reliability.

5 Measurement uncertainty and DBM

Our goal in this research is to explore how uncertainty information can be used to improve DBMs. To achieve this, we developed a simulation environment in which a known geometry is created using a precise mathematical model representing a theoretical seabed. Within this controlled environment, we simulate the measurement process while incorporating our developed uncertainty model. This setup allows us to obtain measurements that include uncertainties while retaining complete knowledge of the geometry, thereby enabling a detailed analysis of the impact of uncertainty on the final DBM.

The core idea is to integrate the estimated uncertainty information into the modeling process. For this purpose, we first clarify the type of surface model we are focusing on.

5.1 Surface model

Considering the potential complexity of underwater geometry and the characteristics of MBES data – such as high resolution, large volumes, and potential gaps – we require a method that efficiently handles these challenges while minimizing computational complexity. To achieve this, we represent the surface as a 2.5-dimensional (2.5D) model, expressed as:

$$z_0 = f(x_0, y_0) \quad (12)$$

where (x_0, y_0, z_0) represents a point on the surface.

To model this surface, we adapt MBA by Lee et al. (1997). The MBA method is based on hierarchical tensor product B-spline surfaces. Any point on the surface is a linear combination of control points and cubic basis functions. The B-Spline surface is defined by a grid of control points, denoted as Φ , which lies parallel to the XY-plane. The positions of these control points are predefined on the grid, serving as the basis for constructing the surface representation. To approximate the surface $f(x,y)$, it is necessary to determine the unknown elements of Φ . This problem is structured as a linear Gauß-Markov Model (GMM), as expressed in Eq. 13 (Mohammadiojdan et al. (2024)). In this formulation, \mathbf{z} represents the observation vector, while \mathbf{v} denotes the residual vector. The matrix \mathbf{A} is a full-rank design matrix, and Φ is the vector of unknown parameters.

$$\mathbf{z} + \mathbf{v} = \mathbf{A}\Phi \quad (13)$$

The Φ can be estimated by minimizing the sum of the squared residuals, according to Eq. 14. If

the assumption is that the observations are equally weighted and uncorrelated, the weight matrix \mathbf{P} will be an identity matrix. If information about the uncertainty of the observations is available, this \mathbf{P} is derived as the inverse of the Variance-Covariance Matrix $\mathbf{\Sigma}$ of the observations, allowing the model to account for varying observation uncertainties. In Eq. 15, $\mathbf{\Sigma}_z$ represents the Variance-Covariance Matrix of the observations, structured as follows:

$$\hat{\phi} = (\mathbf{A}^T \mathbf{P} \mathbf{A})^{-1} \mathbf{A}^T \mathbf{P} \mathbf{z} \tag{14}$$

$$\mathbf{\Sigma}_z = \begin{bmatrix} \sigma_{z_1}^2 & 0 & 0 & 0 \\ 0 & \sigma_{z_2}^2 & 0 & 0 \\ \vdots & \vdots & \ddots & 0 \\ 0 & 0 & \dots & \sigma_{z_n}^2 \end{bmatrix} \tag{15}$$

The assumption that observations remain uncorrelated is still maintained. Incorporating the weight matrix in this way enhances the robustness of the parameter estimation, ensuring a more reliable solution while accounting for observational uncertainties.

It should be noted that GMM does not directly estimate a posteriori variance factor $\hat{\sigma}_0^2$ (cf. Benning, 2011, p. 144). Therefore, for evaluating the adjustment, $\hat{\sigma}_0^2$ is estimated based on $\hat{\phi}$ the updated residuals $\hat{\mathbf{v}}$ as follows:

$$\hat{\mathbf{v}} = \mathbf{A} \hat{\phi} - \mathbf{z} \tag{16}$$

$$\hat{\sigma}_0^2 = \frac{\hat{\mathbf{v}}^T \mathbf{P} \hat{\mathbf{v}}}{n - u} \tag{17}$$

where n is the number of observations and u is the number of unknowns.

5.2 Monte-Carlo simulation experiment

To assess the impact of incorporating uncertainties in the model estimation process, we utilize our survey simulator (see Section 4). However, a single simulation scenario is insufficient for drawing reliable conclusions; therefore, we conduct a Monte-Carlo simulation experiment, in which the entire process is repeated multiple times. By analyzing a large number of iterations, we derive more robust inferences and assessments.

In each iteration, both the geometry and the associated uncertainties are simulated and the data are modeled using MBA. Two versions of the model are generated: one that integrates uncertainty information into the estimation process and another that does not. This comparative approach allows us to assess the effect of incorporating uncertainty on model accuracy and reliability. After numerous repetitions, we determine the optimal model and extract additional insights, such as CIs or uncertainty maps, providing a clearer understanding of the model's precision. Fig. 17 illustrates the general algorithm for the adopted Monte-Carlo simulation experiment. In this algorithm,

N represents the number of Monte-Carlo iterations, which is set to 1,000 in our study.

5.3 Results and discussion

In the initial step, the focus is on evaluating model quality and associated errors in an ideal scenario assuming no measurement error is present. Although the ground-truth geometry described in Section 4 was generated using MBA functions, and the simulated data were also modeled with an MBA approach, the resulting model does not exhibit zero error. Even in the absence of simulated measurement noise, the estimated surface retains some inaccuracy. This is because the ground-truth surface was generated using a multi-layered MBA construction to introduce local deviations, while the subsequent surface approximation used a selected model complexity without reverse-engineering the original structure. Therefore, a residual modeling error naturally remains even in the absence of simulated measurement noise. This effect is expected and is analogous to real-world modeling situations where the true surface structure is unknown. These inaccuracies can arise in the simulation step or the modeling step; the simulated point cloud inherently exhibits variations in

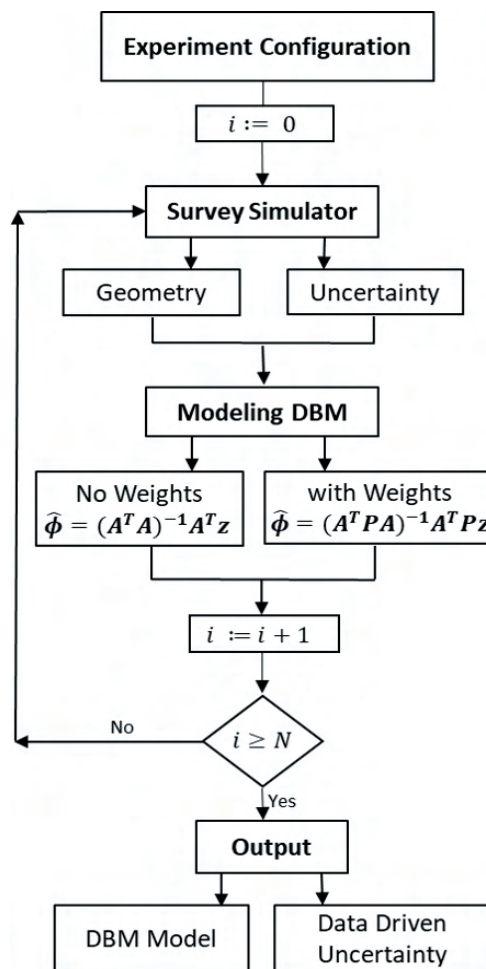


Fig. 17 The general algorithm for the Monte-Carlo simulation experiment.

point density and spatial distribution due to survey parameters, including sensor specifications, water depth, vessel speed, measurement angles, and the underlying geometry of the waterbed. Consequently, these factors result in a non-uniform distribution of data points, inevitably affecting the final model. Additionally, selecting an appropriate model complexity is critical; an excessive number of control points might lead to overfitting, especially if the dataset includes noise or outliers. Thus, choosing the optimal model complexity requires carefully balancing smoothness against accuracy.

To assess model quality, we can look into model error as the spatial distance between the modeled point cloud and the ground truth, either represented as a 3D distance or separately along the X, Y, and Z axes. Of particular interest are the distribution, mean, and Root Mean Squared Error (RMSE) of this error. Fig. 18 illustrates the simulated PC generated by the survey simulator under conditions with zero measurement uncertainty. The points are color-coded according to the magnitude of the 3D model error, representing the distance between the estimated model and the ground truth. The mean model error in this scenario is 0.1 mm, with an RMSE of 3 mm, confirming that, despite being small, a model error clearly exists.

In the experiment, each point in the simulated dataset ends up with 1,000 realizations along the X, Y, and Z components. For each component, we compute the uncertainty value σ , defined as the standard deviation corresponding to the 68 % CL of the distribution. As described in Section 4, the uncertainties are simulated based on the developed uncertainty model in Section 2. Convergence of the Monte Carlo simulations was assessed by monitoring the stability of the estimated mean and standard deviation over increasing numbers of iterations. Statistical metrics stabilized after approximately 800–1,000 iterations, confirming that 1,000 simulations were sufficient. The selected surface modeling approach (MBA) represents a 2.5D model. Like other 2.5D DBMs, its primary emphasis lies on uncertainty in the vertical Z direction. To better visualize and evaluate the impact of vertical uncertainties, we chose uncertainty values of approximately (0.02, 0.02, 0.06) m for position

$(X_{Pose}, Y_{Pose}, Z_{Pose})$ components, respectively. Notice that ratio of the positional uncertainty to vertical one is lower than the real data in the simulation. This was done to minimize the influence of large horizontal positioning errors and better isolate and assess the effect of the modeling process on the vertical (z) component, which was the main focus of this study. The horizontal uncertainties were kept at low levels to avoid masking or distorting the analysis of vertical uncertainty propagation. Fig. 19 illustrates these uncertainties separately for each component (X, Y, and Z) and for each point individually. Fig. 19 provides an XY view of the simulated data points, color-coded according to uncertainty magnitude. It clearly shows that the uncertainty in the Z component (height) is dominant compared to X and Y. In Fig. 19d we see the combined standard uncertainty of the MC simulations. In which the uncertainty is calculated as,

$$\sigma_{XYZ} = \sqrt{\sigma_X^2 + \sigma_Y^2 + \sigma_Z^2} \quad (18)$$

It is important to note that the difference between this uncertainty measure and the TPU values is that TPU refers specifically to extended uncertainties, which are calculated by Eqs. 9 and 10.

This uncertainty information is utilized to construct the weight matrix required for the GMM adjustment. It's important to note that the MBA model is essentially a 2.5D representation, with parameters estimated by minimizing errors specifically in the Z-direction. MBA inherently cannot fully capture or exploit the complete 3D structure of positional uncertainties. This modeling simplification may lead to some loss of fidelity, particularly when significant horizontal errors are present. Consequently, for constructing the weight matrix, we primarily use the estimated uncertainty σ_z , as shown in Fig. 19c (refer to Eq. 15). However, in reality – as well as in our simulations – uncertainty exists in all three spatial dimensions. Even though the MBA model does not explicitly estimate parameters in the X and Y directions, uncertainties in these dimensions can still impact model quality. For this reason, we also explore a scenario in which observations are weighted based on the combined uncertainty σ_{XYZ} . In total, we consider three scenarios in our analysis:

- Case 1: No weighting applied during adjustment
- Case 2: Observations weighted based only on vertical uncertainty σ_z (Eq. 15)
- Case 3: Observations weighted using full 3D uncertainty σ_{XYZ} (Eq. 18)

Comparing these three scenarios allows us to assess not only the general effectiveness of applying uncertainty-based weights but also whether including full 3D uncertainties can meaningfully improve our results for a model inherently focused on vertical accuracy.

Here, we further investigate the Monte-Carlo simulation results, specifically examining the detailed distribution of errors. We consider both the adjustment quality and the difference between the estimated

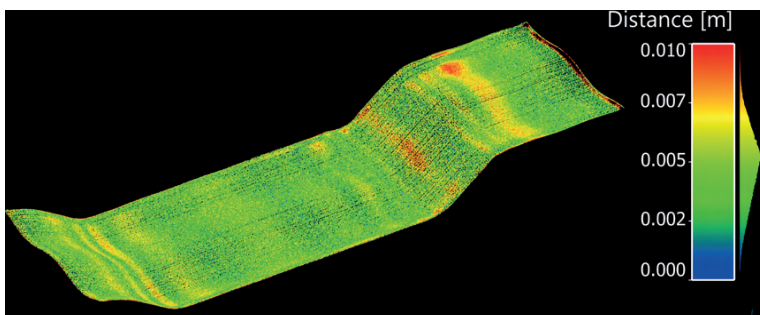


Fig. 18 Simulated PC color-coded by the magnitude of 3D model error (distance between modeled points and ground truth geometry). Simulation performed with zero measurement uncertainty.

model and ground truth. The adjustment quality is evaluated using the residual differences between observations and the estimated model, quantified by root of a posteriori variance factor $\hat{\sigma}_0$ (see Eq. 17). These error distributions are presented in Fig. 20.

The gray histogram represents the distribution of simulated errors, specifically the vertical (Z-direction), distances between simulated points and the ground truth. This distribution is approximately normal, with an RMSE of 0.09 m. The error distributions from all three modeling scenarios align closely with the simulated error distribution, indicating that each scenario effectively captures the error structure. Furthermore, all three adjustment scenarios yield very similar values for the a-posteriori variance factor: 0.081 m, 0.087 m, and 0.078 m for Cases 1, 2, and 3, respectively. These nearly identical values suggest that the application of weights, whether based solely on vertical uncertainty or combined 3D uncertainty, does not significantly impact the overall adjustment quality.

We further assess model quality by evaluating the difference between the estimated model and the ground truth, specifically the vertical (Z-direction), quantified by RMSE of these errors σ_{Model} . Fig. 21 presents the corresponding distributions of these errors for all three cases. In each scenario, the model error is consistently less than half of the a-posteriori variance factor $\hat{\sigma}_0$, indicating that the estimated model gives a much better estimation of the ground truth. The unweighted scenario (Case 1) has the largest error, with $\sigma_{\text{Model}} = 0.044$ m, and its distribution shows clear asymmetry, suggesting the presence of bias. Introducing weighting significantly reduces the error and improves symmetry in the distribution. Case 2, weighted by vertical uncertainty σ_z , achieves the smallest model error, $\sigma_{\text{Model}} = 0.023$ m, demonstrating a narrower and more symmetric distribution. Case 3, weighted by full 3D uncertainty σ_{xyz} , also shows substantial improvement over the unweighted case ($\sigma_{\text{Model}} = 0.032$ m), although its error reduction is slightly less pronounced than in Case 2. These quantitative results are summarized in Table 2. These results highlight that applying uncertainty-based weighting enhances model quality by reducing bias and improving error symmetry. Interestingly, the slightly better performance of Case 2 compared to Case 3 might stem from the inherent nature of the MBA approach as a 2.5D modeling method, which primarily optimizes vertical accuracy. Although considering full 3D uncertainties (Case 3) clearly benefits the model, the inherent vertical emphasis of the MBA model means that its greatest accuracy gains come specifically from weighting by vertical uncertainties. This improves overall results in terms of distribution characteristics, and error symmetry. These subtle improvements in modeling accuracy, summarized in Fig. 21, underscore the importance of selecting appropriate uncertainty weighting – even when ground-truth data are unavailable and biases might otherwise remain unnoticed.

Table 2 Summary of results for Monte-Carlo simulation. is root of "a-posteriori variance factor" (see Eq. 17) and σ_{Model} is RMSE of difference between the estimated model and the ground truth.

	Error [m]		
	Case 1	Case 2	Case 3
$\hat{\sigma}_0$	0.081	0.087	0.078
σ_{Model}	0.044	0.023	0.032

We further leverage the Monte-Carlo simulation results to create CI, enabling us to produce a detailed assessment of model quality. Each simulated realization generates slight variations in modeled values at each point, and by analyzing these variations, we can derive a meaningful CI. Fig. 20 illustrates a CI with a 95 % CL. The figure shows an XY view of the modeled area, with each point color-coded according to the length of its CI.

Comparing this CI map to the uncertainty distribution in Fig. 22, we observe an interesting difference: while the original uncertainties are highest near the edges of each survey swath – primarily due to unfavorable measurement angles – the modeled CIs are actually lower in these boundary regions. This apparent discrepancy arises because the boundaries of adjacent swaths overlap, providing redundant observations that help reduce the uncertainty and improve modeling accuracy, despite initially poorer measurement quality due to higher incidence angles. Thus, these overlapping areas offer enhanced information density, resulting in a higher-quality model with smaller uncertainties, even where individual measurements originally exhibited higher uncertainty.

These CI maps highlight areas with sufficient data coverage and indicate critical regions where data reliability might otherwise be overlooked. This provides users with a powerful visual tool for decision-making, aiding in strategic interpretation and effective risk identification. The generated CI maps have several practical applications. For survey planning, realistic simulation of measurement uncertainty allows surveyors to predict coverage quality, identify areas where higher uncertainties are expected, and optimize survey parameters such as vessel routes, ping rates, and swath overlap. In terms of confidence mapping, the method produces detailed spatial uncertainty maps that incorporate both measurement and modeling errors, allowing users to generate IHO S-44 compliance layers or internal quality indicators for the delivered bathymetric products. Furthermore, for real-time QA/QC, the approach could be adapted to provide near real-time estimates of expected uncertainty during data acquisition. This would allow operators to dynamically adjust survey settings if quality thresholds are not being met.

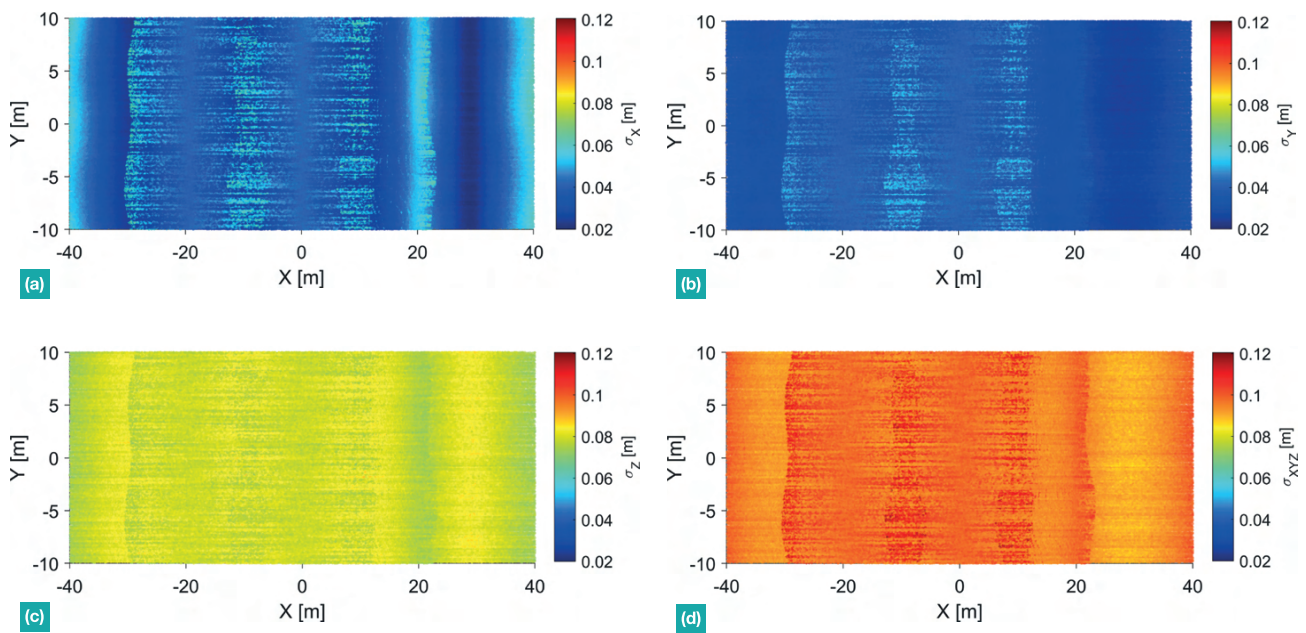


Fig. 19 Estimated uncertainties for each point in Monte-Carlo simulation: (a) uncertainty σ_x in X (Mean = 0.03 m), (b) uncertainty σ_y in Y (Mean = 0.03 m) and (c) uncertainty σ_z in Z (Mean = 0.08 m) and (d) combined uncertainties σ_{xyz} (Mean = 0.09 m) for each point.

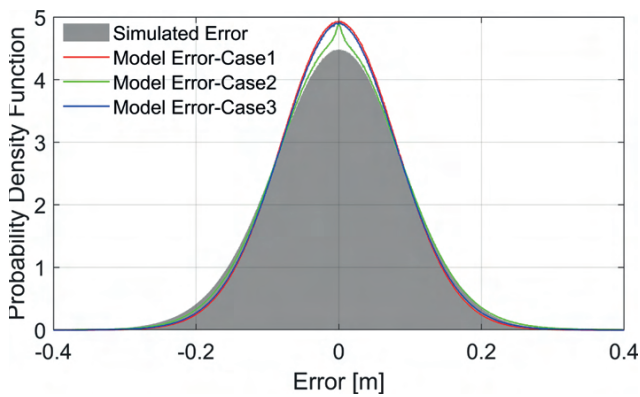


Fig. 20 Histogram of errors after Monte-Carlo simulation. Error measure here is the difference between observations and the estimated model.

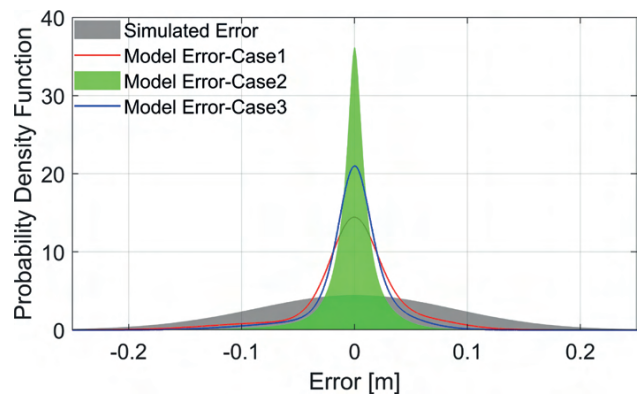


Fig. 21 Histogram of errors after Monte-Carlo simulation. Error measure here is the vertical difference between the estimated model and the ground truth.

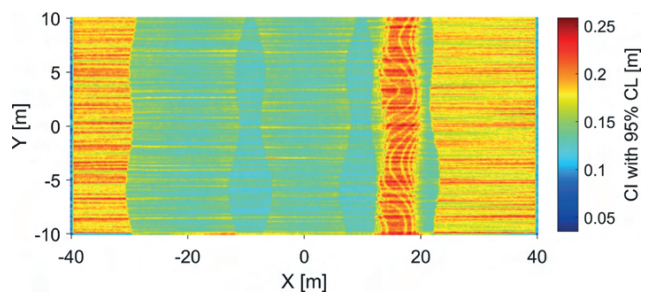


Fig. 22 CI map with a 95 % CL of the model derived from Monte-Carlo simulations. Each point is color-coded according to the magnitude of its CI, highlighting regions of high and low model uncertainty.

6 Conclusion

This study is divided into two parts. In the first part, we developed and evaluated a model to predict uncertainties for a hydrographic survey system. Although the measurement model was designed for a specific survey vessel, the underlying concept and workflow are adaptable to other systems equipped with MBES. Our analysis involved defining uncertainty measures according to classical GUM guidelines and conducting extensive Monte-Carlo simulations. The results indicated strong agreement between the two methods, confirming their consistency. However, MCM offers notable advantages over the classical approach, which is less effective for highly nonlinear measurement models and requires complex partial derivatives, MCM accommodates various PDF distributions and provides uncertainty estimates directly as a complete PDF, enabling more extensive analysis. To validate our developed uncertainty model, we compared its results to those obtained from a commercial software solution. Although the overall uncertainty patterns were generally compatible, systematic deviations were observed, likely due to differences in model parameters and assumptions. These discrepancies, however, do not compromise the primary goal of generating relative weights for subsequent modeling steps, ensuring that the later analyses remain robust and reliable.

In the second part of the study, we developed a survey simulator to generate measurements that incorporate uncertainties derived from our model. This controlled environment allowed us to validate the modeled data against known ground-truth values. Using a Monte-Carlo experiment, we assessed the quality of DBMs by incorporating uncertainty information to weight observations during modeling. The results demonstrated that integrating accurate uncertainty information improved the overall accuracy and

reliability of the models. Although the numerical improvements may be subtle, they significantly enhance confidence in the resulting models. Additionally, the uncertainty data facilitated the creation of quality maps accompanying the DBMs, which effectively highlight regions of varying reliability and provide practical guidance for future survey planning and data interpretation. The generalizability of the simulation framework depends on the validity of the underlying physical models for uncertainty estimation (e.g., Hare, 1995; Wirth, 2011). Significant variations in measurement conditions or system behavior may require adjustment of simulation parameters or model structures to maintain accuracy.

While in this study we used synthetic surfaces to provide a precisely controlled ground truth, future work should explore the application of the proposed uncertainty modeling framework to real-world surfaces derived from dense MBES surveys. This would allow evaluation of model performance under more realistic and complex seabed conditions.

Further investigation of this experiment using a full 3D surface model is recommended. While the MBA model effectively represents 2.5D surfaces, it does not fully capture or propagate full 3D positional uncertainties. This limitation may constrain the fidelity of uncertainty integration, particularly in environments with strong three-dimensional variability. Further investigation using a full 3D surface model and comprehensive 3D uncertainty propagation is recommended. The application of a comprehensive 3D model, along with full-scale 3D uncertainties, has the potential to yield more profound insights into the manner in which uncertainty information influences model performance and accuracy. This analysis could more effectively reveal the benefits of incorporating uncertainties directly into the modeling process.

References

- Abubakar, A. A. and Poerbandono, P. (2023). Effectiveness of vertical error budget model for portable multi-beam echo-sounder in shallow water bathymetric survey. *IOP Conference Series: Earth and Environmental Science*, 1245(1):012041. <https://doi.org/10.1088/1755-1315/1245/1/012041>
- Alkhatib, H., Neumann, I. and Kutterer, H. (2009). Uncertainty modeling of random and systematic errors by means of Monte Carlo and fuzzy techniques. *Journal of Applied Geodesy*, 3, pp. 67–79. <https://doi.org/10.1515/JAG.2009.008>.
- Arnold, J. and Shaw, S. (1993). A surface weaving approach to multibeam depth estimation. *Proceedings of OCEANS'93. II-95*.
- Benning, W. (2011). *Statistik in Geodäsie, Geoinformation und Bauwesen* (4. Aufl.). Berlin, Offenbach: Wichmann.
- BFG (2013). *Neue Entwicklungen in der Gewässervermessung*. Kolloquium am 20./21. November 2012 in Koblenz. – Veranstaltungen 5/2013, Koblenz, Mai 2013, 104 S. https://doi.org/10.5675/BfG_Veranst_2013.5
- Bisquay, H., Freulon, X., De Fouquet, C. and Lajaunie, C. (1998). Multibeam data cleaning for hydrography using geostatistics. *IEEE Oceanic Engineering Society, OCEANS'98. Conference Proceedings (Cat. No.98CH36259)*. pp. 1135–1143. <https://doi.org/10.1109/OCEANS.1998.724413>
- Björke, J. T. and Nilsen, S. (2009). Fast trend extraction and identification of spikes in bathymetric data. *Computers & Geosciences* 35, pp. 1061–1071. <https://doi.org/10.1016/j.cageo.2008.05.009>
- Bottelier, P., Briese, C., Hennis, N., Lindenbergh, R. and Pfeifer, N. (2005). Distinguishing features from outliers in automatic Kriging-based filtering of MBES data: a comparative study. In P.



- Renard and H. Demougeot-Renard (Eds.), *Geostatistics for environmental applications* (pp. 403–414). Berlin and Heidelberg: Springer. https://doi.org/10.1007/3-540-26535-x_34
- Bureick, J., Alkhatib, H. and Neumann, I. (2016). Robust Spatial Approximation of Laser Scanner Point Clouds by Means of Free-form Curve Approaches in Deformation Analysis. *Journal of Applied Geodesy*, 10, pp. 27–35. <https://doi.org/10.1515/jag-2015-0020>
- Delaunay, B. (1934). Sur la sphère vide: Bull. Acad. Science USSR VII, Clas. Sci. Mat. Nat, pp. 793–800.
- Eakins, B. W. and Taylor, L. A. (2010). Seamlessly integrating bathymetric and topographic data to support tsunami modeling and forecasting efforts. *Ocean globe*, pp. 37–56.
- Erdogan, S. (2009). A comparison of interpolation methods for producing digital elevation models at the field scale. *Earth Surface Processes and Landforms*, 34: pp. 366–376. <https://doi.org/https://doi.org/10.1002/esp.1731>
- Haji Mohammadloo, T., Snellen, M. and Simons, D. G. (2018). Multi-beam echo-sounder bathymetric measurements: Implications of using frequency modulated pulses. *The Journal of the Acoustical Society of America*, 144, pp. 842–860. <https://doi.org/10.1121/1.5050816>
- Haji Mohammadloo, T., Snellen, M., Amiri-Simkooei, A. and Simons, D. G. (2019). Assessment of reliability of multi-beam echo-sounder bathymetric uncertainty prediction models. *Proceedings of the 5th Underwater Acoustics Conference and Exhibition*, pp.783–790, Crete, Greece.
- Hare, R. (1995). Depth and Position Error Budgets for Multibeam Echosounding. *The International Hydrographic Review*, 72(2), <https://journals.lib.unb.ca/index.php/ihr/article/view/23178> (last accessed 4 May 2025).
- Hare, Rob, Eakins, B. W. and Amante, C. J. (2011). Modelling Bathymetric Uncertainty. *The International Hydrographic Review*, 6. <https://journals.lib.unb.ca/index.php/ihr/article/view/20888> (last accessed 4 May 2025).
- Harris, C. R., Millman, K. J., van der Walt, S. J., Gommers, R., Virtanen, P., Cournapeau, D., Wieser, E. et al. (2020). Array programming with NumPy. *Nature* (Springer Science and Business Media LLC), 585, pp. 357–362. <https://doi.org/10.1038/s41586-020-2649-2>
- IHO (2022). *Standards for Hydrographic Surveys* (ed. 6.1). IHO Special Publication S-44, International Hydrographic Organization, Monaco. https://iho.int/uploads/user/pubs/standards/s-44/S-44_Edition_6.1.0.pdf (last accessed 4 May 2025).
- ISO/GUM (1995). *Guide to the Expression of Uncertainty in Measurement*. Standard, International Organization for Standardization, Geneva, CH.
- ISO/GUM (1998). *Guide to the Expression of Uncertainty in Measurement (GUM) – Supplement 1: Numerical Methods for the Propagation of Distributions*. Standard, International Organization for Standardization, Geneva, CH.
- Lee, S., Wolberg, G. and Shin, S. Y. (1997). Scattered data interpolation with multilevel B-splines. *IEEE transactions on visualization and computer graphics*, 3, pp. 228–244.
- Lorenz, F., Artz, T., Brüggemann, T., Reich, J., Weiß, R. and Winterscheid, A. (2021). Simulation-based evaluation of hydrographic data analysis for dune tracking on the River Rhine. *PFG–Journal of Photogrammetry, Remote Sensing and Geoinformation Science*, 89(2), pp.111–120.
- Maleika, W. (2013). The influence of track configuration and multi-beam echosounder parameters on the accuracy of seabed DTMs obtained in shallow water. *Earth Science Informatics*, 6, pp. 47–69. <https://doi.org/10.1007/s12145-013-0111-9>
- Maleika, W., Palczynski, M. and Frejlichowski, D. (2012). Effect of Density of Measurement Points Collected from a Multibeam Echosounder on the Accuracy of a Digital Terrain Model. In J.-S. Pan, S.-M. Chen and N. T. Nguyen (Eds.), *Intelligent information and database systems* (pp. 456–465). Berlin: Springer. https://doi.org/10.1007/978-3-642-28493-9_48
- Maune, D. F., Kopp, S. M., Crawford, C. A. and Zervas, C. E. (2007). *Digital elevation model technologies and applications: The DEM users manual*. Bethesda, MD: American Society for Photogrammetry and Remote Sensing, ASPRS.
- Mohammadivojdan, B., Alkhatib, H., Brockmeyer, M., Jahn, C.-H. and Neumann, I. (2020). *Surface Based Modelling of Ground Motion Areas in Lower Saxony*. Institutionelles Repositorium der Leibniz Universität Hannover. <https://doi.org/10.15488/9344>
- Mohammadivojdan, B., Brockmeyer, M., Jahn, C.-H., Neumann, I. and Alkhatib, H. (2021). Regional Ground Movement Detection by Analysis and Modeling PSI Observations. *Remote Sensing*, 13, 2246. <https://doi.org/10.3390/rs13122246>
- Mohammadivojdan, B., Lorenz, F., Artz, T., Weiß, R., Hake, F., Alkhatib, Y., Neumann, I. and Alkhatib, H. (2024). Robust algorithm for automatic surface-based outlier detection in MBES point clouds. *Marine Geodesy*, 48(2), pp. 141–172. <https://doi.org/10.1080/01490419.2024.2408684>
- Paquet, R. (2010). Estimation of interpolation error in DEMs using statistical methods. *FIG Congress 2010 – Facing the Challenges–Building the Capacity*.
- Piegl, L. (1997). *The NURBS Book* (2nd ed.). Berlin and Heidelberg: Springer. <https://doi.org/10.1007/978-3-642-59223-2>
- QPS (2025). *QPS QINSy*. <https://qps.nl/qinsy/> (last accessed 10 March 2025).
- Rishikeshan, C. A., Katiyar, S. K. and Vishnu Mahesh, V. N. (2014). Detailed Evaluation of DEM Interpolation Methods in GIS Using DGPS Data. *2014 International Conference on Computational Intelligence and Communication Networks*, pp. 666–671. <https://doi.org/10.1109/CICN.2014.148>
- Schwarz, W. (2020a). Methoden zur Bestimmung der Messunsicherheit nach GUM – Teil 1. *AVN Allgemeine Vermessungs-Nachrichten*, pp. 69–86.
- Schwarz, W. (2020b). Methoden zur Bestimmung der Messunsicherheit nach GUM – Teil 2. *AVN Allgemeine Vermessungs-Nachrichten*, pp. 211–219.
- Sullivan, C. B. and Kaszynski, A. (2019). PyVista: 3D plotting and mesh analysis through a streamlined interface for the Visualization Toolkit (VTK). *Journal of Open Source Software*, 4, 1450. <https://doi.org/10.21105/joss.01450>
- Tengku A., Afrizal, T., Abbas, M. A., Mustafar, M. A., Said, M. S. M., Hashim, N. M. and Sulaiman, S. A. (2022). Investigating the Vertical Uncertainty in MBES Measurements. *2022 IEEE 18th International Colloquium on Signal Processing & Applications (CSPA)*, pp. 431–435. <https://doi.org/10.1109/CSPA55076.2022.9781857>
- Wirth, H. (2011). *Messunsicherheiten in der Gewässer Vermessung* [Tech. rep.]. BfG-Bericht 1734.
- Włodarczyk-Sielicka, M., Lubczonek, J. and Stateczny, A. (2016). Comparison of selected clustering algorithms of raw data obtained by interferometric methods using artificial neural

- networks. 2016 17th International Radar Symposium (IRS), pp. 1–5. <https://doi.org/10.1109/IRS.2016.7497290>
- WSA (2023). *Peilschiff Uwe Jens Lormsen*. Wasserstraßen- und Schifffahrtsamt Elbe-Weser. https://www.wsa-elbe-nordsee.wsv.de/Webs/WSA/Elbe-Nordsee/DE/1_Wasserstrassen/4_SchiffeMaschinenwesen/UJLormsen/ujlormsen_node.html (last accessed 5 January 2024).
- Yang, C.-S., Kao, S.-P., Lee, F.-B. and Hung, P.-S. (2004). Twelve different interpolation methods: A case study of Surfer 8.0. *Proceedings of the XXth ISPRS congress*, pp. 778–785.

Authors' biographies

Bahareh Mohammadivojdan received her M. Sc. in Geodesy and Geoinformatics from Leibniz University Hannover in 2019 and is currently a researcher at the Geodetic Institute of the same university. Her work focuses on engineering geodesy and geodetic data analysis, with research interests including mathematical surface approximation, uncertainty modeling, and the analysis of geospatial data for hydrographic and topographic applications. <https://orcid.org/0000-0002-0648-1162>



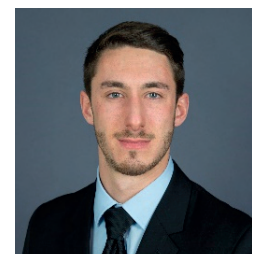
Bahareh Mohammadivojdan

Dr.-Ing. Frederic Hake pursued his studies in the field of geodesy and geoinformatics at Leibniz University Hannover. He was employed at the Geodetic Institute, Leibniz University Hannover, where he completed his doctorate in 2024, undertaking research in the field of damage detection in buildings using machine learning techniques. Since 2024 he has been employed by Allsat GmbH, where he has been engaged in a number of activities, including the monitoring of ground movements and the infrastructural monitoring of risk structures. <https://orcid.org/0000-0001-7424-2270>



Frederic Hake

Felix Lorenz graduated with an M. Sc. degree in Geodesy and Geoinformation from the University of Bonn in 2016. Currently he is working in the Department Geodesy and Remote Sensing of the Federal Institute of Hydrology in Germany as a member of the hydrographic survey working group. He gathered knowledge and experience in the field of dune tracking as a member of the research and development project MAHyD (morphodynamic analyses using hydroacoustic data). In his current position he works consulting the German Waterways and Shipping Administration concerning hydrographic data analysis and sensor specifications.



Felix Lorenz



Jan Ole Böllert

Jan Ole Böllert studied Geodesy and Geoinformatics at Leibniz University of Hannover. He graduated with a Master Thesis on "Uncertainty Modelling of Echosounder Measurements". Since 2024 he is employed at the Saxon State Ministry of Infrastructure and Regional Development (SMIL) in Dresden for a technical traineeship for civil service in surveying..



Robert Weiß

Dr.-Ing. Robert Weiß graduated as geodesist from TU Dresden (Germany) in 2003. He investigated the comparability of water surface levels derived from tide gauges, GNSS stations at tide gauges and satellite altimetry and completed his PhD with the topic 'Detection and description of sea level and its changes in the area of the German Bight' in 2012. He has been working in the Federal Institute of Hydrology in Koblenz since 2005. His current work focuses on the evaluation of new sensors, measurement and evaluation methods in the context of digital terrain modeling, such as the analysis of red and green ALS flights.



Thomas Artz

Dr.-Ing. Thomas Artz graduated as geodesist from the University of Bonn. He conducted research in the field of Very Long Baseline Interferometry, Earth Rotation and Terrestrial Reference Frames and completed his PhD on Subdaily Earth Rotation Variations in 2011. Since 2022 he is head of the department of Geodesy and Remote Sensing at the Federal Institute of Hydrology in Koblenz. His department conducts R&D for geodetic and remote sensing tasks regarding the federal waterways in Germany and consults the German Waterways and Shipping Administration as well as the Federal Ministry for Digital and Transport in these research fields.



Ingo Neumann

Univ.-Prof. Dr.-Ing. Ingo Neumann received his Dipl.-Ing. and Ph.D. in Geodesy and Geoinformatics at the Leibniz Universität Hannover in 2005 and 2009, respectively. Since 2012, he has been a Full Professor in the field of Engineering Geodesy and Geodetic Data Analysis at the Geodetic Institute of Leibniz Universität Hannover. His research areas are: artificial intelligence, adjustment theory and uncertainty models, multi-sensor systems, quality assessment, geodetic monitoring, terrestrial laser scanning, and automation of measurement processes. He is active in national and international scientific associations and an official delegate of the German and International Organization of Standardization (DIN and ISO). <https://orcid.org/0000-0001-9110-7345>



Hamza Alkhatib

PD Dr.-Ing. Hamza Alkhatib studied Surveying Engineering at Karlsruhe Institute of Technology (KIT). He earned his PhD in 2007 from the University of Bonn with a dissertation on "Monte Carlo methods and their applications to satellite gravity missions". Since 2007, he has been leading the research group for Expert-based Data Analysis and Quality Processes at the Geodetic Institute of Leibniz University Hannover. In 2020, he completed his Habilitation on "Advanced Methods and Algorithms for Computer-based Geodetic Data Analysis". His research focuses on machine learning, Bayesian modeling, Monte Carlo methods, and uncertainty quantification in geodetic data analysis. <https://orcid.org/0000-0002-4480-1067>

Surface Based Modeling of Ground Motion Areas in Lower Saxony

Mohammadivojdan¹, Alkhatib², Brockmeyer³, Jahn⁴, Neumann⁵

¹M. Sc. Bahareh Mohammadivojdan, Leibniz Universität Hannover,

Nienburger Str. 1, 30167 Hannover, mohammadivojdan@gih.uni-hannover.de

²Dr.-Ing. Hamza Alkhatib, Leibniz Universität Hannover,

Nienburger Str. 1, 30167 Hannover, alkhatib@gih.uni-hannover.de

³M. Sc. Marco Brockmeyer, Landesamt für Geoinformation und Landesvermessung Niedersachsen (LGLN),

Podbielskistraße 331, 30659 Hannover, Marco.Brockmeyer@lgl.niedersachsen.de

⁴Dr.-Ing. Cord-Hinrich Jahn, Landesamt für Geoinformation und Landesvermessung Niedersachsen (LGLN),

Podbielskistraße 331, 30659 Hannover, Cord-Hinrich.Jahn@lgl.niedersachsen.de

⁵Prof. Dr.-Ing. Ingo Neumann, Leibniz Universität Hannover,

Nienburger Str. 1, 30167 Hannover, neumann@gih.uni-hannover.de

Zusammenfassung

Systematic investigations have shown subsidence in almost 30% of the land area in Lower Saxony. It is essential to model these variations of the Earth surface especially to update the spatial reference system. Since the geodetic observations result in discrete points, it is necessary to mathematically model these measurements to have a continuous surface. This enables the user to do predictions at any position. This is challenging especially because these types of measurements usually result in non-uniformly distributed data. There are different approaches to deal with this problem, here the stochastic method of Kriging and the deterministic method of Multilevel B-Splines are implemented to model ground motion.

This paper investigates the ground motion of specific areas in Lower Saxony through the cooperation of Landesamt für Geoinformation und Landesvermessung Niedersachsen (LGLN) and Geodetic Institute of Hannover. For this investigation, a time series of measurements from leveling, Global Navigation Satellite System (GNSS) observations and height changes that are acquired by Persistent Scatterer Interferometry (PSI) technique are taken into consideration. Evaluation of the results show not only good performance and promising results from both the approaches, but also compatibility between the approximated surface from both of them.

A comparison of the results from the two methods shows the compatibility between the approximated surface of two approaches.

Keywords— Ground motion in Lower Saxony, Multilevel B-Splines, Kriging, Surface Approximation

1 Introduction

To provide a uniform, integrated spatial reference system, it is essential to have an up-to-date benchmark network. Due to variations of the Earth surface, the official spatial reference system differs from the current calculated coordinates. It is important to determine these variations and model the ground movements to be able to update the spatial reference system. This is not an easy task since all geodetic measurement techniques will result in discrete points. Also, these measurements are mostly non-uniformly distributed and contain data gaps. Therefore it is necessary to mathematically model the data set to have a continuous surface. This enables the user to obtain the target quantity at any position and to predict in areas where fewer observations are available. A data set contains both deterministic and stochastic parts. For accurately modeling the underlying function of the data, different methods should be taken into account to deal with both parts of each data set. There are several known deterministic and stochastic approaches to deal with the problem of surface approximation. Among the deterministic approaches, traditional polynomial surface and free-form surfaces, such as Bézier, B-Splines, and Non-uniform rational B-Splines could be mentioned [Piegl & Tiller (1997)]. Least Squares Collocation [Straub (1996)], Gaussian Processes [Rasmussen & Williams (2006)] and Kriging [Montero et al. (2015)] are examples of stochastic approaches.

Deterministic approaches mainly model the trend part of the data set. Whereas stochastic methods deal with the stochastic properties. Stochastic methods are based on spatial or temporal correlation between data points and use a covariance function or a variogram to describe such relations. Both deterministic and stochastic approaches provide optimal solutions based on the complexity of the data set and individual applications. For more information the reader is referred to [Schabenberger & Gotway (2017)]. A common approach for surface approximation is the method of Kriging. It should be noted that in a stochastic method such as Kriging, an assumption is that the data set is homogeneous. Therefore to get reliable results, the trend in the data should be removed. Another assumption is the existence of spatial correlation among the data points which means that neighboring points behave similarly that may not always be the case. Therefore, a method with less such limitations and more computational efficiency might be more appropriate for some applications. B-Splines is a proper alternative to Kriging which has less complexities yet delivering optimized results. Detailed description of these methods and results of their application on real data set are provided in the following sections.

Using the two methods of Kriging and Multilevel B-Splines Approximation (MBA), the ground movement in the area of Hengstlage is modeled. A continuous velocity field based on non-uniformly distributed measurements of height changes and horizontal displacements of the Earth surface is estimated by both methods. In particular height components which are acquired by PSI data in combination with leveling data are analyzed.

This paper is organized as follows. Section 2 reviews the main ideas behind the two approaches of Kriging and MBA. In section 3 the results related to validation and comparison of the analysis of the mentioned methods through applying a closed-loop Monte Carlo (MC) simulation including cross-validation on an exemplary reference data is presented. Section 4 contains the results of applying these approaches to real data sets related to ground movement in the area of Hengstlage.

2 Scattered data approximation

Approximation of scattered data refers to the problem of fitting a surface through a set of non-homogeneously distributed data points which is a common problem in different fields of studies. The main goal is to find the underlying function as a surface, which best describes the behavior of the data and makes it possible to propagate the existing information from the positions where measurements are available to new positions where no data exist. Let (x, y) present an arbitrary position, we look for the function $f(x, y)$ which computes the z value at that position.

$$z = f(x, y) \quad (1)$$

2.1 Approximation with Kriging

Kriging is a geostatistical approach which is based on the assumption that there is a spatial correlation among the data set. This method results in a prediction surface and performs prediction by summing the weighted observations around the desired location. The prediction in Kriging is done by means of Eq. 2 using a linear combination of the observations (z_i) and their weights (λ_i) [Montero et al. (2015)]. In this equation, (x_0, y_0) represents a point where prediction is desired.

$$z^*(x_0, y_0) = \sum_{i=1}^n \lambda_i z_i, \quad (2)$$

The weights $\{\lambda_1, \lambda_2, \dots, \lambda_n\}$ are calculated using a semivariogram. A semivariogram is a variance function which represents the dissimilarities between the data points. In order to derive the semivariogram the first step is calculating an experimental semivariogram based on the observations (see Eq.3, [Montero et al. (2015)]). To derive this semivariogram, it is important for the data to be stationary. The experimental semivariogram values ($\hat{\gamma}(h)$), which show the variability of the data points at different distances, are calculated considering predefined lags (h). Lags are the distances in which the semivariogram is calculated. In Eq. 3, $N(h)$ represents the number of observation pairs within the lag distance.

$$\hat{\gamma}(h) = \frac{1}{2N(h)} \sum_{n=1}^{N(h)} (z_n - z_{n+h})^2 \quad (3)$$

The next step is fitting a theoretical semivariogram (γ) to the discrete function (Eq. 3). Weights for prediction in position (x_0, y_0) can be calculated by solving the following equation for all the observations simultaneously [Montero et al. (2015)]. In Eq. 4 $\gamma((x_i, y_i) - (x_j, y_j))$ is the semivariogram value corresponding to the observation location pairs (x_i, y_i) and (x_j, y_j) and $\gamma((x_i, y_i) - (x_0, y_0))$ is related to semivariogram values relative to the prediction location.

$$\sum_{j=1}^n \lambda_j \gamma((x_i, y_i) - (x_j, y_j)) = \gamma((x_i, y_i) - (x_0, y_0)) \quad (4)$$

It should be noted that in a stochastic method such as Kriging, the basic assumption is the homogeneity of the data. In other words, in order to get reliable results, the trend in the data should be removed in advance.

2.2 Approximation with Multilevel B-Splines

Multilevel B-Splines for scattered data is an approximation method based on hierarchical tensor product B-Splines surfaces. The method was first developed in the 1990s for specific image processing applications such as image morphing [Lee et al. (1995), Lee et al. (1995)]. Lee et al. (1997) introduced a modified version of this method for general scattered data approximation tasks.

The B-Spline surface is defined by a control lattice Φ overlaid on the domain Ω . Where $\Omega = \{(x, y) | 0 \leq x < m, 0 \leq y < n\}$ is a rectangular domain defined in xy plane containing all the observations. The control lattice Φ is an $(m + 3) \times (n + 3)$ lattice which overlaps the integer values of Ω . In which ϕ_{ij} is the value of the ij -th control point on lattice Φ , for $i = -1, 0, \dots, m + 1$ and $j = -1, 0, \dots, n + 1$ (Figure 1).

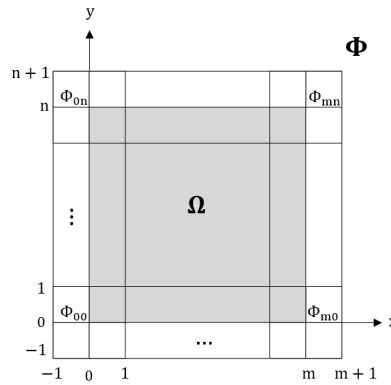


Abbildung 1: Configuration of control lattice Φ [Lee et al. (1997)].

The B-Splines surface f is linear combination of uniform bicubic basis functions ($B_k(s)$, $B_l(t)$) and control points of a control lattice Φ , where $i = \lfloor x \rfloor - 1$, $j = \lfloor y \rfloor - 1$, $s = x - \lfloor x \rfloor$, $t = y - \lfloor y \rfloor$.

$$f(x, y) = \sum_{k=0}^3 \sum_{l=0}^3 B_k(s) B_l(t) \phi_{(i+k)(j+l)} \quad (5)$$

The uniform cubic basis functions $B_k(s)$ for $0 \leq t < 1$, are defined as follows,

$$\begin{aligned} B_0(s) &= \frac{(1-s)^3}{6}, \\ B_1(s) &= \frac{(3s^3 - 6s^2 + 4)}{6}, \\ B_2(s) &= \frac{(-3s^3 + 3s^2 + 3s + 1)}{6}, \\ B_3(s) &= \frac{t^3}{6}. \end{aligned} \quad (6)$$

Similarly, the basis functions $B_l(t)$ are calculated. In the estimation of the control points, all the data points that lie within the 4×4 neighborhood of that control point affect the solution. From each point P_c in the neighborhood of a control point, one

solution can be derived ϕ_c . The unique solution ϕ_{ij} for a control point is derived from minimization of error term $(w_c\phi_{ij} - w_c\phi_c)$ for all points. Where $w_c = B_k(s)B_l(t)$, $k = (i + 1) - \lfloor x_c \rfloor$, $l = (j + 1) - \lfloor y_c \rfloor$, $s = x_c - \lfloor x_c \rfloor$, $t = y_c - \lfloor y_c \rfloor$. The minimization could be solved through a Gauss Markov Model. And the final solution is as follows [Lee et al. (1997)]:

$$\phi_{ij} = \frac{\sum_c w_c^2 \phi_c}{\sum_c w_c^2}. \quad (7)$$

MBA algorithm by Lee et al. (1997) uses a hierarchy of control lattices to generate a sequence of f_k . The sum of all B-Spline surfaces in the hierarchy approximates the final desired surface. The approximation starts with a rough approximation and the resolution of the control lattices increase in each step. For approximation in using MBA, at first step, a hierarchy of control lattices $\Phi_0, \Phi_1, \dots, \Phi_h$ are defined. The refinement here is in a way that from one lattice to the next, the spacing of the grid lines is halved. The first control lattice Φ_0 and the number levels of estimation h are parameters that should be fixed beforehand. The levels of refinement can be chosen based on approximation error. The MBA algorithm starts with the coarsest control point lattice (Φ_0). Then using the deviation of the estimated function to the original observations $\Delta^1 z$ based on (Φ_0), the control lattice of the next level is estimated. This process will continue until the last control lattice is estimated. In general at each level k , for estimation of the control lattices, the function f_k is calculated based on $\Delta^k z$.

$$\Delta^k z = z - \sum_{i=0}^{k-1} f_i(x, y) = \Delta^{k-1} z - f_{k-1}(x, y) \quad (8)$$

$$\Delta^0 z = 0 \quad (9)$$

The final approximation function is defined as the sum of functions in the hierarchy $f(x, y) = \sum_{i=0}^{k-1} f_i(x, y)$. An example of the process is illustrated in Figure 2 for a test data. In this figure, on the left side the original data set is shown and in the middle the control lattice hierarchy and the approximated functions at each level based on the related control lattice are illustrated. The 3D view of the approximated functions show how the estimation levels get refined in each step sequentially.

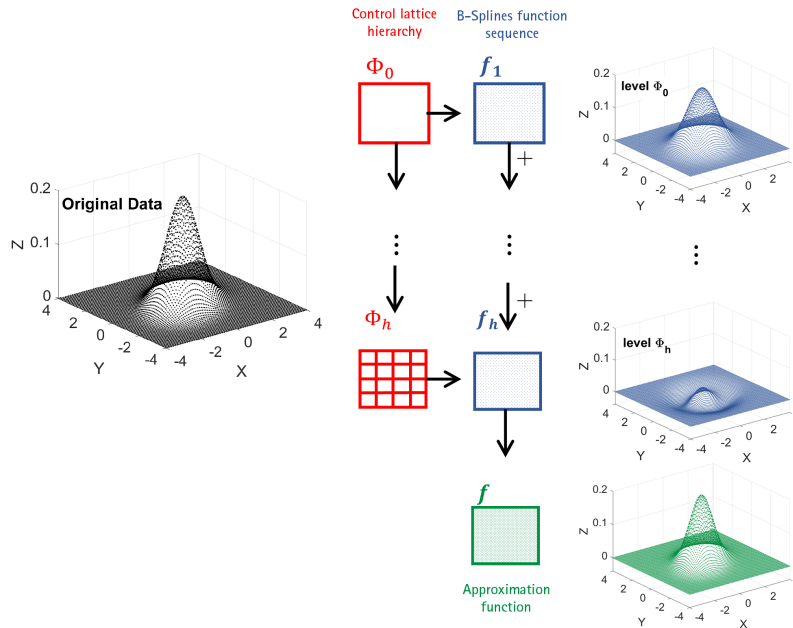


Abbildung 2: Schematic example of MBA approximation.

3 Validation of the methods

Before applying the mentioned surface approximation methods to a real data set, it is important to assess the functionality and performance of the methods to evaluate whether or not its results could be relied on in real applications. In this context, the reliability of the result is referred to as the approximation accuracy. In order to be able to judge such characteristics through a validation process, the true underlying function in a data set should be known beforehand. A ‘segmented cross-validation’ [Esbensen et al. (2010)] method is implemented to assess the performance of the approximation methods individually and at the end a comparison between performances of the approaches is possible.

For this purpose, a reference data set is simulated and the details are explained in section 3.1. The cross-validation is integrated into a MC simulation to include the effect of different realizations of the simulated data set in the validation process (section 3.2).

3.1 Test data

The simulated data set for the cross-validation process is a 3D data set. The only z component of the data set is stochastic, x and y components are assumed to be deterministic. The data set includes 6561 data points. The simulated data set can be split into two parts; the deterministic part or trend and the stochastic part or noise. The trend part of the 3D data set is generated by means of a multivariate Gaussian probability distribution function (PDF). The PDF is a mixture of two Gaussian distributions with the mean (μ) and variance-covariance matrix (Σ) in accordance with

Eq. 10. The x and y locations are equally distanced on a 0.1 grid where $-4 \leq x, y \leq 4$. The trend is constant over the full simulation:

$$z \sim \mathcal{N}(0.6\boldsymbol{\mu}_1 + 0.4\boldsymbol{\mu}_2, \boldsymbol{\Sigma}_{11} + \boldsymbol{\Sigma}_{22}), \quad (10)$$

wherein:

$$\boldsymbol{\mu}_1 = \begin{bmatrix} 0.5 \\ 1 \end{bmatrix}, \quad \boldsymbol{\mu}_2 = \begin{bmatrix} -0.5 \\ -1 \end{bmatrix}, \quad (11)$$

$$\boldsymbol{\Sigma}_{11} = \begin{bmatrix} 2 & 0.5 \\ 0.5 & 0.5 \end{bmatrix}, \quad \boldsymbol{\Sigma}_{22} = \begin{bmatrix} 1 & 0.8 \\ 0.8 & 1 \end{bmatrix}. \quad (12)$$

The result can be seen in Figure 3a. The noise is generated from a Gaussian distribution with zero mean and standard deviation equal to 0.001.

$$\text{noise} \sim \mathcal{N}(0, 0.001^2) \quad (13)$$

The simulated data set is the combination of the deterministic trend and the stochastic noise. Figure 3 illustrates both parts separately. The combination of the two part is the input for the cross-validation process. For every MC run a new noise is simulated and added to the trend. Figure 3 only depicts one example for such a process.

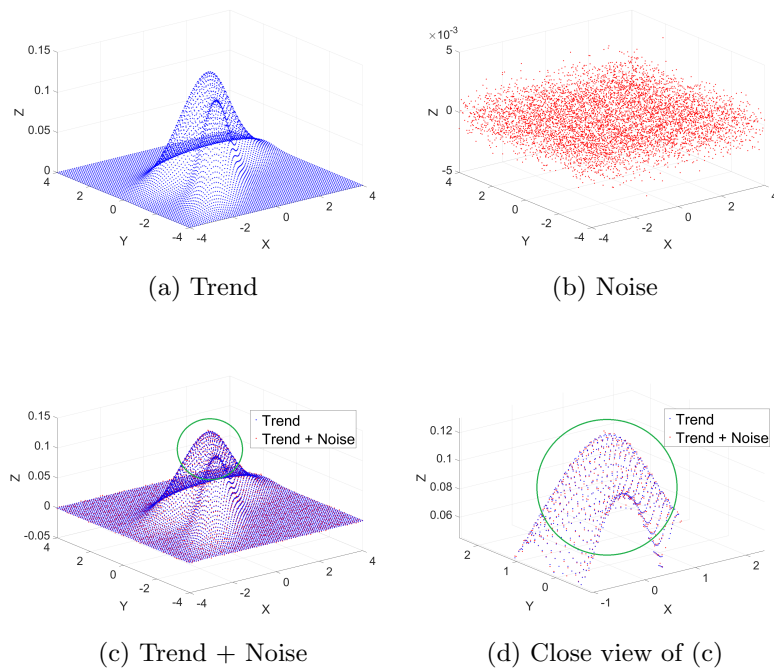


Abbildung 3: Separate visualizations of generated trend and noise.

3.2 Cross validation and Monte Carlo simulation

In segmented cross-validation for each iteration, $q\%$ of the whole data set is selected and eliminated as the test data set. The remaining part, or so-called training data set,

is introduced to the surface approximation method to estimate the underlying function in the data set. Then the approximation method predicts the function values in the position of the test data. Since the true values of the test data are known, at the end the differences between the prediction (z^*) and the true value of the test data are used to assess the performance of the method. Here Root Mean Square Error (RMSE) of the differences, in accordance with Eq. 14, is used as a measure for the prediction error [Maretns & Martens (2001)].

$$RMSE = \sqrt{\frac{1}{n} \sum_{i=1}^n (z_i - z_i^*)^2} \quad (14)$$

However, cross-validation only on one data set will not guarantee the functionality of the methods. To ensure their performance, they should be subjected to different data sets. In this case, through a certain number of MC runs, the cross-validation is repeated for different realizations of the simulated data set. In each realization, a different noise is generated. The general algorithm of the implemented MC simulation environment is outlined in Algorithm 1. Here the number of MC runs (k_2) is set to 500 and the number of cross-validation iterations k_1 is set to 100. The results of the MC simulations are provided in the next section.

Algorithm 1: Monte Carlo Simulation.

```

1 Input: trend part of data set  $\mathbf{Q}_{[n \times 3]} = [\mathbf{x} \ \mathbf{y} \ \mathbf{z}]$  generated from Eq. 10
2 Output: prediction for removed observations, RMSE of cross validations, mean of RMSEs
3 for  $i = 1 \rightarrow k_2$  do
4   generate noise vector ( $\mathbf{noise}_{[n \times 1]}$ ) from Eq. 13
5   set  $\mathbf{P}_{[n \times 3]} = \mathbf{Q}_{[n \times 3]} + \mathbf{noise}_{[n \times 1]}$ 
6   for all surface approximation methods (Kriging and MBA) do
7     for  $j = 1 \rightarrow k_1$  do
8       remove  $m$  points ( $q\%$ ) from  $\mathbf{P}$ 
9       test data set ( $\mathbf{P}''$ ) = the removed  $m$  data points
10      training data set ( $\mathbf{P}'$ ) = data set  $\mathbf{P}$  after removing test data  $\mathbf{P}''$ 
11      model estimation based on  $\mathbf{P}'$ 
12      for  $k = 1 \rightarrow m$  do
13        prediction in  $P_k'' = (x_k, y_k)$ 
14        calculate RMSE (Eq. 14)
15 calculate mean of  $k_1 \times k_2$  RMSEs

```

3.3 Simulation results

In the method of Kriging, an exponential function for a variogram is selected. The effective area for calculation of the weights is considered to be the whole field. In case of applying MBA on a data set, two parameters should be fixed beforehand; the number of control points in the coarsest control lattice Φ_0 and the number of levels in the control lattice hierarchy (h). Through a sensitivity analysis, $m_0 = n_0 = 5$ for the coarsest control lattice with three levels of refinement is selected as an optimal solution. For the evaluation of the aforementioned surface approximation methods, five MC simulations for different cross-validation parameters are applied. The size of the test data increases by 10% in each simulation to study the effect of data gaps on

the performance of the methods. Overall, each simulation contains 500 MC runs and each run includes 100 cross-validation iterations. In each MC run, a new noise vector is generated. The noise is constant during the 100 iterations of cross-validation and only the combination of the test data changes.

The results of the performance of the methods are illustrated in Figure 4. In this figure, the horizontal axis represents different MC simulations based on the size of the test data. Larger test data results in larger data gaps in the training set. The vertical axis presents the mean of the RMSEs from all MC runs. The performance of Kriging and MBA throughout the simulations are relatively steady. MBA has a smaller prediction error in comparison to Kriging. By increasing the size of the data gaps the quality of approximation decreases and especially in the case of Kriging. It can be seen that the prediction error derived with respect to ‘trend + noise’ is in the range of the generated noise. This means that the methods are smoothly predicting the true trend in the data set. Overall, the results show that MBA has smaller prediction error and is the more robust against data gaps.

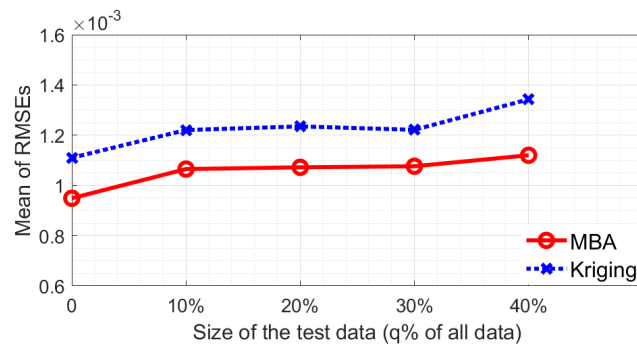


Abbildung 4: Mean of RMSEs for different MC simulations.

4 Ground motion in Hengstlage

Systematic investigations of different data sources in 2007 have shown that approximately 30% of Lower Saxony’s land area is influenced by ground movements due to raw material extraction. These movements are due to the construction and operation of cavern facilities as well as the storage of CO_2 and hydrocarbons in the area [Jahn et al. (2011)]. This emphasized the necessity to update the official spatial reference system in the related area. Here specifically the ground movement in the area of Hengstlage is investigated. For this purpose, both the stochastic method of Kriging and the deterministic method of MBA are employed.

4.1 Data set

To investigate the ground movement, all measurements up to now are used as a basis to derive the related velocity information. In general, data from GNSS observations, leveling and PSI are used as a basis for the investigation of recent movements of the

Earth's crust. For this purpose, the existing time series of vertical and horizontal benchmarks from 'amtlichen Festpunktinformationssystem' (AFIS) in Lower Saxony are gathered [Brockmeyer (2019)].

Since 2008, a uniform coordinate monitoring by the satellite positioning service of the German national survey (SAPOS[®]) reference stations has been continuously carried out in Lower Saxony for quality assurance of the SAPOS[®] services. The results of these weekly GNSS evaluations are free coordinate solutions with complete stochastic information, which are examined in time series analysis to determine the three-dimensional motion behavior of the reference stations. Besides the regular data acquired from leveling and GNSS observations, vertical data which are acquired by the PSI technique, are also taken into consideration. Velocity information from PSI, as a part of the group of differential Interferometric Synthetic Aperture Radar (InSAR), plays an important factor in the analysis of ground movement due to the fact that this method provides denser information especially outside the regular geodetic networks and specifically in urban areas.

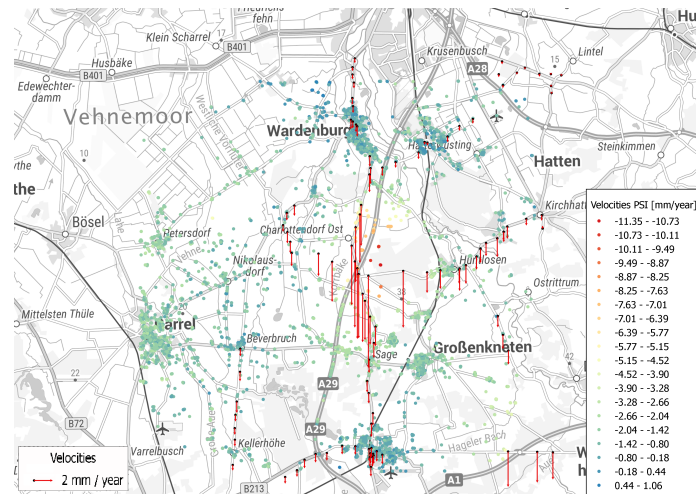
All the velocities, derived from different measurement methods, are considered to be uncorrelated. The variance related to vertical component derived from leveling and horizontal velocities are calculated based on Eq. 15. The variances are based on the accuracy of the individual measurements and time difference between measurements (α_t). The prior standard deviation (σ_0) in this case is considered to be 3 [mm] [Brockmeyer (2019)].

$$\sigma^2 = 2 \frac{1}{\alpha_t^2} \sigma_0^2 \quad (15)$$

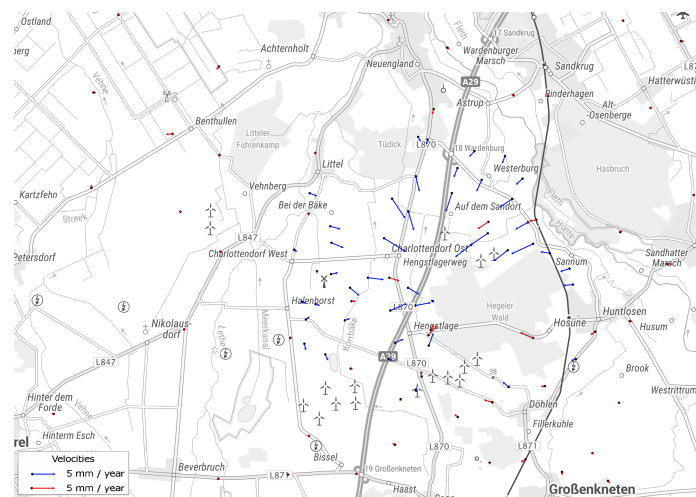
The variance related to PSI velocities is derived following Eq. 16. It should be noted that the PSI observations are considered to be less accurate, the larger uncertainty is included as a parameter to the variance (Δ_{PSI}). Δ_{PSI} shows the instability of points and is considered to be 2 [mm] [Brockmeyer (2019)].

$$\sigma^2 = 2 \frac{1}{\alpha_t^2} \sigma_0^2 + \Delta_{PSI}^2 \quad (16)$$

The vertical data from leveling includes measurements from 20 years (1988 until 2008) related to 106 benchmarks. The maximum observed vertical deformation in the center is -9.9 [mm/year]. The PSI measurements are acquired between 2003 and 2010. The number of these observations after preprocessing is 5962. In Figure 5a the PSI data set and the leveling are shown. The two measurement techniques of leveling and InSAR show comparable observations. The horizontal velocities in this area are derived from 115 benchmarks. The measurements are performed in the time span of 1968 until 2010. In Figure 5b the horizontal velocities acquired from SAPOS[®] measurements (blue arrows) and GNSS-post processing (red arrows) are shown.



(a) Height component



(b) Horizontal component

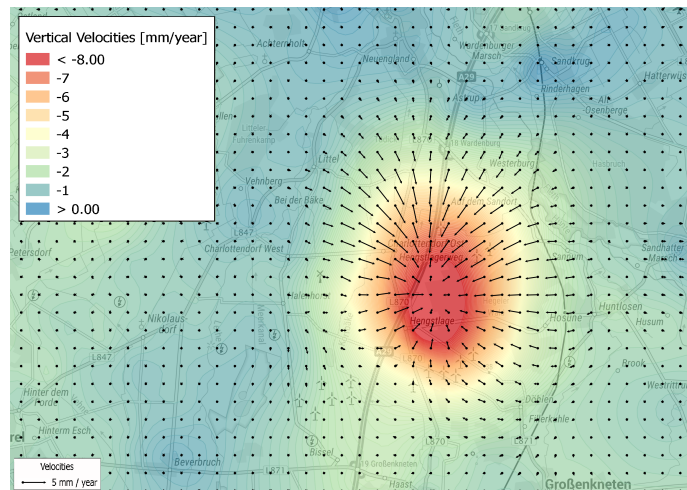
Abbildung 5: (a) PSI and leveling data (red bars), (b) Data from AFIS (red) and SAPOS[®] (blue) in Hengstlage [Brockmeyer (2019)].

4.2 Results of approximation

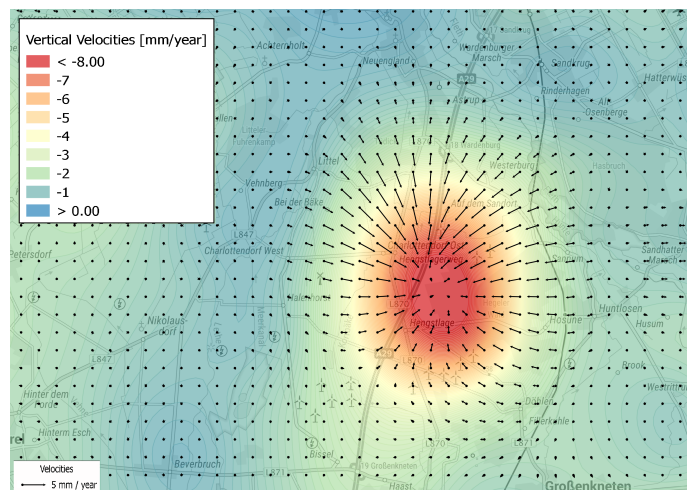
The approximated ground movement for both height changes and horizontal displacements are illustrated together in Figure 6. Height changes are presented as a heat diagram and horizontal displacements are specified as a vector field combining the displacement of the east and north components.

For approximation with MBA three levels of control lattice hierarchy in which the coarsest control lattice is Φ_4 ($m = n = 4$) are selected. Overall three control lattices Φ_4 , Φ_8 and Φ_{16} are used. Figure 6b shows the results of the estimation. The subsidence in the middle of the area is in both approximations distinguished.

For the approximation of horizontal displacement, observations of east and north components are analyzed separately. The methods of Kriging and MBA show similar results. For this analysis, similar specifications are used for the methods as in height changes approximation. The maximum absolute velocities in displacements appear around the edges of the subsided area. In the center of the subsidence area, horizontal displacement is zero.



(a) Kriging



(b) MBA

Abbildung 6: Ground movement approximated by (a) Kriging (b) MBA (height changes are illustrated as heat diagram and vector field represents the horizontal displacements).

Figure 7 shows a 3D view of the approximated surface related to height changes by the two methods. The RMSE representing the prediction error in the location of

the observations for Kriging and MBA are 0.44 and 0.47 [mm/year], respectively.

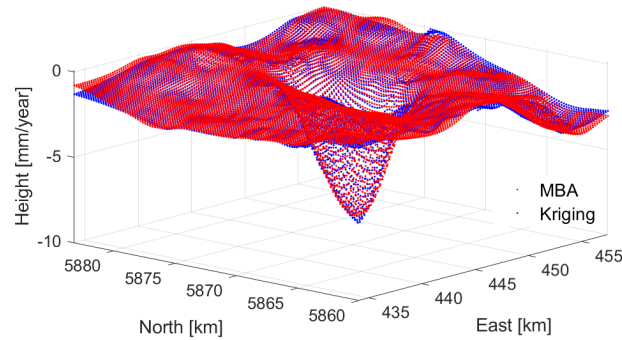


Abbildung 7: Approximation of the two methods of Kriging and MBA.

The approximations show similar behavior but they are not the same. The true function behind the ground movement is not known. To have a comparison between the result of these two approaches, the differences between the approximations are calculated. Figure 8a shows a heat diagram of the absolute differences. Mostly the differences can be seen in areas where less observations are available. This results from different approaches of the two methods in interpolating information from positions with observations to data gaps. The histogram of these differences in Figure 8b shows that they are randomly distributed overall the field.

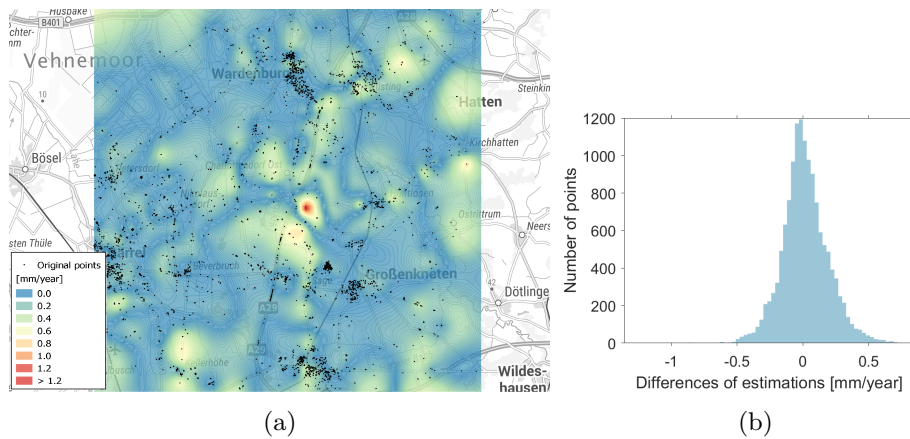


Abbildung 8: (a) Absolute differences (b) Histogram of the differences between approximation of Kriging and MBA.

5 Conclusion

In this paper, a stochastic and a deterministic surface approximation method are used to mathematically model ground movements. Specifically, the stochastic method of

Kriging and a deterministic method based on B-Spline tensor product surfaces (MBA) are used. The performance and implementation of the methods are evaluated using cross-validation integrated into a closed-loop MC simulation. Different data sets are simulated, which contain data gaps in order to be comparable to the real data set. Different appearances of data gaps in the simulated data help to investigate the effect of data gaps on the performance of the approaches. The results show that the quality of the estimation decreases by increasing the size of the data gaps. However, the method of MBA showed better performance in dealing with data gaps.

This research is a collaboration between LGLN and Geodetic Institute of Hannover. All the data set related to the ground movements in Lower Saxony are processed and provided by LGLN. The ground movement in the area of Hengstlage, modeled with the Kriging approach is implemented by LGLN. Height changes in this area are approximated with the two approaches and Kriging shows a smaller prediction error. The approximated surfaces by MBA and Kriging show a similar pattern of subsidence in the area and have comparable prediction errors. The Kriging method is computationally more expensive compared to the MBA. These results are also highly dependent on the used variogram and control lattice hierarchy.

For future research, it would be interesting to combine the deterministic and stochastic approaches. This means to estimate the trend in the data set by means of a deterministic method and model the remaining stochastic part with a stochastic method. In the method of MBA choosing an optimal control lattice hierarchy highly affects the final estimation. It is recommended to investigate an optimal control lattice hierarchy to obtain a more accurate estimation.

Literatur

- [Brockmeyer (2019)] Brockmeyer, M. (2019). *Daten der Landesvermessung zur räumlichen Interpolation von Bodenbewegungen*. GeoMonitoring 2019, pp. 151 – 163, DOI: 10.15488/4519.
- [Chiles & Delfiner (2009)] Chiles, J. & Delfiner, P. (2009). *Geostatistics: modeling spatial uncertainty*. John Wiley & Sons, 497.
- [Esbensen et al. (2010)] Esbensen, K., Guyot, D., Westad, F., Houmoller, L. P. (2010). *Multivariate Data Analysis - in practice*. CAMO Software, Oslo.
- [Forsey & Bartels (1992)] Forsey, D. & Bartels R. (1992). *Tensor products and hierarchical fitting*. Curves and Surfaces in Computer Vision and Graphics II, V. 1610, pp. 88 – 96.
- [Forsey & Bartels (1995)] Forsey, D. & Bartels R. (1995). *Surface fitting with hierarchical splines*. ACM Transactions on Graphics, V. 14, pp. 134 – 161.
- [Jahn et al. (2011)] Jahn, C.-H., Feldmann-Westendorff, U., Grüer, D., Kulle, U., Lembrecht, P. (2011). *Die Erneuerung des Deutschen Haupthöhennetzes in Niedersachsen*. NaVKV, V. 4, pp. 3 – 7.
- [Lee et al. (1995)] Lee, S. Y., Chwa, K.Y., Shin, S.Y., Wolberg, G. (1995). *Image metamorphosis using snakes and free-form deformations*. SIGGRAPH, V. 95, pp. 439 – 448.
- [Lee et al. (1996)] Lee, S. Y., Wolberg, G., Chwa, K.Y., Shin, S.Y. (1995). *Image metamorphosis with scattered feature constraints*. IEEE Transactions on Visualization and Computer Graphics, V. 4, pp. 337 – 354.

- [Lee et al. (1997)] Lee, S. Y., Wolberg, G., Chwa, K.Y., Shin, S.Y. (1997). *Scattered data interpolation with multilevel B-splines*. IEEE transactions on visualization and computer graphics, V. 3, pp. 228 – 244.
- [Maretns & Martens (2001)] Martens, H. & Martens, M. (2001). *Multivariate analysis of quality. An introduction* IOP Publishing.
- [Montero et al. (2015)] Montero, J.P., Delfiner, P., Mateu, J (2015). *Spatial and Spatio-Temporal Geostatistical Modeling and Kriging*. John Wiley and Sons, United Kingdom.
- [Piegl & Tiller (1997)] Piegl, L. & Tiller, W. (1997). *The NURBS Book*. Springer, Berlin.
- [Rasmussen & Williams (2006)] Rasmussen, C.E. & Williams, C.K. (2006). *Gaussian processes for machine learning*. MIT press, Cambridge.
- [Schabenberger & Gotway (2017)] Schabenberger, O., Gotway, C. (2017). *Statistical methods for spatial data analysis*. Chapman and Hall-CRC.
- [Straub (1996)] Straub, C. (1996). *Recent crustal deformation and strain accumulation in the Marmara Sea region, NW Anatolia, inferred from GPS measurements*. PhD diss., ETH Zürich.

A Supplementary Material

A.1 MBA

MBA provides a hierarchical framework for surface approximation, based on tensor-product B-spline surfaces. Originally developed in the 1990s for image processing tasks such as morphing (Lee et al., 1995, 1996), a more general formulation for scattered data approximation was later introduced by Lee et al. (1997). This appendix collects the mathematical details that are referenced in Section 3.2.1 but omitted there to keep Chapter 3 readable. It documents the deterministic construction (Section A.1.1), the multilevel residual refinement (Section A.1.2), the refinement-based evaluation optimization (Section A.1.3), and the stochastic formulation (Section A.1.4) used later for uncertainty propagation.

A.1.1 B-Spline Approximation

Given a 3D PC, ℓ , a rectangular approximation domain Ω is defined in the xy -plane (Fig. A.1). A control lattice Φ is placed over this domain to construct the B-spline surface. Each point $p = (x, y, z)$ in the PC contributes to the approximation, where (x, y) is constrained to lie within Ω , defined as $\Omega = \{(x, y) \mid 0 \leq x < m, 0 \leq y < n\}$.

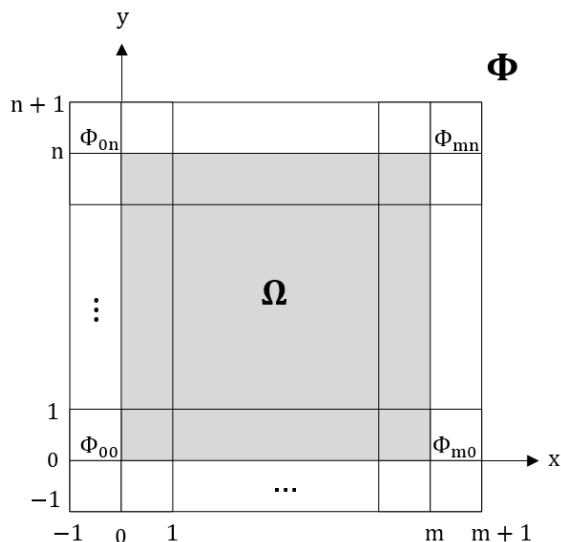


Figure A.1: Configuration of a control lattice Φ in the domain Ω (Lee et al., 1997).

The coordinates (x, y) are obtained by mapping the original PC into the domain Ω based on its bounding box. This transformation is performed according to Eq. (A.2), where $\ell_{x,\min}$, $\ell_{x,\max}$, $\ell_{y,\min}$,

and $\ell_{y,\max}$ denote the minimum and maximum values of the point cloud in the x and y directions.

$$\boldsymbol{\ell}_{[s,3]} = \begin{bmatrix} \ell_{x,1} & \ell_{y,1} & \ell_{z,1} \\ \vdots & \vdots & \vdots \\ \ell_{x,s} & \ell_{y,s} & \ell_{z,s} \end{bmatrix} \quad (\text{A.1})$$

$$\begin{aligned} \mathbf{x} &= \frac{m}{\ell_{x,\max} - \ell_{x,\min}} \cdot \boldsymbol{\ell}_x - \frac{\ell_{x,\min} \times m}{\ell_{x,\max} - \ell_{x,\min}} \\ \mathbf{y} &= \frac{n}{\ell_{y,\max} - \ell_{y,\min}} \cdot \boldsymbol{\ell}_y - \frac{\ell_{y,\min} \times n}{\ell_{y,\max} - \ell_{y,\min}} \end{aligned} \quad (\text{A.2})$$

The B-spline surface, $f(\mathbf{x}, \mathbf{y})$, is constructed as a weighted sum of bicubic basis functions and control points:

$$f(\mathbf{x}, \mathbf{y}) = \sum_{k=0}^3 \sum_{l=0}^3 B_k(s) B_l(t) \phi_{(i+k)(j+l)} \quad (\text{A.3})$$

We first define the index conventions and local coordinates used to evaluate the tensor-product B-spline basis functions on the control lattice. Here, the control lattice Φ is defined over an $(m+3) \times (n+3)$ grid. The index variables and local coordinates are defined as:

$$i = \lfloor x \rfloor - 1, \quad j = \lfloor y \rfloor - 1, \quad s = x - \lfloor x \rfloor, \quad t = y - \lfloor y \rfloor. \quad (\text{A.4})$$

The cubic B-spline basis functions $B_k(s)$ (for $0 \leq s < 1$) are given by:

$$\begin{aligned} B_0(s) &= \frac{(1-s)^3}{6}, \\ B_1(s) &= \frac{3s^3 - 6s^2 + 4}{6}, \\ B_2(s) &= \frac{-3s^3 + 3s^2 + 3s + 1}{6}, \\ B_3(s) &= \frac{s^3}{6}. \end{aligned} \quad (\text{A.5})$$

To determine the unknown control lattice Φ , a point (x_c, y_c, z_c) in ℓ is considered. According to Eq. (A.3), the function value $f(x_c, y_c)$ is influenced by sixteen control points in its neighborhood. Assuming that $1 \leq x_c, y_c < 2$, the corresponding control points are denoted as ϕ_{kl} for $k, l = 0, 1, 2, 3$, and Eq. (A.3) is simplified to:

$$z_c = \sum_{k=0}^3 \sum_{l=0}^3 w_{kl} \phi_{kl}, \quad \text{with } w_{kl} = B_k(s) B_l(t), \quad s = x_c - 1, \quad t = y_c - 1. \quad (\text{A.6})$$

Multiple values of ϕ_{kl} can satisfy Eq. (A.6). To obtain a unique solution, the sum $\sum_{k=0}^3 \sum_{l=0}^3 \phi_{kl}^2$ is minimized in the LS sense (Lee et al., 1997; Hsu et al., 1992). This leads to the following expression:

$$\phi_{kl} = \frac{w_{kl} z_c}{\sum_{a=0}^3 \sum_{b=0}^3 w_{ab}^2} \quad (\text{A.7})$$

Now, the complete point set ℓ is considered. Each control point ϕ_{ij} is influenced by observations

located within its 4×4 neighborhood, referred to as the proximity dataset (see Fig. A.2a):

$$\ell_{ij} = \{(x_c, y_c, z_c) \in \mathcal{L} \mid i - 2 \leq x_c < i + 2, j - 2 \leq y_c < j + 2\}.$$

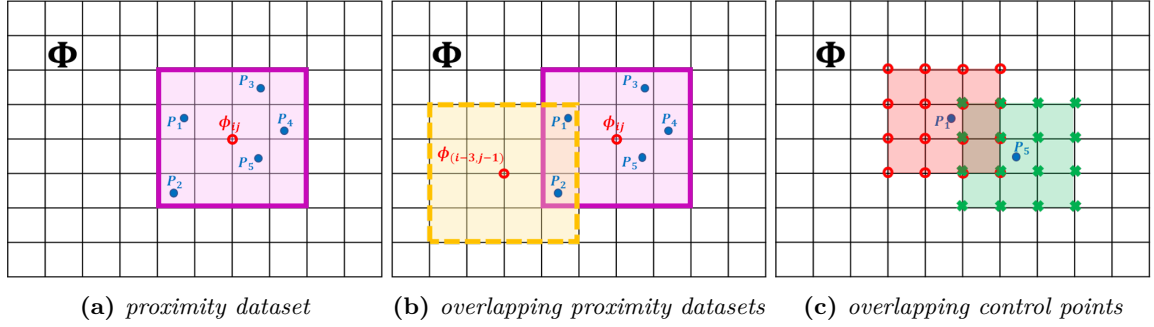


Figure A.2: Positional relationship between data and control points. (a) Proximity points of \mathbf{P}_{ij} , (b) overlapping of proximity datasets of two control points, (c) overlapping control points of neighboring data points.

When control points are sufficiently close, their associated proximity datasets may partially overlap (Fig. A.2b). For each data point, Eq. (A.7) can be applied to compute the corresponding 4×4 neighborhood of control points. These neighborhoods will overlap when the data points themselves are near each other (Fig. A.2c).

To obtain a unique estimate for each ϕ_{ij} , the following error term is minimized: $\sum_c (w_c \phi_{ij} - w_c \phi_c)^2$. The expression $(w_c \phi_{ij} - w_c \phi_c)$ quantifies the deviation between the unknown control point and its local approximations derived from the proximity data. The value ϕ_c is computed for each observation in the proximity set using:

$$\phi_c = \frac{w_c z_c}{\sum_{a=0}^3 \sum_{b=0}^3 w_{ab}^2}, \quad w_c = w_{kl} = B_k(s) B_l(t), \quad (\text{A.8})$$

with indices and local coordinates defined as:

$$k = (i + 1) - \lfloor x_c \rfloor, \quad (\text{A.9})$$

$$l = (j + 1) - \lfloor y_c \rfloor, \quad (\text{A.10})$$

$$s = x_c - \lfloor x_c \rfloor, \quad (\text{A.11})$$

$$t = y_c - \lfloor y_c \rfloor. \quad (\text{A.12})$$

The final estimate for a single control point is then given by:

$$\hat{\phi}_{ij} = \frac{\sum_c w_c^2 \phi_c}{\sum_c w_c^2}, \quad (\text{A.13})$$

For each control point on the lattice, the proximity dataset (ℓ_{ij}) must be identified to compute the optimal solution. Due to the overlapping neighborhoods of adjacent control points, redundant computations may occur, which can significantly increase the overall processing time. To avoid this, Lee et al. (1997) proposed that, for each data point, the numerator and denominator of Eq. (A.13) be accumulated across the 4×4 neighborhoods of control points. This strategy forms the basis of the so-called BA algorithm for calculating the B-spline surface (Algorithm 2). If no nearby data are available for a given control point, it is excluded from the surface definition in Eq. (A.3), and a default value (e. g., zero) is assigned.

Algorithm 2: BA Algorithm (Lee et al., 1997).

```

1 Input: 3D PC  $\ell = [\mathbf{x} \ \mathbf{y} \ \mathbf{z}]$ 
2 Output: control lattice  $\Phi = \{\phi_{ij}\}$   $i = -1, 0, \dots, m+1$  and  $j = -1, 0, \dots, n+1$ 
3 for all  $i, j$  do
4   | let  $\delta_{ij} = 0$  and  $\omega_{ij} = 0$ 
5 for each point  $(x_c, y_c, z_c)$  in  $\ell$  do
6   | let  $i = \lfloor x_c \rfloor - 1$  and  $j = \lfloor y_c \rfloor - 1$ 
7   | let  $s = x_c - \lfloor x_c \rfloor$  and  $t = y_c - \lfloor y_c \rfloor$ 
8   | compute  $w_{kl}$ 's and  $\sum_{a=0}^3 \sum_{b=0}^3 w_{ab}^2$  (Eq. (A.7))
9   | for  $k, l = 0, 1, 2, 3$  do
10  |   | compute  $\phi_{kl}$  with Eq. (A.7)
11  |   | add  $w_{kl}^2 \phi_{kl}$  to  $\delta_{(i+k)(j+l)}$ 
12  |   | add  $w_{kl}^2$  to  $\omega_{(i+k)(j+l)}$ 
13 for all  $i, j$  do
14  | if  $\omega_{ij} \neq 0$  then
15  |   | compute  $\phi_{ij} = \frac{\delta_{ij}}{\omega_{ij}}$ 
16  | else
17  |   | let  $\phi_{ij} = 0$ 

```

A.1.2 Hierarchical B-Spline Approximation

While a single B-spline surface can approximate the data, it offers limited control over local details and model complexity. The multilevel extension addresses this by refining the control lattice in stages and fitting residuals at each level. To build the surface hierarchy, a sequence of control lattices $\Phi_0, \Phi_1, \dots, \Phi_h$ is defined. The initial control lattice Φ_0 and the number of refinement levels h must be specified in advance. Φ_0 represents the coarsest level, containing the fewest control points, while Φ_h defines the finest level, with the highest control point resolution. From one level to the next, the spacing between grid lines is halved, and new control points are inserted between the existing ones. Therefore, if Φ_k is an $(m+3) \times (n+3)$ lattice, then Φ_{k+1} becomes an $(2m+3) \times (2n+3)$ lattice. The position of the (i, j) -th control point in Φ_k coincides with the $(2i, 2j)$ -th control point in Φ_{k+1} .

The MBA process begins with the coarsest control lattice Φ_0 . The corresponding surface estimate, denoted as f_0 , is computed using the BA algorithm. Since this estimate is based on a coarse grid, the resulting surface is smooth but may exhibit large deviations from the original data points in ℓ . The deviation between f_0 and the observed z -values of the original PC is computed for each point $(x_c, y_c, z_c) \in \ell$ using Eq. (A.14).

$$\Delta^{(1)}_{z_c} = z_c - f_0(x_c, y_c) \quad (\text{A.14})$$

In the next step, the finer lattice is applied to the data points ℓ_1 , which use the residuals between the previous level's estimation and the original data as new z values. This results in f_1 as the next surface estimate, and a smaller deviation ($\Delta^{(2)}_z$) between the original z values and the accumulated estimates from the previous levels (f_0, f_1). For a point (x_c, y_c, z_c) , the second-level residual $\Delta^{(2)}_{z_c}$ is given by:

$$\Delta^{(2)}_{z_c} = z_c - f_0(x_c, y_c) - f_1(x_c, y_c). \quad (\text{A.15})$$

In general, at level k , the function f_k is computed using the control lattice Φ_k to approximate the data points ℓ_k . For a point $(x_c, y_c, \Delta^{(k)}z_c)$, the recursive residual is defined as:

$$\Delta^{(k)}z_c = z_c - \sum_{i=0}^{k-1} f_i(x_c, y_c) = \Delta^{(k-1)}z_c - f_{k-1}(x_c, y_c) \quad (\text{A.16})$$

$$\Delta^{(0)}z_c = 0 \quad (\text{A.17})$$

The final approximation function is defined as the sum of all partial estimates f_k , from the coarsest lattice Φ_0 to the finest lattice Φ_h (see Algorithm 3).

$$f(\mathbf{x}, \mathbf{y}) = \sum_{i=0}^{k-1} f_i(\mathbf{x}, \mathbf{y}) \quad (\text{A.18})$$

Algorithm 3: MBA Algorithm (Lee et al., 1997).

```

1 Input: 3D point cloud  $\ell = [\mathbf{x} \ \mathbf{y} \ \mathbf{z}]$ 
2 Output: control lattice hierarchy  $\Phi_0, \Phi_1, \dots, \Phi_h$ 
3 let  $k = 0$  while  $k \leq h$  do
4   let  $\ell_k = (x_c, y_c, \Delta^{(k)}z_c)$ 
5   compute  $\Phi_k$  from  $P_k$  by BA Algorithm 2
6   compute  $\Delta^{(k+1)}z_c = \Delta^{(k)}z_c - f_k(x_c, y_c)$  for each data point
7   let  $k = k + 1$ 

```

A.1.3 Optimization with B-Spline Refinement

So far, the MBA surface has been defined as a sum over level-wise contributions. In practice, repeatedly evaluating all levels can be expensive, especially on dense prediction grids. To reduce this cost, the hierarchy is converted into a single control lattice on the finest grid by refinement. Although the publications mention that the evaluation can be optimized, the details of this refinement step were not included there because of space limitations. The dissertation presents the full formulation to document how the computational cost can be reduced without altering the underlying approximation.

Let $F(\Phi)$ denote the B-spline surface generated by a control lattice Φ . An $(m+3) \times (n+3)$ lattice Φ is refined to an $(2m+3) \times (2n+3)$ lattice Φ' by halving the grid spacing so that the (i, j) -th control point of Φ coincides with the $(2i, 2j)$ -th control point of Φ' . The new control points on Φ' are obtained as fixed linear combinations of neighboring control points on Φ through local masks; specifically the four interleaved positions $\phi'_{2i,2j}$, $\phi'_{2i,2j+1}$, $\phi'_{2i+1,2j}$, and $\phi'_{2i+1,2j+1}$ are computed from the surrounding $\phi_{i-1:j+1, i-1:j+1}$ values according to Eqs. (A.19)–(A.22):

$$\phi'_{2i,2j} = \frac{1}{64} [\phi_{i-1,j-1} + \phi_{i-1,j+1} + \phi_{i+1,j-1} + \phi_{i+1,j+1} + 6(\phi_{i-1,j} + \phi_{i,j-1} + \phi_{i,j+1} + \phi_{i+1,j}) + 36\phi_{ij}] \quad (\text{A.19})$$

$$\phi'_{2i,2j+1} = \frac{1}{16} [\phi_{i-1,j} + \phi_{i-1,j+1} + \phi_{i+1,j} + \phi_{i+1,j+1} + 6(\phi_{i,j} + \phi_{i,j+1})] \quad (\text{A.20})$$

$$\phi'_{2i+1,2j} = \frac{1}{16} [\phi_{i,j-1} + \phi_{i,j+1} + \phi_{i+1,j-1} + \phi_{i+1,j+1} + 6(\phi_{i,j} + \phi_{i+1,j})] \quad (\text{A.21})$$

$$\phi'_{2i+1,2j+1} = \frac{1}{4} [\phi_{ij} + \phi_{i,j+1} + \phi_{i+1,j} + \phi_{i+1,j+1}] \quad (\text{A.22})$$

By construction, refinement preserves the surface at that level, that is $F(\Phi'_k) = \mathbf{f}_k$. The refined control lattices are then accumulated across levels to obtain a single lattice on the finest grid. Starting from the coarsest level, an accumulator Ψ_0 is set to Φ_0 . For $k = 1, \dots, h$, the accumulator Ψ_{k-1} is refined to the grid of Φ_k and updated by control-point addition, yielding $\Psi_k = \Psi'_{k-1} + \Phi_k$. After the last level, Ψ_h defines the final refined control lattice and the approximation is evaluated as a single B-spline surface,

$$F(\Psi_h) = \sum_{i=0}^h \mathbf{f}_i = f. \quad (\text{A.23})$$

This traversal can be summarized by the following pseudocode, which generates Ψ_h directly from the hierarchy Φ_0, \dots, Φ_h (Algorithm 4). Fig. A.3 illustrates this process from coarse to fine. The refinement masks have compact support, so the work at each level is proportional to the number of control points on that level, and only one lattice needs to be carried through the traversal. As a result, the refined formulation evaluates and regenerates the surface as a single B-spline function rather than as a sum of $h + 1$ functions, which reduces runtime and memory traffic, especially when the prediction grid is much denser than the control lattices.

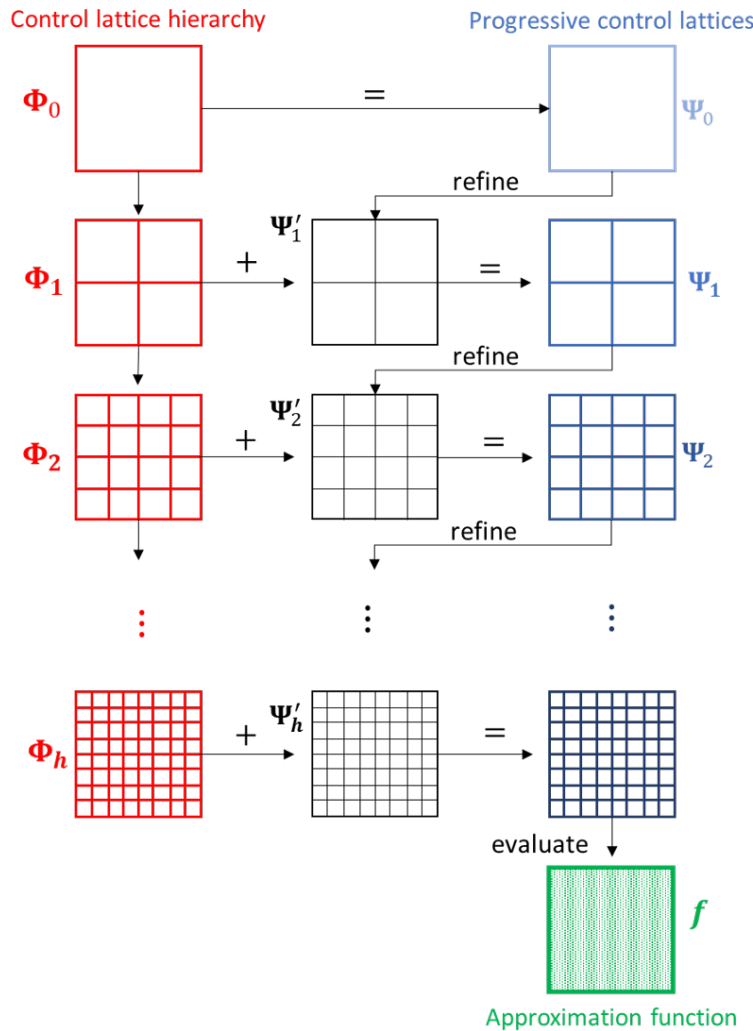


Figure A.3: Schematic representation of control lattice refinement in MBA (Lee et al., 1997).

Algorithm 4: Refinement and accumulation to obtain the final control lattice Ψ_h .

1 **Input:** control lattices $\Phi_0, \Phi_1, \dots, \Phi_h$
2 **Output:** final refined control lattice Ψ_h
3 **Initialize:** $\Psi \leftarrow \Phi_0$
4 **for** $k = 1$ **to** h **do**
5 refine Ψ to the grid of Φ_k using Eqs. (A.19)–(A.22)
6 $\Psi \leftarrow \Psi + \Phi_k$ ▷ control point-wise sum
7 **return** $\Psi_h \leftarrow \Psi$

A.1.4 Stochastic Model of MBA

The development in this subsection is based on the adjustment-theoretic uncertainty modeling presented in Mohammadivojdan (2019). Up to this point, MBA has been described as a deterministic approximation method. For quality assessment and uncertainty propagation in later chapters, a stochastic model that links observation noise to the variability of control points and surface estimates is required. This subsection formulates that model in terms of a linear GMM adjustment. Although the publications present the main conclusions of this stochastic formulation, the full derivation was not included there because of space limitations. The dissertation provides the complete development to document the model and clarify the assumptions behind its use.

As described in Section A.1.1, the solution for a control point depends on its proximity dataset and is given by Eq. (A.13). A unique estimate of ϕ_{ij} is obtained by minimizing the error term $\sum_c (w_c \phi_{ij} - w_c \phi_c)^2$. Here, $(w_c \phi_{ij} - w_c \phi_c)$ denotes the weighted residual of observation c . This minimization is cast as a linear GMM. For a proximity set with c data points, let \mathbf{v} collect the differences between the estimate ϕ_{ij} and the weighted observations, as defined in Eq. (A.24).

$$\begin{bmatrix} v_1 \\ \vdots \\ v_c \end{bmatrix} = \begin{bmatrix} w_1 \\ \vdots \\ w_c \end{bmatrix} \cdot \phi_{ij} - \begin{bmatrix} w_1 \phi_1 \\ \vdots \\ w_c \phi_c \end{bmatrix} \quad (\text{A.24})$$

Here, w_i and ϕ_c are defined by Eq. (A.8). Substituting ϕ_c from Eq. (A.8) into Eq. (A.24) yields Eq. (A.25).

$$\begin{bmatrix} v_1 \\ \vdots \\ v_c \end{bmatrix} = \begin{bmatrix} w_1 \\ \vdots \\ w_c \end{bmatrix} \cdot \phi_{ij} - \begin{bmatrix} w_1 \frac{w_1 z_1}{\sum_{a=0}^3 \sum_{b=0}^3 w_{ab}^2} \\ \vdots \\ w_c \frac{w_c z_c}{\sum_{a=0}^3 \sum_{b=0}^3 w_{ab}^2} \end{bmatrix} \quad (\text{A.25})$$

A linear GMM is given by Eq. (A.26), where \mathbf{z} (also denoted ℓ_z) is the observation vector, \mathbf{v} is the residual vector, \mathbf{A} is the design (Jacobian) matrix, and ϕ is the vector of unknowns. Here, $\mathbf{z} \in \mathbb{R}^c$ and $\mathbf{v} \in \mathbb{R}^c$, and $\mathbf{A} \in \mathbb{R}^{c \times u}$ with $u = \dim(\phi)$. In the MBA proximity adjustment used in this thesis, $u = 1$ so ϕ reduces to a scalar control-point coefficient ϕ_{ij} and $\mathbf{A} \in \mathbb{R}^{c \times 1}$.

$$\mathbf{z} + \mathbf{v} = \mathbf{A} \cdot \phi \quad (\text{A.26})$$

The estimate follows from minimizing the weighted sum of squared residuals, $\mathbf{v}^T \mathbf{P} \mathbf{v}$, where \mathbf{P} is

the residual weight matrix. Within each proximity set, the observations are assumed uncorrelated, which implies a diagonal covariance matrix and therefore a diagonal weight matrix \mathbf{P} with entries given by the inverse variances. Differentiating $\mathbf{v}^T \mathbf{P} \mathbf{v}$ with respect to the unknown parameter vector ϕ leads to Eq. (A.27).

$$\hat{\phi} = (\mathbf{A}^T \mathbf{P} \mathbf{A})^{-1} \mathbf{A}^T \mathbf{P} \mathbf{z}, \quad \text{with } \mathbf{N} = (\mathbf{A}^T \mathbf{P} \mathbf{A}) \quad \text{and} \quad \mathbf{n} = \mathbf{A}^T \mathbf{P} \mathbf{z} \quad (\text{A.27})$$

To cast Eq. (A.25) into the GMM form, the residual vector is transformed using Eq. (A.28). We assume equal pre-transform variances for the observations and residuals, $\sigma_{z_i}^2 = \sigma_{v_i}^2$. By error propagation, the variance of the transformed residuals follows Eq. (A.29). The data vector \mathbf{z} is treated as uncorrelated.

$$\bar{v}_i = \frac{\sum_{a=0}^3 \sum_{b=0}^3 w_{ab}^2}{w_i^2} v_i \quad (\text{A.28})$$

$$\sigma_{\bar{v}_i}^2 = \left(\frac{\sum_{a=0}^3 \sum_{b=0}^3 w_{ab}^2}{w_i^2} \right)^2 \cdot \sigma_{v_i}^2 \quad (\text{A.29})$$

The resulting GMM is

$$\begin{bmatrix} z_1 \\ \vdots \\ z_c \end{bmatrix} + \begin{bmatrix} \bar{v}_1 \\ \vdots \\ \bar{v}_c \end{bmatrix} = \begin{bmatrix} \frac{\sum_{a=0}^3 \sum_{b=0}^3 w_{ab}^2}{w_1} \\ \vdots \\ \frac{\sum_{a=0}^3 \sum_{b=0}^3 w_{ab}^2}{w_c} \end{bmatrix} \cdot \phi_{ij} \quad (\text{A.30})$$

The Variance Covariance Matrix (VCM) of the transformed residuals, $\Sigma_{\bar{\mathbf{v}}\bar{\mathbf{v}}}$, and the weight matrix $\mathbf{P} = (\Sigma_{\bar{\mathbf{v}}\bar{\mathbf{v}}})^{-1}$, are

$$\Sigma_{\bar{\mathbf{v}}\bar{\mathbf{v}}[c \times c]} = \begin{bmatrix} \left(\frac{\sum_{a=0}^3 \sum_{b=0}^3 w_{ab}^2}{w_1} \right)^2 \cdot \sigma_{v_1}^2 & \cdots & 0 \\ \vdots & \ddots & \vdots \\ 0 & \cdots & \left(\frac{\sum_{a=0}^3 \sum_{b=0}^3 w_{ab}^2}{w_c} \right)^2 \cdot \sigma_{v_c}^2 \end{bmatrix} \quad (\text{A.31})$$

$$\mathbf{P}_{[c \times c]} = (\Sigma_{\bar{\mathbf{v}}\bar{\mathbf{v}}})^{-1} = \begin{bmatrix} \frac{w_1^4}{\left(\sum_{a=0}^3 \sum_{b=0}^3 w_{ab}^2 \right)^2} \cdot \frac{1}{\sigma_{v_1}^2} & \cdots & 0 \\ \vdots & \ddots & \vdots \\ 0 & \cdots & \frac{w_c^4}{\left(\sum_{a=0}^3 \sum_{b=0}^3 w_{ab}^2 \right)^2} \cdot \frac{1}{\sigma_{v_c}^2} \end{bmatrix} \quad (\text{A.32})$$

The next steps toward the final estimate, $\hat{\phi}$, are the computation of the normal matrix \mathbf{N} and the vector \mathbf{n} . Here there is a single unknown, the control point ϕ_{ij} . The design matrix has dimension $[c \times 1]$, and the normal matrix is a scalar.

$$\begin{aligned}
\mathbf{N}_{[1 \times 1]} &= \mathbf{A}_{[1 \times c]}^T \mathbf{P}_{[c \times c]} \mathbf{A}_{[c \times 1]} \\
&= \begin{bmatrix} \sum_{a=0}^3 \sum_{b=0}^3 \frac{w_{ab}^2}{w_1} & \dots & \sum_{a=0}^3 \sum_{b=0}^3 \frac{w_{ab}^2}{w_c} \end{bmatrix} \begin{bmatrix} \frac{w_1^4}{(\sum_{a=0}^3 \sum_{b=0}^3 w_{ab}^2)^2} \cdot \frac{1}{\sigma_{v_1}^2} & \dots & 0 \\ \vdots & \ddots & \vdots \\ 0 & \dots & \frac{w_c^4}{(\sum_{a=0}^3 \sum_{b=0}^3 w_{ab}^2)^2} \cdot \frac{1}{\sigma_{v_c}^2} \end{bmatrix} \\
&\times \begin{bmatrix} \sum_{a=0}^3 \sum_{b=0}^3 \frac{w_{ab}^2}{w_1} \\ \vdots \\ \sum_{a=0}^3 \sum_{b=0}^3 \frac{w_{ab}^2}{w_c} \end{bmatrix} = \sum_{i=1}^c w_i^2 \cdot \frac{1}{\sigma_{v_i}^2}
\end{aligned} \tag{A.33}$$

$$\mathbf{N}_{[1 \times 1]}^{-1} = \frac{1}{\sum_{i=1}^c w_i^2 \cdot \frac{1}{\sigma_{v_i}^2}} \tag{A.34}$$

$$\begin{aligned}
\mathbf{n}_{[1 \times 1]} &= \mathbf{A}_{[1 \times c]}^T \mathbf{P}_{[c \times c]} \mathbf{z}_{[c \times 1]} = \begin{bmatrix} \sum_{a=0}^3 \sum_{b=0}^3 \frac{w_{ab}^2}{w_1} & \dots & \sum_{a=0}^3 \sum_{b=0}^3 \frac{w_{ab}^2}{w_c} \end{bmatrix} \\
&\times \begin{bmatrix} \frac{w_1^4}{(\sum_{a=0}^3 \sum_{b=0}^3 w_{ab}^2)^2} \cdot \frac{1}{\sigma_{v_1}^2} & \dots & 0 \\ \vdots & \ddots & \vdots \\ 0 & \dots & \frac{w_c^4}{(\sum_{a=0}^3 \sum_{b=0}^3 w_{ab}^2)^2} \cdot \frac{1}{\sigma_{v_c}^2} \end{bmatrix} \begin{bmatrix} z_1 \\ \vdots \\ z_c \end{bmatrix} \\
&= \sum_{i=1}^c \frac{w_i^3 z_i}{\sum_{a=0}^3 \sum_{b=0}^3 w_{ab}^2} \cdot \frac{1}{\sigma_{v_i}^2}
\end{aligned} \tag{A.35}$$

$$\hat{\phi}_{[1 \times 1]} = \mathbf{N}_{[1 \times 1]}^{-1} \cdot \mathbf{n}_{[1 \times 1]} = \frac{1}{\sum_{i=1}^c w_i^2 \cdot \frac{1}{\sigma_{v_i}^2}} \cdot \sum_{i=1}^c \frac{w_i^3 z_i}{\sum_{a=0}^3 \sum_{b=0}^3 w_{ab}^2} \cdot \frac{1}{\sigma_{v_i}^2} \tag{A.36}$$

If $\sigma_{v_1}^2 = \sigma_{v_2}^2 = \dots = \sigma_{v_c}^2$,

$$\hat{\phi}_{[1 \times 1]} = \frac{\sum_{i=1}^c \frac{w_i^3 z_i}{\sum_{a=0}^3 \sum_{b=0}^3 w_{ab}^2}}{\sum_{i=1}^c w_i^2} = \frac{\sum_{i=0}^c w_i^2 \phi_i}{\sum_{i=1}^c w_i^2}. \tag{A.37}$$

The scalar $\hat{\phi}$ is the final estimate for the control point ϕ_{ij} . This agrees with Section A.1.1 (see Eq. (A.13)). Each control point in the lattice is computed individually using Eq. (A.37). According to Fig. A.2b, control points have overlapping proximity datasets. As a result, their solutions are correlated. The functional relationship between the control point lattice Φ and the data points is given in Eq. (A.38). A control point lattice contains $(m+3) \times (n+3)$ control points ϕ_{ij} , with $i = -1, 0, 1, \dots, m, m+1$ and $j = -1, 0, 1, \dots, n, n+1$. In Eq. (A.38), \mathbf{A}_1 denotes the Jacobian matrix, and \mathbf{z} is the vector of data points.

$$\Phi_{[(m+3)\times(n+3)\times 1]} = \mathbf{A}_1_{[(m+3)\times(n+3)\times s]} \cdot \mathbf{z}_{[s\times 1]} \quad (\text{A.38})$$

$$\begin{bmatrix} \phi_{00} \\ \vdots \\ \phi_{(m+3)\times(n+3)} \end{bmatrix} = \begin{bmatrix} \frac{w_1^3}{(\sum_{a=0}^3 \sum_{b=0}^3 w_{ab}^2) \sum_{i=1}^{c_1} w_i^2} & \cdots & \vdots \\ \vdots & \ddots & \vdots \\ \vdots & \cdots & \vdots \end{bmatrix} \begin{bmatrix} z_1 \\ \vdots \\ z_s \end{bmatrix} \quad (\text{A.39})$$

The elements of the Jacobian matrix are nonzero only for observations in the proximity dataset of the corresponding control point. Based on the law of error propagation, the VCM of the control points, $\Sigma_{\phi\phi}$ can be derived based on Eq. (A.40). Σ_{zz} is the VCM of the data points.

$$\Sigma_{\phi\phi}_{[(m+3)\times(n+3)\times(m+3)\times(n+3)]} = \mathbf{A}_1_{[(m+3)\times(n+3)\times s]} \Sigma_{zz}_{[s\times s]} \mathbf{A}_1^T_{[s\times(m+3)\times(n+3)]} \quad (\text{A.40})$$

A point estimated on the surface by equation Eq. (A.3) has a functional relationship with the 16 control points in its neighborhood. As a result, the estimated points which have overlapping control points are correlated. For a set of c estimated points on the surface $\hat{\mathbf{z}}$, the matrix \mathbf{A}_2 describes the functional relationship between estimated points and the control points.

$$\hat{\mathbf{z}}_{[s\times 1]} = \mathbf{A}_2_{[s\times(m+3)\times(n+3)]} \cdot \hat{\Phi}_{[(m+3)\times(n+3)\times 1]} \quad (\text{A.41})$$

Using the VCM of the control points, VCM of $\hat{\mathbf{z}}$, can be derived based on the law of error propagation.

$$\Sigma_{\hat{\mathbf{z}}\hat{\mathbf{z}}}_{[s\times s]} = \mathbf{A}_2_{[s\times(m+3)\times(n+3)]} \cdot \Sigma_{\phi\phi}_{[(m+3)\times(n+3)\times(m+3)\times(n+3)]} \cdot \mathbf{A}_2^T_{[(m+3)\times(n+3)\times c]} \quad (\text{A.42})$$

Up to this point, the stochastic model of the BA algorithm is complete. We have the estimator for the control points (Eq. (A.37)), the VCM of the estimated control points (Eq. (A.40)), and the VCM of a set of surface estimates given the control points (Eq. (A.42)). The next step is the stochastic model of the MBA algorithm. The control lattice at level k is used to generate $\Delta^{k+1}\mathbf{z}$ for the next level (see Eq. (A.16)). Table A.1 summarizes the propagation of VCMs from the coarsest level Φ_0 to the finest level Φ_h .

Table A.1: *Stochastic model of MBA algorithm.*

Level	VCM of control points	New z values	VCM of the estimated function	VCM of the new z values
Φ_0	$\Sigma_{\phi_0\phi_0} = \mathbf{A}_1 \Sigma_{zz} \mathbf{A}_1^T$	$\Delta^1\mathbf{z} = \mathbf{z} - \mathbf{f}_0$	$\Sigma_{\mathbf{f}_0\mathbf{f}_0} = \mathbf{A}_2 \Sigma_{\phi_0\phi_0} \mathbf{A}_2^T$	$\Sigma_{\Delta^1 z \Delta^1 z} = \Sigma_{zz} + \Sigma_{\mathbf{f}_0\mathbf{f}_0}$
Φ_1	$\Sigma_{\phi_1\phi_1} = \mathbf{A}_1 \Sigma_{\Delta^1 z \Delta^1 z} \mathbf{A}_1^T$	$\Delta^2\mathbf{z} = \mathbf{z} - \mathbf{f}_0 - \mathbf{f}_1$	$\Sigma_{\mathbf{f}_1\mathbf{f}_1} = \mathbf{A}_2 \Sigma_{\phi_1\phi_1} \mathbf{A}_2^T$	$\Sigma_{\Delta^2 z \Delta^2 z} = \Sigma_{zz} + \Sigma_{\mathbf{f}_0\mathbf{f}_0} + \Sigma_{\mathbf{f}_1\mathbf{f}_1}$
\vdots	\vdots	\vdots	\vdots	\vdots
Φ_k	$\Sigma_{\phi_k\phi_k} = \mathbf{A}_1 \Sigma_{\Delta^k z \Delta^k z} \mathbf{A}_1^T$	$\Delta^{k+1}\mathbf{z} = \mathbf{z} - \sum_{i=0}^k \mathbf{f}_i$	$\Sigma_{\mathbf{f}_k\mathbf{f}_k} = \mathbf{A}_2 \Sigma_{\phi_k\phi_k} \mathbf{A}_2^T$	$\Sigma_{\Delta^{k+1} z \Delta^{k+1} z} = \Sigma_{zz} + \sum_{i=0}^k \Sigma_{\mathbf{f}_i\mathbf{f}_i}$
\vdots	\vdots	\vdots	\vdots	\vdots
Φ_h	$\Sigma_{\phi_h\phi_h} = \mathbf{A}_1 \Sigma_{\Delta^h z \Delta^h z} \mathbf{A}_1^T$	-	$\Sigma_{\mathbf{f}_h\mathbf{f}_h} = \mathbf{A}_2 \Sigma_{\phi_h\phi_h} \mathbf{A}_2^T$	$\Sigma_{\Delta^{h+1} z \Delta^{h+1} z} = \Sigma_{zz} + \sum_{i=0}^h \Sigma_{\mathbf{f}_i\mathbf{f}_i}$

Bibliography

- [Abubakar & Poerbandono 2023] ABUBAKAR, Aliyu A. ; POERBANDONO, Purbo: Effectiveness of vertical error budget model for portable multi-beam echo-sounder in shallow water bathymetric survey. In: *IOP Conference Series: Earth and Environmental Science* 1245 (2023), No. 1, pp. 012041. – ISSN 1755-1307
- [Aggarwal 2017] AGGARWAL, Charu C.: *Outlier Analysis*. 2nd ed. 2017. Cham : Springer, 2017 (Springer eBook Collection Computer Science). – <https://doi.org/10.1007/978-3-319-47578-3>. – ISBN 9783319475783
- [Aguiar et al. 2021] AGUIAR, Pedro ; CUNHA, António ; BAKON, Matus ; RUIZ-ARMENTEROS, Antonio M. ; SOUSA, Joaquim J.: Multivariate Outlier Detection in Postprocessing of Multi-temporal PS-InSAR Results using Deep Learning. In: *Procedia Computer Science* 181 (2021), pp. 1146–1153
- [Alkhatib et al. 2018] ALKHATIB, Hamza ; KARGOLL, Boris ; PAFFENHOLZ, Jens-André: Further Results on a Robust Multivariate Time Series Analysis in Nonlinear Models with Autoregressive and t-Distributed Errors. In: ROJAS, Ignacio (Ed.) ; POMARES, Héctor (Ed.) ; VALENZUELA, Olga (Ed.): *Time Series Analysis and Forecasting*. Cham : Springer International Publishing, 2018, pp. 25–38. – ISBN 978-3-319-96944-2
- [Anselin 1995] ANSELIN, Luc: Local indicators of spatial association–LISA. In: *Geographical analysis* 27 (1995), No. 2, pp. 93–115
- [Arlot & Celisse 2010] ARLOT, Sylvain ; CELISSE, Alain: A survey of cross-validation procedures for model selection. In: *Statistics Surveys* 4 (2010), Januar, No. none. – URL <http://dx.doi.org/10.1214/09-SS054>. – ISSN 1935-7516
- [Arnold & Shaw 1993] ARNOLD, Jams ; SHAW, Scott: A surface weaving approach to multibeam depth estimation. In: *Proceedings of OCEANS'93 IEEE (Conf.)*, 1993, pp. II–95
- [Artz et al. 2021] ARTZ, Thomas ; BROCKMANN, Herbert ; HENNECKE, Sonja ; WILLERSINN, Dieter: Auf dem Weg zu einer digitalen Bundeswasserstraße: Maßnahmenplanung (Teil-)Autonomes Messen als Grundlage für den Masterplan Binnenschifffahrt / Bundesanstalt für Gewässerkunde (BfG). Koblenz, 2021 (BfG-2074). – Research report. <https://doi.org/10.567/BfG-2074>, Auftraggeber: BMVI
- [Barends et al. 1995] BARENDs, Frans ; BROUWER, Frits ; SCHRÖDER, Frans: *Land Subsidence*. Rotterdam, The Netherlands : A. A. Balkema, 1995. – xi–xiv p. – ISBN 90-5410-589-5
- [Barnett & Lewis 1984] BARNETT, Vic ; LEWIS, Toby: *Outliers in statistical data*. 2. ed. Chichester [u.a : Wiley, 1984 (Wiley series in probability and mathematical statistics : Applied probability and statistics). – ISBN 0471905070
- [Barnhill 1977] BARNHILL, Robert E.: Representation and Approximation of Surfaces. In: RICE, John R. (Ed.): *Mathematical Software*. Academic Press, 1977, pp. 69–120. – ISBN 978-0-12-587260-7

- [Berger et al. 2017] BERGER, Matthew ; TAGLIASACCHI, Andrea ; SEVERSKY, Lee M. ; ALLIEZ, Pierre ; GUENNEBAUD, Gaël ; LEVINE, Joshua A. ; SHARF, Andrei ; SILVA, Claudio T.: A survey of surface reconstruction from point clouds. In: *Computer Graphics Forum* 36 (2017), No. 1, pp. 301–329. – <https://doi.org/10.1111/cgf.12802>
- [BGR 2025] BGR, Bundesanstalt für Geowissenschaften und Rohstoffe: *Bodenbewegungsdienst Deutschland*. 2025. – URL <https://bodenbewegungsdienst.bgr.de/>. – Accessed: 2025-08-29
- [BMDV 2016] BMDV, Bundesministerium für Digitales und Verkehr: *Bundesverkehrswegeplan 2030*. 2016. – URL https://www.bmv.de/SharedDocs/DE/Publikationen/G/bundesverkehrswegeplan-2030-gesamtplan.pdf?__blob=publicationFile. – Accessed: 2025-08-28
- [BMDV 2024] BMDV, Bundesministerium für Digitales und Verkehr: *Sicherheit auf dem Wasser*. 2024. – URL https://www.bmv.de/SharedDocs/DE/Publikationen/WS/sicherheit-auf-dem-wasser.pdf?__blob=publicationFile. – Accessed: 2025-08-28
- [Bolle & Vemuri 1991] BOLLE, Ruud M. ; VEMURI, Baba C.: On three-dimensional surface reconstruction methods. In: *IEEE Transactions on Pattern Analysis and Machine Intelligence* 13 (1991), No. 1, pp. 1–13
- [Bottelier et al. 2005] BOTTELIER, Peter ; BRIESE, Christian ; HENNIS, Natasha ; LINDENBERGH, Roderik ; PFEIFER, Norbert: Distinguishing features from outliers in automatic Kriging-based filtering of MBES data: a comparative study. In: RENARD, Philippe (Ed.) ; DEMOUGEOT-RENARD, Hélène (Ed.): *Geostatistics for environmental applications*. Berlin and Heidelberg : Springer, 2005, pp. 403–414. – https://doi.org/10.1007/3-540-26535-x_34. – ISBN 3540265333
- [Bracco et al. 2018] BRACCO, Cesare ; GIANNELLI, Carlotta ; GROSSMANN, David ; SESTINI, Alessandra: Adaptive fitting with THB-splines: Error analysis and industrial applications. In: *Computer Aided Geometric Design* 62 (2018), pp. 239–252. – URL <https://www.sciencedirect.com/science/article/pii/S0167839618300402>. – <https://doi.org/10.1016/j.cagd.2018.03.026>. – ISSN 0167-8396
- [Breunig et al. 2000] BREUNIG, Markus M. ; KRIEGEL, Hans-Peter ; NG, Raymond T. ; SANDER, Jörg: LOF: identifying density-based local outliers. In: *Proceedings of the 2000 ACM SIGMOD international conference on Management of data*, 2000, pp. 93–104
- [Brockmeyer 2019] BROCKMEYER, Marco: Daten der Landesvermessung zur räumlichen Interpolation von Bodenbewegungen. In: *Tagungsband Geomonitoring 2019* Vol. 2019, Forschungsdaten-Repositorium der LUH, 2019, pp. 151–163. – <https://doi.org/10.15488/4519>
- [Brockmeyer 2024a] BROCKMEYER, Marco: *Modellierung von Bodenbewegungen anhand heterogener Messverfahren am Beispiel der niedersächsischen Landesfläche*. Hannover, Leibniz Universität Hannover, PhD dissertation, 2024. – Auch veröffentlicht in Veröffentlichungen der DGK, Reihe C, Dissertationen, Heft 918, Bayerische Akademie der Wissenschaften, München. ISBN 978-3-7696-5330-4. ISSN 0065-5325
- [Brockmeyer 2024b] BROCKMEYER, Marco: *Modellierung von Bodenbewegungen anhand heterogener Messverfahren am Beispiel der niedersächsischen Landesfläche*, Gottfried Wilhelm Leibniz Universität Hannover, Dissertation, 2024
- [Brockmeyer et al. 2020] BROCKMEYER, Marco ; SCHNACK, Christian ; JAHN, Cord-Hinrich: Datenanalyse und flächenhafte Modellierung der PSI-Informationen des Bodenbewegungsdienst Deutschlands für die Landesfläche Niedersachsens. In: *ZfV - Zeitschrift für Geodäsie, Geoinformation und Landmanagement* 3 (2020), pp. 154–167

- [Bureick et al. 2019] BUREICK, Johannes ; ALKHATIB, Hamza ; NEUMANN, Ingo: Fast converging elitist genetic algorithm for knot adjustment in B-spline curve approximation. In: *Journal of Applied Geodesy* 13 (2019), No. 4, pp. 317–328. – <https://doi.org/10.1515/jag-2019-0021>
- [Cazals & Giesen 2006] CAZALS, Frederic ; GIESEN, Joachim: Delaunay Triangulation Based Surface Reconstruction. In: *Effective Computational Geometry for Curves and Surfaces*. Springer, 2006, pp. 231–276. – https://doi.org/10.1007/3-540-33259-8_6
- [Chandola et al. 2009] CHANDOLA, Varun ; BANERJEE, Arindam ; KUMAR, Vipin: Anomaly detection. In: *ACM Computing Surveys* 41 (2009), No. 3, pp. 1–58. – <https://doi.org/10.1145/1541880.1541882>. – ISSN 0360-0300
- [Colin Ware et al. 1991] COLIN WARE ; WILLIAM KNIGHT ; DAVID WELLS: Memory intensive statistical algorithms for multibeam bathymetric data. In: *Computers & Geosciences* 17 (1991), No. 7, pp. 985–993. – URL <https://www.sciencedirect.com/science/article/pii/009830049190093S>. – [https://doi.org/10.1016/0098-3004\(91\)90093-S](https://doi.org/10.1016/0098-3004(91)90093-S). – ISSN 00983004
- [Cong et al. 2023] CONG, Zheng ; MA, Teng ; LI, Ye ; YUAN, Mingxiao ; LING, Yu ; DU, Haohan ; QI, Chi ; LI, Ziyuan ; XU, Shuo ; ZHANG, Qiang: A Storage-Saving Quadtree-Based Multibeam Bathymetry Map Representation Method. In: *Journal of Marine Science and Engineering* 11 (2023), No. 4. – URL <https://www.mdpi.com/2077-1312/11/4/709>. – ISSN 2077-1312
- [Cox 1971] COX, Michael G.: Curve fitting with piecewise polynomials. In: *IMA Journal of Applied Mathematics* 8 (1971), No. 1, pp. 36–52
- [Crosetto et al. 2021] CROSETTO, M. ; SOLARI, L. ; BALASIS-LEVINSEN, J. ; BATESON, L. ; CASAGLI, N. ; FREI, M. ; OYEN, A. ; MOLDESTAD, D. A. ; MRÓZ, M.: Deformation Monitoring at European Scale: the Copernicus Ground Motion Service. In: *The International Archives of the Photogrammetry, Remote Sensing and Spatial Information Sciences XLIII-B3-2021* (2021), pp. 141–146. – URL <https://isprs-archives.copernicus.org/articles/XLIII-B3-2021/141/2021/>
- [Crosetto et al. 2016] CROSETTO, Michele ; MONSERRAT, Oriol ; CUEVAS-GONZÁLEZ, María ; DEVANTHÉRY, Núria ; CRIPPA, Bruno: Persistent Scatterer Interferometry: A review. In: *ISPRS Journal of Photogrammetry and Remote Sensing* 115 (2016), pp. 78–89. – URL <https://www.sciencedirect.com/science/article/pii/S0924271615002415>. – Theme issue 'State-of-the-art in photogrammetry, remote sensing and spatial information science'. – ISSN 0924-2716
- [Curlander & McDonough 1991] CURLANDER, John C. ; MCDONOUGH, Robert N.: *Synthetic Aperture Radar: Systems and Signal Processing*. New York : John Wiley & Sons, Inc., 1991. – ISBN 9780471857709
- [Davies & Gather 1993] DAVIES, Laurie ; GATHER, Ursula: The Identification of Multiple Outliers. In: *Journal of the American Statistical Association* 88 (1993), No. 423, pp. 782–792. – <https://doi.org/10.1080/01621459.1993.10476339>. – ISSN 0162-1459
- [Debese 2007] DEBESE, Nathalie: Multibeam echosounder data cleaning through an adaptive surface-based approach. In: *Us Hydro* 7 (2007)
- [Debese & Bisquay 1999a] DEBESE, Nathalie ; BISQUAY, Hervé: Automatic Detection of Punctual Errors in Multibeam Data Using a Robust Estimator. In: *The International Hydrographic Review* (1999). – URL <https://journals.lib.unb.ca/index.php/ihr/article/view/26159>. – ISSN 0020-6946
- [Debese & Bisquay 1999b] DEBESE, Nathalie ; BISQUAY, Hervé: Automatic Detection of Punctual Errors in Multibeam Data Using a Robust Estimator. In: *The International Hydrographic Review* 76 (1999), No. 1, pp. 49–63

- [Debese et al. 1998] DEBESE, Nathalie ; FREULON, Xavier ; MÉVEL, Catherine: Application d'un estimateur robuste à la détection des erreurs ponctuelles dans les données bathymétriques. In: *Proceedings of the Canadian Hydrographic Conference (CHC'98)*. Victoria, Canada, 1998. – In French
- [Debese et al. 2012] DEBESE, Nathalie ; MOITIÉ, Rodéric ; SEUBE, Nicolas: Multibeam echosounder data cleaning through a hierarchic adaptive and robust local surfacing. In: *Computers & Geosciences* 46 (2012), pp. 330–339. – URL <https://www.sciencedirect.com/science/article/pii/S0098300412000143>. – <https://doi.org/10.1016/j.cageo.2012.01.012>. – ISSN 00983004
- [Dineng Zhao et al. 2015] DINENG ZHAO ; ZIYIN WU ; JIEQIONG ZHOU ; JIABIAO LI ; JIHONG SHANG ; SHOUJUN LI: A New Method of Automatic SVP Optimization Based on MOV Algorithm. In: *Marine Geodesy* 38 (2015), No. 3, pp. 225–240. – <https://doi.org/10.1080/01490419.2015.1006798>. – ISSN 0149-0419
- [Dolan & Lucieer 2013] DOLAN, Margaret ; LUCIEER, Vanessa: The New Wave of Bathymetry Data—Uses and Limitations for Marine Benthic Habitat Mapping and Geomorphology. In: *Geohab (Marine Geology and Benthic Habitat Mapping)*. Rome : Italian Geological Survey, 2013
- [Drewes & Heidbach 2005] DREWES, Hermann ; HEIDBACH, Oliver: Deformation of the South American crust estimated from finite element and collocation methods. In: *A Window on the Future of Geodesy*. Springer, 2005, pp. 544–549
- [Du et al. 1996] DU, Ziqin ; WELLS, David ; MAYER, Larry: An approach to automatic detection of outliers in multibeam echo sounding data. In: *Oceanographic Literature Review* 7 (1996), No. 43, pp. 737
- [Eakins & Taylor 2010] EAKINS, Barry W. ; TAYLOR, Lisa A.: Seamlessly integrating bathymetric and topographic data to support tsunami modeling and forecasting efforts. In: *Ocean globe* (2010), pp. 37–56
- [Efron 1981] EFRON, Bradley: Censored data and the bootstrap. In: *Journal of the American Statistical Association* 76 (1981), No. 374, pp. 312–319
- [Efron & Tibshirani 1994] EFRON, Bradley ; TIBSHIRANI, Robert J.: *An introduction to the bootstrap*. CRC press, 1994
- [Elachi et al. 1982] ELACHI, Charles ; BICKNELL, Tom ; JORDAN, Rolando L. ; WU, Chialin: Spaceborne Synthetic-Aperture Imaging Radar: Applications, Techniques and Technology. In: *Proceedings of the IEEE* 70 (1982), No. 10, pp. 1174–1209. – <https://doi.org/10.1109/PROC.1982.12448>
- [Esbensen et al. 2010] ESBENSEN, Kim ; GUYOT, Dominique ; WESTAD, Frank ; HOUMOLLER, Lars P.: *Multivariate Data Analysis - in practice*. 5th. Oslo : CAMO Software, 2010
- [Ebner von Eschenbach et al. 2022] ESCHENBACH, Anna-Dorothea Ebner von ; HELMS, Martin ; MAURER, Thomas ; NILSON, Enno ; HÄMMERLE, Martin ; WURMS, Sven ; ORLOVIUS, Andreas: Untersuchung wasserbaulicher und wasserwirtschaftlicher Optionen zur Sicherstellung zuverlässig kalkulierbarer Transportbedingungen am Rhein bei Niedrigwasser / Bundesanstalt für Gewässerkunde (BfG) und Bundesanstalt für Wasserbau (BAW). Koblenz und Karlsruhe, 2022. – Research report. Aktionsplan Niedrigwasser Rhein, BfG-Nr. M39610204073, BAW-Nr. B3953.02.06.10197
- [European Commission 2021] EUROPEAN COMMISSION: NAIADES III: Boosting future-proof European inland waterway transport / European Commission. Brussels, 2021 (COM(2021)

- 324 final). – Communication from the Commission. – URL <https://eur-lex.europa.eu/legal-content/EN/ALL/?uri=CELEX:52021DC0324>. – Accessed: 2025-08-28
- [European Commission 2025] EUROPEAN COMMISSION: Inland Water Transport Digitalisation Vision / European Commission, Directorate-General for Mobility and Transport. Brussels, 2025. – Vision paper. – URL https://transport.ec.europa.eu/document/download/14b2195a-d175-49d9-a0dd-6662232b1370_en?filename=IWT_Digitalisation_Vision.pdf. – Accessed: 2025-08-28. Prepared by the NAIADES and DINA expert groups. This paper reflects the views of the expert groups, not the Commission
- [European Space Agency 2020] EUROPEAN SPACE AGENCY: *Sentinel-1*. 2020. – URL <https://sentinel.esa.int/web/sentinel/missions/sentinel-1>. – Accessed: 2020-09-01
- [Ferretti et al. 2007] FERRETTI, Alessandro ; SAVIO, Giuliano ; BARZAGHI, Riccardo ; BORGHI, Alessandra ; MUSAZZI, Sergio ; NOVALI, Fabrizio ; PRATI, Claudio ; ROCCA, Fabio: Submillimeter accuracy of InSAR time series: Experimental validation. In: *IEEE Transactions on Geoscience and Remote Sensing* 45 (2007), No. 5, pp. 1142–1153. – <https://doi.org/10.1109/TGRS.2007.894440>
- [Fleishman et al. 2005] FLEISHMAN, Shachar ; COHEN-OR, Daniel ; SILVA, Cláudio T.: Robust Moving Least-Squares Fitting with Sharp Features. In: *ACM Transactions on Graphics* 24 (2005), No. 3, pp. 544–552. – <https://doi.org/10.1145/1073204.1073227>
- [Fonseca & Mayer 2007] FONSECA, Luciano ; MAYER, Larry: Remote estimation of surficial seafloor properties through the application Angular Range Analysis to multibeam sonar data. In: *Marine Geophysical Researches* 28 (2007), No. 2, pp. 119–126
- [Forsy & Bartels 1992] FORSEY, David R. ; BARTELS, Richard H.: Tensor products and hierarchical fitting. In: *Curves and Surfaces in Computer Vision and Graphics II* Vol. 1610 International Society for Optics and Photonics (Conf.), 1992, pp. 88–96
- [Forsy & Bartels 1995] FORSEY, David R. ; BARTELS, Richard H.: Surface fitting with hierarchical splines. In: *ACM Transactions on Graphics* 14 (1995), No. 2, pp. 134–161
- [Foumelis et al. 2022] FOUMELIS, Michael ; DELGADO BLASCO, Jose M. ; BRITO, Fabrice ; PACINI, Fabrizio ; PAPAGEORGIOU, Elena ; PISHEHVAR, Panteha ; BALLY, Philippe: SNAPPING Services on the Geohazards Exploitation Platform for Copernicus Sentinel-1 Surface Motion Mapping. In: *Remote Sensing* 14 (2022), No. 23. – URL <https://www.mdpi.com/2072-4292/14/23/6075>. – ISSN 2072-4292
- [Franke & Nielson 1980] FRANKE, Richard ; NIELSON, Greg: Smooth interpolation of large sets of scattered data. In: *International journal for numerical methods in engineering* 15 (1980), No. 11, pp. 1691–1704
- [Franke & Nielson 1991] FRANKE, Richard ; NIELSON, Gregory M.: Scattered data interpolation and applications: A tutorial and survey. In: *Geometric Modeling*. Springer, 1991, pp. 131–160
- [Giannelli et al. 2012] GIANNELLI, Carlotta ; JÜTTLER, Bert ; SPELEERS, Hendrik: THB-splines: The truncated basis for hierarchical splines. In: *Computer Aided Geometric Design* 29 (2012), No. 7, pp. 485–498
- [Goovaerts 1997] GOOVAERTS, Pierre: *Geostatistics for Natural Resources Evaluation*. Oxford University Press, 1997. – <https://doi.org/10.1093/oso/9780195115383.001.0001>. – ISBN 9780195115383

- [Gostnell et al. 2006] GOSTNELL, Caleb ; YOOS, Jake ; BRODET, Steve: NOAA test and evaluation of phase differencing bathymetric sonar technology. In: *Proceedings of the Canadian Hydrographic Conference*. Halifax, Canada, 2006
- [Haining 1993] HAINING, Robert: *Spatial data analysis in the social and environmental sciences*. Cambridge University Press, 1993
- [Haji Mohammadloo et al. 2019] HAJI MOHAMMADLOO, Tannaz ; SNELLEN, Mirjam ; AMIRI-SIMKOOEI, A. ; SIMONS, D. G.: Assessment of reliability of multi-beam echo-sounder bathymetric uncertainty prediction models. In: *Proceedings of the 5th Underwater Acoustics Conference and Exhibition, Crete, Greece, 2019*, pp. 783–790
- [Haji Mohammadloo et al. 2018] HAJI MOHAMMADLOO, Tannaz ; SNELLEN, Mirjam ; SIMONS, Dick: Multi-beam echo-sounder bathymetric measurements: Implications of using frequency modulated pulses. In: *The Journal of the Acoustical Society of America* 144 (2018), pp. 842–860. – <https://doi.org/10.1121/1.5050816>
- [Hanssen 2001] HANSEN, Ramon F.: Radar Interferometry. In: *1567-3200* 1 (2001). – <https://doi.org/10.1007/0-306-47633-9>. – ISSN 1567-3200
- [Hardy 1971] HARDY, Rolland L.: Multiquadric equations of topography and other irregular surfaces. In: *Journal of geophysical research* 76 (1971), No. 8, pp. 1905–1915
- [Hare 1995] HARE, Rob: Depth and Position Error Budgets for Multibeam Echosounding. In: *The International Hydrographic Review* (1995). – URL <https://journals.lib.unb.ca/index.php/ihr/article/view/23178>. – ISSN 0020-6946
- [Hare et al. 2011] HARE, Rob ; EAKINS, Barry W. ; AMANTE, Christopher J.: Modelling Bathymetric Uncertainty. In: *The International Hydrographic Review* (2011). – URL <https://journals.lib.unb.ca/index.php/ihr/article/view/20888>. – ISSN 0020-6946
- [Harmening 2020] HARMENING, Corinna: *Spatio-temporal deformation analysis using enhanced B-spline models of laser scanning point clouds*. Vienna, Austria, Technische Universität Wien, Dissertation, 2020. – URL <https://www.tuwien.at/bibliothek>
- [Harmening & Neuner 2015] HARMENING, Corinna ; NEUNER, Hans: A constraint-based parameterization technique for B-spline surfaces. In: *Journal of Applied Geodesy* 9 (2015), No. 3, pp. 143–161. – <https://doi.org/10.1515/jag-2015-0003>
- [Harmening & Neuner 2020] HARMENING, Corinna ; NEUNER, Hans: A spatio-temporal deformation model for laser scanning point clouds. In: *Journal of Geodesy* 94 (2020), No. 2, pp. 26
- [Haslett et al. 1991] HASLETT, John ; BRADLEY, Ronan ; CRAIG, Peter ; UNWIN, Antony ; WILLS, Graham: Dynamic graphics for exploring spatial data with application to locating global and local anomalies. In: *The American Statistician* 45 (1991), No. 3, pp. 234–242
- [Hawkins 1980] HAWKINS, Douglas M.: *Identification of outliers*. Vol. 11. Springer, 1980
- [Henderson & Lewis 1998] HENDERSON, Floyd M. (Ed.) ; LEWIS, Anthony J. (Ed.): *Principles and Applications of Imaging Radar*. Vol. 2. 3. New York : John Wiley & Sons, Inc., 1998
- [Herlihy et al. 1992] HERLIHY, Daniel R. ; STEPKA, Thomas N. ; RULON, Timothy D.: Le filtrage des sondes erronées dans les sondages multifaisceaux. In: *International Hydrographic Review* 69 (1992), No. 2

- [Herrmann & Möser 2008] HERRMANN, Jörg ; MÖSER, Michael: Reverse Engineering – Vom Objekt zum Modell. In: *Allgemeine Vermessungsnachrichten (avn)* 115 (2008), No. 5, pp. 185–187
- [Hoschek et al. 1993] HOSCHEK, Josef ; LASSER, Dieter ; SCHUMAKER, Larry L.: *Fundamentals of computer aided geometric design*. AK Peters, Ltd., 1993
- [Hsu et al. 1992] HSU, William M. ; HUGHES, John F. ; KAUFMAN, Henry: Direct manipulation of free-form deformations. In: *ACM Siggraph Computer Graphics* Vol. 26 ACM (Conf.), 1992, pp. 177–184
- [Huang et al. 2020] HUANG, Xianyuan ; HUANG, Chenhu ; ZHAI, Guojun ; LU, Xiuping ; XIAO, Guorui ; SUI, Lifan ; DENG, Kailiang: Data Processing Method of Multibeam Bathymetry Based on Sparse Weighted LS-SVM Machine Algorithm. In: *IEEE Journal of Oceanic Engineering* 45 (2020), No. 4, pp. 1538–1551. – ISSN 0364-9059
- [Huang et al. 2022] HUANG, Zhangjin ; WEN, Yuxin ; WANG, Zihao ; REN, Jinjuan ; JIA, Kui: *Surface Reconstruction from Point Clouds: A Survey and a Benchmark*. <http://arxiv.org/pdf/2205.02413>. Mai 2022. – arXiv preprint arXiv:2205.02413
- [Huber & Ronchetti 2009] HUBER, Peter J. ; RONCHETTI, Elvezio M.: *Robust Statistics*. 2nd Ed. Hoboken, New Jersey : Wiley, 2009. – ISBN 978-0-470-12990-6
- [International Hydrographic Organization 2022] INTERNATIONAL HYDROGRAPHIC ORGANIZATION: *Standards for Hydrographic Surveys S-44 Edition 6.1.0*. 2022
- [ISO/GUM-Suppl1:1998(E) 1998] ISO: Guide to the Expression of Uncertainty in Measurement (GUM) – Supplement 1: Numerical Methods for the Propagation of Distributions / International Organization for Standardization. Geneva, Switzerland, 1998. – Standard
- [ISO/GUM:1995(E) 1995] ISO: Guide to the Expression of Uncertainty in Measurement / International Organization for Standardization. Geneva, Switzerland, 1995. – Standard. – ISBN 92-67-10188-9
- [Jahn et al. 2011] JAHN, Cord-Hinrich ; FELDMANN-WESTENDORFF, Uwe ; GRÜER, Dieter ; KULLE, Ullrich ; LEMBRECHT, Peter: Die Erneuerung des Deutschen Haupthöhennetzes in Niedersachsen. In: *NaVKV* 4 (2011), pp. 3–7
- [Jain et al. 1999] JAIN, Anil K. ; MURTY, M N. ; FLYNN, Patrick J.: Data clustering: a review. In: *ACM computing surveys (CSUR)* 31 (1999), No. 3, pp. 264–323
- [Kalia et al. 2017] KALIA, Andre C. ; FREI, Michaela ; LEGE, Thomas: A Copernicus downstream-service for the nationwide monitoring of surface displacements in Germany. In: *Remote Sensing of Environment* 202 (2017), pp. 234–249
- [Kalia et al. 2021] KALIA, Andre C. ; FREI, Michaela ; LEGE, Thomas: BodenBewegungsdi-
enst Deutschland (BBD): Konzept, Umsetzung und Service-Plattform. In: *zfv, Zeitschrift für Geodäsie, Geoinformation und Landmanagement* (2021), Dezember, pp. 273–279. – ISSN 1618-8950
- [Kermarrec & Morgenstern 2022] KERMARREC, Gaël ; MORGENSTERN, Philipp: Multilevel T-spline Approximation for Scattered Observations with Application to Land Remote Sensing. In: *Computer-Aided Design* 146 (2022), pp. 103193. – URL <https://www.sciencedirect.com/science/article/pii/S001044852200001X>. – <https://doi.org/10.1016/j.cad.2022.103193>. – ISSN 0010-4485

- [Knorr et al. 2000] KNORR, Edwin M. ; NG, Raymond T. ; TUCAKOV, Vladimir: Distance-based outliers: algorithms and applications. In: *The VLDB Journal* 8 (2000), No. 3-4, pp. 237–253
- [Kongsberg Maritime 2013] KONGSBERG MARITIME: *EM2040C Multibeam Echo Sounder: Product Specification*. Hamburg: Kongsberg Maritime AS (Conf.), 2013. – URL <https://www.kongsberg.com/globalassets/kongsberg-discovery/commerce/seafloor-mapping/em2040c-mkii/em-2040-c-kompaktes-facherecholot-fur-flachwasser/>. – Rev. C
- [Lancaster & Salkauskas 1981] LANCASTER, Peter ; SALKAUSKAS, Kestutis: Surfaces generated by moving least squares methods. In: *Mathematics of Computation* 37 (1981), No. 155, pp. 141–158
- [Le Deunf et al. 2020] LE DEUNF, Julian ; DEBESE, Nathalie ; SCHMITT, Thierry ; BILLOT, Romain: A Review of Data Cleaning Approaches in a Hydrographic Framework with a Focus on Bathymetric Multibeam Echosounder Datasets. In: *Geosciences* 10 (2020), No. 7, pp. 254. – <https://doi.org/10.3390/geosciences10070254>
- [Lee et al. 1995] LEE, Seung-Yong ; CHWA, Kyung-Yong ; SHIN, Sung Y. ; WOLBERG, George: Image metamorphosis using snakes and free-form deformations. In: *SIGGRAPH* Vol. 95 Citeseer (Conf.), 1995, pp. 439–448
- [Lee et al. 1996] LEE, Seungyong ; WOLBERG, George ; CHWA, Kyung-Yong ; SHIN, Sung Y.: Image metamorphosis with scattered feature constraints. In: *IEEE Transactions on Visualization and Computer Graphics* 2 (1996), No. 4, pp. 337–354
- [Lee et al. 1997] LEE, Seungyong ; WOLBERG, George ; SHIN, Sung Y.: Scattered data interpolation with multilevel B-splines. In: *IEEE transactions on visualization and computer graphics* 3 (1997), No. 3, pp. 228–244
- [Li et al. 2010] LI, Xin ; DENG, Jiansong ; CHEN, Falai: Polynomial splines over general T-meshes. In: *The Visual Computer* 26 (2010), No. 4, pp. 277–286
- [Li et al. 2012] LI, Xin ; ZHENG, Jianmin ; SEDERBERG, Thomas W. ; HUGHES, Thomas J. ; SCOTT, Michael A.: On linear independence of T-spline blending functions. In: *Computer Aided Geometric Design* 29 (2012), No. 1, pp. 63–76. – URL <https://www.sciencedirect.com/science/article/pii/S0167839611000938>. – Geometric Constraints and Reasoning. – ISSN 0167-8396
- [Li et al. 2015] LI, Zhi W. ; YANG, Ze F. ; ZHU, Jian J. ; HU, Jun ; WANG, Yun J. ; LI, Pei X. ; CHEN, Guo L.: Retrieving three-dimensional displacement fields of mining areas from a single InSAR pair. In: *Journal of Geodesy* 89 (2015), No. 1, pp. 17–32
- [Lim & Haron 2014] LIM, Seng P. ; HARON, Habibollah: Surface reconstruction techniques: a review. In: *Artificial Intelligence Review* 42 (2014), No. 1, pp. 59–78
- [Lindgren et al. 2011] LINDGREN, Finn ; RUE, Håvard ; LINDSTRÖM, Johan: An Explicit Link between Gaussian Fields and Gaussian Markov Random Fields: The Stochastic Partial Differential Equation Approach. In: *Journal of the Royal Statistical Society Series B: Statistical Methodology* 73 (2011), No. 4, pp. 423–498. – ISSN 1369-7412
- [Lirakis & Bongiovanni 2000] LIRAKIS, Christopher B. ; BONGIOVANNI, Kevin P.: Outlier detection for swath bathymetric data sets. In: *Oceanic Imaging Conference, 2000*
- [Long et al. 2023] LONG, Jiawei ; ZHANG, Hongmei ; ZHAO, Jianhu: A Comprehensive Deep Learning-Based Outlier Removal Method for Multibeam Bathymetric Point Cloud. In: *IEEE Transactions on Geoscience and Remote Sensing* 61 (2023), pp. 1–22

- [Lorenz et al. 2021] LORENZ, Felix ; ARTZ, Thomas ; BRÜGGEMANN, Thomas ; REICH, Julius ; WEISS, Robert ; WINTERSCHIED, Axel: Simulation-based Evaluation of Hydrographic Data Analysis for Dune Tracking on the River Rhine. In: *PFG – Journal of Photogrammetry, Remote Sensing and Geoinformation Science* 89 (2021), No. 2, pp. 111–120. – <https://doi.org/10.1007/s41064-021-00145-0>. – ISSN 2512-2789
- [Lu et al. 2010a] LU, Dan ; LI, Haisen ; WEI, Yukuo ; ZHOU, Tian: Automatic outlier detection in multibeam bathymetric data using robust LTS estimation. In: TAN, Zheng-Hua (Ed.): *2010 3rd International Congress on Image and Signal Processing (CISP 2010)*. Piscataway, NJ : IEEE, 2010, pp. 4032–4036. – <https://doi.org/10.1109/CISP.2010.5648184>. – ISBN 978-1-4244-6513-2
- [Lu et al. 2010b] LU, Dan ; LI, Haisen ; WEI, Yukuo ; ZHOU, Tian: Automatic outlier detection in multibeam bathymetric data using robust LTS estimation. In: *2010 3rd International Congress on Image and Signal Processing* Vol. 9, 2010, pp. 4032–4036
- [Lucieer et al. 2016] LUCIEER, Vanessa ; HUANG, Zhi ; SIWABESSY, Justy: Analyzing Uncertainty in Multibeam Bathymetric Data and the Impact on Derived Seafloor Attributes. In: *Marine Geodesy* 39 (2016), No. 1, pp. 32–52. – <https://doi.org/10.1080/01490419.2015.1121173>. – ISSN 0149-0419
- [Lurton 2003] LURTON, Xavier: Theoretical modelling of acoustical measurement accuracy for swath bathymetric sonars. In: *International Hydrographic Review* 4 (2003), pp. 17–30
- [Lurton 2010] LURTON, Xavier: *An Introduction to Underwater Acoustics: Principles and Applications*. 2. Springer Berlin, Heidelberg, 2010 (Springer Praxis Books). – Jointly published with Praxis Publishing, UK. – ISBN 978-3-540-78480-7
- [Lurton & Augustin 2010] LURTON, Xavier ; AUGUSTIN, Jean-Marie: A measurement quality factor for swath bathymetry sounders. In: *IEEE Journal of Oceanic Engineering* 35 (2010), pp. 852–862
- [Maleika 2013] MALEIKA, Wojciech: The influence of track configuration and multibeam echosounder parameters on the accuracy of seabed DTMs obtained in shallow water. In: *Earth Science Informatics* 6 (2013), No. 2, pp. 47–69. – URL <https://link.springer.com/article/10.1007/s12145-013-0111-9>. – <https://doi.org/10.1007/s12145-013-0111-9>. – ISSN 1865-0481
- [Massey Jr 1951] MASSEY JR, Frank J.: The Kolmogorov-Smirnov Test for Goodness of Fit. In: *Journal of the American Statistical Association* (1951), No. 46, pp. 68–78. – ISSN 0162-1459
- [Mohammadivojdan 2019] MOHAMMADIVOJDAN, Bahareh: *Surface Based Modelling of Ground Motion Areas in Lower Saxony*. Hannover, Germany, Leibniz Universität Hannover, Geodätisches Institut Hannover, Master’s thesis, Oktober 2019. – Masterarbeit. German title: Flächenhafte Modellierung von Bodenbewegungsgebieten in Niedersachsen. Examiners: Ingo Neumann and Cord-Hinrich Jahn. Supervisors: Hamza Alkhatib and Marco Brockmeyer.
- [Mohammadivojdan et al. 2020] MOHAMMADIVOJDAN, Bahareh ; ALKHATIB, Hamza ; BROCKMEYER, Marco ; JAHN, Cord-Hinrich ; NEUMANN, Ingo: *Surface Based Modelling of Ground Motion Areas in Lower Saxony*. Hannover : Institutionelles Repositorium der Leibniz Universität Hannover, 2020. – 107–122 p. – <https://doi.org/10.15488/9344>
- [Mohammadivojdan et al. 2021] MOHAMMADIVOJDAN, Bahareh ; BROCKMEYER, Marco ; JAHN, Cord-Hinrich ; NEUMANN, Ingo ; ALKHATIB, Hamza: Regional Ground Movement Detection by Analysis and Modeling PSI Observations. In: *Remote Sensing* 13 (2021), No. 12, pp. 2246
- [Mohammadivojdan et al. 2025] MOHAMMADIVOJDAN, Bahareh ; HAKE, Frederic ; LORENZ, Felix ; BÖLLERT, Jan-Ole ; WEISS, Robert ; ARTZ, Thomas ; NEUMANN, Ingo ; ALKHATIB,

- Hamza: Enhancing digital bathymetric models by advanced measurement uncertainty analysis. In: *The International Hydrographic Review* 31(1) (2025), pp. 28–50. – URL <https://ihr.iho.int>. – <https://doi.org/10.58440/ihr-31-1-a09>
- [Mohammadivojdan et al. 2024] MOHAMMADIVOJDAN, Bahareh ; LORENZ, Felix ; ARTZ, Thomas ; WEISS, Robert ; HAKE, Frederic ; ALKHATIB, Yazan ; NEUMANN, Ingo ; ALKHATIB, Hamza: Robust algorithm for automatic surface-based outlier detection in MBES point clouds. In: *Marine Geodesy* 48 (2024), No. 2, pp. 141–172. – <https://doi.org/10.1080/01490419.2024.2408684>
- [Montella et al. 2018] MONTELLA, Raffaele ; MARCELLINO, Livia ; GALLETTI, Ardelio ; DI LUCCIO, Diana ; KOSTA, Sokol ; LACCETTI, Giuliano ; GIUNTA, Giulio: Marine Bathymetry Processing Through GPGPU Virtualization in High-Performance Cloud Computing. In: *Concurrency and Computation: Practice and Experience* 30 (2018), No. 24. – ISSN 1532-0626
- [Moran 1950] MORAN, Patrick Alfred P.: Notes on Continuous Stochastic Phenomena. In: *Biometrika* 37 (1950), 06, No. 1-2, pp. 17–23. – URL <https://doi.org/10.1093/biomet/37.1-2.17>. – ISSN 0006-3444
- [Moreira et al. 2013] MOREIRA, Alberto ; PRATS-IRAOLA, Pau ; YOUNIS, Marwan ; KRIEGER, Gerhard ; HAJNSEK, Irena ; PAPATHANASSIOU, Konstantinos P.: A tutorial on synthetic aperture radar. In: *IEEE Geoscience and Remote Sensing Magazine* 1 (2013), No. 1, pp. 6–43. – <https://doi.org/10.1109/MGRS.2013.2248301>
- [Niu et al. 2024] NIU, Tianlin ; SHAO, Zhenying ; ZHU, Geyi: Toward greener freight: Overview of inland waterway transport for freight in the European Union / International Council on Clean Transportation. URL https://theicct.org/wp-content/uploads/2024/08/ID-152-%E2%80%93-93-Inland-waterway_final.pdf. – Accessed: 2025-08-28, aug 2024 (ID 152). – Research Brief
- [Nowacki et al. 1998] NOWACKI, Horst ; WESTGAARD, Geir ; HEIMANN, Justus: *Creation of fair surfaces based on higher order fairness measures with interpolation constraints*. B. G. Teubner, 1998
- [Nuckelt 2007] NUCKELT, André: *Dreidimensionale Plattenkinematik: Strainanalyse auf B-Spline-Approximationsflächen am Beispiel der Vrancea-Zone/Rumänien*. Univ.-Verlag Karlsruhe, 2007
- [Ogayar-Anguita et al. 2023] OGAYAR-ANGUITA, Carlos J. ; LÓPEZ-RUIZ, Alfonso ; RUEDA-RUIZ, Antonio J. ; SEGURA-SÁNCHEZ, Rafael J.: Nested spatial data structures for optimal indexing of LiDAR data. In: *ISPRS Journal of Photogrammetry and Remote Sensing* 195 (2023), pp. 287–297. – URL <https://www.sciencedirect.com/science/article/pii/S0924271622003112>. – ISSN 0924-2716
- [Oreni et al. 2014] ORENI, Daniela ; BRUMANA, Raffaella ; DELLA TORRE, Stefano ; BANFI, Fabrizio ; BARAZZETTI, Luigi ; PREVITALI, Mattia et al.: Survey turned into HBIM: the Basilica di Collemaggio 3D model from laser data to interpretive model. In: *ISPRS Annals of Photogrammetry, Remote Sensing and Spatial Information Sciences* II-5 (2014), pp. 267–273. – <https://doi.org/10.5194/isprsannals-II-5-267-2014>
- [Paffenholz & Wujanz 2019] PAFFENHOLZ, Jens-André ; WUJANZ, Daniel: Spatio-temporal monitoring of a bridge based on 3D point clouds – A comparison among several deformation measurement approaches. In: *Proceedings of the 4th Joint International Symposium on Deformation Monitoring (JISDM)*. Athens, Greece, 2019, pp. 1–7. – 15th – 17th May 2019
- [Pannatier 2012] PANNATIER, Yvan: *VARIOWIN: Software for spatial data analysis in 2D*. Springer Science & Business Media, 2012

- [Papadimitriou et al. 2003] PAPANIMITRIOU, Spiros ; KITAGAWA, Hiroyuki ; GIBBONS, Phillip B. ; FALOUTSOS, Christos: Loci: Fast outlier detection using the local correlation integral. In: *Proceedings 19th international conference on data engineering (Cat. No. 03CH37405)* IEEE (Conf.), 2003, pp. 315–326
- [Patane 2016] PATANE, Giuseppe: Heterogeneous data approximation for terrain modeling in GIS. In: *Mathematics of Surfaces XIV*. Springer, 2016, pp. 65–102
- [Patrizi et al. 2020] PATRIZI, Francesco ; MANNI, Carla ; PELOSI, Francesca ; SPELEERS, Hendrik: Adaptive refinement with locally linearly independent LR B-splines: Theory and applications. In: *Computer Methods in Applied Mechanics and Engineering* 369 (2020), pp. 113230
- [Peter 2000] PETER, Yannick F.: *Present-day crustal dynamics in the Adriatic-Aegean plate boundary zone inferred from continuous GPS-measurements*, ETH Zurich, Dissertation, 2000
- [Pfeifer & Winterhalder 2004] PFEIFER, Norbert ; WINTERHALDER, Daniel: Modelling of tree cross sections from terrestrial laser scanning data with free-form curves. In: *International Archives of Photogrammetry, Remote Sensing and Spatial Information Sciences* 36 (2004), No. 8, pp. 1–6
- [Piegl & Tiller 1997] PIEGL, L. ; TILLER, W.: *The NURBS Book*. 2. Berlin : Springer, 1997
- [Poland 1984] POLAND, Joseph F.: *Guidebook to Studies of Land Subsidence Due to Ground-Water Withdrawal*. Chelsea, Massachusetts : Book Crafters, 1984. – 16 p. – Prepared for the International Hydrological Programme, Working Group 8.4, UNESCO
- [R. Hare et al. 2011] R. HARE ; B. EAKINS ; C. AMANTE: Modelling Bathymetric Uncertainty. In: *The International Hydrographic Review* (2011). – URL <https://journals.lib.unb.ca/index.php/ihr/article/view/20888>. – ISSN 0020-6946
- [Raja & Fernandes 2008] RAJA, Vinesh ; FERNANDES, Kiran J.: *Reverse Engineering*. London : Springer London, 2008. – <https://doi.org/10.1007/978-1-84628-856-2>
- [Ronczyk et al. 2022] RONCZYK, Levente ; ZELENKA-HEGYI, András ; TÖRÖK, Gábor ; ORBÁN, Zoltán ; DEFILIPPI, Marco ; KOVÁCS, István P. ; KOVÁCS, Dániel M. ; BURAI, Péter ; PASQUALI, Paolo: Nationwide, Operational Sentinel-1 Based InSAR Monitoring System in the Cloud for Strategic Water Facilities in Hungary. In: *Remote Sensing* 14 (2022), No. 14. – URL <https://www.mdpi.com/2072-4292/14/14/3251>. – ISSN 2072-4292
- [Rousseeuw 1987] ROUSSEEUW, Peter J.: *Robust regression and outlier detection*. New York : Wiley, 1987 (Wiley series in probability and mathematical statistics. Applied probability and statistics). – <https://doi.org/10.1002/0471725382>. – ISBN 9780471852339
- [Saranti et al. 2024] SARANTI, Anna ; PFEIFER, Bastian ; GOLLOB, Christoph ; STAMPFER, Karl ; HOLZINGER, Andreas: From 3D point-cloud data to explainable geometric deep learning: State-of-the-art and future challenges. In: *WIREs Data Mining and Knowledge Discovery* 14 (2024), No. 6. – ISSN 1942-4787
- [Schumaker 1976] SCHUMAKER, Larry L.: Fitting surfaces to scattered data / TEXAS UNIV AT AUSTIN DEPT OF MATHEMATICS. 1976. – Research report
- [Schumaker & Wang 2012] SCHUMAKER, Larry L. ; WANG, Lujun: Approximation power of polynomial splines on T-meshes. In: *Computer Aided Geometric Design* 29 (2012), No. 8, pp. 599–612. – URL <https://www.sciencedirect.com/science/article/pii/S0167839612000556>. – ISSN 0167-8396

- [Schütz et al. 2020] SCHÜTZ, Markus ; OHRHALLINGER, Stefan ; WIMMER, Michael: Fast Out-of-Core Octree Generation for Massive Point Clouds. In: *Computer Graphics Forum* 39 (2020), No. 7, pp. 155–167. – ISSN 0167-7055
- [Scott et al. 2012] SCOTT, Michael A. ; LI, Xin ; SEDERBERG, Thomas W. ; HUGHES, Thomas J.: Local refinement of analysis-suitable T-splines. In: *Computer Methods in Applied Mechanics and Engineering* 213-216 (2012), pp. 206–222. – URL <https://www.sciencedirect.com/science/article/pii/S0045782511003689>. – <https://doi.org/10.1016/j.cma.2011.11.022>. – ISSN 0045-7825
- [Sederberg et al. 2003] SEDERBERG, Thomas W. ; ZHENG, Jianmin ; BAKENOV, Almaz ; NASRI, Ahmad: T-splines and T-NURCCs. In: *ACM Trans. Graph.* 22 (2003), Juli, No. 3, pp. 477–484. – URL <https://doi.org/10.1145/882262.882295>. – ISSN 0730-0301
- [Shamshiri et al. 2014] SHAMSHIRI, Roghayeh ; MOTAGH, Mahdi ; BAES, Marzieh ; SHARIFI, Mohammad A.: Deformation analysis of the Lake Urmia causeway (LUC) embankments in northwest Iran: insights from multi-sensor interferometry synthetic aperture radar (InSAR) data and finite element modeling (FEM). In: *Journal of Geodesy* 88 (2014), No. 12, pp. 1171–1185
- [Shen et al. 2011] SHEN, Jing ; LIU, Jiping ; ZHAO, Rong ; LIN, Xiangguo: A kd-tree-based outlier detection method for airborne LiDAR point clouds. In: *2011 International Symposium on Image and Data Fusion IEEE (Conf.)*, 2011, pp. 1–4
- [Shepard 1968] SHEPARD, Donald: A two-dimensional interpolation function for irregularly-spaced data. In: *Proceedings of the 1968 23rd ACM national conference* (1968), pp. 517–524
- [Skolnik 1962] SKOLNIK, Merrill I.: *Introduction to Radar Systems*. Tokyo : McGraw-Hill Kogakusha, Ltd., 1962
- [Skytt et al. 2017] SKYTT, Vibeke ; HARPHAM, Quillon ; DOKKEN, Tor ; DAHL, Heidi E. I.: Deconfliction and Surface Generation from Bathymetry Data Using LR B-splines. In: FLOATER, Michael (Ed.) ; LYCHE, Tom (Ed.) ; MAZURE, Marie-Laurence (Ed.) ; MØRKEN, Knut (Ed.) ; SCHUMAKER, Larry L. (Ed.): *Mathematical Methods for Curves and Surfaces*. Cham : Springer International Publishing, 2017, pp. 270–295. – ISBN 978-3-319-67885-6
- [Sotoodeh 2007] SOTOODEH, Soheil: Hierarchical clustered outlier detection in laser scanner point clouds. In: *International Archives of the Photogrammetry, Remote Sensing and Spatial Information Sciences* 36 (2007), No. 3/W52, pp. 383–388
- [Spreckels 2023] SPRECKELS, Volker: Multisensor monitoring of ground movements over large areas to conduct the change from the active underground hard coal mining ages to the post-mining era. In: *5th Joint International Symposium on Deformation Monitoring (JISDM 2022)* Editorial Universitat Politècnica de València (Conf.), 2023, pp. 637–644
- [Stephens et al. 2020] STEPHENS, David ; SMITH, Andrew ; REDFERN, Thomas ; TALBOT, Andrew ; LESSNOFF, Andrew ; DEMPSEY, Kari: Using three dimensional convolutional neural networks for denoising echosounder point cloud data. In: *Applied Computing and Geosciences* 5 (2020), pp. 100016. – URL <https://www.sciencedirect.com/science/article/pii/S2590197419300163>. – ISSN 2590-1974
- [Straub 1996] STRAUB, Christian: *Recent crustal deformation and strain accumulation in the Marmara Sea region, NW Anatolia, inferred from GPS measurements*, ETH Zurich, Dissertation, 1996
- [Strozzi et al. 2001] STROZZI, Tazlo ; WEGMULLER, Urs ; TOSI, Luigi ; BITELLI, Gabrlele ; SPRECKELS, Volker et al.: Land subsidence monitoring with differential SAR interferometry. In: *Photogrammetric engineering and remote sensing* 67 (2001), No. 11, pp. 1261–1270

- [Tengku Ali et al. 2022] TENGKU ALI, Tengku A. ; ABBAS, Mohd A. ; MUSTAFAR, Mohamad A. ; SAID, Mohd Shahmy M. ; HASHIM, Norshahrizan M. ; SULAIMAN, Saiful A.: Investigating the Vertical Uncertainty in MBES Measurements. In: *2022 IEEE 18th International Colloquium on Signal Processing & Applications (CSPA)*, 2022, pp. 431–435. – <https://doi.org/10.1109/CSPA55076.2022.9781857>
- [Tobler 1970] TOBLER, Waldo R.: A computer movie simulating urban growth in the Detroit region. In: *Economic geography* 46 (1970), No. sup1, pp. 234–240
- [Vásquez et al. 2007] VÁSQUEZ, Miguel E. ; NICHOLS, S ; CLARKE, JH et al.: *Tuning the CARIS implementation of CUBE for Patagonian Waters.*, Master’s Thesis, Department of Geodesy and Geomatics Engineering, The University of New Brunswick, New Brunswick, Canada., Dissertation, 2007
- [Viard et al. 2011] VIARD, Thomas ; CAUMON, Guillaume ; LÉVY, Bruno: Adjacent versus coincident representations of geospatial uncertainty: Which promote better decisions? In: *Computers & Geosciences* 37 (2011), No. 4, pp. 511–520. – <https://doi.org/10.1016/j.cageo.2010.08.004>
- [Vosselman & Maas 2010] VOSSELMAN, George (Ed.) ; MAAS, Hans-Gerd (Ed.): *Airborne and terrestrial laser scanning.* Whittles Publishing, 2010. – ISBN 978-1904445-87-6
- [Wackernagel 2003] WACKERNAGEL, Hans: *Multivariate Geostatistics: An Introduction with Applications.* 3. Springer Berlin, Heidelberg, 2003. – XV+388 p. – <https://doi.org/10.1007/978-3-662-05294-5>. – ISBN 978-3-540-44142-7
- [Wiley 1965] WILEY, Carl A.: *Pulsed Doppler Radar Methods and Apparatus.* U.S. Patent US3196436A. 1965. – Filed July 23, 1954. Issued July 20, 1965
- [WSA 2023] WSA: *Wasserstraßen- und Schifffahrtsamt Elbe-Weser.* 2023. – URL https://www.wsa-elbe.wsv.de/Webs/WSA/Elbe-Nordsee/DE/1_Wasserstrassen/4_SchiffeMaschinenwesen/UJLornsen/ujlornsen_node.html. – Accessed: 2024-01-05
- [Wu et al. 2021] WU, Ziyin ; YANG, Fanlin ; TANG, Yong: *Multi-beam Bathymetric Technology.* pp. 21–76. In: *High-resolution Seafloor Survey and Applications.* Singapore : Springer Singapore, 2021. – https://doi.org/10.1007/978-981-15-9750-3_2. – ISBN 978-981-15-9750-3
- [You et al. 2020] YOU, Cheng C. ; LIM, Seng P. ; LIM, Seng C. ; TAN, Joi S. ; LEE, Chen K. ; KHAW, Yen Min J.: A survey on surface reconstruction techniques for structured and unstructured data. In: *2020 IEEE Conference on Open Systems (ICOS)*, IEEE, 2020, pp. 37–42

List of Figures

1.1	Examples of outlier types: isolated points and spatially coherent clusters.	5
1.2	Overview of original publications on the cumulative dissertation.	6
1.3	PSI data of Hengstlage.	11
1.4	PSI point distribution over the Hanover region.	12
1.5	Geometry of an MBES system.	13
1.6	Fundamental time-angle measurement of bathymetry by a MBES system.	14
1.7	Survey area of the Kiel Canal.	16
1.8	Survey vessel UJL.	16
1.9	A 100 m segment of MBES PC from the Kiel Canal.	17
1.10	Simulated geometry as a PC.	17
2.1	Conceptual view of observation deviation scores.	20
3.1	Schematic representation of the "Data Adaptive Outlier Detection" approach.	34
3.2	Histogram of residuals after each iteration of the IESP algorithm.	36
3.3	Hannover data; detected outliers (red) vs. inliers (blue).	36
3.4	Flowchart of IESP algorithm.	38
3.5	Details of IESP iterations on a section of the Kiel Canal data.	39
3.6	Schematic representation of the MBA concept.	42
3.7	Simulator input for the evaluation of MBA.	44
3.8	MC simulation results for evaluation of MBA.	45
3.9	Modeled ground movement in Hengstlage.	46
3.10	Illustrative 2D example of the bootstrapping method.	48
3.11	Bootstrapping; 3D visualization of CIs for the MBA model.	49
3.12	Bootstrapping; Profile line selection and observational context.	50
3.13	Bootstrapping; CIs along Line 1.	50
3.14	Bootstrapping; CIs along Line 2.	50
3.15	Estimated 95 % CI heatmaps for PSI-based regional ground movement.	51
3.16	Overview of the MC simulation experiment workflow for uncertainty integration.	53
3.17	Comparison of surface models and their uncertainty distributions.	54
A.1	Configuration of control lattice Φ	163
A.2	Positional relationship between data and control points.	165
A.3	Schematic representation of control lattice refinement in MBA.	168

List of Tables

3.1	Mapping of research questions to publications.	31
3.2	Confusion matrix.	35
3.3	Performance metrics for outlier classification.	35
3.4	Comparison of the "Data Adaptive Outlier Detection" with results of Brockmeyer et al. (2020).	37
3.5	Results of IESP's algorithm on the Kiel Canal data (Publication B).	40
4.1	Evidence supporting RQ1.	56
A.1	Stochastic model of MBA algorithm.	172

List of Algorithms

- 1 MC Simulation (Publication D). 44
- 2 BA Algorithm (Lee et al., 1997). 166
- 3 MBA Algorithm (Lee et al., 1997). 167
- 4 Refinement and accumulation to obtain the final control lattice Ψ_h 169

Acknowledgments

This dissertation was completed with the help of many people, and I would like to express my sincere gratitude to all of them.

First and foremost, I thank Prof. Dr.-Ing. Ingo Neumann. His trust made it possible for me to pursue this work at the Geodetic Institute of Leibniz University Hannover. I am grateful for the academic freedom he provided, for his clear expectations, and for his steady encouragement to aim for strong, well-founded results. His perspective and feedback helped shape both the direction of the research and the final dissertation.

I am particularly grateful to PD Dr.-Ing. Hamza Alkhatib for his guidance and continued commitment throughout the entire process. His careful comments, constructive critique, and practical advice were essential at every stage. I especially valued our discussions, which helped me refine ideas, resolve uncertainties, and move forward with a clear plan. I also appreciate his patience, reliability, and the confidence he conveyed during both productive phases and challenging periods.

I am grateful to the members of my examination committee. I thank Prof. Dr.-Ing. habil. Christian Heipke for chairing the committee. I thank Prof. Dr.-Ing. habil. Jürgen Müller and Prof. Dr. techn. Corinna Harmening for serving as co-reviewers and for their careful reading and valuable comments.

I also thank my colleagues at the Geodetic Institute for the friendly and constructive working atmosphere. Many conversations, shared problem-solving moments, and day-to-day cooperation contributed to this dissertation in important ways.

Finally, I thank my family and friends. Your encouragement and patience carried me through the long phases of this work. Thank you for understanding when my time was limited, for listening when problems felt overwhelming, and for reminding me that progress often comes in small steps. You kept me grounded, helped me keep perspective, and made the demanding periods easier to handle. This dissertation is also a reflection of your faith in me.

Curriculum Vitae

Personal Information

Name: Bahareh Mohammadivojdan
Date of Birth: 23.07.1990
Place of Birth: Kermanshah, Iran

Work Experience

since 10.2019 Geodetic Institute
Leibniz Universität Hannover
Research Assistant

11.2017 – 09.2019 Geodetic Institute
Leibniz Universität Hannover
Student Assistant

Education

12.2019 – 12.2025 Geodetic Institute
Leibniz Universität Hannover
PhD student

10.2016 – 09.2019 Degree Course Geodesy and Geoinformatics
Leibniz Universität Hannover
Master of Science

10.2012 – 04.2015 Degree Course Structural Engineering
Razi University of Kermanshah
Master of Science

10.2008 – 08.2012 Degree Course Civil Engineering
Razi University of Kermanshah
Bachelor of Science

